AUGUST, 2020

COMPUTATIONAL MODELING OF A 50 kWth INDIRECTLY HEATED BUBBLING FLUIDIZED BED STEAM REFORMER

FIDLLAN NURKHOIR

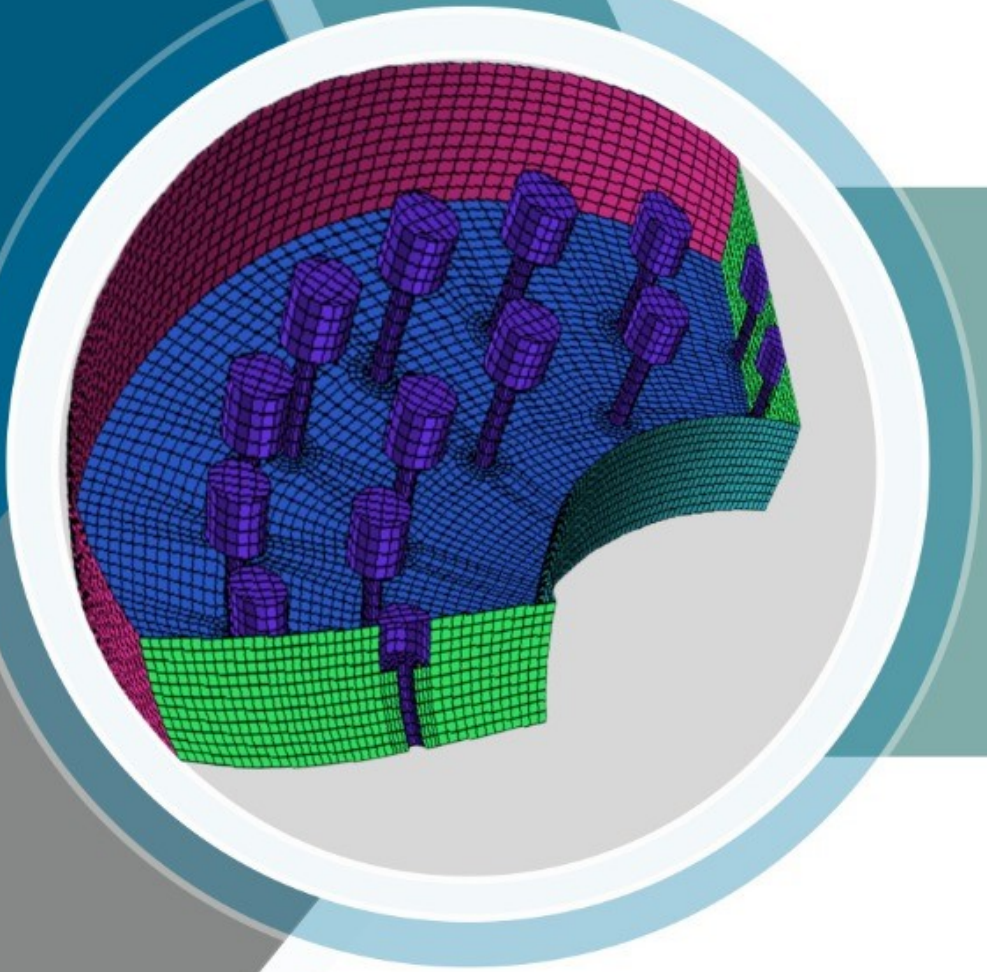

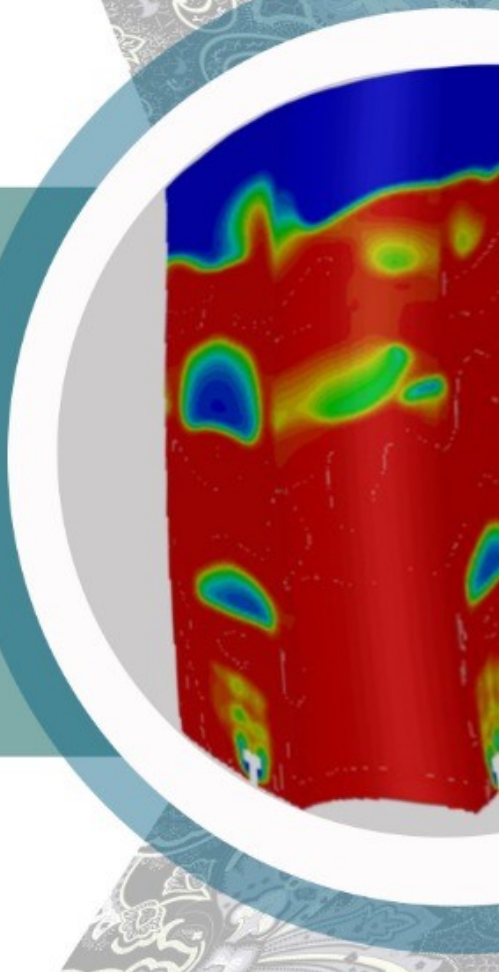

TU Delft Delft University of Technology

lpdp lembaga pengelola dana pendidikan

PETROGAS GAS SYSTEMS

Computational Modeling of A 50 kWth Indirectly Heated Bubbling Fluidized Bed Steam Reformer

by

FIDLLAN NURKHOIR

towards partial fulfillment for the degree of

MASTER OF SCIENCE

in Sustainable Energy Technology
Track - Biomass & Solar Systems
at the faculty of Electrical Engineering, Mathematics and Computer Science,
Delft University of Technology

to be defended publicly on Friday, 21 August 2020.

Student number:	4796500	
Project duration:	January 2020 – August 2020	
Daily supervisor:	Christos Tsekos M.Sc.	
Thesis committee:	Prof. Dr. Ir. J. T. Padding,	Supervisor, Chair
	Prof. Dr. D. J. E. M. Roekaerts,	Supervisor
	Dr. E. M. Moghaddam,	Supervisor
	Dr. Ir. J. W. R. Peeters,	

TU Delft Delft University of Technology

lpdp lembaga pengelola dana pendidikan

PETROGAS GAS SYSTEMS

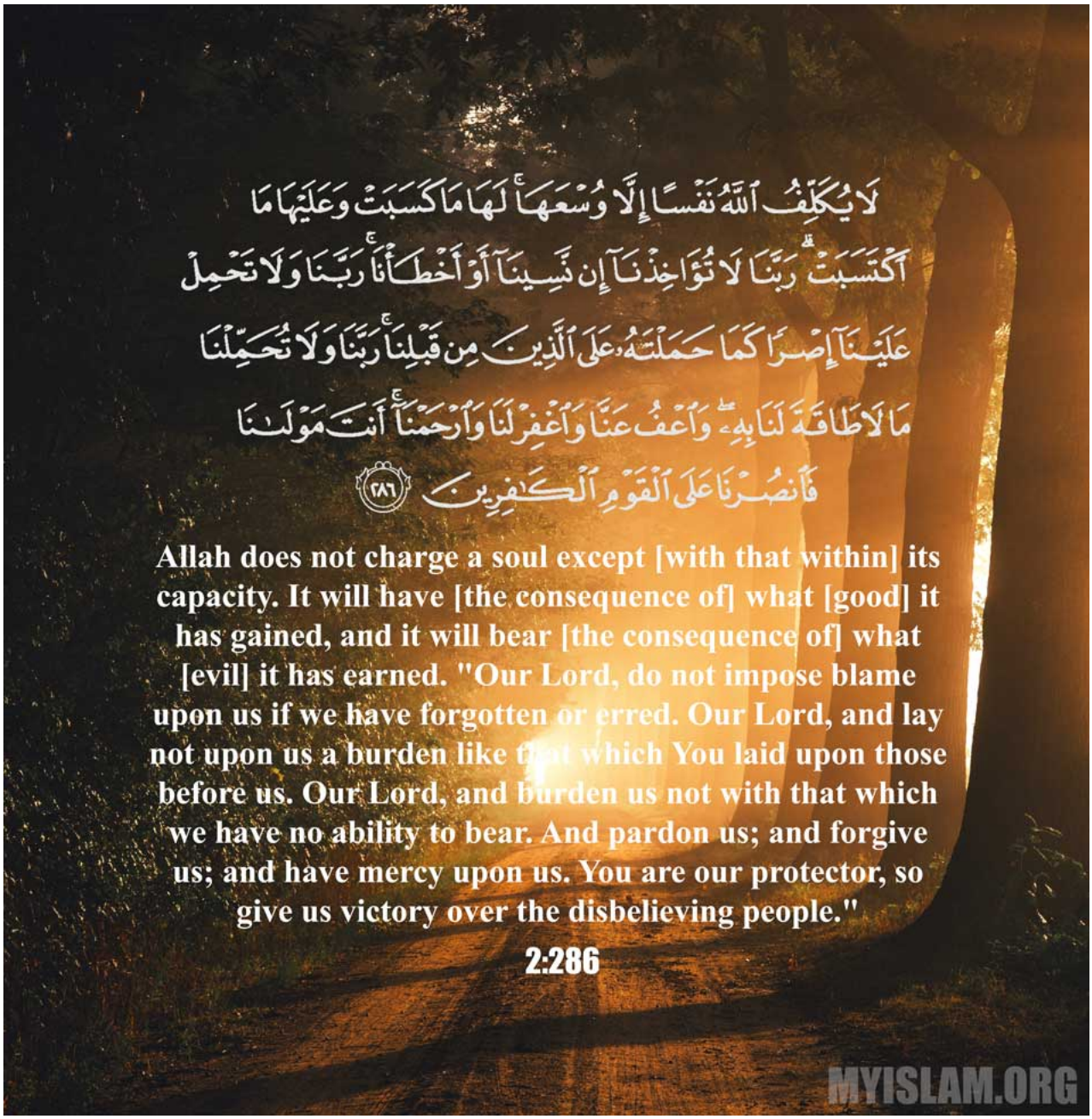
لَا يُكَلِّفُ ٱللَّهُ نَفْسًا إِلَّا وُسْعَهَا ۚ لَهَا مَا كَسَبَتْ وَعَلَيْهَا مَا
ٱكْتَسَبَتْ ۗ رَبَّنَا لَا تُؤَاخِذْنَآ إِن نَّسِينَآ أَوْ أَخْطَأْنَا ۚ رَبَّنَا وَلَا تَحْمِلْ
عَلَيْنَآ إِصْرًا كَمَا حَمَلْتَهُۥ عَلَى ٱلَّذِينَ مِن قَبْلِنَا ۚ رَبَّنَا وَلَا تُحَمِّلْنَا
مَا لَا طَاقَةَ لَنَا بِهِۦ ۖ وَٱعْفُ عَنَّا وَٱغْفِرْ لَنَا وَٱرْحَمْنَآ ۚ أَنتَ مَوْلَىٰنَا
فَٱنصُرْنَا عَلَى ٱلْقَوْمِ ٱلْكَٰفِرِينَ ٢٨٦
Allah does not charge a soul except [with that within] its capacity. It will have [the consequence of] what [good] it has gained, and it will bear [the consequence of] what [evil] it has earned. "Our Lord, do not impose blame upon us if we have forgotten or erred. Our Lord, and lay not upon us a burden like that which You laid upon those before us. Our Lord, and burden us not with that which we have no ability to bear. And pardon us; and forgive us; and have mercy upon us. You are our protector, so give us victory over the disbelieving people."
2:286
MYISLAM.ORG

Acknowledgements

First and foremost, I would like to say "Alhamdulillahi rabbil 'Alamin," all the praises and thanks be to Allah, the Lord of the universe. The enormous support from my parents and my little family who have accompanied me in Delft, for the support they have given to me. Without their blessings, I wouldn't even have the means to come here at T.U. Delft in the first place. Heartfelt thanks to the love of my life, Devie my wife, and my little baby Chayra for being the pillars of my confidence through this master's journey and being there for me through thick and thin.

Special Thanks to Prof. Dr. Ir. J.T. Padding and Prof. Dr. D.J.E.M. Roekaerts, for being my thesis supervisor. Your guidance and inputs from time to time have been monumental towards the work I have been able to do in this thesis. Dr. Ir. E. M. Moghaddam that taught me all about C.F.D. modeling from scratch and helped me set up the simulation since the very beginning. Christos, who had been a critical and meticulous daily supervisor on guiding me through phase by the phase of my thesis work, even for his great contribution to building this masterpiece of mine. Also to Dr.ir. J.W.R. Peeters for giving me the privilege of having you onboard in my thesis committee.

This Graduation thesis would not have been possible without the support system around me. Special mention to Dr. Ir. M.J.B.M. Pourquie for being a very nice cluster system admin who always responds as fast as light, and tries his best effort to fix all issues. Deepest gratitude for my S.E.T. fellow, Rasyid, who always be an excellent partner for teamwork and discussion, and Indra for all the motivational support as my "bezorging" peep and Indonesia's Muslim activist for helping me charging my spiritual level to its fullest.

Fidllan Nurkhoir
August 14, 2020

Abstract

The CFD modeling based on the two-fluid model (TFM) was used on studying the novel indirectly heated bubbling fluidized bed steam reformer (IHBFB-SR). This is a collaborative project between Petrogas and TU Delft for testing the advance's reactor configuration, which indirectly supplies the heat via radiant burner on the center toward the surrounding bed, thereby improving heat transfer efficiency and reduced the losses. The present work aimed to observe the hydrodynamic and heat transfer of the reactor by first employing air as the fluidizing gas and corundum (Geldart B size) as the bed material. The minimum fluidization condition, bubbles development, and voidage profile are the main objectives for the hydrodynamic simulation. In the heat transfer study, the effect of radiative heat transfer, bubbles and voidage profiles, and different radiative models (P1 and DO) on the heat transfer mechanism were examined. The 2D and 3D models were built, and three drag models: Gidaspow, adjusted Syamlal, and EMMS/Bubbling was employed. The simulation results were then compared to the experimental data obtained, such as minimum fluidization flowrate, pressure drop, bed expansion, and temperature profile on a specific flow rate.

Initially, a grid independency test was conducted using five different grid sizes. It is concluded that the appropriate grid size for simulating the IHBFB-SR with a bed material particle size of 0.496 mm should be at least 7.5 mm or 15 times the corundum particle size. The present research used 2.5 mm or five times dp. The minimum fluidization obtained was in the range of 14-16 kg/h based on both 2D and 3D simulation. Nonetheless, if primarily refers to the 3D model results, the minimum fluidization condition should lie around 14 kg/h. Three drag models have also been compared. It was found that the adjusted Syamlal gives the closest result compared to the experimental data. Nevertheless, the drag modification, based only on minimum fluidization conditions like modified Syamlal, tends to overpredict the drag coefficient on the entire range of solid volume fraction. There are also no significant differences in the bubbles or voidage profiles among those three drag models. Adjusted Syamlal has a slightly larger bubble while Gidaspow and EMMS bubbling has a bit smaller one. The expected better result of using the EMMS bubbling drag model does not appear to have a considerable impact on the case of Geldart B or larger particles. There was also an underprediction of pressure drop and bed expansion on the simulation. Two major factors were the absence of proper particle shape representation through a sphericity factor and the lack of precise simulation of particle size distribution. Only a perfect rounded sphere of corundum with a sphericity factor of one and one uniform size of the particle was assumed .

In the case of heat transfer simulation, bubbles and voidage effect firstly studied. It was found that the increase of the bubbles frequency and size, as represented on the voidage profile, would improve the heat transfer process indicated by the increase of the heat flux. The bubbles' occurrence on the bed plays a critical role in the mass transfer's improvement from and to the vicinity of the radiant burner wall, thus increasing heat transfer. In contrast with the voidage, the increase of superficial gas velocity does not directly influence the heat flux. It was also proved that the radiative heat transfer improved the overall heat flux in this bubbling fluidized bed reactor by about 16.11 %. Though it appears small, this contribution fits the range of other proven works, with a similar operating environment and particle size used. There are two different radiative models performed in the simulation: first-order spherical harmonics method (P1) and discrete ordinate method (DO). Both models presented a similar trend, with P1, has a slightly higher magnitude. However, the P1 model shows a peculiar result of having a strange lower temperature lower on the bottom part of the bed. On the contrary, that is not the case for the DO, which is well known for its accuracy but a higher computational cost demand. It is then concluded that for the present setup, the DO model could perform better. Lastly, the overall heat transfer process was investigated. Since no specific experimental data available for validating the heat transfer properties, only the final steady temperature values of five different thermocouples were used. Comparing these two, it was found that the present model did not give satisfactory results due to overprediction of air temperature above the bed and underprediction of bed temperature at the same time. Some improvements are required, as will be presented in the recommendations section.

Contents

List of Figures

List of Tables

List of Abbreviations

Bcm	Billion cubic metres.
BioHPR	Biomass Heat Pipe Reformer.
CFD	Computational Fluid Dynamics.
CGPM	Coarse Grain Particle Method.
CHP	Combined Heat and Power.
COP21	21st Conference of the Parties.
CPU	Central Processing Unit.
DEM	Discrete Element Method.
DFB	Dual Fluidized Bed.
DO	Discrete Ordinate.
DPM	Discrete Particle Method.
DPRS	Dense Particulate Reaction System.
DTRM	Discrete Transfer Radiation Model.
ECN	Energy research Centre of the Netherlands.
EMMS	Energy Minimization Multi-Scale.
EU	European Union.
FBG	Fluidized Bed Gasifier.
FCC	Fluid Catalytic Craking.
FT	Fischer-Tropsch.
GHG	Greenhouse Gases.
IHBFB-SR	Indirectly Heated Bubbling Fluidised Bed Steam Reformer.
KTGF	Kinetic Theory of Granular Flow.
LES	Large Eddy Simulation.
MFM	Multi-Fluid Model.
PSD	Particle Size Distribution.
PVF	Phase Volume Fraction.
RANS	Reynolds-averaged Navier–Stokes.
RTE	Radiative Transfer Equation.
S2S	Surface to Surface.
SC	Specularity Coefficient.
SF	Sphericity Factor.
SNG	Synthetic Natural Gas.
TDH	Transport Disengaging Height.
TFM	Two-Fluid Model.
UDF	User-Defined Functions.

List of Symbols

Δp_b	Pressure drop accross the bed.
Θ_s	Granular temperature.
α	Volume fraction.
$\alpha_{s,max}$	Maximum packing limit.
β	Extinction coefficient.
ϵ	Voidage .
ϵ_d	Voidage at the intersection of fitting H_d and 1.
ϵ_{mf}	Voidage at minimum fluidization.
η	Wavenumber.
γ_{Θ_s}	Collisional dissipation energy.
κ	Thermal conductivity.
κ_b	Bed thermal conductivity.
κ_{eff}	Effective thermal conductivity.
κ_m	Thermal conductivity of the packet.
λ	Wavelength/bulk viscosity.
μ	Viscosity.
$\mu_{s,col}$	Collisional viscosity.
$\mu_{s,fr}$	Frictional viscosity.
$\mu_{s,kin}$	Kinetic viscosity.
μ_s	Shear viscosity.
ν	Frequency.
ω	Angular frequency.
$\overline{\overline{\tau}}$	Stress-strain tensor.
ϕ	Internal friction angle.
ϕ_s	Sphericity factor.
ρ^s	Hemispherical reflectance.
ρ_g	Gas density.
ρ_{rs}	Volume-averaged density.
ρ_s	Solid density.
σ	Scattering coefficient.
τ	Optical thickness.
A	Interfacial area.
a	Absorption coefficient.
A_m	Contact area of the packet with surface.
A_t	Cross sectional area of tube.
Ar	Archimedes number.
C_{abs}	Absorption cross-section.
C_D	Drag coefficient .
C_{ext}	Extinction cross-section.
C_p	Specific heat.
C_{sca}	Scattering cross-section.
d_{b0}	Initial bubble's diameter.
d_{bm}	Maximum bubble's diameter.
d_b	Bubble's diameter.
d_p	Particle's diameter.
d_p*	Dimensionless particle's diameter.
d_t	Bed's diameter.
e	Emissivity.
e_λ	Hemispherical emissivity.
e_{ss}	Restitution coefficient.
e_{sw}	Restitution coefficient for collisions between particles and the boundary.
f	Drag coefficient.

$g_{0,ss}$	Radial distribution.
h	Volumetric heat transfer coefficient between phases.
H_d	Heterogeneous index .
h_i	Local instantaneous heat transfer coefficient.
I	Incident energy.
I_{2D}	Effective stress.
K	Interphase momentum exchange coefficient.
k	Boltzman's constant.
k_{Θ_s}	Diffusive flux of granular energy.
L_{mf}	Minimum fluidization height.
l_{or}	Spacing between adjacent holes in orifice plate.
m	Complex index of refraction.
n	Refractive index.
N_{or}	Number of orifices per unit area.
Nu	Nusselt number.
p	Pressure.
Pr	Prandtl number.
Q	Volumetric heat transfer between phases.
q	Conductive heat flux.
Q_{abs}	Absorption efficiency factor.
Q_{ext}	Extinction efficiency factor.
q_m	Instantaneous rate of heat flow into a packet .
Q_{sca}	Scattering efficiency factor.
R	Interaction forces between phases.
Re_p	Reynolds number of particle.
S	Other sources term.
s	Distance between grains.
t_p	Period for particle's contact with the surface.
u_0	Superficial gas velocity.
$u_{b,ms}$	Minimum slugging velocity .
u_{br}	Bubble rise velocity .
u_b	Bubble velocity .
u_{mf}	Superficial gas velocity at minimum fluidization .
$U_{s,\|\|}$	Particle slip velocity parallel to wall.
u_t	Terminal velocity .
$u_t{}^*$	Dimensionless terminal velocity .
u^*	Dimensionless superficial gas velocity.
v	Velocity.
$v_{r,s}$	Dimensionless terminal velocity .
x	Size parameter.
X_1	Mixture composition.
z	Bed's height.
z_s	Height at which slugging is completely developed .

1 Introduction

1.1 Background

The end of natural gas era

The share of natural gas in primary energy usage in the Netherlands has remained relatively stable over the last decade, fluctuating about 40% (2018:41% [1], equivalent to approximately 36 Bcm of gas consumption). This is significantly higher than the EU average of 23% [2]. The high share (the largest in the European Union) is attributed to a variety of factors: strong domestic production; the presence of a distribution grid serving the whole country; the dominant role that gas plays in building heating (95%) and the historically relatively low cost of gas for major industrial and agricultural consumers. Due to all the reasons mentioned above, users in these sectors have been encouraged to employ gas [3]. In the generation heat of the Netherland, natural gas has quite a large share of about 90% for the buildings and 40-50% industrial's heat [4].

EU member states have the goal of reducing their GHG emissions by 40 percent by 2030, on the road to an 80-95 percent reduction by 2050. In line with the Paris agreement reached at COP21 in December 2015, achieving this goal is widely seen as important in mitigating the impact of global climate change. Based on the "Energy transition in the Netherland - phasing out of gas" report published by the Dutch Government [5], it is clear that natural gas will soon be replaced as the primary source of energy. One critical approach is the substitution of natural gas for industrial and transportation purposes by renewable sources in the context of syngas production and then further processed to produce the renewable counterparts (e.g. synthetic natural gas (SNG), Fischer-Tropsch fuels (FT-fuels))[6]. One of the energy scenarios from McKinseyCompany [7] as shown in Figure 1.1 proposed the increase of the system's renewable power generation capacity to 80% by 2040 with some flexibility schemes such as demand-side management and energy storage. In this scenario, biomass is considered to contribute 8% of total energy supply.

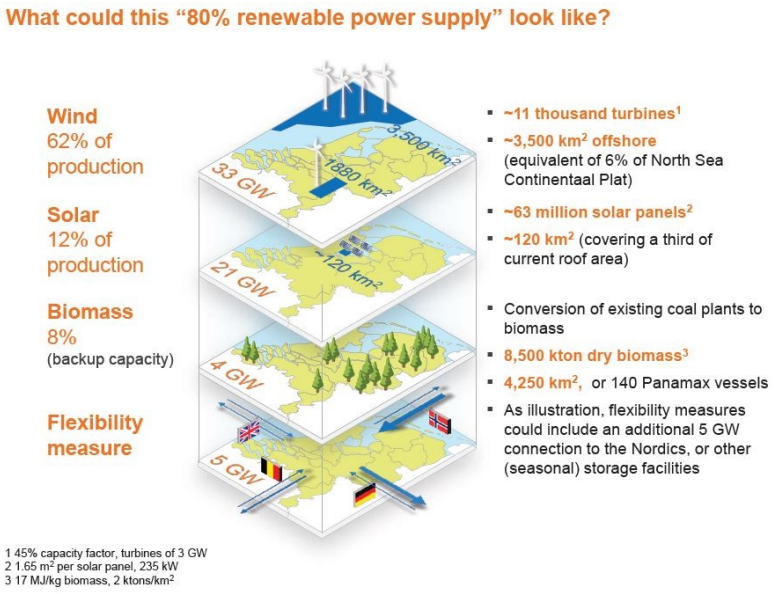

Figure 1.1: 80% renewable energy scenario in Netherland 2040 [7]

Biomass steam gasification/reformer

The use of biomass for renewable energy conversion processes has become increasingly important in the global race toward sustainability and cleaner ways of producing energy, as biomass is potentially a CO_2-neutral source of energy. Biomass can be used to produce various sources of energy by different processes, depending on the characteristics and demand. The net energy available from the biomass combustion varies from about 8 MJ/kg to 20 MJ/kg compared to about 27 MJ/kg for coal[8].

Thermochemical and biochemical are two general types of processes for converting biomass into different forms of energy[9]. In thermochemical conversion processes, biomass breaks down into its elements, such as bio-fuels, gasses and chemicals, by adding heat and pressure. There are four different types of thermochemical processes: combustion, gasification, pyrolysis, and liquefaction [10]. Biochemical processes decompose biomass into biofuels by the intervention of the living organism or its materials. Biochemical processes yield a significant volume of hydrogen relative to other methods [11]. However, the lower efficiency of the biochemical process makes it less attractive to industries compared to thermochemical processes [12].

Biomass thermo-conversion is one of the leading short-term options for sustainable hydrogen production and has the potential to produce a significant fraction of the transport fuel required in the future [13]. Thermochemical conversion is the heating and or oxidation control of biomass as one of the steps for producing intermediate energy carriers or heat, as shown in Figure 1.2. Direct combustion is the major bioenergy pathway in the world that aims to provide thermal energy from the oxidation of biomass to CO_2 and H_2O. While in contrast, the pyrolysis is the thermal decomposition in the absence of oxygen and, thus, the endothermic process. The primary purpose of pyrolysis is to produce various gaseous, liquid, and solid intermediate [14].

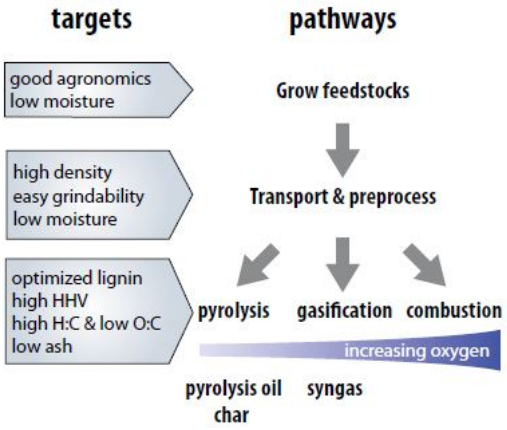

Figure 1.2: Various pathways for biomass thermochemical conversion process [14]

In between the combustion and pyrolysis process in terms of oxygen requirement, there is gasification, which is an exothermic partial oxidation process. Gasification represents an attractive and flexible technology to transform a wide variety of biomass into commodity gas composed mainly of CO, H_2, CO_2, H_2O, and CH_4, which can be used for (combined) heat and power (CHP) processing, transport fuels and chemicals. In a gasifier, steam is frequently used as a gasification medium along with the air to increase the hydrogen content of the producer gas. This process was then called biomass steam gasification/reformer [12].

Bubbling fluidized bed

Fluidization is a process by which solid particles are transformed into a fluid-like state by suspension in a gas or liquid form. If the fluid is passed up through a bed of fine particles, as shown in Fig. 1.2(a) at a low flow rate, the fluid percolates only through empty spaces between stationary particles; this state called a fixed bed. Along with an increase in the flow rate, the particles move apart, have some vibration, and move in restricted regions. This state is then called an expanded bed. At an even greater velocity, a point is reached where all the upward moving gas or liquid just suspends the particles. At this state, the frictional force between the particle and the fluid simply counterbalances the weight of the particles, the longitudinal portion of the compressive force between the neighboring particles disappear, and the pressure drops across every segment of the bed roughly equal to the weight of the fluid and the particles in that segment. The bed is considered to start the fluidization and is referred to as an incipiently fluidized bed or bed at a minimum of fluidization; see Fig. 1.2(b) [15].

With an increase in the flow rate beyond the minimum fluidization point, massive bubbling and gas channeling are observed. Increasing more the flow rates, will make the agitation becomes more violent and the movement of the solids more stronger. In can also be noted that the bed does not expand much beyond its volume at a minimum level of fluidization. Such a bed is called an aggregative fluid bed, a heterogeneous fluid bed, or a bubbling fluidized bed; see Fig. 1.2(d) of this. In gas-solid systems, the gas bubbles coalesce and grow as they arise, and may eventually become large enough to spread across the vessel in a deep enough bed of small diameter. In the case of small particles, they float seamlessly down the wall around the raising gas void. It is called slugging, with axial slugs, as shown in Fig. 1.2(e). In the case of coarse material, the section of the bed above the bubble is forced upwards, like a piston. Particles are raining down from the slug, which finally disintegrates. About this time, another slug form, and this unstable oscillatory motion is repeated. This is called the flat slug; see Fig. 1.2(f) of this. Slugging is particularly severe in long, narrow, fluid beds [15].

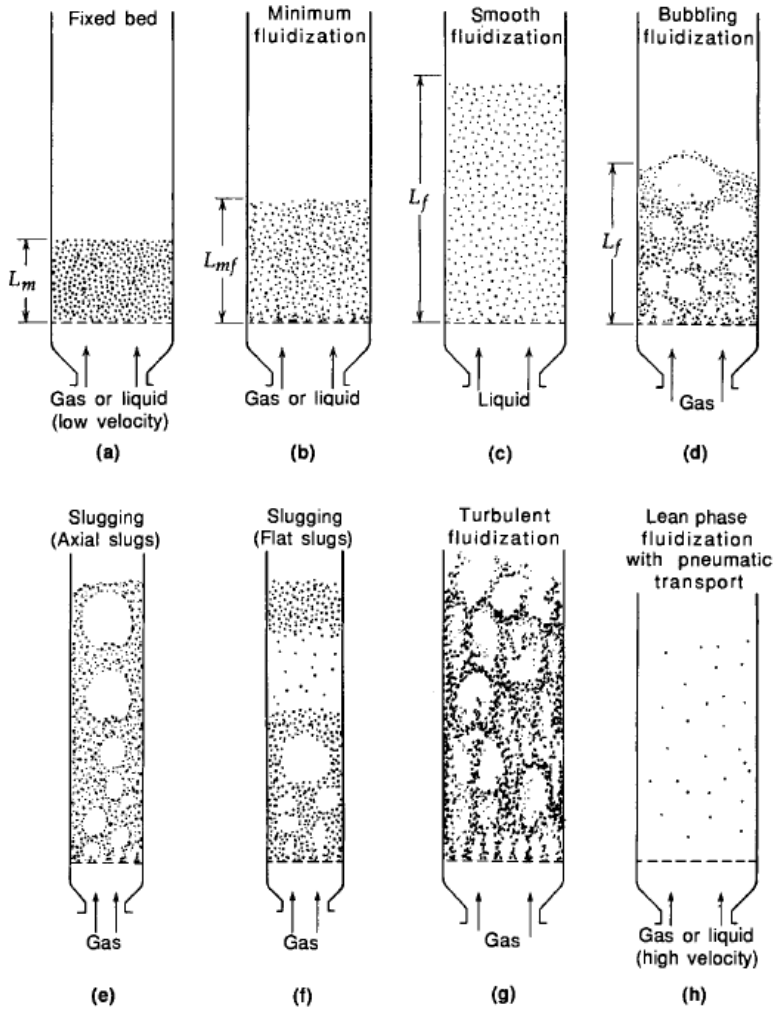

Figure 1.3: Various types of contacting mode of solid particles by fluid [15]

Once small particles are fluidized at a sufficiently high rate of gas flux, the terminal velocity of the solids is reached, the upper surface of the bed disappears, the entrainment is evident, and instead of bubbles, the turbulent motion of particle clusters and gas voids of different sizes and forms will be developed. This type of regime is called a turbulent fluid bed, as seen in Fig. 1.2(g). Finally, with a further increase in gas velocity, solids are expelled from the gas bed. In this condition, we have a dispersed, diluted, or lean-phase fluidized bed with a pneumatic transport of solids; see Fig. 1.2(h) [15].

Based on those aforementioned behaviors, the desirable characteristic of a fluidized bed are described below [15]:

- The steady, liquid-like movement of particles allows continuous automatically controlled flow with the ease of handling.
- The fast mixing of solids contributes to near-isothermal conditions in the reactor; thus, the process can be managed easily and efficiently.
- The whole vessel of well-mixed solids is a sizeable thermal flywheel that handles sudden temperature changes, responds gradually to drastic changes in operating conditions, and provides a large margin of safety at high-exothermic operation.
- The circulation of solids between two fluid beds makes it possible to extract (or add) vast amounts of heat generated (or needed) in large reactors.
- Suitable for large-scale operations.
- Heat and mass transfer rates between gas and particulate matter are high compared to other types of reactors such as a fixed bed or moving bed.
- The heat transfer rate between the fluidized bed and the immersed body is high; thus, the heat exchangers inside the fluidized beds need relatively small surface areas.

The drawbacks of a fluidized bed configuration of a reactor include the following [15]:

- In the case of bubbling beds of fine particles, the flow of gas is difficult to describe. It has a substantial deviation from the plug flow, thus represents an inefficient contact. This becomes particularly critical when the high conversion of the gaseous reactant or high selectivity of the intermediate reaction is required.
- The intense mixing of the solids in the bed contributes to the non-uniform residence time of the solids in the reactor. This results in a non-uniform product and poor performance for continuous treatment of solids, particularly at high conversion levels. In the case of catalytic reactions, the movement of porous catalyst particles, which continuously capture and release reactant gas molecules, contributes to the back mixing of the gaseous reactant, which reduces yield and performance.
- Friable solids are shattered and carried by the gas must be replaced.
- Particle-abrasion erosion of pipes and vessels can be severe.
- For non-catalytic high temperatures operations, the agglomeration and sintering of fine particles may require a lowering of the operating temperature, thereby significantly reducing the reaction rate.

Indirectly heated fluidized bed

Bubbling fluidized bed technology is attractive for biomass gasification of small to medium scale. The process takes place in a bed of small particles fluidized by an acceptable gasification medium. The excellent gas-solid mixing ensures uniform temperature through the bed and contributes to the mass and heat transfer [15]. To improve further the quality of the gas product, indirectly heated gasification, also known as second-generation or allothermal gasification can be used [16].

Allothermal gasification processes are based on the fact that the heat needed to run the gasification reactions is delivered from outside to the gasification reactor. Heat is generated by combustion and is generally transferred to the gasification system by a heat carrier (e.g., circulating bed material in dual FBGs) or a heat exchanger (e.g., heat pipe heat exchanger or radiant burner). The mechanism of both methods is seen schematically in Fig. 1.4. This allothermal gasification is often referred to as "indirect" gasification because it is supplied indirectly by heat transfer to the reactor and is not generated directly in the gasifier [17].

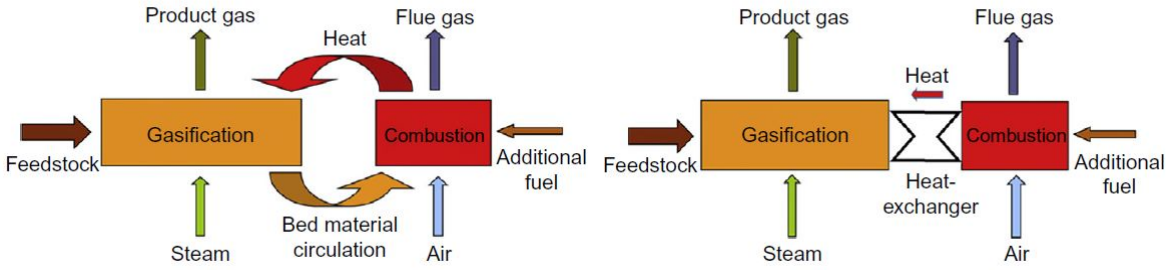

Figure 1.4: Schematic representation of allothermal gasification systems [17]

The significant difference between the two schemes of the DFB in Fig. 1.4 is the transport of heat from the combustion reactor to the gasification reactor. On the left arrangement, the heat transport is carried out employing a bed material circulating between the combustion reactor and the gasification reactor. The bed material from the gasification reactor is heated up in the combustion reactor and fed back to the gasification reactor. By doing this, sensible heat is transferred from the combustion reactor to the gasification reactor, i.e., from outside the gasification reactor. The DFB gasifier on the right shows where the heat is transported from the combustion to the gasification reactor via a high-temperature heat exchanger. These allothermal DFB gasifiers allow high-grade product gas production without the need for pure oxygen, thus avoiding a costly and energy-intensive air separation unit.

One of the recent applications for the first type of DFB employing the circulation of bed material is MILENA indirectly heated gasifier [18], which firstly designed in 1999 by the research institute ECN in Netherland. MILENA, as shown in Figure 1.5, works with the principle of the heat direction going from the outside (combustor) to the inside (gasifier). Biomass first enters the from the bottom together with steam as a gasification agent. Unreacted biomass and char produced from the gasification process leave the gasifier through the riser and moving to the combustion chamber. In the combustion chamber, located around the reactor's gasifier volume, the solids are combusted to provide the heat required to the reformer section. The remaining solids particles that are not entirely burned will recirculate towards the reformer.

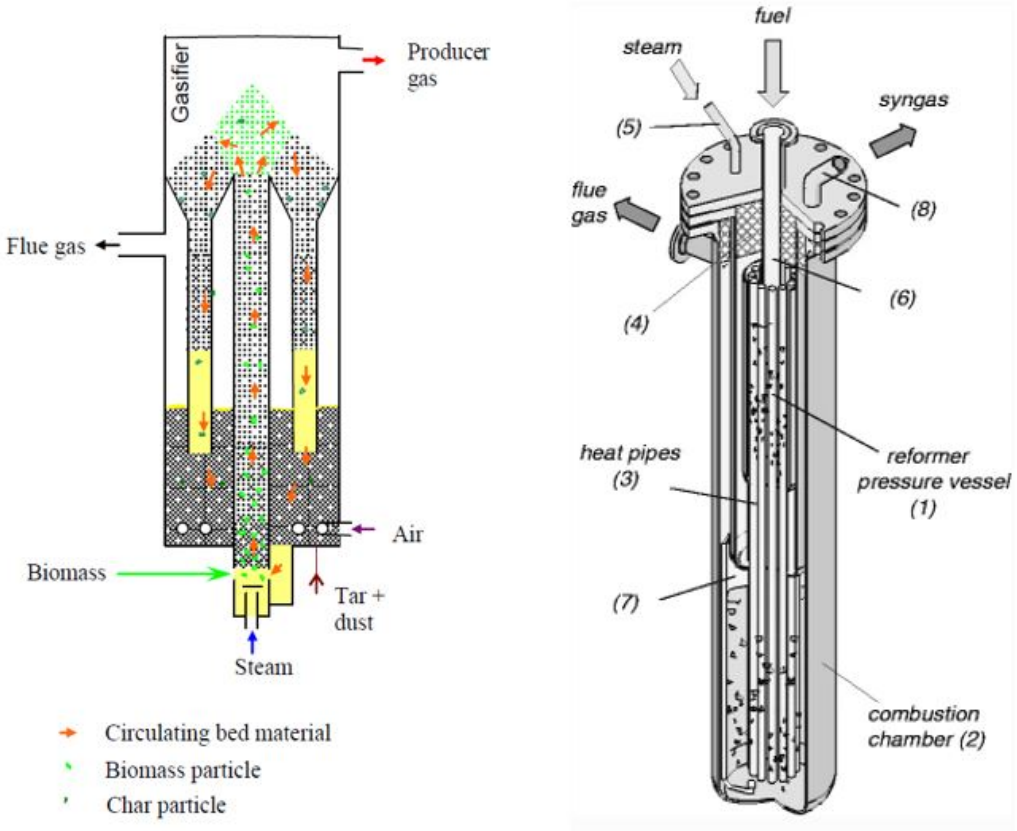

Figure 1.5: The design of allothermal gasification process technology developed by MILENA of ECN[18] (left) and BioHPR[19] (right)

MILENA has an operating condition in the range of 650-950 ^{o}C. The carbon conversion could reach 100% due to the continuous unreacted solids recirculation and cold gas efficiency of about 80%, including tar removal and combustion [20] [21]. This MILENA technology has successfully completed the lab-scale test from 30 kW capacity, and the 800 kW of pilot plant has been launched. This particular technology has also been used further for the Alkmaar 4 MW bio-SNG demo project [22].

Another development of the allothermal gasification is Biomass Heat Pipe Reformer (BioHPR), which is focused on the improvement of the overall heat transfer coefficient by reducing the heat exchange surface, and thus reduced the investment cost. BioHPR was introduced by J. Karl [19] by implementing the heat pipe as the means for heat exchanger between two separate fluidized bed of combustion and gasification, instead of the recirculation of hot solids. This design allows for the use of different fuels and pressures in the combustor and gasifier.

The right part of Figure 1.5 shows the component of BioHPR. The reformer pressure vessel (1) is integrated inside the combustion chamber (2). The heat produced from the combustion is transferred via the heat pipes (3) from the combustor to the reformer. There is inner insulation (4) on the top of the reformer to ensure the upper flange close to the ambient temperature. The excellent feature in this integrated design is no moving part facing the high temperatures, and thus the heat losses are kept low. The steam as a fluidizing agent will first enter the reformer through the steam inlet (5). The solid fuel or biomass will be loaded to the gasifier via a lock hopper system and standpipe (6). The syngas produced will be discharged through an upper outlet (8), where the external candle filter will filter the dust and char particle. Air preheater component (7) is also included on the combustor to reduce the exhaust losses [19].

The optimal operating temperature is above 800 ^{o}C to reduce the tar and methane content. Char conversion rate up to 80 % and cold gas efficiency >70 % was observed. The initial thermal input capacity is 120 kW. Then the first pilot plant with 500 kW was developed by Agnion Energy. The first commercial plant was commisioned in Grassau, Germany 2012 with thermal input capacity 1.3 MW [19].

CFD modeling

With the rapid advancement of computer science, computational fluid dynamics (CFD) multiphase modeling has been considered as one of the most suitable methods for an intuitive understanding of fundamental phenomena, as well as a more precise and efficient method for researching dense particulate reaction system (DPRS) [23]. CFD has made it possible to study the complicated multiphase flows in a comprehensive mathematical way. A variety of physical properties can be tested using a validated CFD model that would otherwise have been a rather cumbersome, erroneous, and costly experimental exercise.

A fundamental issue in DPRS is the description of the gas-particle flow. There are primarily two types of CFD multiphase modeling techniques in which the particles are assumed to be much smaller than the CFD grid size, namely the Eulerian-Eulerian and namely the Eulerian–Eulerian and Eulerian-Lagrangian approaches [23]. The two phases are viewed mathematically as inter-penetrating continua in the Eulerian–Eulerian model, and hence the model is often called the Two-Fluid Model (TFM). In addition to the fluid flow, an Eulerian structure is often used to explain the motion of solid particles in which the kinetic theory of granular flow (KTGF) is integrated into most models to simulate particle collision for closing equation systems [24]. The Eulerian–Eulerian solution has the advantage of being superior in computational simplicity. However, the downside is that although empirical relationships include the physical characteristics of solid particles such as shape and size in the continuum representation, such models can not consider the distinct character of the solid phase that is important in many DPRS. The drawback strongly restricts the application of the Eulerian–Eulerian method to basic science related to particle physics [23]. One example of an eulerian-eulerian simulation result done by Taghipour et al.[25] is displayed in Fig. 1.6

An alternative approach is to handle the particle process using the discrete element/particle method (DEM/DPM) as in the Lagrangian-Eulerian model [26]. DEM models a finite number of discrete particles that interact through contact and non-contact forces, and each particle moves in a considered system defined by Newton's motion equations translationally and rotatively. DEM can provide dynamic information such as the trajectories and transient forces acting on individual particles and is therefore very common for simulating a system that contains a large solid particles [23]. However, this type of approach is extremely computationally expensive (CPU and memory capacity requirement) along with the increase of particle numbers [27]. Another example of a eulerian-lagrangian simulation result performed by Lu et al.[28] is displayed in Fig. 1.6. As shown, both methods from Eulerian-Eulerian and Eulerian–Lagrangian are useful in studying fundamental dense gas–particle flow behaviour. The preferences of two approaches depend on the context of the topic of study and application.

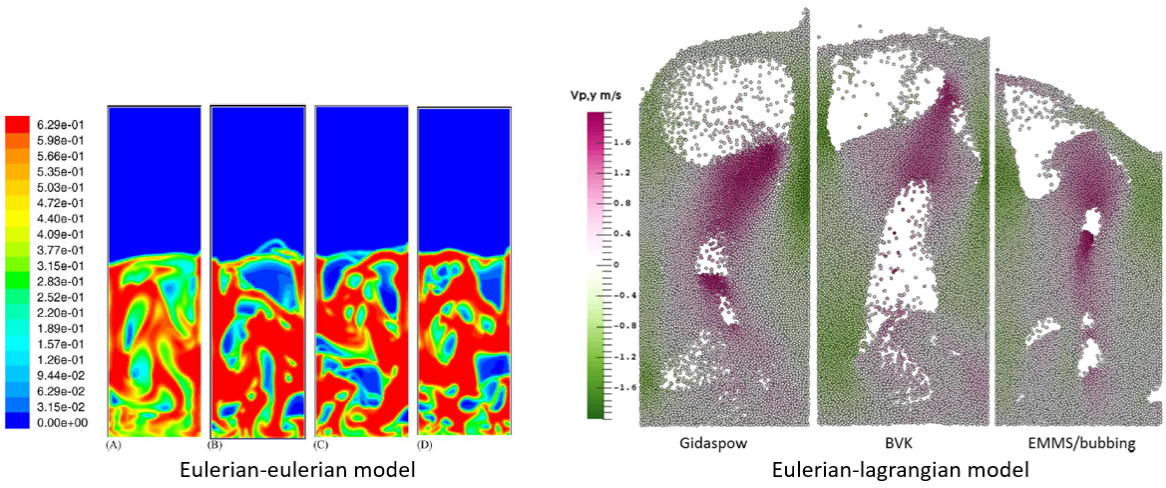

Figure 1.6: Typical solid distribution or concentration profile modelled using eulerian-eulerian model (left [25]) and eulerian-lagrangian (right [28])

In the present work, the TFM numerical method is employed. The main reason is the expected 3D model simulation for the real domain/dimension of the pilot plant, which will require expensive computational resources. As the first 3D model built for this setup, the more straightforward method is preferable for the initialization of the CFD model. The hydrodynamic variables that will be observed are also limited to the possible experimental work for validation; thus, only the minimum fluidization and general bubbles behavior will be studied. The details of bubbles shape, size, velocity, etc is expected to be further study on the subsequent development of the model and will require the distinct character of solid-phase modeling as the Eulerian-lagrangian method does.

Petrogas and T.U. Delft pilot project
T.U. Delft's 3mE faculty Process and Energy department and Petrogas Gas-Systems B.V. are working together to create a novel 50 kWth Indirectly Heated Bubbling Fluidised Bed Steam Reformer (IHBFB-SR) heated by two vertically mounted radiant tube burners (Figure 1.7). These radiant burners facilitate the heat transfer into the gasifier section. It also has a similar concept with the aforementioned MILENA and BioHPR, which have a separated combustion chamber and the gasifier. The main difference is the heat direction, which goes from inside to outside, instead of from outside to inside like all other designs. It is then expected to have a lower heat loss since the hottest part (heat transfer surface) is far from the ambient condition, and thus will have higher energy efficiency. Using the radiant burner could also overcome the problem encountered by using the heat pipes: hydrogen diffusion and erosion of the heat pipes.

The biomass will be fed up from the bottom side of the reactor while the air and steam as fluidizing agents entering the reactor through the windbox area from the bottom via the tuyere nozzle distributor. The air and natural gas will directly enter the separate combustion chamber on each of the radiant burners and then combusted to supply the heat required by the system. One of the drawbacks of this design can be quickly notified that there is no recirculation of biomass possible like MILENA that can ensure 100 % of carbon conversion due to the fully separated system. The product gas is discharged through the top side of the reactor.

A significant part of the work is the modeling, design, and testing of a new form of the gasifier. It also ensures that produced gas is free of dust, sulfur, and tar, improving the gas for further catalytic conversion and scaling up from laboratory to factory scale. T.U. Delft university will research together with Petrogas Gas Systems B.V. how this technology can be further developed and ultimately brought into the market. Clearly, the project has tremendous commercial potential for Petrogas Gas Systems B.V. The plan for the future is to build a scaled-up test plant [29].

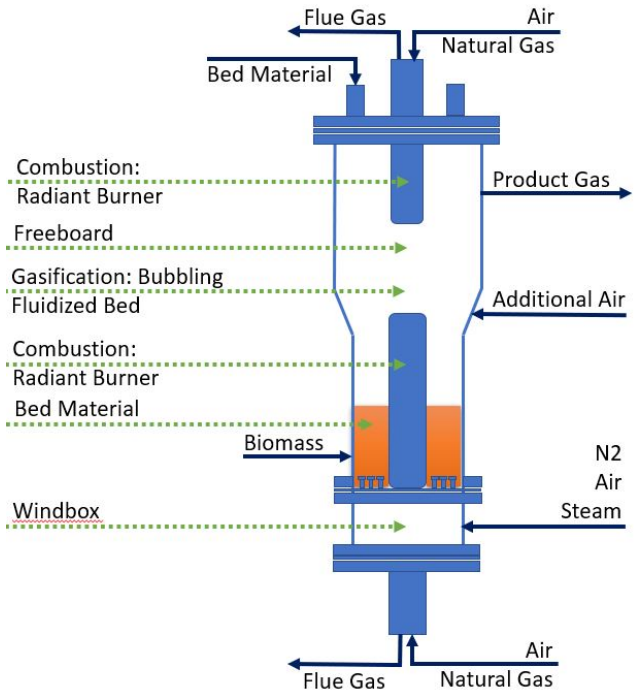

Figure 1.7: Petrogas and TU Delft biomass steam reformer pilot project

1.2 Research Focus

The main objective of this study was to investigate the hydrodynamics and heat transfer occurring inside the reactor, using the techniques of "Computational Fluid Dynamics" (CFD) with a two-fluid model (TFM). The research was carried out using ANSYS ® FLUENT, a commercial CFD program. The physical phenomena developing inside the reactor were examined, and then the models and parameters developed to explain the physical aspects were researched. The steam flow will be replaced by air for simplicity of the experiment, and the biomass will not be included yet in the present work. First, the hydrodynamic activity was analyzed and then how the heat transfer could be coupled with the hydrodynamics in the reactor was investigated.

1.3 Research Question

Considering that there are infinite parameter choices for experimentally optimizing and/or validating, a set of research questions is formulated which is the core of the study.

1. What is the optimal grid size of the CFD mesh model?
2. What is the minimum fluidization condition on the current setup?
3. Which drag model (gidaspow or adjusted syamlal) could give the closest result to the experimental data?
4. What is the bubbling and slugging flow regime?
5. How can the bubbling and voidage behavior of the bed be described? How much is the significance of using Energy Minimization Multi-Scale (EMMS) drag model?
6. How is the effect of bubbling and voidage behavior on the heat transfer process?
7. How significant the radiative heat transfer affecting the overall heat transfer process?
8. What is the proper radiative heat transfer model for this simulation?
9. How close the CFD simulation result could depict the heat transfer process of the reactor?

1.4 Report Structure

Chapter 2 contains a review of the literature's necessary background to fully understand the concepts relevant to the research questions and the simulation parameters' choices. Chapter 3 summarizes the pertinent recent researches with the present hydrodynamic and heat transfer modeling work. Chapter 4 provides the model's development process, from the detail of reactor geometry and its components, structured mesh creation with ICEM CFD, and the setting of multiphase CFD in Fluent. Chapter 5 describes the findings and discussion compare with experimental data, where the conclusion and recommendation drawn on the final Chapter 6. The user-defined functions (UDF) built and used for the whole simulation are provided in the Appendix A section.

2 Theoretical Background

Dense particulate reaction system (DPRS) is a system involving high concentration of particles and simultaneous chemical reaction. It is one of the most complex multi-phase reaction systems and is widely used in the chemical and process industries including energy conversion, petrochemical and mineral processing, chemical engineering and pharmaceutical manufacturing. Fluidized bed, spouted bed, blast furnace, and rotary kiln are all common DPRS process and applied widely to these sectors [23]. In all the above-mentioned applications, one of the most important common characteristics is that physical and chemical processes may occur simultaneously and influence one another. The knowledge of the gas– particle flow characteristics and chemical reaction mechanism in DPRS is crucial for improving the efficiency of the thermodynamic system and helps to scale-up, re-design and optimize the thermodynamic reaction processes of different reactors [23]. In general, there are four typical characteristic of DPRS: high particle concentration, strong gas-particle/particle-particle interaction, complex chemical reaction and significant mass and heat transfer.

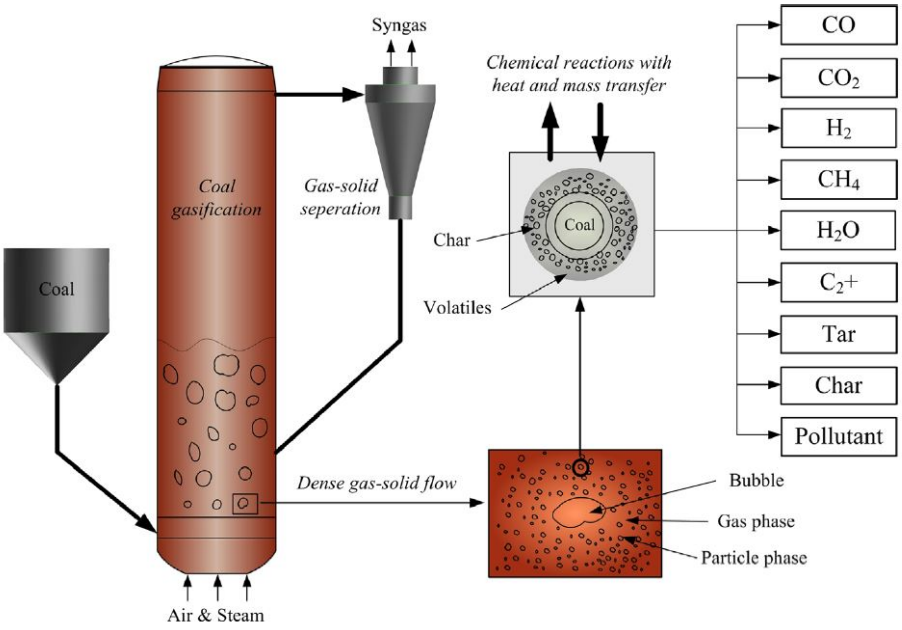

Figure 2.1: Coal gasification in a bubbling fluidized beds as a typical dense gas particulate reaction system [23]

In a bubbling fluidized bed gasifier as shown in Figure 2.1, all the four key characteristic of DPRS can be found. It is shown that the fluidizing gas and gasifying agent (air and steam) from the bottom of the reactor flows by solid particles creating some bubbles. Due to the offset of drag force and gravity, solid particles are suspended in the fluid at a certain velocity, and a quasi-stable fluidization of the bubble is established. The entire bed can be divided into two major areas: the dense zone at the bottom and the upper dilute zone (freeboard). The volume fraction of particle in the compact region below is high ($> 40\%$). Owing to the strong interaction between solid particles and particle and gas, the average porosity in the upper half of the bed is comparatively lower and more dynamic [23].

A completed reaction to coal gasification undergoes a sequence of conversion processes. During these processes the gas and particle movement is closely coupled and the turbulent gas flow's stochastic nature makes the problem even more complex. Furthermore, most chemical reactions will include coal pyrolysis, char combustion, steam gasification, CO_2 gasification, methanation, combustion volatiles (CO, H_2, and CH_4), and water–gas shift reaction. According to [30], the DPRS will be of about thirty reactions. These reactions will be accompanied by significant heat and mass transfer along with the chaotic gas-particle interaction. Therefore, the optimal designing and controlling cannot be achieved without a deep understanding on the hydrodynamic and heat transfer characteristic of the process [23].

2.1 Bubbling Fluidized Bed

Minimum fluidization velocity

The first step to create an effective design and operation and control of the fluidized bed is to define the minimum fluidization velocity. As it has been widely known, in the case of bed material resting on top of gas distributor, and assumed the uniform flow of the gas upward in the bottom part of the reactor, the onset fluidization occurs when:

$$(drag\ force\ by\ upward\ moving\ gas) = (weight\ of\ particles) \tag{1}$$

or

$$\begin{aligned}(pressure\ drop\ accross\ the\ bed)\,(cross\ sectional\ area\ of\ tube) = \\ (volume\ of\ bed)\,(fraction\ of\ solid)\,(specific\ weight\ of\ solid)\end{aligned} \tag{2}$$

or with the mathematical expression:

$$\Delta p_b A_t = W = A_t L_{mf}(1-\epsilon_{mf})\left[(\rho_s - \rho_g \frac{g}{g_c})\right] \tag{3}$$

with some rearrangement, minimum fluidization state can be formulated as:

$$\frac{\Delta p_b}{L_{mf}} = (1-\epsilon_{mf})(\rho_s - \rho_g)\frac{g}{g_c} \tag{4}$$

Then superficial gas velocity at minimum fluidization can be drawn from the combination of this equation with the expression of frictional pressure drop derived by Ergun et al. for the bed consists of a single size of isotropic solids with the diameter of d_p will yield:

$$\frac{1.75}{\epsilon_{mf}^3 \phi_s}\left(\frac{d_p u_{mf}\rho_g}{\mu}\right)^2 + \frac{150\,(1-\epsilon_{mf})}{\epsilon_{mf}^3\phi_s^2}\left(\frac{d_p u_{mf}\rho_g}{\mu}\right) = \frac{d_p^3 \rho_g\,(\rho_s-\rho_g)\,g}{\mu^2} \tag{5}$$

or

$$\frac{1.75}{\epsilon_{mf}^3\phi_s} Re_{p,mf}^2 + \frac{150\,(1-\epsilon_{mf})}{\epsilon_{mf}^3\phi_s^2} Re_{p,mf} = Ar \tag{6}$$

where Ar is Archimedes number or also commonly called Galileo number, Ga.

Pressure drop versus velocity diagram

The pressure drop versus velocity diagram is beneficial to identify roughly the behavior of fluidization and its quality, mainly when the visual observations are not possible. As shown in Figure 2.2, initially, the bed material is resting. Then gradually, the gas velocity is increased. On the low velocity, the bed is still on the fixed bed state, where pressure drop approximately proportional to the gas velocity. It usually reaches its maximum at the pressure drop slightly higher than the bed's static pressure. Along with the further increase of the gas velocity, at one point, the fixed bed will be "unlock" where the voidage of the bed (ϵ_m) increases to the minimum fluidization voidage (ϵ_{mf}). This finally leads to the pressure drop equal to the static pressure of the bed. Increasing the velocity beyond the minimum fluidization condition will induce more bed expansion and bubbles formation. However, it can be noted that the pressure drop of the system remains the same. This is because of the well-aerated and easily deformed behavior of the sand particle, and thus it has no appreciable resistance on dense gas-solid phase.

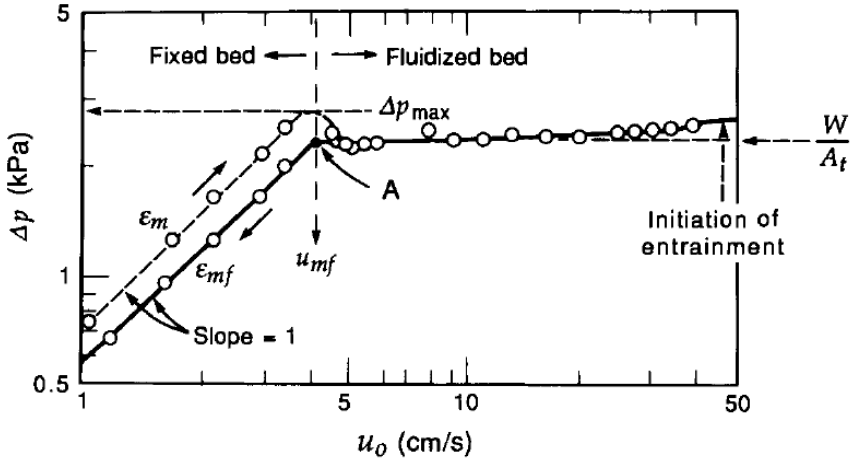

Figure 2.2: Pressure drop versus gas velocity for uniformly size sharp sand with ideal behavior; 160 μm particle diameter and 4.1 tube diameter. [15]

Beside minimum fluidization velocity (u_{mf}), another critical stage indicating the fluidization behavior is minimum bubbling velocity (u_{mb}). This happens at the state where bubbles are first observed. In liquid-solid or small particles systems, u_{mb} usually has no meaning due to the smooth fluidization occurs throughout the bed. In contrast, gas-solid beds of large particles, has bubbles formation just after the gas velocity exceeds u_{mf}, hence $u_{mb} \approx u_{mf}$ [15].

The development of bubbles can be shown from the FCC catalyst's bed expansion profile with a diameter of 64.7 μm in Figure 2.3, where L_f is average fluidized bed height. As the gas velocity increases beyond u_{mf}, at first, the bed expands smoothly. When it reaches a velocity of about $3u_{mf}$, bubbles start to develop, and bed height begins to decrease.

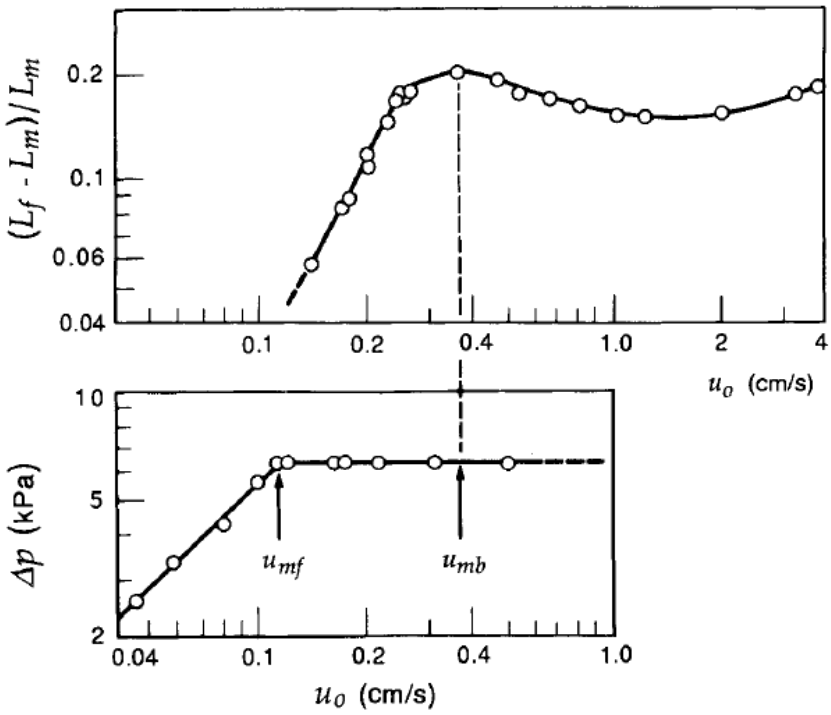

Figure 2.3: Bed expansion and pressure drop profile of FCC catalyst; d_p=64.7μm, ρ_{bulk}= 0.5 g/cm^3, d_t= 6.6 cm, L_m= 130.8 cm, perforated plate distributor [15].

Geldart classification of particles

Considerable efforts have been made to establish a standard for forecasting the fluidization phase and transition from one stage to another. One of the unique and straightforward approaches was established by Geldart [31], as shown in Figure 2.4 and widely used in many research related to fluidization. The chart is applicable for fluidization using air under ambient conditions and u_o less than $10u_{mf}$. By referring to the density ρ_s and mean particle diameter d_p for any solid/granular material, the estimated type of expected fluidization can be determined. The classification focuses on the particle's characteristics, which influence the fluidization behavior. It differentiated the solid particles into four different groups of particles from the smallest to the largest and elaborated as follows:

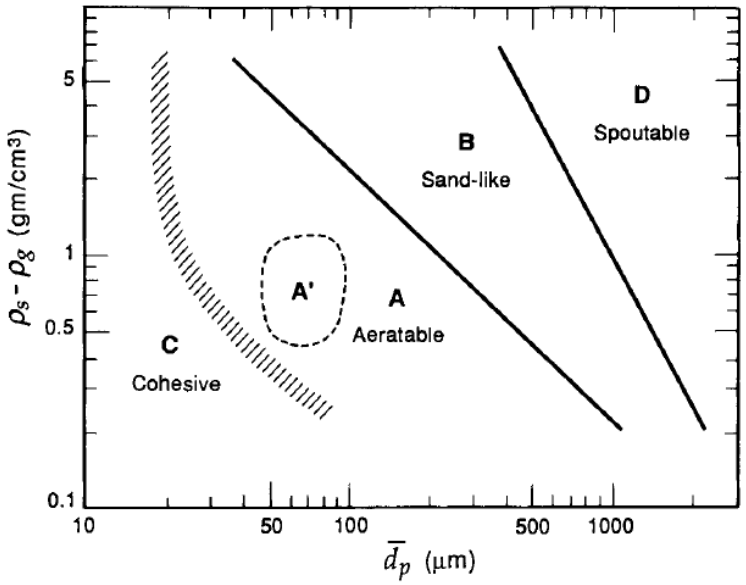

Figure 2.4: Classification of particles for fluidization with air at ambient condition by Geldart [31]

Geldart C: cohesive, or tiny particles. In this type of powder, fluidization is hardly occurring due to the high interparticle forces compared to the action of the fluidizing agent. Face powders, flour, and starch are some of the solid materials that lie in this group.

Geldart C particles tend to rise as a plug of solids in small diameter beds instead of fluidizing once the gas velocity increases. For larger bed diameter, a channel will be formed starting from the gas distributor until the bed's surface. One alternative to handle Geldart C particles is mixing them with the same solid material but larger size, preferably the one from Geldart B. Another challenge to process these particles is that they will not get entrained immediately, even the size is very fine. Instead, they will stay around several minutes in the bed, which is too long for their physical as well as chemical transformation.

Geldart A: aeratable, or particle with small mean size and or low density (<1.4 g/cm^3). This group of particles is easily fluidized and presents smooth fluidization and transition from one regime to another. At the raising gas velocity beyond minimum fluidization, the bed expands considerably before forming bubbles. Small bubbles formation usually happens at higher velocities, which is higher than u_{mb}. One of the most common examples of this is the FCC catalyst.

There are several unique features of bubbles within Geldart A material. Firstly the gas bubbles rise faster than the gas flowing in the emulsion phase. Consequently, they split and frequently coalesce as they rise through the bed. Most commonly, the maximum bubble size is about 10 cm, even in a large bed environment. Secondly, the inner side of the bed has a less significant effect on the fluidization. Thirdly, the gross circulation of solid typically occurs even in the case of a few bubbles, and this becomes more vigorous in the larger bed. Finally, when there is a chance of bubble growing up to the size of vessel diameter, it will turn into an axial slug.

Geldart B: sandlike, or particle with the size on the range of 40 μm < d_p < 500 μm and density 1.4 g/cm^3 < ρ_s < 4 g/cm^3. Group B is characterized by good fluidization and vigorous bubbling. Bubbles are normally much larger than Geldart A and grow bigger along with the increase of the size.

Geldart B solid is well known for its bubbles formation as soon as the gas velocity exceeds u_{mf}. In contrast with Geldart A particle, it typically follows the correlation of $u_{mf} \approx u_{mb}$. At higher gas velocities, it firstly generates small bubbles at the distributor, which then coalesce and grow larger along with the height of the bed. Secondly, bubbles develop roughly linear with the distance above the distributor and excess gas velocity above minimum fluidization condition. It is also observed that the size of the bubble is independent of the mean particle size. Finally, vigorous bubbling formation influences the gross circulation of solids.

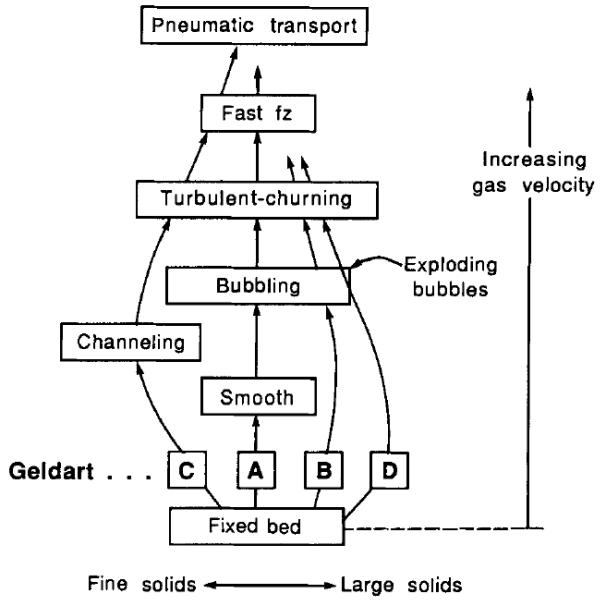

Figure 2.5: Schematic change in gas solid contacting mode with the increase of gas velocity [15]

Geldart D: spoutable or large particle size. This type of solid is difficult to fluidize, especially under the deep bed conditions. It is characterized by having random behavior, large exploding bubbles, or serious channeling or spouting behavior, especially at uneven gas distribution. Some examples are gasifying coal and roasting metal ore. They are usually treated in a spouting regime and or shallow bed.

The solid particle group, which has the largest size according to Geldart classification has several characteristics: firstly, the bubbles coalesce rapidly and develop to large sizes. Secondly, the bubble rise velocity is lower than that of the gas percolating through the emulsion phase. If the bubbles grow closer to the bed diameter, flat slugging usually occurs. Finally, in contrast with Geldart B solid, these particles spout easily.

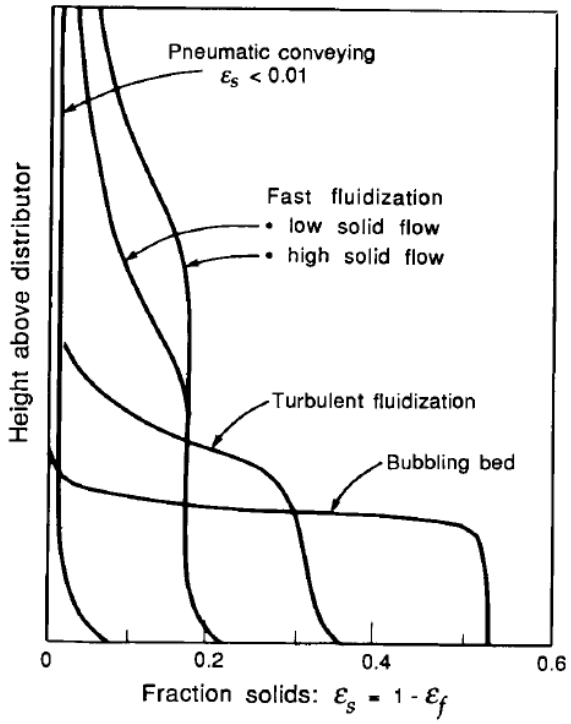

Figure 2.6: Axial voidage profile for each of fluidization regime [15]

At the higher gas velocities above the bubbling regime, the bed will turn to turbulent/churning fluidization, fast fluidization, and, finally, the pneumatic transport regime. Since all the contacting modes above bubbling regime will not be the concern of the present work, the following figure 2.5 summarizes briefly the behavior of different in Geldart group particle started from gas percolating in the bed until the pneumatic regime. Furthermore, in Figure 2.6, the typical axial solid distribution along the height of the vessel for each flow regime is displayed. These curves imply that each fluidization regime has its unique density-height curve.

Bubbles in fluidized bed

At the early development phase of bubbling fluidized bed, the two-phase model proposed by Toomey and Johnstone [32] assumed that all gas flow above u_{mf}, which is $u_o - u_{mf}$, passed through the bed in the form of bubbles. On the other side, the emulsion phase remains quiescent at minimum fluidization conditions and only moving aside a little bit to let the bubbles through. However, recent investigations and researches have shown that it is somewhat more complicated than that early theory.

In the study with a larger bed ($>$ 30 cm), some assumptions made on the two-phase theory were proved to have some flaws since it is not well met the experimental result. Firstly, the gas bubble produced is not directly followed by $u_o - u_{mf}$. Secondly, the voidage inside the emulsion ϵ_e is not equal to ϵ_{mf} once the gas velocity raised above the u_{mf}. Finally, it was observed that the emulsion is not at quiescent mode, but it presents a unique flow pattern, called gulf streaming, due to the uneven formation and channeling of bubbles.

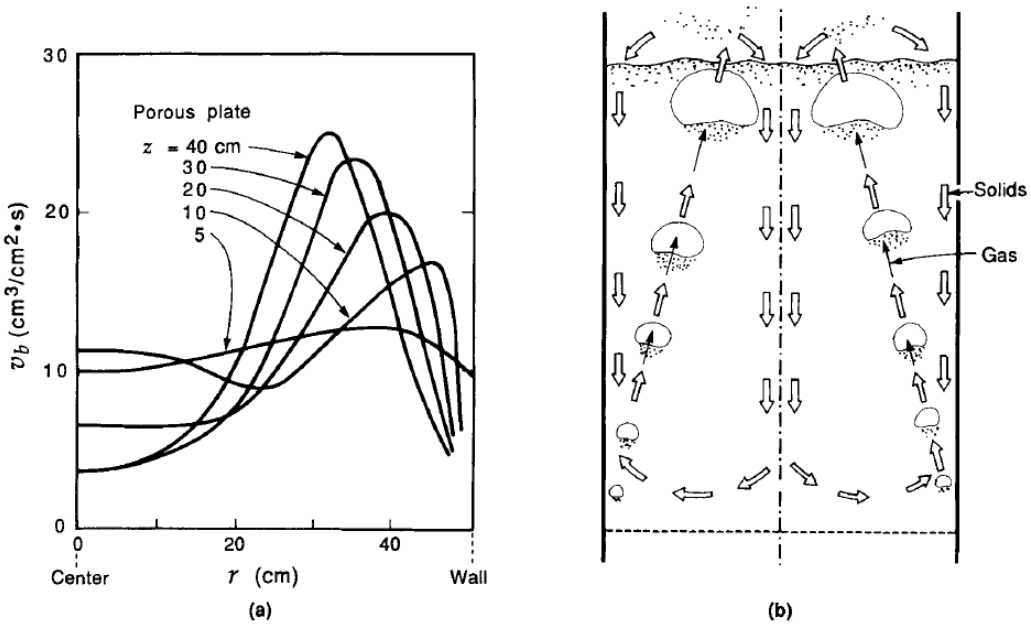

Figure 2.7: (a) Bubble's flow at various height above porous plate distributor; (b) solid emulsion movement's pattern [33]

One of the studies that investigated emulsion movement by Werther and Molerus [33] was conducted on a shallow bed of Geldart B particles (quartz sand, d_p= 103 μm), d_t= 1 m at u_o= 20 cm/s with 1.35 cm/s of u_{mf}. It used a high-pressure drop porous plate distributor, which theoretically would keep an even distribution of gas flow across the bed. However, as shown in Figure 2.8, they found a strong upflow of emulsion solid in the vicinity of the vessel's wall, starting from an area close to the bottom of the bed. At a higher position in the bed, the upflow pattern shifted to the center of the bed.

Furthermore, by referring to the investigations of Whitehead [34], Yamazaki et al. [35], Lin et al. [36], Tsutsui et al. [37] and some other relevant studies, the generalization of emulsion flow in Geldart B's fluidized bed can be formulated as follows:

- In bed with an aspect ratio (height/diameter) close to but less than 1 with low fluidizing velocity, emulsion solid circulate following a vortex ring with upflow at the wall and downflow at the center as shown in Figure 2.8a. The reverse pattern might be observed at higher gas flowrate due to large raising bubbles (Figure 2.8b).
- In the case of the bed aspect ratio close to 1, the emulsion of solids start to move downwards at the wall near the bed surface (Figure 2.8c).
- A second vortex ring appears in deeper beds (aspect ratio $>$ 1) above the first vortex ring, with upflow in the middle of the bed (Figure 2.8d). At higher gas flows, the strong circulation in the upper vortex ring becomes more intense and dominates the overall emulsion stream.
- In very shallow beds with aspect ratio $<$ 0.5 and uniform distributors, typical vortex ring of aspect ratio $\approx$ 1 might develop; see Figure 2.8e. However, the emulsion's circulation pattern can be controlled by using high-pressure drop tuyeres, as shown in Figure 2.8f.
- In the beds of Geldart A particles, the transition to the emulsion upflow is even closer to the u_{mf} than in the beds of Geldart B.

Such movement of emulsion illustrates the rising trend of gas bubbles within the bed. Bubbles should be abundant in upflow emulsion regions, and few, if ever, growing bubbles should be found in downflow regions.

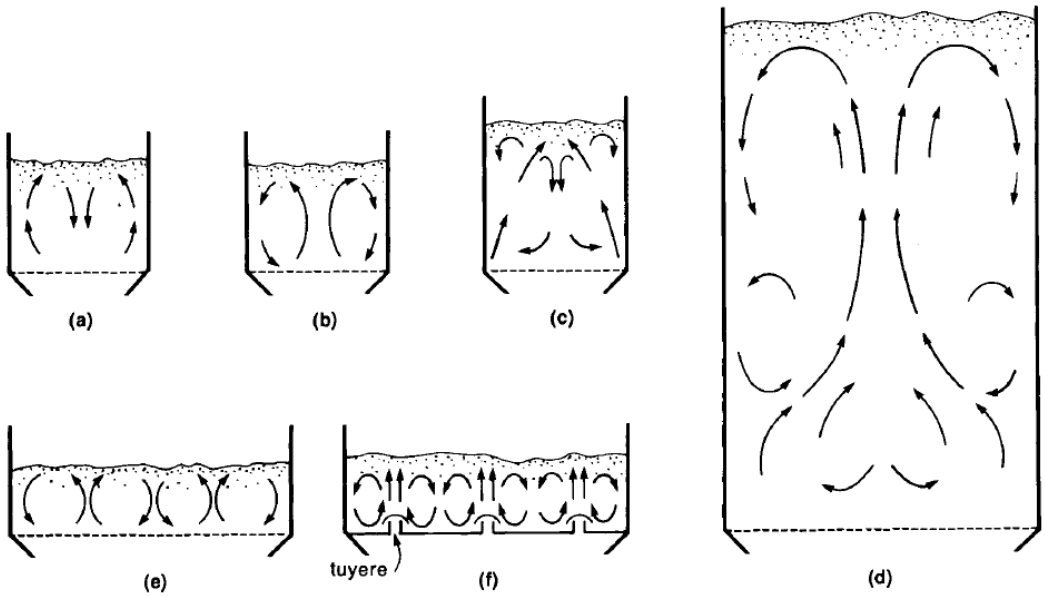

Figure 2.8: Circulation pattern of solid emulsion in bubbling fluidized bed (a) z/dt ≈ 1, low u_o; (b) z/dt ≈ 1, high u_o; (c) z/dt ≈ 2, high u_o; (d) general pattern in deep bed; (e) shallow bed, uniform distributor; (f) bed, tuyeres [15]

Bubble size and bubble growth

In general, the bubble's size and shape may vary significantly in such a bubbling fluidized bed. The average bubble size is somewhat irregular and hard to characterize. However, referring to some investigations on this particular subject, with the assumption of spherical bubbles of diameter d_b, the mean volumetric size can be estimated.

Bubbles in the beds of fine particles such as FCC catalyst (Geldart A), rapidly grow to a few centimeters in size and remain at the same size once reaching the equilibrium between bubbling splitting and coalescing. Figure 2.9 shows the bubble's growth in the about 0.5 m bed diameter from Werther [33] and Yamazaki et al. [35].

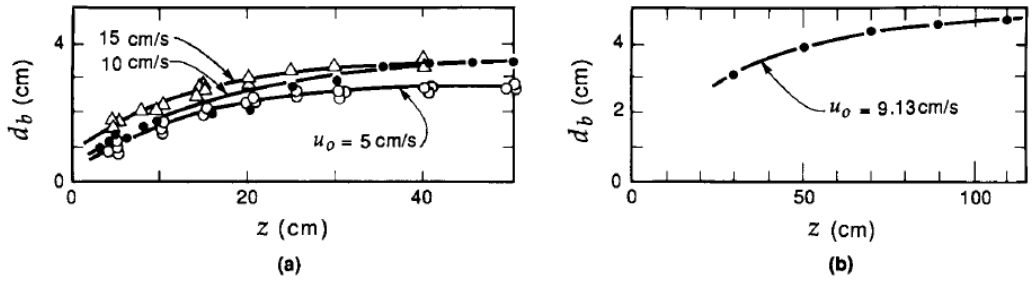

Figure 2.9: Bubble's growth profile of Geldart A solid of (a) cracking catalyst, u_{mf} = 0.23 cm/s, porous plate distributor [33]; (b) spent cracking catalyst, u_{mf} = 0.13 cm/s, d_p = 63 μm, perforated plate distributor [35].

In the bed of bigger particles (Geldart B), bubbles develop steadily along with the vessel's height and reach tens of centimeters in size. It was also noted that bubbles produced on nozzle or tuyere distributors are bigger than that of perforated distributors at similar fluidizing velocity. For Geldart D particles, bubbles will grow even bigger as one might expect. Figure 2.10 shows the bubble's growth in a large bed of 1x1 m with a perforated plate distributor from Golfers [38] and Glicksman et al. [39].

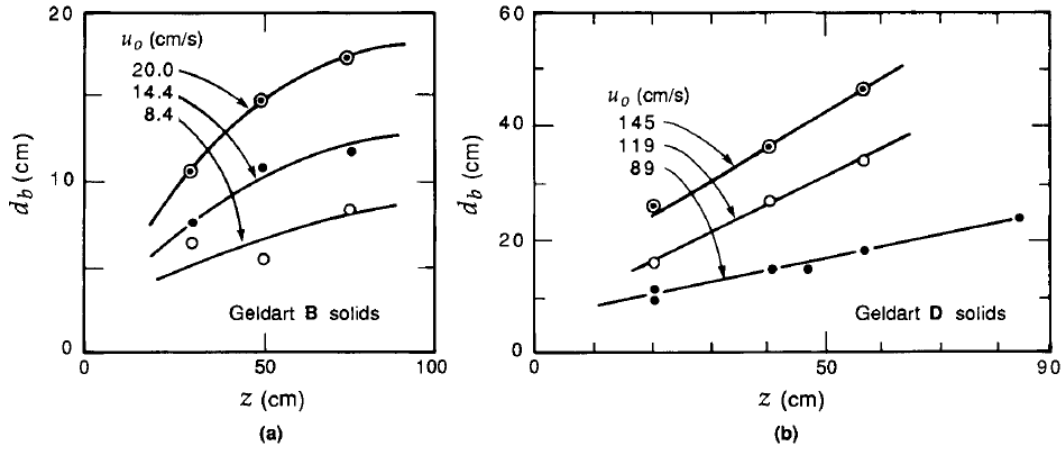

Figure 2.10: Bubble's growth profile of (a) Geldart B solids, d_p = 184 μm, u_{mf} = 3.5 cm/s [38]; (b) Geldart D solids, d_p = 1 mm, u_{mf} = 58 cm/s [39].

Bubble size correlations. Based on several findings, bubbles will reach a small limited size in the case of fine particles, while they will become bigger in larger particle sizes and most likely grow limitless in the huge particle system. Several researchers were trying to draw some correlations for the bubble's growth estimation in fluidized bed referring to experiments, mainly on Geldart B particle system in small bed diameter. It is still reasonably applicable for large diameter bed according to Golfers [38].

For Geldart B and D solids, Mori and Wen [40] proposed the correlation of bubble size d_b at any height z in the bed as follows:

$$\frac{d_{bm} - d_b}{d_{bm} - d_{b0}} = e^{-0.3z/d_t} \tag{7}$$

where d_{b0} is the initial bubble size developed in the bottom of the bed which calculated from [15]:

$$d_{b0} = \frac{1.3}{g^{0.2}} \left[\frac{u_o - u_{mf}}{N_{or}}\right]^{0.4}, d_{b0} \leq l_{or}, [cm] \tag{8}$$

for the low gas flow rate, and following this form for a higher gas flow rate:

$$d_{b0} = \frac{2.78}{g}(u_o - u_{mf})^2, d_{b0} > l_{or}, [cm] \tag{9}$$

with l_{or} is the spacing between adjacent holes and N_{or} is the number of orifices per unit area, thus:

$$N_{or} = \frac{1}{l_{or}^2} for\ square\ array\ of\ holes \tag{10}$$

$$N_{or} = \frac{2}{\sqrt{3} l_{or}^2} for\ an\ equilateral\ array\ of\ holes \tag{11}$$

In the case of tuyere nozzle distributor, N_{or} takes the following equation:

$$N_{or} = \left(\frac{tuyeres}{area}\right)\left(\frac{number\ of\ holes}{tuyere}\right) \tag{12}$$

and d_{bm} is the maximum bubble diameter at a very deep bed. It follows:

$$d_{bm} = 0.65 \left[\frac{\pi}{4} d_t^2 (u_o - u_{mf})\right]^{0.4}, [cm] \tag{13}$$

Hence, by calculating d_{bo} and d_{bm} and use these as input for the Eq.7 will give the mean bubble size d_b at any height z in the bed with the diameter of d_t. The range of condition that validates this formulation is

- $d_t \leq$ 1.3 m, 0.5$\leq u_{mf} \leq$ 20 cm/s
- 60$\leq d_p \leq$ 450 μm, u_o-$u_{mf} \leq$ 48 cm/s

Werther [33] proposed another formulation for the bubble mean size at any height z, especially for bed with Geldart B particle and using porous plate distributor

$$d_b = 0.853[1 + 0.272(u_o - u_{mf})]^{1/3}(1 + 0.0684z)^{1.21}, [cm] \tag{14}$$

with the range of operating condition from which the equation was derived

- $d_t >$ 20 cm, 1$\leq u_{mf} \leq$ 8 cm/s
- 100$\leq d_p \leq$ 350 μm, 5$\leq u_o$-$u_{mf} \leq$ 30 cm/s

For another type of distributor such as nozzle or tuyere model, the d_b-vs-z curve should be adjusted to fit the initial bubble size d_{bo} at an initial height z_o. The detail examples of calculation can be found further in Chapter 4 of this book [15].

Terminal velocity (u_t)

In the case of moderate gas flow, where approximately at the $u_o < 10u_{mf}$, there will be not much solid particle carryover by the gas. However, in the higher gas flows, more particles reach the reactor's freeboard zone, where some of them will return to the bed, and others carried out by the gas out of bed. One variable governs this phenomenon is called the terminal velocity, u_t. Terminal velocity occurs when the sum of the drag force and buoyancy is equal to the downward force of gravity in the particle. This terminal free-fall velocity can be estimated from the fluid mechanic expression [15]:

$$u_t = \left[\frac{4d_p(\rho_s - \rho_g)g}{3\rho_g C_D}\right]^{1/2} \tag{15}$$

where C_D is the drag coefficient determined from the experiment. There will be some dedicated drag models provided in the later section, while here the general form obtained from [15] is presented:

$$C_D = \frac{24}{Re_p} + 3.3643Re_p^{0.3471} + \frac{0.4607Re_p}{Re_p + 2682.5} \tag{16}$$

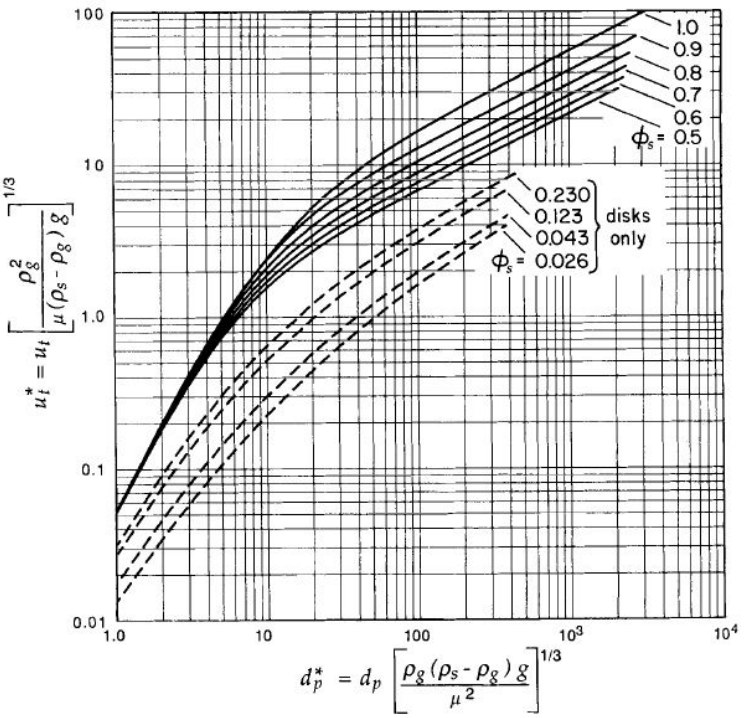

Figure 2.11: Terminal velocity correlation with the particle's diameter represented in the form of non-dimensional parameters developed by Haider and Levenspiel [15]

Figure 2.11 shows a graphical representation of terminal velocity against the particle diameter. The direct examination of u_t can be performed by introducing a dimensionless gas velocity u^* and a dimensionless particle size d^*. Those variables are expressed as:

$$d_p^* = d_p \left[\frac{\rho_g(\rho_s - \rho_g)g}{\mu^2}\right]^{1/3} = Ar^{1/3} = \left(\frac{3}{4} C_D Re_p^2\right)^{1/3} \tag{17}$$

$$u^* = u \left[\frac{\rho_g^2}{\mu(\rho_s - \rho_g)g}\right]^{1/3} = \frac{Re_p}{Ar^{1/3}} = \left(\frac{4}{3}\frac{Re_p}{C_D}\right)^{1/3} \tag{18}$$

$$u_t^* = \left[\frac{18}{(d_p^*)^2} + \frac{2.335 - 1.744\phi_s}{(d_p^*)^{0.5}}\right]^{-1}, 0.5 < \phi_s < 1 \tag{19}$$

The carryover of particles in fluidized bed can be controlled via the interplay of gas velocity in between u_{mf} and u_t. The mean diameter of particles is used for the calculation of the u_{mf}, while for the u_t, the smallest particle size with appreciable quantities is considered. The ratio of u_t/u_{mf} heavily relies on the particle size. It is about 78 for fine solids while 9.2 for the larger one. Figure 2.12 provides the relationship between this ratio and particle size and sphericity.

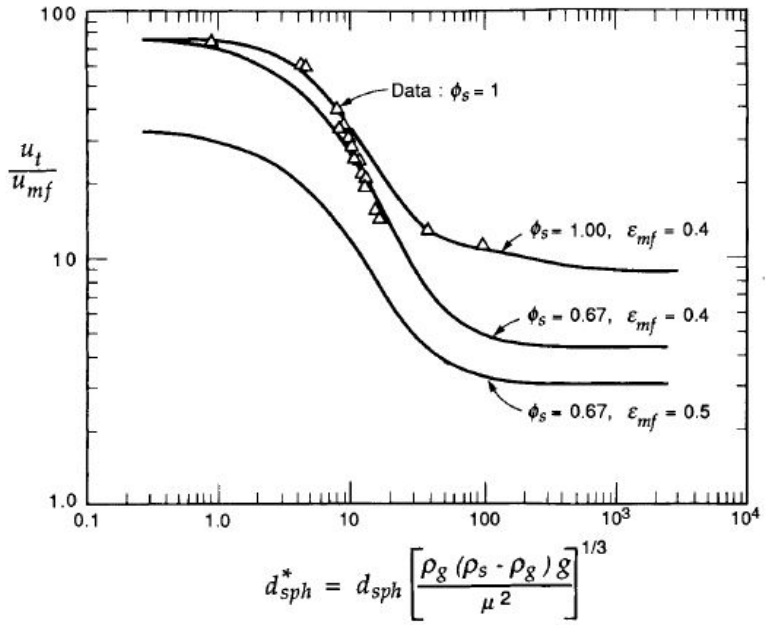

Figure 2.12: The effect of particle size and sphericity to the terminal to the minimum fluidization velocity ratio (u_t/u_{mf}), based on the data from Pinchbeck and Popper [15]

Slug flow

Bubbles formed inside the bed can grow to diameters equal to the bed diameter and create slugs when fluidizing at a tall and narrow bed of solids. For beds of small particles with good fluidization, as seen in Figure 2.13a, particles rain on the bed wall to follow the growth of these slugs. Those are referred to as axial slugs. At higher gas velocity, the growing slugs appear to cling and slip to the wall either due to the particles' nonsphericity or the rough wall of the vessel, as seen in Figure 2.13b. Those are known as wall slugs [15].

Another mode of slugging is seen with Geldart D solids, as shown in Figure 2.13c. In this case, the bed is separated by gas to form emulsion slices. These gas and emulsion breaks rise from slice to slice, along with the relentless raining of solids. The first emulsion slice at the top, unreplenished with raining solids, finally disappears, and from the bottom of the bed, new fresh slices or slugs will rise. Such is referred to as flat slugs [15].

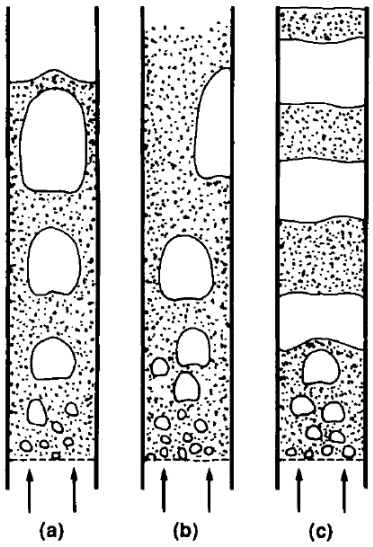

Figure 2.13: Slugging type in fluidized bed; (a) axial slugs-for fine small particles; (b) wall slugs-higher gas velocity, fine rough particles, rough walls; (c) flat slugs- for Geldart D particles. [15]

Stewart and Davidson [41] initially developed the formulation of bubbling rise velocity based on the analysis of forces pushing a slug in its place against the water flowing at u_{br} at the liquid-solid system. This concept was then tested on fluidized beds environment, and the experimental result agreed well with the equation. Hence, for slugs in the fluidized bed, the following correlation is proposed

$$u_{br} = 0.35(gd_t)^{1/2} \tag{20}$$

For continuous gas flow introduction on the bed, Stewart dan Davidson [41] assumed that excess gas beyond u_{mf} (u_o-u_{mf}) might drive the slugs or slice of solid at a velocity higher than u_{br} which follows

$$u_b = const(u_o - u_{mf}) + 0.35(gd_t)^{1/2} \tag{21}$$

And they also derive the equation for minimum slugging velocity ($u_{b,ms}$) where at below following rise gas velocity, slugging could be avoided

$$u_{b,ms} = u_{mf} + 0.07(gd_t)^{1/2} \tag{22}$$

Baeyens and Geldart [42] further studied this slugging behavior and found out that except for the smallest column diameter, neither particle size nor the distributors affected slugging. They then made the formulation for height in the bed at which complete slugging is developed

$$z_s = 60d_t^{0.175}, [cm] \tag{23}$$

Therefore, it is assumed that in the mode of fluidization in the deep bed should develop slugging if superficial gas velocity is beyond $u_{b,ms}$ and at the height above z_s above distributor. And thus, the shallow bed below z_s should have no slugging.

2.2 Heat Transfer

Unsteady-state heat diffusion

One of the most relevant and frequently used heat transfer models in the fluidized bed phenomena to determine the heat transfer coefficient in the vicinity of a heated wall is the emulsion phases model. The model developed by Mickley and Fairbanks [43], also known as the packet renewal model, assumes that the fluidized bed consists of the emulsion (continuous phase) and bubble (discrete phase). They suggested that heat is transmitted to the "packets" of the emulsion phase and is regularly replaced by bubbles from the heat transfer surface. Their main finding was that the process controlling mechanism in fluidized bed heat transfer is unsteady-state diffusion of heat into a packet of particles of quiescent bed material. This is illustrated in Figure 2.14 as follows, where q_m is the instantaneous rate of heat flow into a packet, A_m is the contact area of the packet with the surface, T_0 is bed temperature and T_1 heated surface temperature:

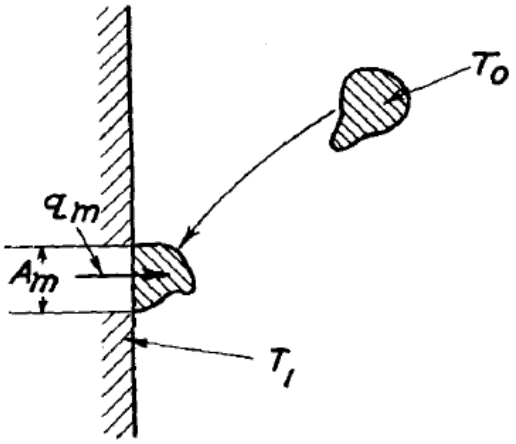

Figure 2.14: Heat transfer process of a packet of particle to a heated surface [43]

Based on the packet renewal model, the local instantaneous heat transfer coefficient h_i is given by:

$$h_i = \sqrt{\frac{\kappa_m \left(\rho C_p\right)_m}{\pi t_p}} \tag{24}$$

where t_p is the period for which the packet was in contact with the surface of heat transfer source and κ_m is the thermal conductivity of the packet.

Within this model, the thermophysical properties in the packet are considered uniform and usually examined during the incipient fluidization of the bed. However, due to the variation of the bed voidage in the vicinity of the heat transfer surface, the thermophysical properties of the packet near the surface may differ from those in the bulk of the emulsion phase. The approximate thickness of the surface layer where principal voidage variation occurs is one particle diameter [44].

TFM on heat transfer

The two-fluid model (TFM) implemented on the fluidized bed's heat transfer has been developed and has the advantage over previous models, e.g., emulsion phase model mentioned earlier. Through this model, the bed hydrodynamics and behavior evolved naturally from the mass and momentum equation solution, thus eliminating the usage of such empirical parameters, e.g., packet residence time. Two empirical correlations of interphase momentum transfer coefficient and the interphase heat transfer coefficient will be incorporated to account for microscale momentum and heat transfer between medium.

A separate enthalpy equation is written for fluid phase (f) and solid phase (s) to describe the conservation of energy as follows [45]:

$$\frac{\partial}{\partial t}\left(\alpha_f \rho_f C_{p,f}\right) + \bigtriangledown.\left(\alpha_f \rho_f \vec{u}_f C_{p,f}\right) = \alpha_f \frac{\partial p_f}{\partial t} + \bar{\bar{\tau}}_f : \bigtriangledown \vec{u}_f - \bigtriangledown.\vec{q}_f + S_f + Q_{fs} \tag{25}$$

$$\frac{\partial}{\partial t}\left(\alpha_s \rho_s C_{p,s}\right) + \bigtriangledown.\left(\alpha_s \rho_s \vec{u}_s C_{p,s}\right) = \alpha_s \frac{\partial p_s}{\partial t} + \bar{\bar{\tau}}_s : \bigtriangledown \vec{u}_s - \bigtriangledown.\vec{q}_s + S_s + Q_{sf} \tag{26}$$

where C_p is the specific enthalpy, $\vec{q}$ is the conductive heat flux, and S is the source term that accomodate sources of enthalpy e.g. due to chemical reaction or radiation. Then Q is the heat exchange between phases, where it should comply with the local balance condition Q_{fs} = - Q_{sf} and $Q_{ss} = 0$.

The correct interpretation of the constitutive equations for the effective thermal conductivities $k_{eff,f}$ and $k_{eff,s}$ raises a significant challenge in the theoretical formulation. In the context of the TFM method, both $k_{eff,f}$ and $k_{eff,s}$ must be interpreted as effective transport properties, which depend on α_f, k_f, k_s, and particle geometry.

Based on the Fourier's law of heat conduction, the expression of conductive heat fluxes for both solid and fluid phase, $\vec{q}_s$ and $\vec{q}_f$ respectively, can be written as follows:

$$\vec{q} = \vec{q}_f + \vec{q}_s = -\left[\alpha_f \kappa_{eff,f} \bigtriangledown T_f + (1-\alpha_f)\,\kappa_{eff,s} \bigtriangledown T_s\right] \tag{27}$$

which reduces to:

$$\vec{q} = -\left[\alpha_f \kappa_{eff,f} + (1-\alpha_f)\,\kappa_{eff,s}\right] \bigtriangledown T = -\kappa_m \bigtriangledown T \tag{28}$$

when the system reaches a thermodynamic equilibrium, where T_f=T_s=T. The mixture conductivity (κ_m) can be defined as:

$$\kappa_m = \alpha_f \kappa_{eff,f} + (1-\alpha_f)\,\kappa_{eff,s} \tag{29}$$

The mixture conductivity corresponds to the effective bed conductivity, κ_b which can be determined experimentally can best be approximated by the model of Zehner and Schlunder [46]:

$$\kappa_b = \kappa_{b,f} + \kappa_{b,s} \tag{30}$$

where

$$\kappa_{b,f} = \left(1 - \sqrt{(1-\alpha_f)}\right) \kappa_f \tag{31}$$

$$\kappa_{b,s} = \sqrt{(1-\alpha_f)}\,\{\omega A + (1-\omega)\,\Gamma\}\,\kappa_f \tag{32}$$

and

$$\Gamma = \frac{2}{\left(1-\frac{B}{A}\right)} \left\{ \frac{(A-1)}{\left(1-\frac{B}{A}\right)^2} \frac{B}{A} ln \frac{A}{B} - \frac{(B-1)}{\left(1-\frac{B}{A}\right)} - \frac{1}{2}\,(B+1) \right\} \tag{33}$$

$$B = 1.25 \left(\frac{1-\alpha_f}{\alpha_f}\right)^{10/9} \tag{34}$$

where for the case of spherical particles:

$$A = \frac{\kappa_s}{\kappa_f} \tag{35}$$

$$\omega = 7.26 \times 10^{-3} \tag{36}$$

Then, finally the $\kappa_{eff,f}$ and $\kappa_{eff,s}$ can be obtained from:

$$\kappa_{eff,f} = \frac{\kappa_{b,f}}{\alpha_f} \tag{37}$$

$$\kappa_{eff,s} = \frac{\kappa_{b,s}}{1-\alpha_f} \tag{38}$$

The volumetric energy transfer rate between phases (Q) is assumed to be a function of the interfacial area which can be calculated with the symmetric model (A_{fs}=$6\alpha_f$(1-α_f)/d_p) and the temperature difference:

$$Q_{fs} = h_{fs} A_{fs}\,(T_f - T_s) \tag{39}$$

$$Q_{sf} = h_{sf} A_{fs}\,(T_s - T_f) \tag{40}$$

where h_{fs} (=h_{sf}) is the volumetric heat transfer coefficient between phases. The heat transfer coefficient is related to Nusselt number (Nu_s) by:

$$h_{sf} = \frac{\kappa_f Nu_s}{d_p} \tag{41}$$

On the Eq. 41 κ_f is the thermal conductivity, while d_p is the particle's diameter.

On determining the volumetric heat transfer coefficient, there are several approaches available in ANSYS Fluent. However, the most relevant correlation for managing multiphase simulation that includes the granular phase is Gunn [47] model. It is applicable for the solid particle with a porosity range of 0.35-1.0 and a Reynolds number up to 10^5. The Nusselt formulation takes the following form:

$$Nu_s = \left(7 - 10\alpha_f + 5\alpha_f^2\right)\left(1 + 0.7Re_s^{0.2}Pr^{1/3}\right) + \left(1.33 - 2.4\alpha_f + 1.2\alpha_f^2\right)Re_s^{0.7}Pr^{1/3} \tag{42}$$

where the Reynolds and Prandtl number are defined as follow:

$$Re_s = \frac{\alpha_f \rho_f \left|\bar{u} - \bar{v}\right| d_p}{\mu_f} \tag{43}$$

$$Pr = \frac{C_{p,f}\mu_f}{\kappa_f} \tag{44}$$

where the Nusselt number obtained from the Eq.42 approaches 2 for the case of an isolated particle in an infinite stagnant medium:

$$lim_{\alpha_f -> 1, Re_s -> 0}\left(Nu_s\right) = 2 \tag{45}$$

Radiative heat transfer

Radiative heat transfer is widely used to describe the concept of heat transfer caused by electromagnetic waves. Several prominent examples of our daily lives are the heating effect of sunshine on a clear, bright day, or whenever one standing in front of the fire-the body's side facing the fire feels much hotter than the back and so on. Thermal radiation's more fine examples are that sunsets are red, clear skies are blue, and during a clear winter night, we feel more comfortable in a room with the drawn curtains than in a place with that open one.

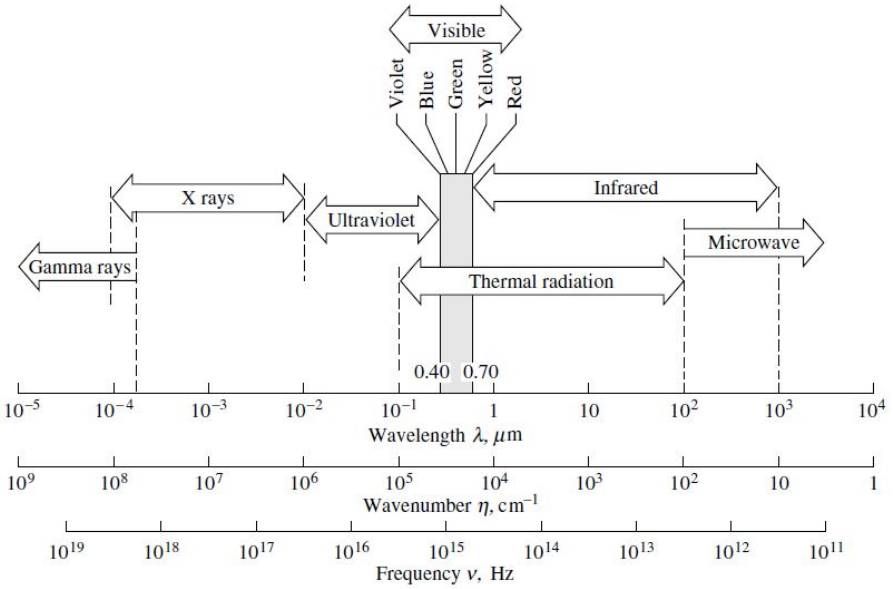

Figure 2.15: Electromagnetic wave spectrum on the emphasis of the thermal radiation wavelength range [48]

By nature, all materials continuously emit and absorb electromagnetic waves or photons by lowering or raising their molecular energy level. This emission wavelength and characteristic very much depend on its temperature. In terms of the heat transfer process, ultraviolet, visible and infrared in the range of wavelength between 10^{-7}m and 10^{-3}m (Figure 2.15) are of the significant importance. Each wave is identified by its:

frequency, ν (measured in cycles/s=s^{-1}= Hz);
wavelength, λ (measured in μm=10^{-6} m or nm = 10^{-9} m);
wavenumber, η (measured in cm^{-1};

angular frequency, ω (measured in radians/s = s^{-1});

All these quantities are correlated one another through the expression:

$$\nu = \frac{\omega}{2\pi} = \frac{c}{\lambda} = c\eta \tag{46}$$

When an electromagnetic wave passing through a medium (or vacuum) hits the surface of another material (a solid or liquid surface, a particle or a bubble), the wave may be reflected (either partly or entirely), and any unreflected component may penetrate the medium. When moving through the medium, the wave can be continuously attenuated. If the attenuation is complete so that no penetrating radiation re-emerges, it is known as "opaque". If a wave moves through a medium without attenuation, it is called "transparent", whereas a body with partial attenuation is considered "semitransparent".

A perfect absorber or black absorber is an opaque surface that does not reflect any radiation but absorbs everything. Because black surfaces absorb the highest amount of radiative energy available, they must also emit the maximum possible energy and thus act as a measure for the classification of all other surfaces. The radiative heat flux (emissive power) emitted by the blackbody is well explained by the Planck's law:

$$E_{b\nu}(T,\nu) = \frac{2\pi h\nu^3 n^2}{c_0^2\left[e^{h\nu/kT}-1\right]} \tag{47}$$

where k = 1.3807 x 10^{-23} J/K is known as Boltzmann's constant. If the refractive index is independent of the frequency or wavelength, which is undoubtedly true for vacuum and ordinary gas, and some semitransparent media, the spectral emissive power will be:

$$E_{b\lambda}(T,\lambda) = \frac{2\pi hc_0^2}{n^2\lambda^5\left[e^{hc_0/n\lambda kT}-1\right]} \tag{48}$$

with some introduction for the abbrevations for brevity:

$$C_1 = 2\pi hc_0^2 = 3.7418\times10^{-16} Wm^2 \tag{49}$$

$$C_2 = hc_0/k = 1.4388 cmK \tag{50}$$

the Eq.48 can be re-arranged in the form:

$$\frac{E_{b\lambda}}{n^3T^5} = \frac{C_1}{(n\lambda T)^5\left[e^{C_2/(n\lambda T)}-1\right]} \tag{51}$$

Based on this this expression (Eq.51), it is possible to plot the normalized emissive a power as a single line vs. the product of wavelength in vacuum (nλ) and T as shown in Figure.2.16. The maximum point of this curve will lead to a transcendental equation which is solved by Wiens's displacement law and yields:

$$(n\lambda T)_{max} = C_3 = 2898\mu mK \tag{52}$$

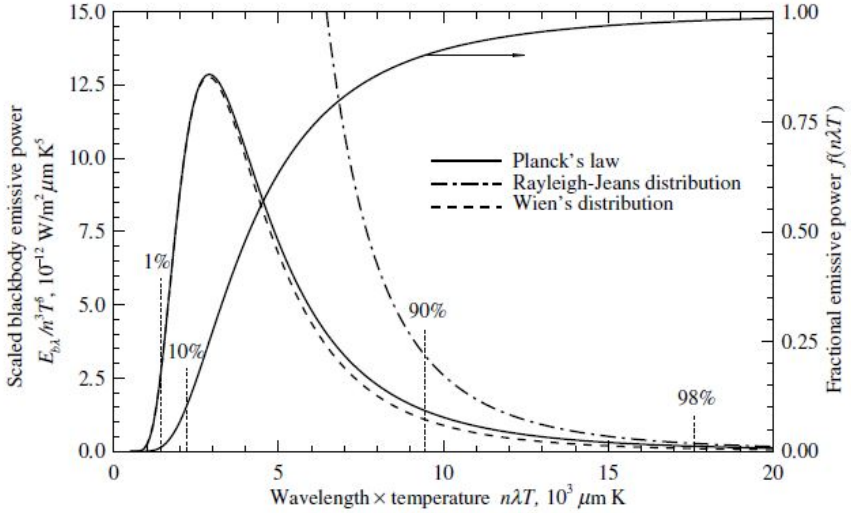

Figure 2.16: Normalized blackbody emissive power spectrum [48]

Referring to the spectral emissive power equation (Eq.51), the total blackbody emissive power will be:

$$E_b(T) = \int_0^\infty E_{b\lambda}(T,\lambda)\, d\lambda = C_1 n^2 T^4 \int_0^\infty \frac{d(n\lambda T)}{(n\lambda T)^5 \left[e^{C_2/(n\lambda T)} - 1\right]} \tag{53}$$

$$E_b(T) = n^2 \sigma T^4, \sigma = \frac{\pi^4 C_1}{15 C_2^4} = 5.670 \times 10^{-8} \frac{W}{m^2 K^4} \tag{54}$$

If an incident electromagnetic radiation is partly absorbed by the body, it is considered a gray body. The ratio of thermal radiation of the gray body to the thermal radiation of the black body at the same temperature is called the emissivity of the gray body:

$$e = \frac{E(T)}{E_b(T)} \tag{55}$$

Radiative transfer in participating media

Three distinct processes may arise in the event of an incident on the surface: absorption, reflection, and propagation. Absorptivity (α), reflectivity (ρ), and transmissivity (τ) are defined to describe surface properties. Due to energy conservation, the sum of the absorbed, reflected, and transmitted energy is always equal to that of the incident radiative energy, such that $\alpha+\rho+\tau$ is equal to 1. If the medium in which the radiative energy passes is "participating", each incident beam should be attenuated through absorption and scattering as it moves through the medium as seen schematically in the Figure 2.17.

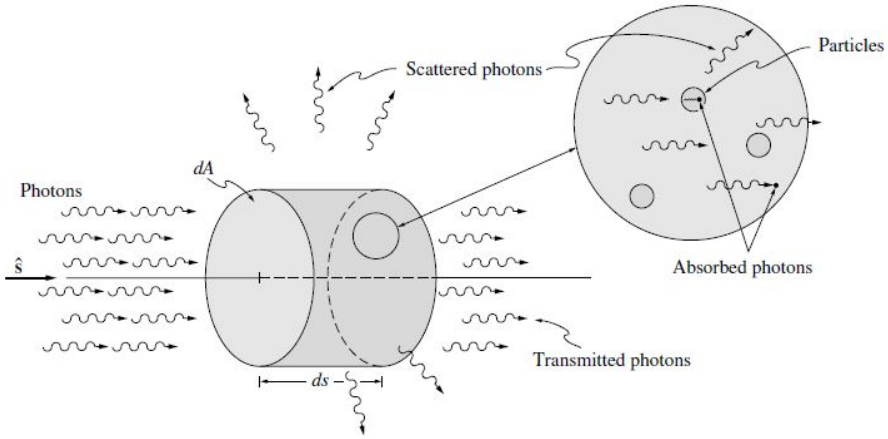

Figure 2.17: Attenuation of radiative intensity by absorption and scattering [48]

The absolute amount of absorption was found to be directly proportional to the magnitude of the incident energy, as well as the distance the beam passes through the medium. So, the expression will be:

$$(dI_\eta)_{abs} = -a_\eta I_\eta ds \tag{56}$$

where the proportionality constant a_η is defined as the (linear) absorption coefficient and the negative sign has been added as the amplitude decreases.

The integration of eq. 56 over the geometric length s yields:

$$I_\eta(s) = I_\eta(0)\, exp\left(\int_0^s a_\eta ds\right) = I_\eta(0)\, e^{-\tau_\eta} \tag{57}$$

where

$$\tau_\eta = \int_0^s a_\eta ds \tag{58}$$

is the absorption's optical thickness through which the beam has traveled and $I_\eta(0)$ is the initial intensity entering the medium at s=0.

Attenuation by scattering is somewhat similar to absorption because part of the incoming intensity is separated from the direction of propagation. The discrepancy is that the absorbed energy is turned into internal energy, while the emitted energy is merely redirected and appears as augmentation along another direction, given by:

$$(dI_\eta)_{sca} = -\sigma_\eta I_\eta ds \tag{59}$$

where the proportionality constant $\sigma_{s\eta}$ is defined as the (linear) scattering coefficient from the pencil of rays under consideration into all other directions.

The total attenuation of the intensity in a pencil of rays by both absorption and scattering is known as extinction. Thus, an extinction coefficient is defined as:

$$\beta_\eta = a_\eta + \sigma_\eta \tag{60}$$

where

$$\tau_\eta = \int_0^s \beta_\eta ds \tag{61}$$

is the optical thickness based on extinction.

Radiative properties of particulate media
When an electromagnetic wave or a photon interacts with a medium that contains small particles, as is the case of the fluidized bed, absorption and scattering may change the radiative intensity. Three separate phenomena, namely (i) diffraction (the presence of the particle alter the wave propagation direction), (ii) reflection (waves reflected from the surface of the sphere), and (iii) refraction (waves that penetrate reemerges traveling into a different direction) induce the scattering of a wavelength by the vicinity of the particle. Figure 2.18 illustrated these phenomena.

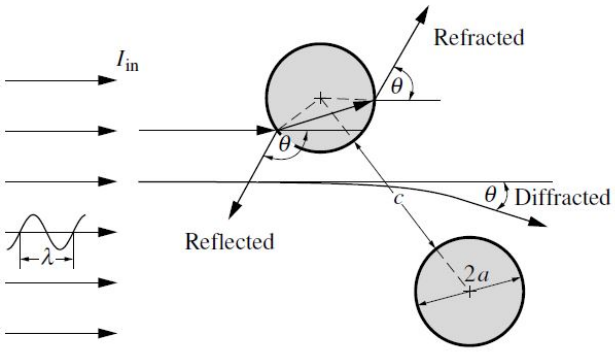

Figure 2.18: Interaction between electromagnetic wave and spherical particles [48]

Three independent nondimensional parameters govern the radiative properties of a cloud of spherical particles of radius r, which interacts with a wavelength passing through its vicinity:

- complex index of refraction: m = n - ik
- size parameter: x = 2π r/λ
- clearance-to-wavelength ratio: c/λ

In the case of independent scattering (c/λ), where the scattering of one particle is not affected by the surrounding particles, only the first two parameters are taken into account. And this is the case for the fluidized bed, according to Tien et al.[49], where most of the scattering regime has c/$\lambda > 0.5$.

Radiative heat transfer in the fluidized bed deals with an extensive collection of particles. Since the scattering is independent, the effect of a large number of particles is additive. If N_T is the number of particles with radius r per unit volume of the bed, it can be expressed as the function of solid volume fraction [48]:

$$N_T = \frac{\alpha_s}{\frac{4}{3}\pi r^3} \tag{62}$$

Thus, the absorption, scattering, and extinction coefficient of cloud particle are then defined as:

$$\sigma_\lambda = N_T C_{sca} = \frac{3\alpha_s}{4r} Q_{sca} \tag{63}$$

$$a_\lambda = N_T C_{abs} = \frac{3\alpha_s}{4r} Q_{abs} \tag{64}$$

$$\beta_\lambda = a_\lambda + \sigma_\lambda = N_T C_{ext} = \frac{3\alpha_s}{4r} Q_{ext} \tag{65}$$

where C_{sca}, C_{abs}, C_{ext} are scattering, absorption, and extinction cross-section respectively, and Q_{sca}, Q_{abs}, Q_{ext} are scattering, absorption, and extinction efficiency factor respectively.

With respect of particle size (size parameter), scattering phenomena on the particulate system can be distinguished into three categories:

- x « 1 or Rayleigh scattering. Such behavior can generally be observed on gas molecules.
- x ≈ 1 or Mie scattering. This generally can be found in dust, smoke, water droplets, and other particles in the lower portion of the atmosphere.
- x » 1 or commonly called non-selective scattering. In this case, the surface of the particle may be viewed as a regular surface, and the properties may be determined by geometric optics.

Scattering in the fluidized bed generally lies in the third category, where the particle size is much larger than the wavelength of the interest. Thus the material properties can be obtained through geometric optics. Since Q_{ext} equal to 2 for a large sphere, and diffraction accounts for half of it, the rest is the portion of absorption and scattering. However, the diffraction can be further neglected as the phase function (Figure 2.19) for the large sphere demonstrates that almost all energy is scattered forward within the narrow cone $(<150/x)^o$ from the direction of transmission. Hence, the final Q_{ext} on the heat transfer should equal to 1.

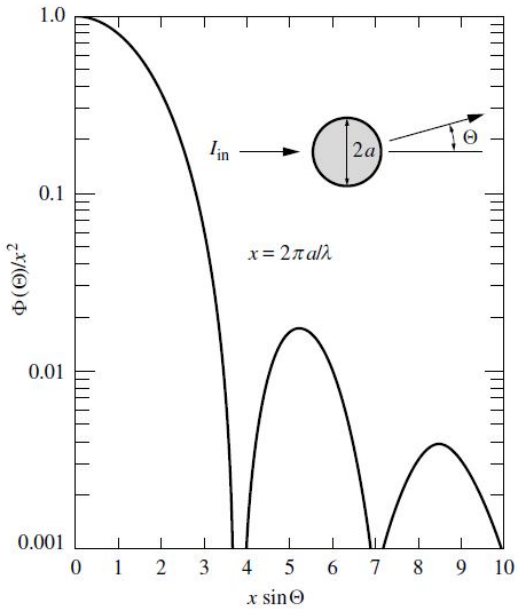

Figure 2.19: Phase function for diffraction over a large sphere. [48]

The scattering efficiency for large, opaque, specularly reflecting particle is simply [48]:

$$Q_{sca} = \frac{dQ_s}{dQ_i} = \rho^s \tag{66}$$

where ρ^s is the hemisperical reflectance, averaged over all incoming directions. Thus, the absorption efficiency follows as:

$$Q_{abs} = Q_{ext} - Q_{sca} = 1 - \rho^s = a \tag{67}$$

where a is the hemisperical absorptivity.

In the case of dielectric material, e.g., corundum particles, where k«n, the hemispherical absorptivity is equal to hemispherical emissivity e_λ derived by Dunkle et al. [48]:

$$e_{\parallel} = \frac{4\,(2n+1)}{3\,(n+1)^2} \tag{68}$$

$$e_{\perp} = \frac{4n^3\left(n^2+2n-1\right)}{(n^2+1)\left(n^4-1\right)} + \frac{2n^2\left(n^2-1\right)^2}{(n^2+1)^3}\ln\left(\frac{n+1}{n-1}\right) - \frac{16n^4\left(n^4+1\right)\ln n}{(n^2+1)\left(n^4-1\right)^2} \tag{69}$$

$$e_\lambda = \frac{1}{2}\left(e_{\parallel} + e_{\perp}\right) \tag{70}$$

2.3 Eulerian Multiphase Model

In the Eulerian – Eulerian method, all gas and solid phases are viewed mathematically as inter-penetrating continua. The basic concept is to use the governing equations that correlate the gas – particle flow changes in each computing unit to represent the gas and solid phase properties. One does not have to track single solid particle's trajectory. The Eulerian–Eulerian method is thus one inexpensive modeling methodology that could perform DPRS simulation at a pilot or industrial scale. In this method the definition of phase volume fraction (PVF) is implemented for the purpose of separating the area occupied by solid and fluid. The PVF is considered to be continuous in space and time functions, and the sum of the gas and particle phase PVF is equal to one [50]. This explanation is clearly described through the following expression in Eq. 71-73 [45]:

$$V_s = \int_V \alpha_s dV \tag{71}$$

$$\sum_{s=1}^{n} \alpha_s = 1 \tag{72}$$

$$\hat{\rho}_s = \alpha_s \rho_s \tag{73}$$

where $\hat{\rho}_s$ and ρ_s are the effective density and the physical density of phase s respectively .

This method allows all particle-scale processes such as collision, drag, friction forces, and heterogeneous chemical reactions to be resolved in an Eulerian grid and integrated into governing equations in terms of phase interaction. The developed DPRS models through the Eulerian-Eulerian method can handle hydrodynamics, heat transfer, and chemical reactions in multiphase systems together based on the Eulerian–Eulerian method. The unsteady equilibrium equations for mass, momentum, energy, and species for the gas and particle phases were solved to determine the transient nature of the gas-solid flow. Meanwhile, various turbulent models are used to estimate the turbulent effect of the gas phase and reduce the computational load. KTGF-based granular stress equations are used to model the constitutive relations for the solid phase [23].

One of the platforms to build CFD simulation with the Eulerian-Eulerian model that frequently used as it offers a full academic license is ANSYS Fluent. In ANSYS Fluent, the solution is based on the following [51]:

- A single pressure is shared by all phases involved
- Momentum and continuity equations are solved for each phase
- Granular temperature, which represents solid fluctuating energy, can be calculated for each solid phase
- Solid-phase shear and bulk viscosities are calculated based on kinetic theory to granular flow

2.3.1 Conservation Equations

Conservation of mass

The theory of general mass conservation or continuity equations is based on the assumption that all mass flow rates in the modeling domain are equal to the sum of all mass flow rates out and the rate of change in time. This can be extended to the individual flow components as well as to the overall flow stream. The continuity equation for gas (f) and solid (s) phase take the form [45]:

$$\frac{\partial}{\partial t}(\alpha_f \rho_f) + \bigtriangledown.(\alpha_f \rho_f \vec{v}_f) = 0 \tag{74}$$

$$\frac{\partial}{\partial t}(\alpha_s \rho_s) + \bigtriangledown.(\alpha_s \rho_s \vec{v}_s) = 0 \tag{75}$$

where $\vec{\mathrm{v}}_f$ and $\vec{\mathrm{v}}_s$ are the velocity phase for gas and solid phase respectively. The typical expression will appear in the equations of momentum and enthalpy.

Based on the above mass conservation equation, the volume fraction of each phase can be calculated following:

$$\frac{1}{\rho_{rs}}\left(\frac{\partial}{\partial t}(\alpha_s \rho_s) + \bigtriangledown.(\alpha_s \rho_s \vec{v}_s) = 0\right) \tag{76}$$

where ρ_{rs} is the volume-averaged density or the phase reference density of the s^{th} phase in the solution domain. The secondary phase equation will be solved according to the Eq. 76, and along with the sum of α_f and α_s is one (referring to Eq. 72), the primary phase volume fraction can be obtained.

Conservation of momentum

Momentum is a vector quantity that has directional properties of each phase and magnitude. Similar to the continuity equation, momentum equation, which is described by Newton's second law of motion should also be conserved. The conservation equations of momentum are defined by observing the forces acting on the system's fluid mass; the mass flows into and out of the systems. In the present fluidized bed case, there is no lifting force (particles are too small in size for lifting force to be significant) and a virtual mass force (only significant when $\rho_s \ll \rho_f$). Thus, only drag and buoyancy forces are considered. The momentum balance for gas (f) phase expressed as follows [45]:

$$\frac{\partial}{\partial t}\left(\alpha_f \rho_f \vec{v}_f\right) + \bigtriangledown.\left(\alpha_f \rho_f \vec{v}_f \vec{v}_f\right) = -\alpha_f \bigtriangledown p + \bigtriangledown.\bar{\bar{\tau}}_f + \alpha_f \rho_f \vec{g} + \overrightarrow{R}_{sf} \tag{77}$$

Taking into account the inelasticity of the granular phase, the solid-phase stresses are derived by making an analogy between the unpredictable particle motion arising from particle-particle collisions and the thermal motion of molecules in a gas. As is the case for a gas, the magnitude of the fluctuations in particle velocity determines the solid phase stresses, viscosity and pressure. The kinetic energy associated with the variations in particle velocity is measured by a "pseudothermal" or granular temperature that is proportional to the mean square of the particle random motion. The conservation of momentum for solid (s) phase yields [45]:

$$\frac{\partial}{\partial t}\left(\alpha_s \rho_s \vec{v}_s\right) + \bigtriangledown.\left(\alpha_s \rho_s \vec{v}_s \vec{v}_s\right) = -\alpha_s \bigtriangledown p - \bigtriangledown p_s + \bigtriangledown.\bar{\bar{\tau}}_s + \alpha_s \rho_s \vec{g} + \overrightarrow{R}_{fs} \tag{78}$$

where $\bar{\bar{\tau}}_f$ and $\bar{\bar{\tau}}_s$ are the stress-strain tensor:

$$\bar{\bar{\tau}}_f = \mu_f \left[\bigtriangledown \vec{v}_f + \left(\bigtriangledown \vec{v}_f\right)^T\right] - \frac{2}{3}\mu_f \bigtriangledown .\vec{v}_f \tag{79}$$

$$\bar{\bar{\tau}}_s = \mu_s \left[\bigtriangledown \vec{v}_s + \left(\bigtriangledown \vec{v}_s\right)^T\right] + \left(\lambda_s - \frac{2}{3}\mu_s\right) \bigtriangledown .\vec{v}_s \tag{80}$$

where μ and λ are the shear and bulk viscosity, $\overrightarrow{R}$ is an interaction force between phases and p is the shared pressure for all phases.

Eq. 77 and 78 which have the interphase force $\overrightarrow{R}_{fs}$ and $\overrightarrow{R}_{sf}$ component should be closed with appropriate expressions. This force depends on the friction, pressure, cohesion, and other effects, and is defined as $\overrightarrow{R}_{fs} = -\overrightarrow{R}_{sf}$ and $\overrightarrow{R}_{ss} = 0$. In ANSYS Fluent, a simple interaction term for $\overrightarrow{R}_{fs}$ in the following form is used [45]:

$$\overrightarrow{R}_{fs} = K_{fs}\left(\vec{v}_f - \vec{v}_s\right) \tag{81}$$

where K_{fs} ($=K_{sf}$) is the inter-phase momentum exchange coefficient. It should be noted that the Eq. 81 does not include any contribution due to turbulence. Instead, the turbulent inter-phase momentum exchange is incorporated through the turbulent dispersion force.

2.3.2 Drag functions

In the solid-gas flow, buoyancy and drag forces are stated to be dominant and act as a control mechanism for the gas-solid momentum transfer due to the significant density difference between solid and fluid phases. In the case of very dense flows, frictional stress becomes more significant. In the case of relatively small particles with densities that are much greater than the continuous gas system density, the fluid particulate drag force is superior over other forces such as lift and virtual mass. Wen and Yu modeled the fluid drag coefficient of particulate matter, which was only valid for dilute systems. Gidaspow et al. [52] combined the Ergun equation coefficients with the Wen and Yu model for the fluid drag coefficient applicable to dense fluid beds. Syamlal and O'Brien [53] have developed a drag model based on the correlation between the drag of a sphere and the multi-particle system and have a broader range of applications. Zhong et al. [23] mentioned another recently developed drag model, which is a heterogeneous drag model or Energy Minimization Multi-Scale model.

Since the Wen Yu drag model is not applicable for dense fluidized bed, only three drag models mentioned earlier will be examined in the next section. For the Syamlal O'Brien model [53], the parameterized or adjusted version will be employed due to its accuracy enhancement via parameter adjustment referring to the expected minimum fluidization condition. Finally, the EMMS drag model used is the one developed by Shi et al. [54], which has been adjusted for TFM modeling of bubbling fluidized bed. This modified drag model then called an EMMS-Bubbling model.

Fluid-solid exchange coefficient
In general, the fluid-solid exchange coefficient K_{sf} can be formulated in the following general form[45]:

$$K_{sf} = \frac{\alpha_s \rho_s f}{\tau_s} \tag{82}$$

where the different exchange-coefficient models are described f term, or drag model differently, and τ_s is particulate relaxation time shown as follows:

$$\tau_s = \frac{\rho_s d_p^2}{18\mu_f} \tag{83}$$

where d_p is diameter of particles.

Syamlal-O'Brien model
Drag model from Syamlal-O'brien has following expression [55]:

$$f = \frac{C_D Re_s \alpha_f}{24 v_{r,s}^2} \tag{84}$$

where the drag function (C_D) has a form:

$$C_D = \left(0.63 + \frac{4.8}{\sqrt{Re_s / v_{r,s}}}\right)^2 \tag{85}$$

This model is based on measurements of the terminal particle velocity in fluidized or settling fields, with correlations depending on the volume fraction and the relative Reynolds number [56]:

$$Re_s = \frac{\rho_f d_p |\vec{v}_s - \vec{v}_f|}{\mu_f} \tag{86}$$

The fluid-solid exchange coefficient then is formulated as follows:

$$K_{sf} = \frac{3\alpha_s \alpha_f \rho_f}{4 v_{r,s}^2 d_s} C_D \frac{Re_s}{v_{r,s}} |\vec{v}_s - \vec{v}_f| \tag{87}$$

where $v_{r,s}$ is the dimensionless terminal velocity related to the solid phase [57]:

$$v_{r,s} = 0.5\left(A - 0.06Re_s + \sqrt{(0.06Re_s)^2 + 0.12Re_s(2B - A) + A^2}\right) \tag{88}$$

for $\alpha_f \leq 0.85$

$$A = \alpha_f^{4.14} \tag{89}$$

$$B = 0.8\alpha_f^{1.28} \tag{90}$$

for $\alpha_f > 0.85$

$$B = \alpha_f^{2.65} \tag{91}$$

Parameterized Syamlal-O'Brien model
The Syamlal-O'Brien parameterized model [55] is an improvement of the Syamlal-O'Brien model in which the values of 0.8 and 2.65 in Eq. 90 and 91 are replaced by parameters that are modified based on fluid flow properties and the predicted minimum fluidization velocity. This overcomes the trend of the original Syamlal-O'Brien model to underestimate or overestimate bed expansion in fluid bed reactors.

The parameters are derived from the velocity correlation between single and multiple particle systems at the terminal or minimum fluidization conditions. In the case of multiple particle systems, the relative number of Reynolds at the minimum fluidization condition is expressed as:

$$Re_s = Re_{single}\left[\frac{A + 0.06BRe_{single}}{1 + 0.06Re_{single}}\right] \tag{92}$$

where Re_{single} is the Reynolds number at the terminal settling condition for a single particle and can be expressed as:

$$Re_{single} = \left[\frac{\left(4.8^2 + 2.52\sqrt{4\frac{Ar}{3}}\right)^{0.5} - 4.8}{1.26} \right]^2 \tag{93}$$

The Archimedes number, Ar, can be expressed as a function of the drag coefficient, C_D, and the Reynolds number, Re_s:

$$Ar = \frac{3}{4} C_D Re_s^2 \tag{94}$$

$$C_D = \left(\frac{0.63}{v_{r,s}} + \frac{4.8}{\sqrt{v_{r,s} Re_s}} \right)^2 \tag{95}$$

where $v_{r,s}$ is calculated from Eq. 88, A from Eq. 89 and B is reformulated as follows:

$$B = c1\alpha_f^{1.28} (\alpha_f \leq 0.85); \alpha_f^{d1} (\alpha_f > 0.85) \tag{96}$$

$$d1 = 1.28 + log_{10^{c1}} / log_{10^{0.85}} \tag{97}$$

Coefficient c1 and d1 are calculated by iteratively solving Eq. 92-96, after particle diameter and predicted minimum fluidization velocity is known.

The implementation of this model is limited to the use in gas-solid flows in which the gas phase is the primary phase and is incompressible. In addition, the model is only suitable for the particles of Geldart Group B.

Gidaspow model

The Gidaspow is widely used and recommended for dense fluidized bed simulation [23]. It has the following expression [52]:

for $\alpha_f > 0.8$, the fluid-solid exchange coefficient is expressed:

$$K_{sf} = \frac{3}{4} C_D \frac{\alpha_s \alpha_f \rho_f |\vec{v}_s - \vec{v}_f|}{d_s} \alpha_f^{-2.65} \tag{98}$$

$$C_D = \frac{24}{\alpha_f Re_s} \left[1 + 0.15 \left(\alpha_f Re_s \right)^{0.687} \right] \tag{99}$$

for the case of $\alpha_f \leq 0.85$, it will follow:

$$K_{sf} = 150 \frac{\alpha_s \left(1 - \alpha_f\right) \mu_f}{\alpha_f d_s^2} + 1.75 \frac{\rho_f \alpha_s |\vec{v}_s - \vec{v}_f|}{d_s} \tag{100}$$

Bubble-based EMMS model

The foundation of the energy minimization multi-scale (EMMS) theory is focused on the identification, stochastically in time and space, of a joint control of the stability of the system by both gas and solid particles in the formation of meso-scale structure [23]. The meso-scale structure is the key for CFD simulation related to drag modelling. In bubbling fluidized bed for instance, the meso-scale structure may relate with bubbles [58]. Bubble is the common meso-scale structure in a low-velocity gas-fluidized beds, as is the position of clusters in the circulation of fluidized beds (CFB).

The energy minimization multi-scale model (EMMS) was proposed [59] to describe the effects of such meso-scale structures, originally for circulating fluidized beds. Three separate scales were differentiated in the EMMS model, i.e. the micro-scale of particles, the meso-scale of clusters and the macro-scale of the entire bed. In addition to the hydrodynamic conservation equations, the meso-scale parameter of clusters was closed by invoking a stability condition, while the stability condition was derived by the compromise between gas dominance and solids dominance [59].

Since the EMMS approach was originally mesoscale modeling based on the cluster principle, its implementation was mainly limited to high-velocity fluidized beds in which clustering prevails. Therefore, it is a reasonable option to explore the possibility of developing the EMMS-based models with some other characteristic structures, e.g., bubbles, so that applications can be used in a broader range of flow regimes from bubbling to fast fluidizations.

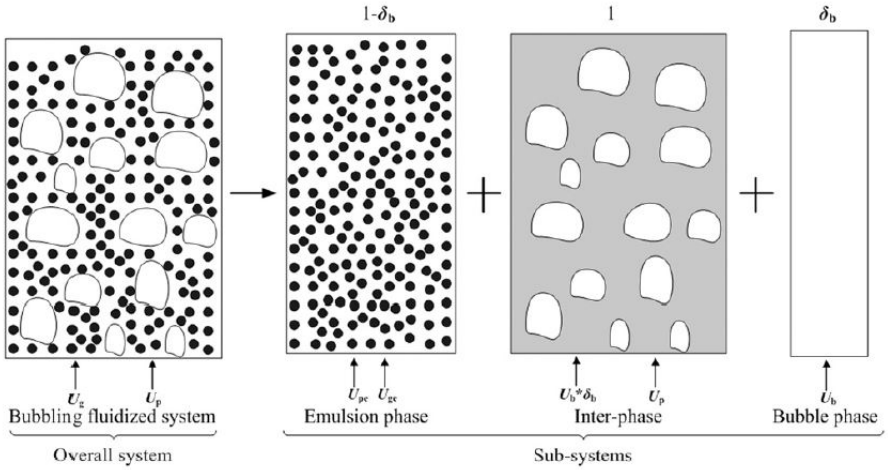

Figure 2.20: System resolution for bubbling fluidized bed [54]

In bubbling fluidized bed much higher than the transport disengaging height (TDH), gas flows upward, and bed materials are suspended with some internal circulation. It has nearly omissible particle transport out of bed, and the gas flow is distinguished into the bubble and emulsion phase. Within this condition, the interactions inside a bubbling fluidized bed will mainly consist of that interaction between the gas and solids in the emulsion, those between the emulsion and the bubble, and finally those between the bubbles. Figure 2.20 shows the system division into three sub-systems or phases, i.e., the emulsion, bubble and inter-phase [54].

The drag function of the bubble-based EMMS [54] has the following expression

$$K_{sf} = 150\frac{\epsilon_s\left(1-\epsilon_f\right)\mu_f}{\epsilon_f d_s^2} + 1.75\frac{\rho_f \epsilon_s |\vec{v}_f - \vec{v}_s|}{d_s} \tag{101}$$

for $\epsilon_f < \epsilon_{mf}$

$$K_{sf} = \frac{3}{4}C_D\frac{\epsilon_s\epsilon_f\rho_f|\vec{v}_f - \vec{v}_s|}{d_s}\epsilon_f^{-2.65}H_d \tag{102}$$

for $\epsilon_{mf} \leq \epsilon_f < \epsilon_d$

$$K_{sf} = \frac{3}{4}C_D\frac{\epsilon_s\epsilon_f\rho_f|\vec{v}_f - \vec{v}_s|}{d_s}\epsilon_g^{-2.65} \tag{103}$$

for $\epsilon_f \geq \epsilon_d$

where H_d is heterogeneous index which is defined as dimensionless drag coefficient compared with Wen Yu drag coefficient

$$H_d = K_{sf,EMMS}/K_{sf,Wen\ \&\ Yu} \tag{104}$$

2.3.3 Kinetic theory of granular flow (KTGF)

Solid pressure

In the granular-phase momentum equation, a solids pressure is determined separately for granular flows in the compressible regime (i.e. where the solids volume fraction is less than its maximum allowable value), and used for the pressure gradient expression $\bigtriangledown p_s$. Since the particles use a Maxwellian velocity distribution, a granular temperature is introduced into the model, and and appears in the expression of the solids pressure and viscosities. Due to particle collisions, the solids pressure is composed of a kinetic term and a second term [45]:

$$p_s = \alpha_s\rho_s\Theta_s + 2\rho_s\left(1+e_{ss}\right)\alpha_s^2 g_{0,ss}\Theta_s \tag{105}$$

where $g_{0,ss}$ is the radial distribution function, e_{ss} is the restitution coefficient for particle collision and Θ_s is the granular temperature. In ANSYS Fluent, e_{ss} is set at 0.9 default value but can be adjusted to fit the granular type. The granular temperature Θ_s is proportional to the fluctuating particle motion's kinetic energy, and will be discussed further in a later section. Function $g_{0,ss}$ is a distribution function that plays a role in the transition from the "compressible" condition with $\alpha < \alpha_{s,max}$, where the spacing between the solid particles can proceed further to decrease, to the "incompressible" state $\alpha = \alpha_{s,max}$, where the spacing cannot be reduced anymore. As the default,

$\alpha_{s,max}$ is set at 0.63 and can be adjusted appropriately.

Radial distribution function

The radial distribution feature is a correction factor that governs the probability of collisions between grains when the solid granular phase becomes dense. This function can be expressed as the non-dimensional number density of particles at a distance of one particle's diameter from a given particle, compared to the expected number density at that distance if the particles would be randomly distributed:

$$g_0 = \frac{s + d_p}{s} \tag{106}$$

where s is the distance between grains. Based on Eq. 106, it can be inferred that for a dilute solid phase where $s \to \infty$, therefore the $g_0 \to 1$. Conversely, when the solid distance goes denser, particles increasingly order themselves and g_0 becomes larger than one. It will be increasing with the higher solids packing fraction and diverging to infinity as the maximum packing limit is reached, $g_0 \to \infty$.

Maximum packing limit in binary mixture

The packing limit is not a fixed quantity and can differ by the number of particles and its diameter present within a given volume. The packing limit will become larger, whenever small particles accumulate amid larger particles. For a binary mixture, ANSYS Fluent makes use of the formulation suggested by [60]. When the diameters d1>d2, the mixture composition is defined as $X_1 = \frac{\alpha_1}{\alpha_1 + \alpha_2}$, where:

$$X_1 \leq \frac{\alpha_{1,max}}{(\alpha_{1,max} + (1 - \alpha_{1,max})\,\alpha_{2,max})} \tag{107}$$

as this is a condition for implementing of the maximum packing limit for binary mixtures. Then the maximum packing limit for the mixture $\alpha_{s,max}$ is the minimum of Eq. 108 and Eq. 109:

$$\left(\alpha_{1,max} - \alpha_{2,max} + \left[1 - \sqrt{\frac{d2}{d1}}\right](1 - \alpha_{1,max})\,\alpha_{2,max}\right) * (\alpha_{1,max} + (1 - \alpha_{1,max})\,\alpha_{2,max})\,\frac{X_1}{\alpha_{1,max}} + \alpha_{2,max} \tag{108}$$

$$\left[1 - \sqrt{\frac{d2}{d1}}\right](\alpha_{1,max} + (1 - \alpha_{1,max})\,\alpha_{2,max})\,(1 - X_1) + \alpha_{1,max} \tag{109}$$

Solid shear stresses

Owing to translation and collision, the solids stress tensor includes shear and bulk viscosities resulting from particle momentum exchange. A frictional aspect of viscosity may also be included to accommodate the viscous-plastic transition that occurs when solid-phase particles exceed the maximum solid volume fraction. This can be expressed as follows:

$$\mu_s = \mu_{s,col} + \mu_{s,kin} + \mu_{s,fr} \tag{110}$$

The collisional part of the viscosity [61] yields:

$$\mu_{s,col} = \frac{4}{5}\alpha_s \rho_s d_s g_{0,ss}\,(1 + e_{ss})\left(\frac{\Theta_s}{\pi}\right)^{1/2}\alpha_s \tag{111}$$

For the kinetic viscosity, ANSYS Fluent provides two formulations. The default one is the one proposed by Syamlal et al. [53] that is expressed as:

$$\mu_{s,kin} = \frac{\alpha_s \rho_s d_s \sqrt{\Theta_s \pi}}{6\,(3 - e_{ss})}\left[1 + \frac{2}{5}\,(1 + e_{ss})\,(3e_{ss} - 1)\,\alpha_s g_{0,ss}\right] \tag{112}$$

and the other one is the one proposed by Gidaspow et al. [61]:

$$\mu_{s,kin} = \frac{10\rho_s d_s \sqrt{\Theta_s \pi}}{96\alpha_s\,(1 + e_{ss})\,g_{0,ss}}\left[1 + \frac{4}{5} g_{0,ss}\alpha_s\,(1 + e_{ss})\right]^2 \alpha_s \tag{113}$$

In dense flow at low shear, where the secondary volume fraction for a solid phase approaches the packing limit, stress generation is mainly due to friction among particles. As the default, the solids shear viscosity measured by ANSYS Fluent doesn't include this friction between particles. Where the frictional viscosity is included in the calculation, the Schaeffer [62] expression is used:

$$\mu_{s,fr} = \frac{p_s sin\phi}{2\sqrt{I_{2D}}} \tag{114}$$

where p_s is the solid pressure, ϕ is internal friction angle and I_{2D} is the second invariant of the deviatoric stress tensor, or in other words, it refers to the effective stress.

Instant collisions are less significant in granular flows with large volume fraction of the solids. It is no longer necessary to extend kinetic theory to granular flows because particles are in contact and the resultant frictional stresses need to be taken into account [45].

Bulk viscosity
The solids bulk viscosity represents the resistance of the granular particles to compression and expansion. The following expression from Lun et al. [63] is used:

$$\lambda_s = \frac{4}{3}\alpha_s^2 \rho_s d_s g_{0,ss} \left(1 + e_{ss}\right) \left(\frac{\Theta_s}{\pi}\right)^{1/2} \tag{115}$$

Granular temperature
The granular temperature for the s^{th} solids phase is corresponding to the kinetic energy of random particle motion [45]. The basic expression is:

$$\Theta_s = \frac{1}{3} u_{s,i} u_{s,i} \tag{116}$$

In equation 116 $u_{s,i}$ represents the i^{th} component of the solid velocity fluctuation in the Cartesian coordinate system. This is characterized as an ensemble average of the random velocity of the particles within a finite volume and time period. Particle number per unit volume is used as averaging basis following [52] and [64].

The transport equation acquired from kinetic theory takes the form [52]:

$$\frac{3}{2}\left[\frac{\partial}{\partial t}\left(\rho_s \alpha_s \Theta_s\right) + \bigtriangledown.\left(\rho_s \alpha_s \vec{v}_s \Theta_s\right)\right] = \left(-p_s \overline{\overline{I}} + \overline{\overline{\tau}}_s\right) : \bigtriangledown \vec{v}_s + \bigtriangledown.\left(k_{\Theta_s} \bigtriangledown \Theta_s\right) - \gamma_{\Theta_s} + \phi_{fs} \tag{117}$$

where $\left(-p_s \overline{\overline{I}} + \overline{\overline{\tau}}_s\right) : \bigtriangledown \vec{v}_s$ is the energy generation by the solid stress tensor, $k_{\Theta_s} \bigtriangledown \Theta_s$ is the diffusion energy with k_{Θ_s} as diffusive flux of granular energy, $\gamma \Theta_s$ is collisional dissipation energy and ϕ_{fs} is the energy exchange between f^{th} fluid or solid phase and s^{th} solid phase.

The model developed by Syamlal et al. [53] is used as the default model in Fluent for the diffusive flux of granular energy (k_{Θ_s}). The expression is presented below:

$$k_{\Theta_s} = \frac{15 d_s \rho_s \alpha_s \sqrt{\Theta_s \pi}}{4\left(41 - 33\eta\right)} \left[1 + \frac{12}{5}\eta^2 \left(4\eta - 3\right) \alpha_s g_{0,ss} + \frac{16}{15\phi}\left(41 - 33\eta\right)\eta \alpha_s g_{0,ss}\right] \tag{118}$$

where $\eta = \frac{1}{2}\left(1 + e_{ss}\right)$.

Another form of k_{Θ_s} is also described by Gidaspow et al. [52] as follows:

$$k_{\Theta_s} = \frac{150 d_s \rho_s \sqrt{\Theta \pi}}{384\left(1 + e_{ss}\right) g_{0,ss}} \left[1 + \frac{6}{5}\alpha_s g_{0,ss}\left(1 + e_s\right)\right]^2 + 2\rho_s \alpha_s^2 d_s \left(1 + e_{ss}\right) g_{0,ss} \sqrt{\frac{\Theta_s}{\pi}} \tag{119}$$

The energy dissipation rate due to collision between particles within the s^{th} solids phase (γ_{Θ_s}) takes the form of Lun et al. [63] as follows:

$$\gamma_{\Theta s} = \frac{12\left(1 - e_{ss}^2\right) g_{0,ss}}{d_s \sqrt{\pi}} \rho_s \alpha_s^2 \Theta_s^{3/2} \tag{120}$$

The kinetic energy transfer of random fluctuation in solid particle velocity from the s^{th} solid phase to the f^{th} solid or fluid phase expressed by ϕ_{fs} referring to Gidaspow et al. [61]:

$$\phi_{fs} = -3 K_{fs} \Theta_s \tag{121}$$

For the general boundary condition of granular temperature at the wall, the expression of Johnson et al. [65] is referred:

$$q_s = \frac{\pi}{6}\sqrt{3}\phi \frac{\alpha_s}{\alpha_{s,max}} \rho_s g_0 \sqrt{\Theta_s} \overrightarrow{U_{s,||}}. + \overrightarrow{U_{s,||}} \frac{-\pi}{4}\sqrt{3}\frac{\alpha_s}{\alpha_{s,max}}\left(1 - e_{sw}^2\right) \rho_s g_0 \Theta_s^{3/2} \tag{122}$$

where e_{sw}, is the coefficient of restitution for collisions between particles and the boundary, the $\overrightarrow{U_{s,||}}$ is particle slip velocity parallel to wall, ϕ is the specularity coefficient between the wall and particle, $\alpha_{s,max}$ is maximum particle volume fraction at the packing limit and g_0 is radial distribution function.

2.3.4 Turbulence Models

According to Zhong et al. [23], the k-ϵ turbulence model is one of the two most common turbulence models used in practical engineering calculation for DPRS simulation beside the Large Eddy Simulation (LES). Although it is less accurate than LES, it has a compromise computation resource requirement. This model is one type of Reynolds-averaged Navier–Stokes equations (RANS) based model. The increase in turbulence is expressed by an increase in effective viscosity. And the Reynolds stresses are in positive correlation to the mean velocity through this viscosity. The k and ϵ represent the transported variable, where k stands for turbulent kinetic energy, while ϵ refers to turbulent dissipation. The turbulent kinetic energy determines the energy of turbulence, while turbulence dissipation defines the scale of turbulence.

In the approach of turbulence modelling using k-ϵ model in multiphase cases, ANSYS Fluent offers three turbulence model options: the mixing turbulence model (the default), the distributed turbulence model or a per-phase turbulence model.

k-ϵ Mixture Turbulence Model
The default model of k-ϵ in ANSYS Fluent is mixtures turbulence models. It represents the first extension of the single-phase k-ϵ model. It is valid for stratified (or nearly stratified) multiphase flows, when the phases separated, and when the density ratio between phases is near one. The k and ϵ expressions that (exclude buoyancy, dilation and source term) employed are as follows[45]:

$$\frac{\partial}{\partial t}\left(\rho_m k\right) + \bigtriangledown.\left(\rho_m \vec{v}_m k\right) = \bigtriangledown.\left(\left(\mu_m + \frac{\mu_{t,m}}{\sigma_k}\right) \bigtriangledown k\right) + G_{k,m} - \rho_m \epsilon + \Pi_{k_m} \tag{123}$$

$$\frac{\partial}{\partial t}\left(\rho_m \epsilon\right) + \bigtriangledown.\left(\rho_m \vec{v}_m \epsilon\right) = \bigtriangledown.\left(\left(\mu_m + \frac{\mu_{t,m}}{\sigma_\epsilon}\right) \bigtriangledown \epsilon\right) + \frac{\epsilon}{k}\left(C_{1\epsilon} G_{k,m} - C_{2\epsilon}\rho_m \epsilon\right) + \Pi_{\epsilon_m} \tag{124}$$

where ρ_m, μ_m and $\vec{v}_m$ are mixture density, molecular viscosity and velocity respectively and calculated from:

$$\rho_m = \sum_{i=1}^{N} \alpha_i \rho_i \tag{125}$$

$$\mu_m = \sum_{i=1}^{n} \alpha_i \mu_i \tag{126}$$

$$\vec{v}_m = \frac{\sum_{i=1}^{N} \alpha_i \rho_i \vec{v}_i}{\sum_{i=1}^{N} \alpha_i \rho_i} \tag{127}$$

where α_i, ρ_i, μ_i and $\vec{v}_i$ represent the volume fraction, density, viscosity and velocity of the ith phase respectively.

For the turbulent viscosity of the mixture and the phase i, $\mu_{t,m}$ and $\mu_{t,i}$, the equation follows:

$$\mu_{t,m} = \rho_m C_\mu \frac{k^2}{\epsilon} \tag{128}$$

$$\mu_{t,i} = \frac{\rho_i}{\rho_m} \mu_{t,m} \tag{129}$$

then the turbulence kinetic energy, $G_{k,m}$, can be computed from:

$$G_{k,m} = \mu_{t,m}\left(\bigtriangledown \vec{v}_m + \left(\bigtriangledown \vec{v}_m\right)^T\right) : \bigtriangledown \vec{v}_m \tag{130}$$

Finally Π_{ϵ_m} and Π_{k_m} are the source terms that can be utilized for modeling the turbulent relationship between the distributed phases and the continuous phase.

k-ϵ Dispersed Turbulence Model
The dispersed turbulence model is the suitable model when the secondary phase concentrations dilute, or when granular model is employed. In terms of the mean characteristics of the primary phase and the ratio of the particle relaxation time as well as the eddy-particle interaction time, fluctuating quantities of the secondary phases may be given. The model is valid when there is clearly one primary continuous phase, and the other dilute secondary phases are spread.

There are several assumptions used for turbulences modelling of the dispersed method, which are listed below:

- Continuous phase basing on a modified $k-\epsilon$ model.
  Supplementary terms related to interphase turbulent momentum transfer are added for the turbulent predictions of the continuous phase using the standard k-ϵ model.
- Dispersed phase adopting Tchen-theory correlations.
  Predictions for turbulence quantities for the dispersed phases are made using the Tchen principle of discrete particle dispersion by homogeneous turbulence [66].
- Interphase turbulent momentum transfer.
  The correlation emerges between the instantaneous distribution of the dispersed phase and the turbulent fluid motion is basically included on the momentum exchange coefficient in turbulent multiphase flow. Hence, it is possible to employ the dispersion of the dispersed phase movement by the turbulent fluid motion.
- A phase-weighted averaging process.
  ANSYS Fluent uses phase-weighted averages where there are no volume fraction variations in the continuity equations. This differs with a two-step averaging process which leads to the fluctuation of the phase volume fractions.

Average fluctuating quantities are computed using the eddy viscosity model. For continuous process the Reynolds stress tensor takes the following form [45]:

$$\overline{\overline{\tau}}_q'' = -\frac{2}{3}\left(\rho_q k_q + \rho_q v_{t,q} \bigtriangledown . \overrightarrow{U}_q\right)\overline{\overline{I}} + \rho_q v_{t,q}\left(\bigtriangledown \overrightarrow{U}_q + \bigtriangledown \overrightarrow{U}_q^T\right) \tag{131}$$

where $\overrightarrow{U}_q$ is the phase-weighted velocity.

The turbulent kinetic energy of phase q is used on the turbulent viscosity ($\mu_{t,q}$) formula:

$$\mu_{t,q} = \rho_q C_\mu \frac{k_q^2}{\epsilon_q} \tag{132}$$

and the characteristic time of the energetic turbulent eddies takes the form:

$$\tau_{t,q} = \frac{3}{2} C_\mu \frac{k_q}{\epsilon_q} \tag{133}$$

where C_μ=0.09 and ϵ_q is dissipation rate.

The length scale of the turbulent eddies yields:

$$L_{t,q} = \sqrt{\frac{3}{2}} C_\mu \frac{{k_q}^{3/2}}{\epsilon_q} \tag{134}$$

as mentioned, the turbulent predictions are utilizing the modified k-ϵ model. The transports equation (which does not include bouyancy, dilation and user-defined source term) are as follows:

$$\frac{\partial}{\partial t}\left(\alpha_q \rho_q k_q\right) + \bigtriangledown .\left(\alpha_q \rho_q \overrightarrow{U}_q k_q\right) = \bigtriangledown .\left(\alpha_q\left(\mu_q + \frac{\mu_{t,q}}{\sigma_k}\right)\bigtriangledown k_q\right) + \alpha_q G_{k,q} - \alpha_q \rho_q \epsilon_q + \alpha_q \rho_q \Pi_{k_q} \tag{135}$$

$$\frac{\partial}{\partial t}\left(\alpha_q \rho_q \epsilon_q\right) + \bigtriangledown .\left(\alpha_q \rho_q \overrightarrow{U}_q \epsilon_q\right) = \bigtriangledown .\left(\alpha_q\left(\mu_q + \frac{\mu_{t,q}}{\sigma_\epsilon}\right)\bigtriangledown \epsilon_q\right) + \alpha_q \frac{\epsilon_q}{k_q}\left(C_{1\epsilon} G_{k,q} - C_{2\epsilon}\rho_q \epsilon_q\right) + \alpha_q \rho_q \Pi_{\epsilon_q} \tag{136}$$

On the Eq.135 and 136 the term Π_{ϵ_q} and Π_{k_q} are source terms that can be used as a supplementary terms to cover the influence of the dispersed phase on the continuous phase q. $G_{k,q}$ is the turbulent kinetic energy production.

k-ϵ Turbulence Model for Each Phase

Each phase $k-\epsilon$ turbulence model is the most general multiphase turbulence model which solves a set of k and ϵ transport equation phase separately. This model is a good option whenever the turbulence transfer among the phases has a significant role. Since the two additional transport equations for each secondary phase should be solved by the Fluent, this model is by far the most computational intensive method among others.

Under this model, the Reynold's stress tensor and turbulent viscosity can be calculated with the same formula (Eq. 131 and Eq. 132). The turbulence calculation is using the following form [45]:

$$\frac{\partial}{\partial t}\left(\alpha_q \rho_q k_q\right) + \bigtriangledown.\left(\alpha_q \rho_q \overrightarrow{U}_q k_q\right) = \bigtriangledown.\left(\alpha_q\left(\mu_q + \frac{\mu_{t,q}}{\sigma_k}\right)\bigtriangledown k_q\right) + \left(\alpha_q G_{k,q} - \alpha_q \rho_q \epsilon_q\right) + \sum_{l=1}^{N} K_{lq}\left(C_{lq}k_l - C_{ql}k_q\right) - \sum_{l=1}^{N} K_{lq}\left(\overrightarrow{U}_l - \overrightarrow{U}_q\right).\frac{\mu_{t,l}}{\alpha_l \sigma_l}\bigtriangledown \alpha_l + \sum_{l=1}^{N} K_{lq}\left(\overrightarrow{U}_l - \overrightarrow{U}_q\right).\frac{\mu_{t,q}}{\alpha_q \sigma_q}\bigtriangledown \alpha_q + \Pi_{k_q} \tag{137}$$

$$\frac{\partial}{\partial t}\left(\alpha_q \rho_q \epsilon_q\right) + \bigtriangledown.\left(\alpha_q \rho_q \overrightarrow{U}_q \epsilon_q\right) = \bigtriangledown.\left(\alpha_q\left(\mu_q + \frac{\mu_{t,q}}{\sigma_\epsilon}\right)\bigtriangledown \epsilon_q\right) + \frac{\epsilon_q}{k_q}\left[C_{1\epsilon}\alpha_q G_{k,q} - C_{2\epsilon}\alpha_q \rho_q \epsilon_q + C_{3\epsilon}\left(\sum_{l=1}^{N} K_{lq}\left(C_{lq}k_l - C_{ql}k_q\right) - \sum_{l=1}^{N} K_{lq}\left(\overrightarrow{U}_l - \overrightarrow{U}_q\right).\frac{\mu_{t,l}}{\alpha_l \sigma_l}\bigtriangledown \alpha_l + \sum_{l=1}^{N} K_{lq}\left(\overrightarrow{U}_l - \overrightarrow{U}_q\right).\frac{\mu_{t,q}}{\alpha_q \sigma_q}\bigtriangledown \alpha_q + \Pi_{\epsilon_q}\right.\right. \tag{138}$$

where C_{lq} and C_{ql} can be calculated from:

$$C_{lq} = 2, C_{ql} = 2\left(\frac{\eta_{lq}}{1+\eta_{lq}}\right) \tag{139}$$

where η_{lq} is the characteristic times ratio and the term Π_{ϵ_q} and Π_{k_q} are source terms to model the influence of the inter-phase turbulence interaction for which the details can be found at Simonin et al.[67].

3 Literature Study

In this chapter, the relevant established researches and investigations on CFD simulation using TFM will be discussed. Several findings from different authors related to various aspects of the present work will be elaborated. The main purpose is to provide the background of the CFD method employed as well as the discussion of simulation results on the Chapter 5.

3.1 Hydrodynamics

3.1.1 Grid independency test

One of the very first critical steps in doing numerical calculation with finite volume technique is to make sure that the solution produced from the simulation does not change considerably with the change of grid size. Some flow variables commonly used in fluidized bed problems as the reference for the examination of these grid-independency tests are pressure drop and bed expansion. Gosavi et al. [68] performed their grid-independency test by using four different computational grids. The pressure drop and bed expansion resulted from the simulation of 231 μm particle's diameter are plotted in Figure 3.1.

The estimated pressure drop values for 10 mm of the grid size are higher, as can be seen. The expected pressure drop is decreased by about 14 percent, as the grid dimensions are lowered from 10 mm to 5 mm. As this grid size is further reduced to 3 mm and 1 mm, the pressure drop and be expansion, do not change significantly. However, more grid points for the accuracy of the solution are often desirable. A compromise must be reached between accuracy, time, and computational resources. In Gosavi's case, therefore, the grid size 5 mm (about 20 times of particle's diameter) was selected as it sufficiently captures the physic of the system accurately.

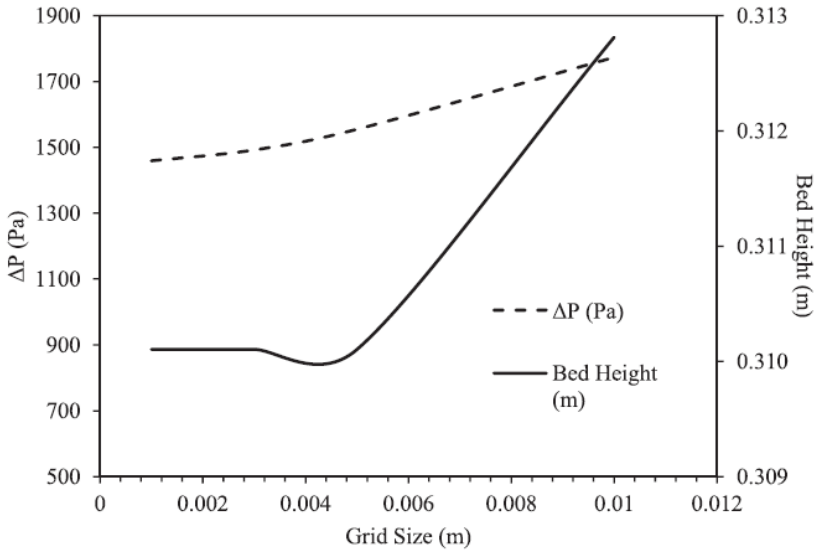

Figure 3.1: Grid size sensitivity analysis for pressure drop and bed expansion for 231 μm particle's diameter (H_o= 0.3 m, u_g= 0.016 m/s and T= 200 ^{o}C) [68]

This grid independency method performed by Gosavi et al. will be used in the present simulation and discussed further on the section 5.1.

3.1.2 Minimum fluidization velocity

As discussed in Chapter 2, minimum fluidization condition is an essential characteristic of the design, operation, and control of a fluidized bed. Along with the increase of superficial gas velocity, basically, the bed expansion will become larger, and pressure drop will be increased accordingly. At a certain point, the weight of the bed is equally balanced with the upward force generated by the airflow and is generally indicated by constant gas pressure at further gas flow increase.

Taghipour et al. [25] performed the hydrodynamic simulation of gas-solid fluidized bed utilizing 250-300 μm spherical glass beads using three different drag models: Syamlal-O'Brien, Gidaspow, and Wen yu. The CFD simulation was conducted using a multifluid Eulerian model. There was a unique finding from their result as shown in Figure 3.2 that at the superficial gas velocity below the minimum fluidization condition, the solids were not being fluidized.

They reasoned that the interparticle frictional forces are more dominant. This can also be inferred that the multifluid eulerian model has a particular limitation on simulating gas-solid phases.

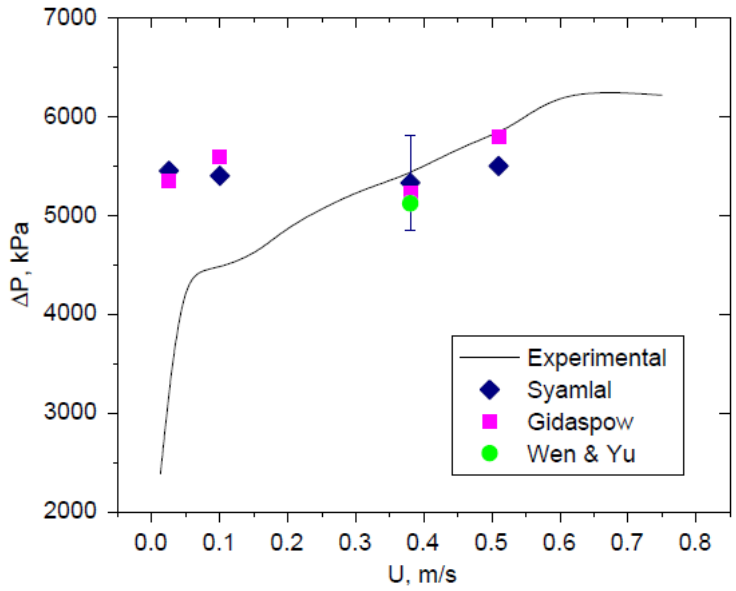

Figure 3.2: Comparison between simulation and experiment result of bed pressure drop (d_p= 275 μm and e_{ss}= 0.9) using three different drag models [25]

This evidence shows that through the TFM model, the simulation could not yield the appropriate result for the gas velocity below the minimum fluidization condition.

On another side, Subramani et al. [69] studied the minimum fluidization of Geldart B particles at elevated temperatures. After cross-checking with the many published results, the authors came up with the empirical correlation for determining minimum fluidization velocity and its voidage for relatively high bed temperature (298-973 K) with Geldart B particles as follows:

$$Re_{mf} = \frac{Ar}{1502} \tag{140}$$

$$\epsilon_{mf} = 0.3507 Ar^{0.0387} Re_{mf}^{-0.0704} \tag{141}$$

where

$$Ar = \frac{d_p^3 \rho_f (\rho_p - \rho_f) g}{\mu^2} \tag{142}$$

$$Re_{mf} = \frac{d_p \rho_f U_{mf}}{\mu} \tag{143}$$

These correlations will be used later in the present simulation and elaborated in section 5.2 to double-check the minimum fluidization velocity/flow rate obtained from the experiment and simulation.

3.1.3 Particle's size and sphericity factor

Ostermeier et al. [70] investigated the effect of employing two widely used numerical CFD methods for the multiphase problem: Two-fluid model (TFM) and Multi-fluid model (MFM). The main different aspect is the number of solid phases that are involved in the simulation. In TFM, the particles are represented by one solid phase with one size of diameter only, while in MFM, at least two different solid sizes are included. In his research, Ostermeier et al. [70] used the Geldart B corundum particles, which are classified into two distinct size categories, small particle mean diameter (174 μm, 45%wt) and large particle mean diameter (221 μm, 55%wt). They also studied the influence of particle shape in the form sphericity factor (ψ), where the value ranges from 0-1. The closer the shape to a sphere, then the sphericity factor will be approaching one.

The simulation result of pressure drop and bed expansion compared with the experimental data are displayed in Figure 3.3. As can be seen, the pressure drop and bed expansion using TFM and ψ=0.82 have the lowest value

and are far from the experiment's data. The use of MFM with ψ= 1 led to improved results, while the best approximation of the experimental values was obtained with the use of MFM with psi = 0.82, which is actually a more realistic particle shape.

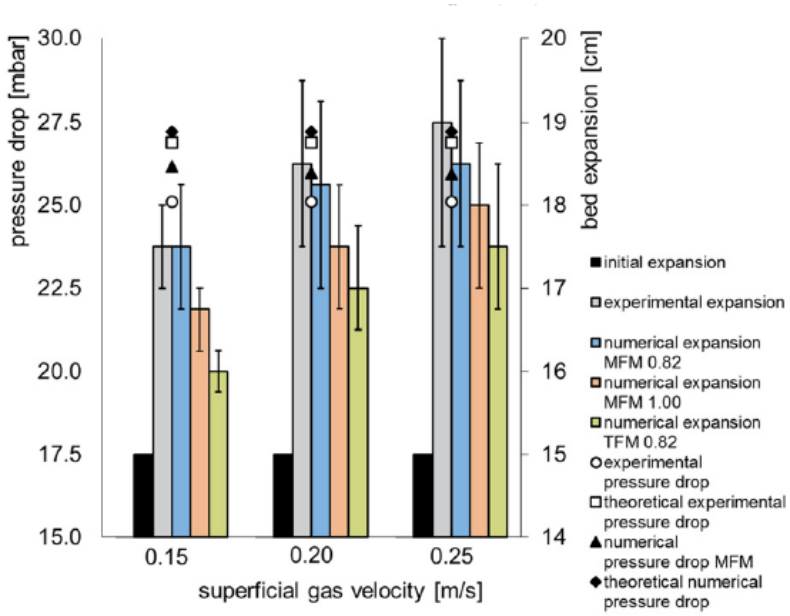

Figure 3.3: Comparison of experimental and numerical (TFM and MFM) pressure drop and bed expansion for different superficial gas velocities [70]

The authors further verified their findings by performing 3D simulation and comparing the results to a video taken for their transparent setup at three instantaneous fluidizing times (9, 10, and 11 s) (Figure 3.4). It is shown that the spontaneous local bed expansion behavior is best demonstrated by MFM and a sphericity factor of 0.82. It is the only approach that captures the instant movement of particles clearly above 20 cm in height. The internal movement of the particles may also show a similar difference between the three approaches.

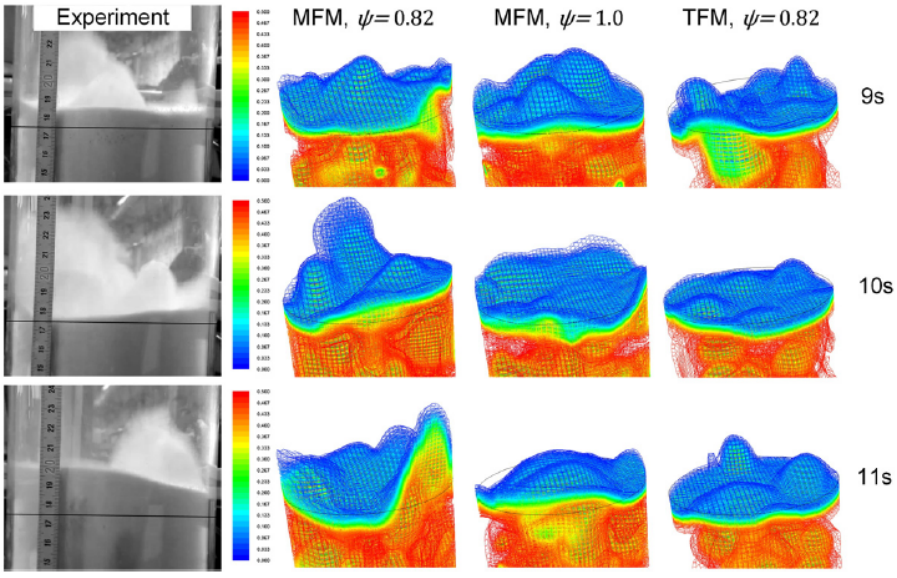

Figure 3.4: Comparison of experimental and numerical (TFM and MFM) bed expansion with two different sphericity factors [70]

The findings show that both the particle size distribution (PSD, through MFM method) and the non-sphericity (through the sphericity factor) of particles should be taken into account in achieving a realistic bed expansion. This result is supported by the strong agreement between the experimental and numerical pressure drop and bed expansion.

As the simulation performed in the present work will be based on TFM, which is only considered one particle size for the modeling's simplicity, a certain extend of underprediction can be predicted. The sphericity effect will be examined and elaborated in section 5.4.

3.1.4 Drag models

Buoyancy, drag, and momentum transfer affected by the mass transfer have been regarded as governing mechanisms for gas-solid mass transfer. These are the main forces because of the significant difference in density between the particles and the fluidizing gas. Although the inherent instabilities due to buoyancy inclusion have not yet been completely solved, the prediction of a drag model covering the entire range of Reynold 's number and the phasic volume portion was regarded as the critical challenge of many multi-phase modeling studies. Such attempts culminated in the discovery of a large number of drag correlations. However, by far, no drag function can give exact results in its own original way, given the abundance of drag models in the literature [71].

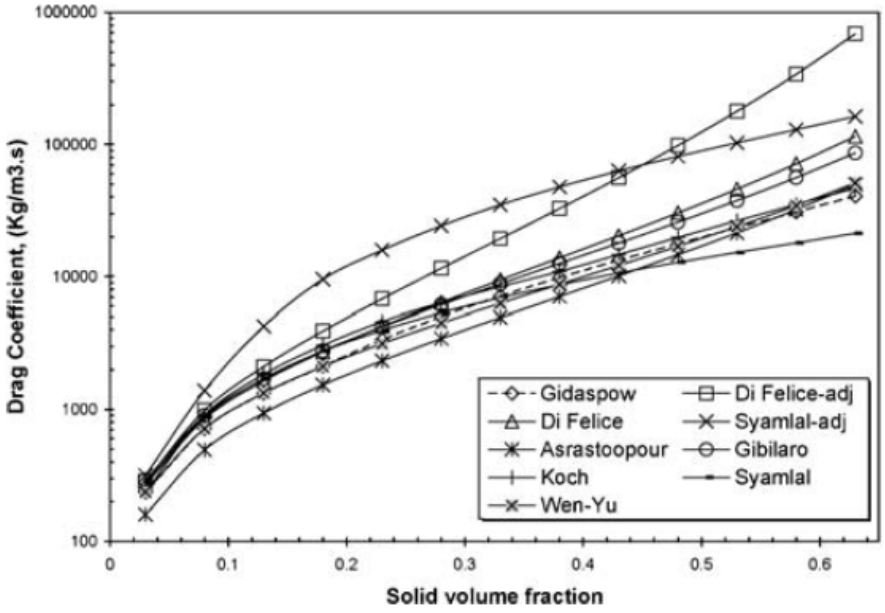

Figure 3.5: Variation of drag coefficient against solid volume fraction in several drag models [71].

Vejahati et al. [71] examined eight different drag models available in the literature using the multi-fluid Eulerian model on Geldart B particle with 275μm size. Their goal was to formulate a better drag model adjustment instead of the one proposed by Syamlal et al. [53]. In Figure 3.5, a comparison of each drag model employed by Vejahati et al. is presented. All of the drag functions display an increasing drag value trend with an increase in the solid volume fraction. However, the chart shows that the modification of drag models based on minimum fluidizing velocity, as done for the adjusted Syamlal model [53], results in higher drag coefficient values predicting the entire range of solid volumes.

Another result of the adjusted drag model comparison was also presented by Esmaili et al. [72]. They have performed their simulation with the Eulerian-eulerian approach on Geldart B particle with 275 μm diameter. The contours of the solid volume fraction result for several drag models are shown in Figure 3.6. The comparison was made in this figure between all models for drag and experimental snapshot with respect to bed height and bubble shape and size. It is easy to note that the best performance is seen on the two adjusted models (i.e., the adjusted model of Di Felice and the adjusted model of Syamlal – O'Brien) which have the closest bed expansion compared to the experiment.

These results from Vejahati et al. and Esmaili et al. indicate that the Gidaspow drag model used on the current work on its original form will not give a satisfactory drag coefficient. The adjusted Syamlal O'Brien drag model, which already included the correction factor, will show better agreement with the actual result. However, some overprediction of the drag model might occur.

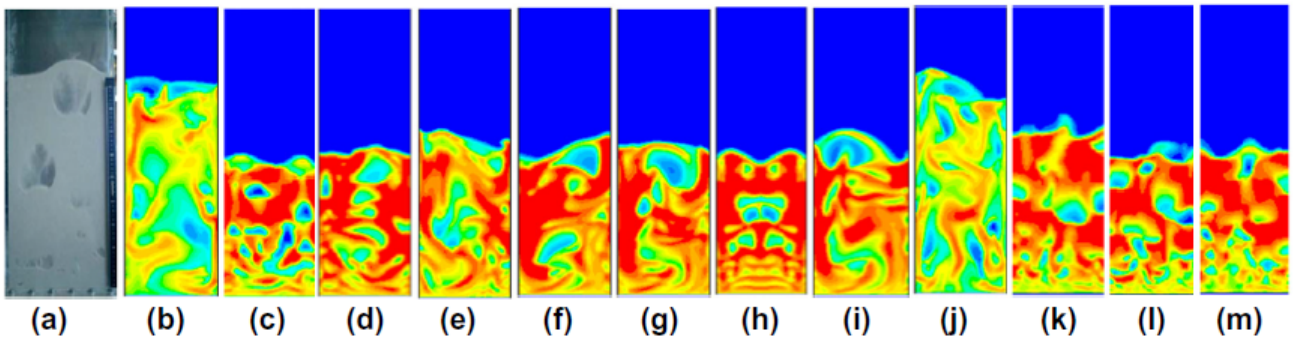

Figure 3.6: Solid volume fraction contours at u_g= 0.21 m/s after 10s simulation with various drag models: (a) experiment; (b) Syamlal-O'Brien adjusted; (c) Syamlal-O'Brien; (d) Arastoopour; (e) Gibilaro; (f) Hill Koch Ladd; (g) Zhang-Reese; (h) Richardson-Zaki; (i) RUC; (j) Di Felice adjusted; (k) Di Felice; (i) Wen-Yu and (m) Gidaspow [72].

Apart from the well-established drag models discussed earlier, a heterogeneous drag model (i.e. EMMS) that considers small bubbles and clusters of particles recently has drawn much interest. TFM numerical model with course grid simulation coupled with energy minimization multi-scale method (EMMS) would be the attractive choice to improve solution accuracy as well as reduce computational cost. Another alternative is using the discrete element method (CFD-DEM) but lumping the particles in computation parcels. This method is commonly called the coarse grain particle method (CGPM) [28].

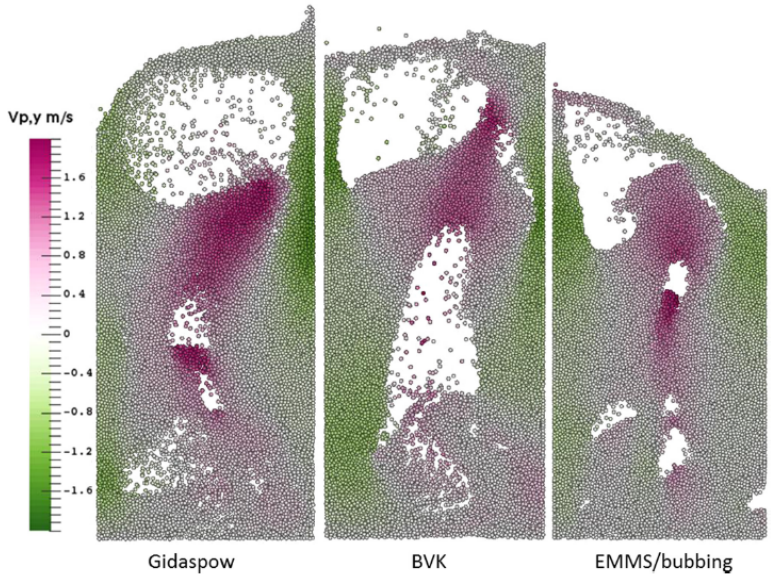

Figure 3.7: Particle velocity distribution on a parcel with CFD DEM simulation at 15.0 s with different drag model and grid resolution 34 d_p x 30 d_p x 30 d_p [28]

Lu et al. [28] observed the hydrodynamics of bubbling fluidized bed by employing the 0.275 mm particle's diameter with three different parcel sizes: 15, 10, 5 mm, and three different drag models: Gidaspow, BVK, and EMMS/Bubbling. The CGPM model was used for the simulation. Figure 3.7 shows the vertical velocity colored of the instantaneous parcel distribution. The specific models of the drag presented, with particular downflow at the wall limits and an upward flow of particles clearly visible at the center of the bed due to fast-growing bubbles, projected identical solid flow patterns. It is apparent that the lower gas inlet produces smaller bubbles, and then they get bigger as the center. In comparison with the EMMS / bubbling drag model, however, the bubbles are larger. This is mainly due to the fact that the drag force predicted by the EMMS / bubbling model in the dense phase is smaller than Gidaspow and BVK. Therefore, the EMMS / bubbling model is expected to have a denser emulsion phase and smaller bubbles, resulting in a noticeably lower expansion of the bed.

The bubbles characteristics, as shown in Figure 3.8, were also investigated. Figure 3.8(a) and (b) show that at the height just above the gas distributor, the smallest bubbles start to emerge in large numbers. As the tiny bubbles rise, they get bigger and bigger due to the interaction and merging with neighbor bubbles. The number of bubbles becomes smaller, along with the increase of height following the volume conservation. It can also be noted that

the EMMS drag model generated much smaller bubbles than two other drag models. This is because of the lower resistance of the EMMS drag force for gas flowing through the emulsion. Figure 3.8(c) and (d) show that the volume of the bubble fraction below 5 cm represents about 30% of the EMMS drag scale. The number of bubbles smaller than 5 cm only makes up approximately 14% for BVK and Gidaspow versions. Note that even if the volume fraction is only about 14%, the number of these small bubbles is around 74%. This shows that the BVK and Gidaspow drag models have missed many small bubbles. CFD grids should be optimized then to accommodate these tiny bubbles.

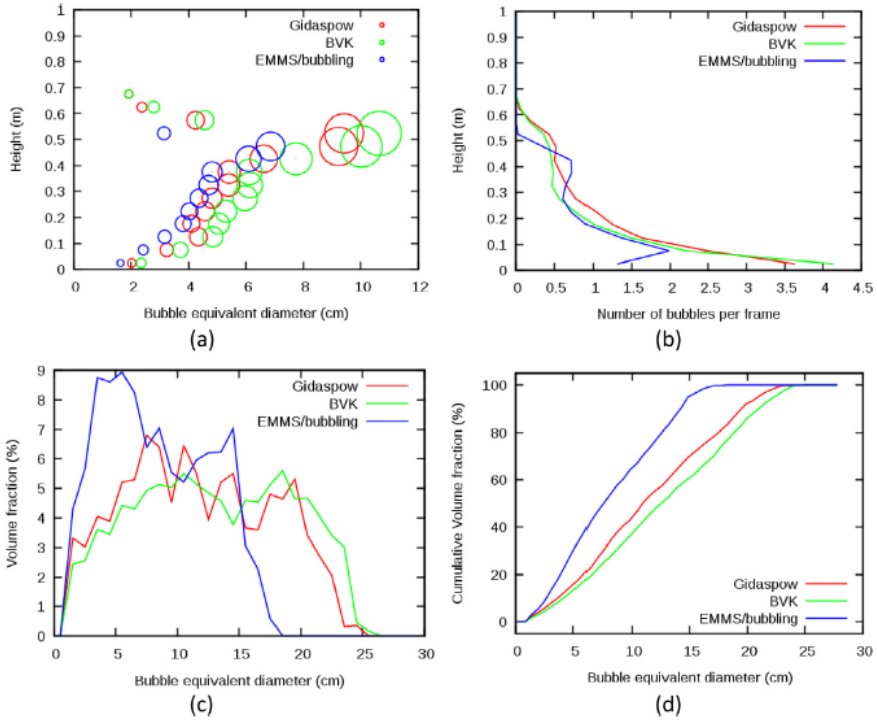

Figure 3.8: Simulation result of bubble properties with three different drag model: (a) axial bubble equivalent diameter; (b) number of bubbles observed per second; (c) bubble size distribution; and (d) cumulative bubble size distribution [28]

Figure 3.9(a) provides a comparison of experimental and simulation results of the time-averaged radial voidage profile at 0.2 m above the gas distributor. This comparison reveals that the simulated voidage profile of EMMS / bubbling drag correlates well to experimental results while BVK and Gidaspow overpredict that gas volume fraction profile. These results are in good agreement with the distribution of particles shown in Figure 3.7 and the distribution of axial voidage in Figure 3.9(b). This figure shows that both homogenous drag models foresee greater voidage in the dense area and the bed's expansion height. In contrast, the heterogeneous drag (EMMS / Bubbling) predicted the smaller void fraction distribution over bed height.

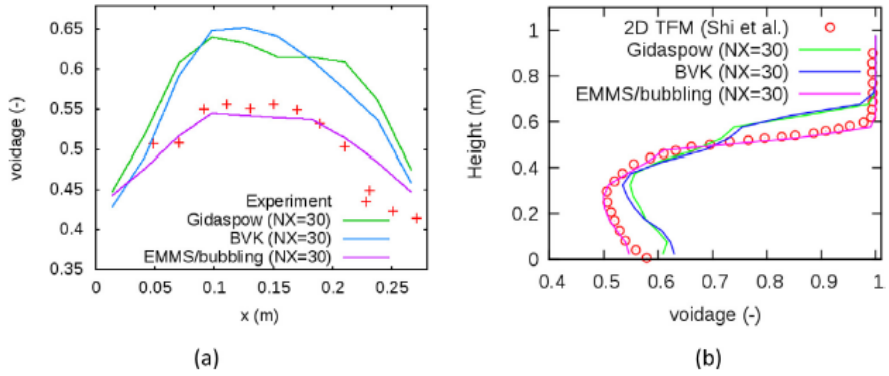

Figure 3.9: Voidage distribution using three different drag models and grid resolution 34 d_p x 30 d_p x 30 d_p: (a) radial direction at 0.2 m height; (b) axial direction [28]

While Lu et al. [28] implemented the EMMS / bubbling drag model on CGPM based on the eulerian-lagrangian method, Shi et al. [54] used a TFM eulerian-eulerian model. The latter researchers examined two different particle

groups: Geldart A from Zhu et al. [73] and B from Taghipour et al. [25] in order to observe the influence of the EMMS / bubbling drag model in a different range of particles size.

Fig. 3.10 displays time-averaged solid concentration axial profiles, using various drag models on Geldart A particle size. The simulation results are consistent with available experimental data when using the EMMS / bubbling model (drag B). The grid refining test demonstrates that such a grid resolution (40 x 200) is sufficient to predict flow behavior correctly. However, the bed expansion is overestimated by using the hybrid drag model proposed by Wen & Yu and Ergun (drag G). The drag G method forecasts a nearly vertical curve in the bed height, with a uniform solid distribution, contrary with the heterogeneous and turbulent distribution prediction for drag B. Refining grids of 10 times the diameter of the particle (417 x 962) did not have any significant impact in this situation.

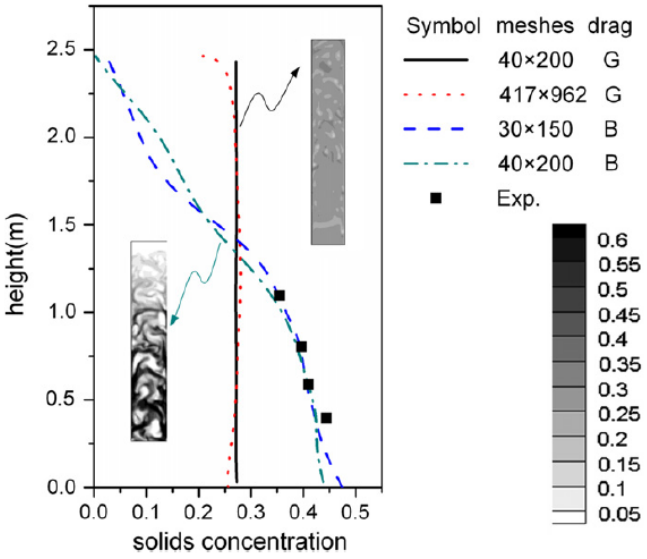

Figure 3.10: Comparison of axial solid volume fraction using two different drag models with experimental data [59]

The comparison of experimental and simulation results of the time-averaged radial voidage profile for Geldart B particles at 0.2 m above the gas distributor is shown in Figure 3.11. Unlike the simulation result for Geldart A particles, there is no significant difference between drag G and drag B results represented in this figure. Both of the drag models predict reasonably well for the radial voidage profile on two different gas velocities. This indicates that EMMS / bubbling drag model did not improve the simulation results for Geldart B particle size compare to the standard well-established drag model.

Based on this review, the high expectation and more confident results for the hydrodynamic simulation are offered by the EMMS-bubbling drag model. Especially for bubbles size produced and their distribution. For both axial and radial voidage profiles, the insignificant difference with the standard drag model (e.g., Gidaspow) is expected. This will be discussed further with the result of the simulation in section 5.3.

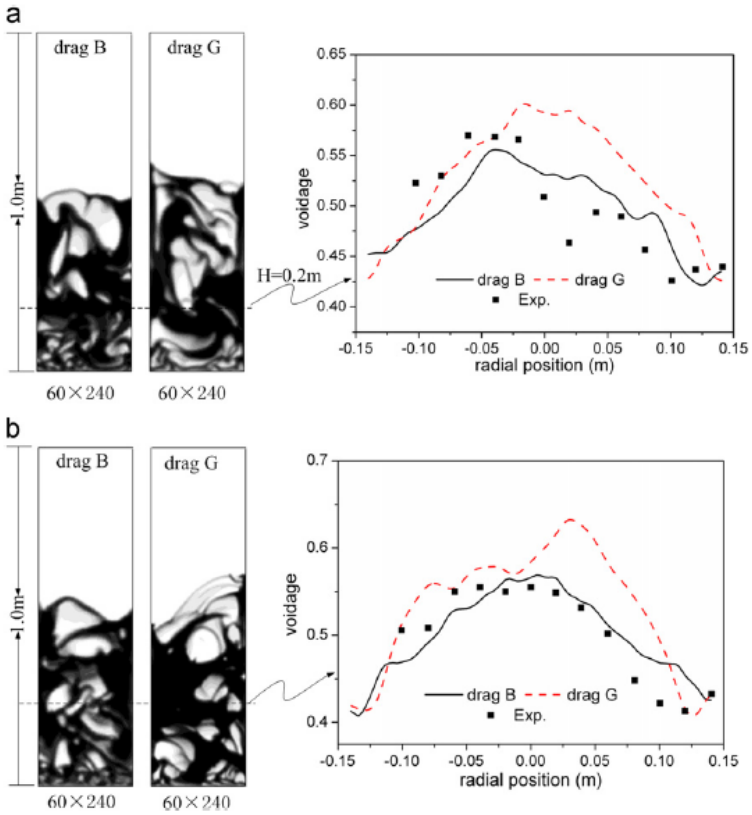

Figure 3.11: Comparison of radial solid volume fraction at 0.2 m height using two different drag models with experimental data [59]

3.1.5 Other parameters

This last part of the hydrodynamic literature review will focus on the findings and discussions related to some other parameters that also affect the flow behavior of solid-gas fluidized beds: 2D versus 3D, wall specularity, and restitution coefficient.

Ostermeier et al. [70] performed a study on the effect of 2D and 3D simulation together with the wall effect. The 2D and 3D simulations for a chosen gas velocity, height, and nozzle configuration are seen in Figure 3.12 for a comparison of the bubble and large particle velocity. First of all, the 2D simulations display a much steeper radial gradient for bubble and particle velocity and contribute to a negative bubble velocity in the proximity area to the wall, regardless of the coefficient of specularity. Referring to [74], the absence of wall impact in the third direction could lead to overprediction of gas and solid velocity. This behavior occurs because the gas and granular phases have little chance of dissipating energy horizontally, contributing to higher vertical velocity. Then Ostermeier et al. [70] concluded that the 2D system could not be used to represent the hydrodynamic behavior accurately.

This particular issue for the simulation results differences between 2D and 3D will be discussed further in section 5.2 and 5.3. In those sections of the report, the bubbles' behavior in both 2D and 3D will be observed, especially on determining the minimum fluidization condition and the voidage of profile in the bed.

Secondly, a low specularity coefficient of 0.01, which almost does not reflect any friction between wall and object, contributes to unphysical behavior in 3D simulations. The theoretically realistic 3D result with a specularity factor of 0.5 to 1.0 displays mild radial gradients and a favorable positive bubble velocity across the bed's cross-section. On the first analysis, it also seems acceptable to presume a diffuse collision with a specularity factor of 1.0. However, a thorough study of the hydrodynamic bubbles and particle activity in the wall area reveals that the experimental particles can be modeled better with a specularity coefficient of 0.5.

The effect of specularity will be examined together with the sphericity factor in the dedicated section of 5.4. A unique finding for the difference between the no-slip boundary with the specularity coefficient close to zero will also be discussed.

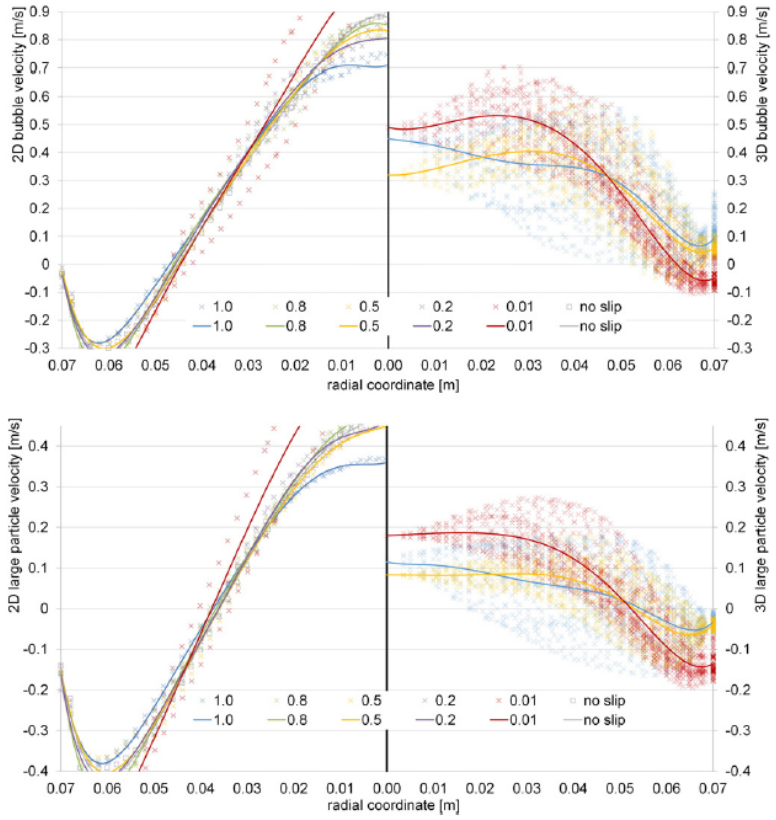

Figure 3.12: Time averaged and time and radial averaged bubble and large particle velocity at 0.2 m/s air superficial velocity at 0.1 m height using Multi Fluid Model (MFM) and sphericity factor 0.82: bubble velocity (top); particle velocity (bottom); left (2D); and right (3D) [70]

Goldschmidt [75] conducted another study for the effect of a collision between particles in the form of restitution coefficient. Figure 3.13 provides experimental snapshots and measurements of specific values for the restitution coefficient on the bed surface when a bubble eruption occurs. The colliding processes that become less ideal (and dissipate more energy due to the inelastic collisions) mean that particles are packaged closer to the denser regions of the bed, leading to sharper porosity contours and larger bubbles. Bubble formation did not appear for velocities below three u_{mf} in simulations with ideal particles.

The same authors observed that the simulated dynamics of bubbles were too strong for the restitution coefficient (e_{ss}) equal to 0.73. The best representation between the experiment and the simulations were achieved for e_{ss}= 0.9, based on the snap-shot and video of the experiment and the simulations. Besides, the kinetic theory of granular flows has been derived here for slightly inelastic spheres, and its implementation is uncertain for e_{ss}<0.9 [75].

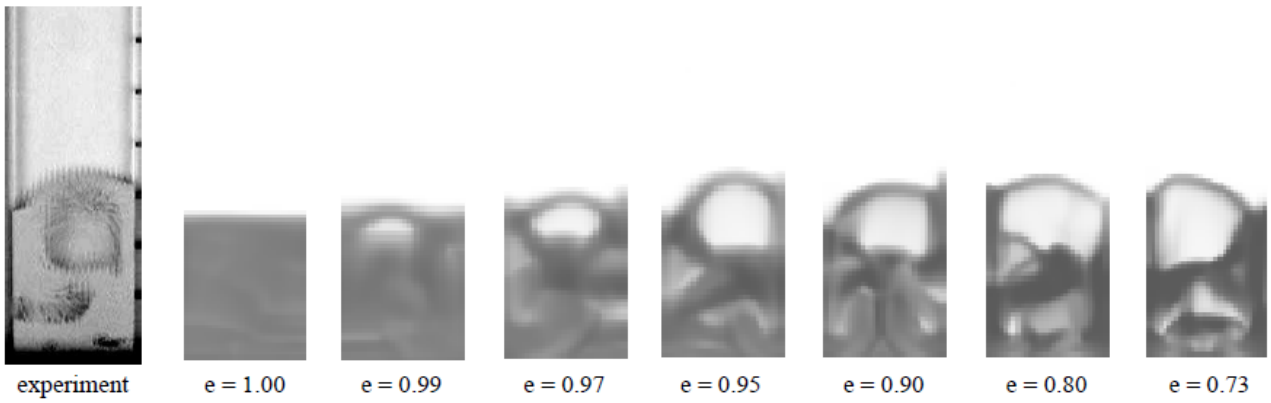

Figure 3.13: Comparison of experiment and bubbles simulation with various restitution coefficient values [75]

The effect of the restitution coefficient will be simulated following the Goldschmidt's observation. It will then confirm whether the solid-gas interaction within the bed in the form of bubble shape is affected by the restitution coefficient, and the best representation of the bubble is depicted with e_{ss}= 0.9.

3.2 Heat Transfer

3.2.1 Grid refinement

Similar to the hydrodynamic, simulation of heat transfer will very much depend on grid division. Preliminary measurements by Kuiper et al. [24] indicated very high-temperature gradients along the heated wall, which required the use of a grid refining technique to reflect the thin thermal boundary layer temperature profiles accurately. It was not used in the basic numerical model.

They suggested that the original hydrodynamic cells should be refined by a subdivision towards the normal direction of the heated wall, as shown in Figure 3.14. The number of subcells n required is troublesome and should be determined through a convergence analysis concerning the measured numerical heat transfer coefficients. Differentiation into seven sub-cells was found to be adequate in order to establish a grid-independent solution under the conditions of their work [24].

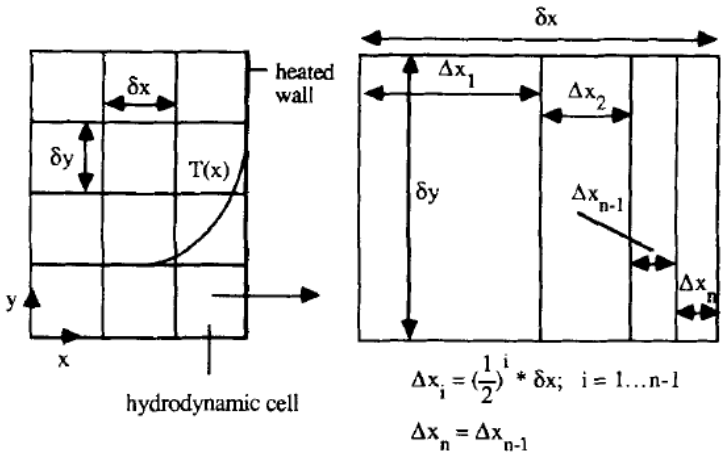

Figure 3.14: Grid refinement method of hydrodynamic computational cells into subcells in heated wall proximity (n= number of subcells) [76]

This grid refinement method performed by Kuiper et al. will be implemented in the present simulation and discussed further in section 5.5. The heat flux differences obtained from different cell subdivision simulations will be compared.

3.2.2 Heat transfer coefficient in a quiescent bed

The proper specification of the constituting equations for $k_{eff,f}$ and $k_{eff,s}$ thermal conductivities presents a significant difficulty in the theory as discussed in section 2.2. In the TFM approach $k_{eff,f}$ and $k_{eff,s}$, both must be transformed as effective transport properties, meaning that the microscopic transport coefficients k_f and k_s can not be directly used. Both $k_{eff,f}$ and $k_{eff,s}$ should depend on ϵ, k_f, k_s, and particle geometry, where functional dependence should, in part, be determined employing experimental data [76].

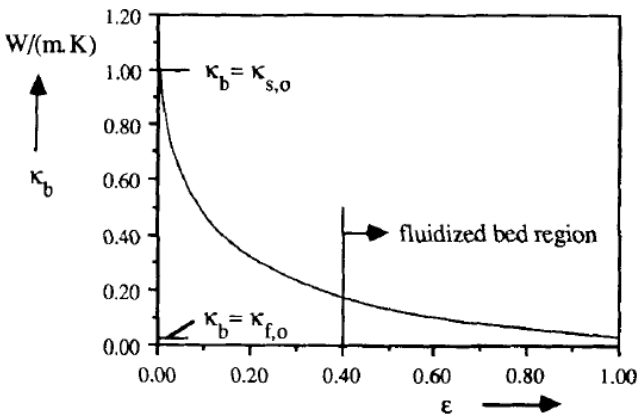

Figure 3.15: Effective bed conductivity of fluid-particle system (air with k_f= 0.0257 W/mK; glass beads with k_s 1.00 W/mK) against the bed voidage with marked typical region of fluidized bed [76]

Figure 3.15 demonstrates the effective bed conductivity k_b for spherical glass beads in the air against bed porosity ϵ based on the Zehner and Schlunder model [46]. Remarkably, the conductivity of the bed (k_b) is considerably smaller than the original solid conductivity (k_s). The effective conductivity decreases from 1 to 0.2 W/mK, which is about 20 % of the initial value.

This finding will be compared with the present simulation, whether the effective bed conductivity will be decreased that much. The discussion is provided in section 5.6.

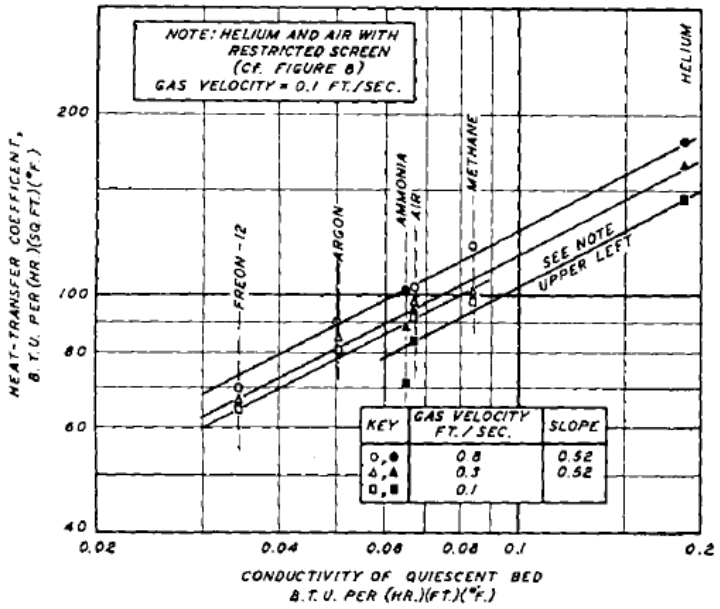

Figure 3.16: Heat transfer coefficient of glass beads as a function of quiescent-bed conductivity [43].

According to Mickley and Fairbanks [43], one of their most critical finding was obtained whenever they compare various gases' heat transfer coefficient with the bed's quiescent conductivity. It is shown in Figure 3.16 and demonstrated that at most of the cases, for a given solid and gas velocity, the heat transfer coefficient corresponds to 0.52-0.55 power of quiescent conductivity.

The consistency of the evidence in this figure shows that the heat transfer model proposed based on unsteady heat diffusion remains accurate. The effect of quiescent conductivity is predicted to be very similar to the square root range. Had heat transfer, on the other hand, been regulated by conduction of the laminar layer of solid, the estimated value will be the first power of quiescent conductivity. While if a gas film is a controlling factor, the slope of the graphic will be of about 1.5 [43].

The theory presented by Mickley and Fairbanks is interesting to be discussed further to see how far this concept applicable, particularly in this present novel IHBFB pilot reactor. Section 5.10 discusses the comparison between the heat transfer obtained from the square root of quiescent bed conductivity with the one obtained from the solution of the CFD simulation.

3.2.3 Heat transfer coefficient and penetration theory

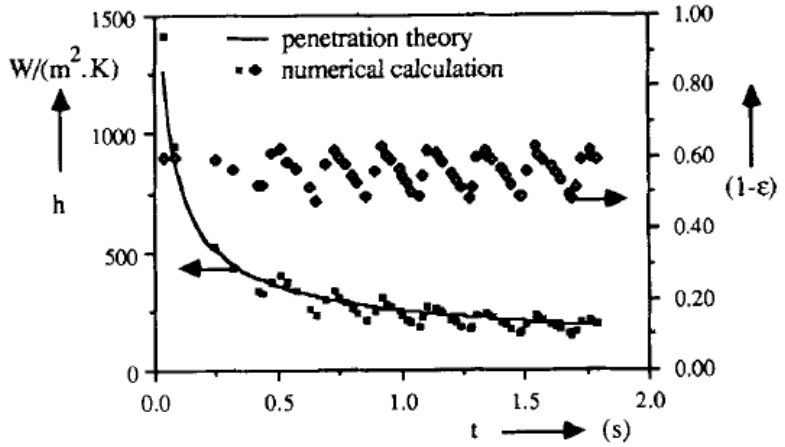

Figure 3.17: Simulation result for the local wall to bed heat transfer coefficient (h) and a local solid fraction (1-ϵ) versus time (t) at incipient fluidization condition at approximately 0.24 m above gas distributor. The solid line is penetration theory [76]

Packet renewal model proposed by Mickley and Fairbanks [43] states that heat is transmitted through the emulsion process "packets" exchanged periodically with bubbles from the heat transfer surface. It defines the emulsion phase as a continuous phase, and the bubbles are the discrete phase. The common penetration theory can be obtained via a semi-infinite medium at the incipient or minimum fluidization condition.

Kuiper et al. [24] observe the wall to bed heat transfer coefficient on Geldart B particle using TFM numerical solution. They compare the heat transfer coefficient with the penetration theory at an incipiently fluidized bed, as shown in Figure 3.17. The numerically determined local wall to bed heat transfer coefficient h can be shown to quickly decrease with an increasing time t in line with penetration theory predictions. The local numerical coefficient of heat transfer, however, reveals a decay that requires a slight oscillation. This was induced by the fluctuation of the solid fraction in the bed. Similar findings were also observed at specific points above the gas distributor.

The penetration theory employed by Kuiper et al. is somewhat similar with the unsteady state heat diffusion theory presented by Mickley and Fairbanks. As mentioned earlier, this comparison study will be provided in section 5.10.

3.2.4 Heat transfer coefficient and bubbles (voidage)

Another interesting finding from Kuiper et al. [24] was the investigation of the bubble effect on the numerical heat transfer simulation result. Compared to an incipiently fluidized bed, one could expect the wall-to-bed heat transfer to be improved because the bubble replaces the solid particles adjacent to the heat exchange surface.

In Figure 3.18, the measured local instantaneous heat transfer coefficients are shown as a function of time at four different heights above the gas distributor. At each point, as the growing bubble moves, the numerically determined local heat transfer coefficient can be seen dramatically decreasing due to the relatively low thermal conductivity in the bubble. The local heat-transfer coefficient increases dramatically after the bubble passage passes through a maximum and decreases again slowly. Figure 3.18 indicates that for an increase of height over the distributor of gas, the magnitude of this peak declines. This possibly related to the increasing penetration of heat into the emulsion process of a bubble wake. The measured heat transfer coefficient at y= 0.545 m over the gas distributor represents the cumulative results of the bed expansion and the collapse of the bed afterward.

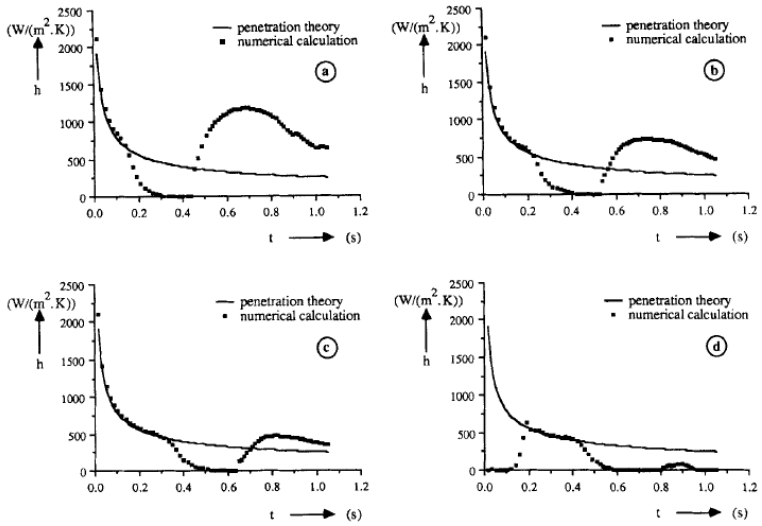

Figure 3.18: Simulation result of local instantaneous heat transfer coefficient against time at four different heights above the gas distributor at bubbling bed:(a) y= 0.245 m; (b) y= 0.345 m, (c) y= 0.445; (d) y= 0.545 m [76]

The instantaneous average wall-to-bed heat transfer coefficient, as shown in Figure 3.19 obtained by the integration of local heat transfer coefficients over the incipient height fluidizing bed h. The penetration theory's heat transfer coefficient profile is also displayed as a comparison. In the beginning, the calculated average heat transfer coefficient from wall to bed was compliant with the approach of penetration theory. However, the available effective heat exchange duration decreased dramatically during the final stage of the bubble production due to a bubble 's existence, thus dropping the average heat transfer coefficient from the wall to bed below the penetration [76].

Throughout its rise over the heated wall, the bubble causes the material in the bed next to the wall to renew. Eventually, the average heat transfer coefficient measured from wall to bed exceeds that of penetration theory. The effect of bed material refreshment explicitly compensates for the lack of effective thermal exchange due to the bubble existence.

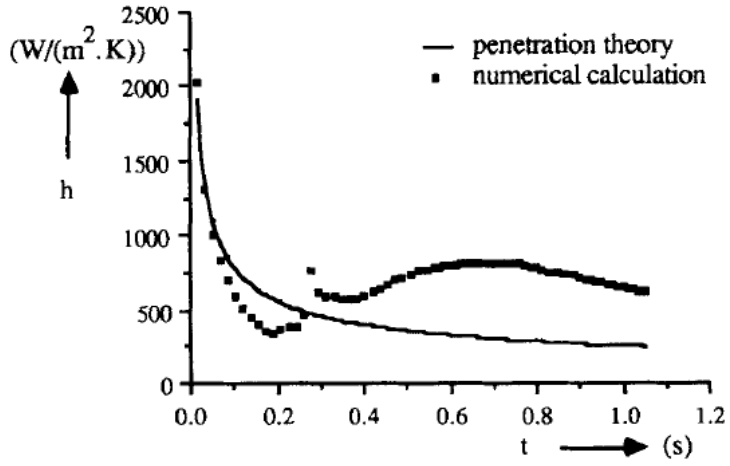

Figure 3.19: Comparison of an instantaneous average wall to bed heat transfer with penetration as a function of time [76]

Since the bubbles will always occur during the simulation above u_{mf}, the bubbles' effect on the present simulation is very critical. This specific section 5.9 observes the heat flux profile on different bubbling or voidage conditions.

3.2.5 Significancy of radiative heat transfer

Gas fluidized beds are used at high temperatures in a variety of chemical and metallurgical applications. In these operating circumstances the radiative mode is used to transfer a significant proportion of the total thermal energy. Saxena et al.[77] summarized some findings on the radiative heat transfer experiment from several different authors, as shown in Table 3.1.

Il'Chenko et al.[78] worked with five particles from five different bed materials across a variety of sizes and temperatures. They calculated both total and radiative heat fluxes, which increased with temperature. They found out that particulate shapes are not crucial in thermal transport, as they are in conductive heat transfer at high temperatures. Particularly for zirconium dioxide the relative radiative flow rate, q_r / q_T, was seen to rise from approximately 5% to 26% when there was a rise in the bed-temperature from 900 to 1375 K.

The findings of Basu [79] have been similar to the results of Il'chenko et al.[78]. He observed that the radiation flux is not particularly affected by the fluidizing velocity. He also states that q_r / q_T is at an order of 5-10 % in the temperature range 1073-1173 K, and both heat fluxes increased in a linear manner with temperature. He also experimented with sand particles of four different mean sizes at high temperatures and observed that the maximum heat transfer coefficient decreased as the particular mean diameter increased (0.2 – 0.7 mm).

Mathur and Saxena [80] examined the magnitude of total and radiative coefficients, based on bed temperature and fluidizing velocity, for two medium particle beds, 559 and 751 μm. In both particle grains, the radiative coefficient of heat transfer is increased with the gas velocity and bed temperature and has an almost constant value at higher gas speeds. As shown in the Table 3.1, in the case of 559 μm particle, the radiative contribution increased from 7 % to 11 % for the temperature increase from 675 to 985 K. While for the larger sand particles, the radiative portion is 5 % at 675 K and 13 % at 1175 K. These results indicate that radiative heat transfer may not be too prone to minor changes in particle size, particularly if the gas velocity changes are paid little attention.

Table 3.1: Comparison of radiative and total heat transfer coefficient / flux of some experimental investigation [77]

Investigators	**Fluidizing Velocity (m/s)**	**Bed Material**	**Particle Size (μm)**	**Bed Temp. (K)**	**Gaseous Environment**	**%h_{wr}/h_{wT} or %q_r/q_T**
Il' Chenko et. al. [78]	0.48 - 1.26	Zirconium dioxide	570	1223	Air and combustion products of natural gas	20 ± 1
	0.48 - 1.26	Zirconium dioxide	570	900 - 1375	Air and combustion products of natural gas	5 - 26
Basu [79]	0.21 - 0.47	Sand	325 - 500	1173	Air and coal combustion products	7
	0.28	Sand	280	1073 - 1173	Air and coal combustion products	5 - 10
Mathur and Saxena [80]	0.18 - 0.50	Sand	559	675 - 985	Air and propane combustion products	7 - 11
	0.50 - 1.10	Sand	751	675 - 1175	Air and propane combustion products	5 - 13

All of these investigations give a hint for radiative heat transfer significance in the fluidized bed, in what order of improvement. As the corundum particles will be employed on the present work has the similar physical form as sand, in the range of particle size and operating temperature conducted by Mathur and Saxena, and Basu, the expected q_r/q_T is on the range 5-13 %. Section 5.8 discusses this particular issue.

4 Model Development

On this chapter, the step by step of model development will be described. Aligning with the common practice of CFD simulation, the explanation will begin with the IHBFB-SR's geometry, meshing work, and, finally, all the considerations for model selection part by part. The general illustration of the IHBFB-SR reactor has been briefly discussed in Figure 1.7 on Chapter 1. In this study of hydrodynamic and heat transfer, the steam flow was replaced by air as the fluidization agent, and biomass will not be involved. Only corundum as bed material and the fluidization media are considered, as mentioned in section 1.4.

The specific setup and the instrumentations employed are described in Figure 4.1. The main gas flow will consist of air and primary nitrogen entering the reactor via the nozzle distributor. Secondary nitrogen flows into the reactor from the reactor's side to keep the pressure sensors, especially the feeding system and bunker pressurized. Five thermocouples at different heights and two pressure differential sensors actively measured the temperature and pressure during the experiment. The radiant burner will continuously supply the heat via the combustion of natural gas to maintain the 650 ^{o}C of average bed temperature (of all five thermocouples), with 600 ^{o}C of actual average bed temperature (of first two thermocouples) involve on fluidization. In the simulation, the total flow of fluidizing agent will be represented by air only (no primary nitrogen), and the secondary nitrogen from the side of the reactor will be neglected. For hydrodynamic case, cold flow modeling with 600 ^{o}C isothermal and atmospheric condition was assumed.

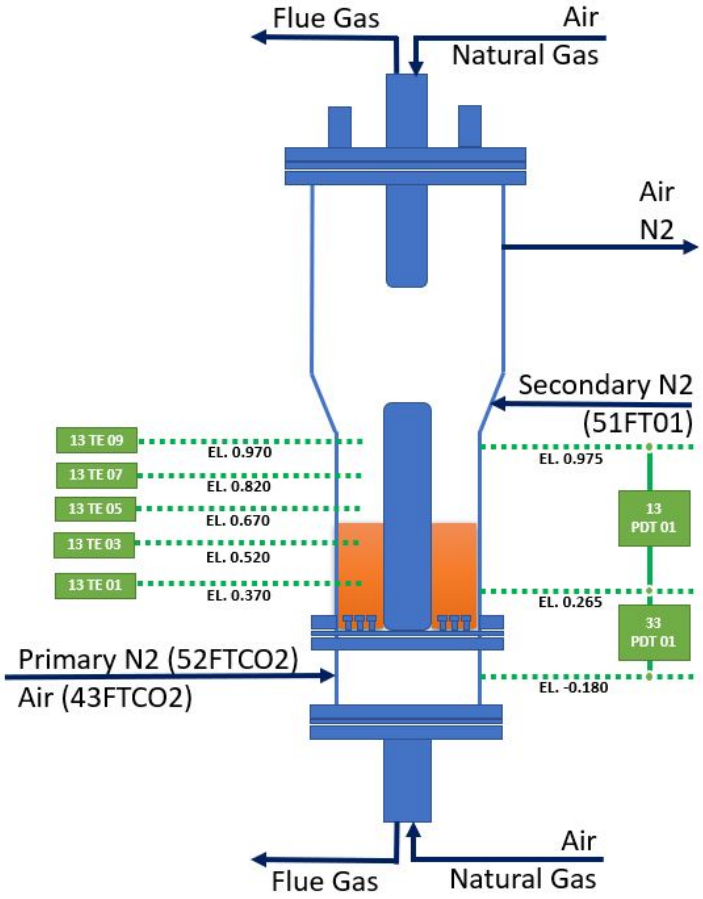

Figure 4.1: IHBFB-SR actual setup illustration on the experiment: 75 kg of bed material (corundum) loading

In Table 4.1, the summary of critical parameters employed on the overall simulation is provided. Some of them will be elaborated further on the next section, and some of them are just a default setting, which is widely used or suggested by the Fluent manual on typical simulations. "Specified" means the parameters were selected based on some considerations, while "Fixed value" means the parameters which are already given as the based for the simulation.

4.1 Geometry

The bubbling fluidized bed pilot reactor examined in the present work has several components. Some major parts included in the model's geometry were: reactor body, radiant burner wall, and nozzle distributor. Due to the consideration of computational resources, the domain of the reactor is limited until the a height of 1.8 m for 2D

Table 4.1: Simulation model parameters

Parameters	Description	Comment
Numerical method	Eulerian multiphase	Section 4.3.2
Simulation domain	2D & 3D	Specified
Fluid phase	Air	Fixed value
Solid phase	1 (TFM), corundum	Specified
Solid density, ρ_s	3950 kg/m^3	Fixed value
Solid diameter, d_p	496 μm	Fixed value
Sphericity factor, ϕ	1 (sphere)	Specified
Specularity coefficient	no-slip	Specified
Drag model	Gidaspow, adjusted Syamlal, EMMS	Section 4.3.2
Interphase heat transfer	Gunn	Specified
Radiative model	P1 and DO	Section 4.3.2
Restitution coefficient, e_{ss}	0.8-0.99	Range in literature
Viscous model	Realizable k-ϵ	Section 4.3.2
Initial solid packing	0.41	Specified
Max. Packing limit	0.63	Specified
Superficial gas velocity, U	0.10-0.21 m/s	Specified
Static Bed Height	0.61 m	Fixed value
Bed inner diameter	0.150 m	Fixed value
Bed outer diameter	0.343 m	Fixed value
Grid interval spacing	0.0025 m	Specified
Time steps	0.001 s	Specified
Max. Iterations	50 for 3D, 75 for 2D	Specified

and 1 m for 3D, which is from the bottom part of the reactor (started just after the top of nozzle distributor plate) until some part of the upper reactor body with also the exclusion of top radiant burner (C150). The illustration of the modeling domain is shown in Fig. 4.2 as follows

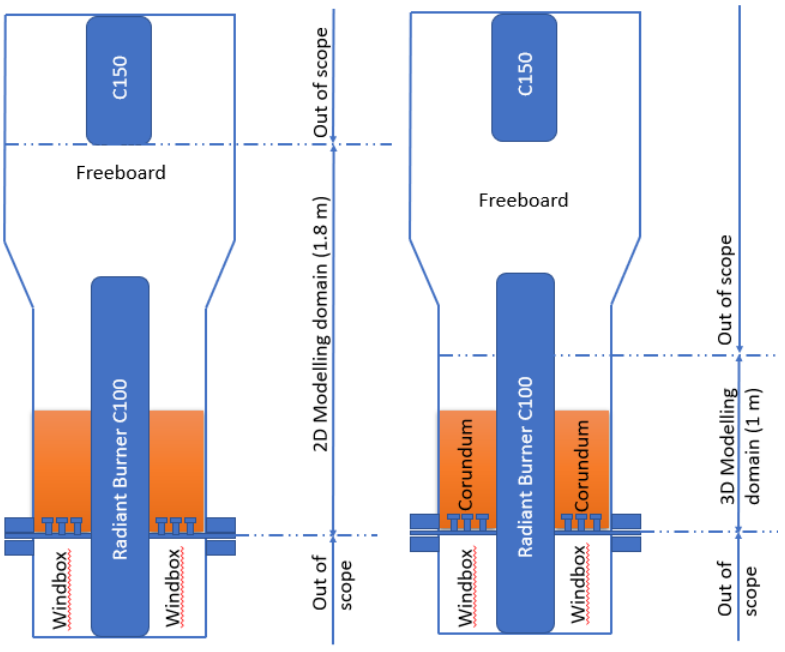

Figure 4.2: Scope illustration for modelling domain: 2D on the left side and 3D on the right side

The reactor body has two different diameters, the smaller one on the bottom is 343 mm, and the bigger on the top is 444.3 mm. The thickness of the material is not considered on the present work, thus only inside diameter is used. The same holds for the radiant burner on the bottom part (C100), where only the outer diameter of 150 mm, interfacing the fluid domain is considered. Furthermore, to have an effective CFD simulation referring to the symmetrical shape of the reactor, only a quarter of total volume is employed. The final reactor body geometry is displayed in Fig. 4.3.

The 2D model was used in hydrodynamic and heat transfer simulations, while 3D was used for hydrodynamic only due to the computational resource limitation. For instance, to perform the stable result for heat transfer simulation, at least 5s of simulation is required. While if the simulation is performed on the 3D domain, 1s simulation takes almost one full day with the currently available resources.

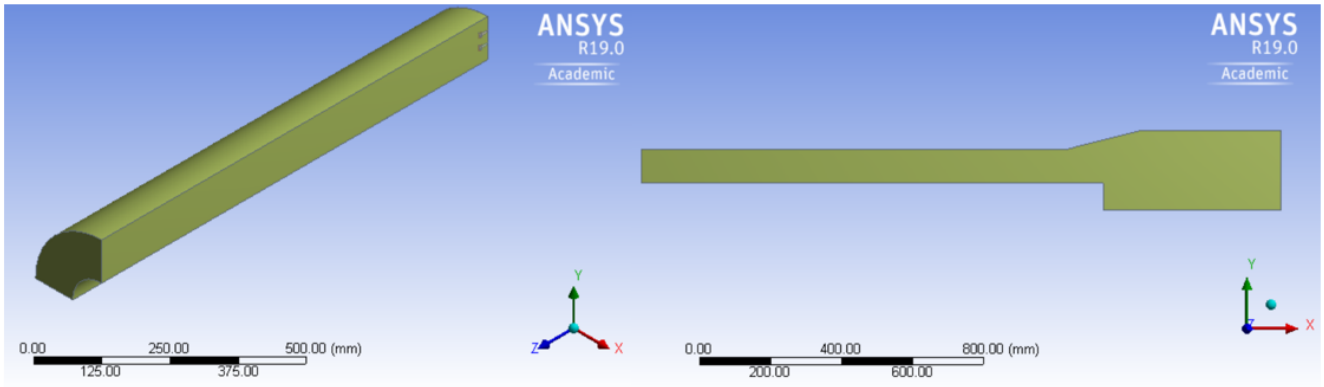

Figure 4.3: Reactor body domain modelled using ANSYS R19.0 Design Modeller: 3D on the left picture and 2D on the right

Nozzle distributor, as shown in Fig. 4.4 was built following the detailed drawing and specifications from Petrogas. This tuyere type nozzle has two steep outlet holes with 20^o angle from the vertical axis of its body and facing downward. The threaded connection on the bottom of the nozzle, which was the part that connected to the distributor plate, was not modeled for the simplicity and its negligible influence.

In total, there are fifty nozzles inside the reactor. Twenty nozzles with the 18^o angular distance were located on the inner ring while the rest thirty nozzles were placed on the outer ring with 12^o distance each. Following the quarter volume of the body, the total nozzles remaining on the simulation body are only eleven full bodies and three half body nozzles, as shown in Fig. 4.4. The 2D model doesn't include this nozzle due to the unfeasibility of modeling it in the 2D domain. The gas flow in the 2D domain was then introduced via the bottom part of the reactor's full cross-section surface.

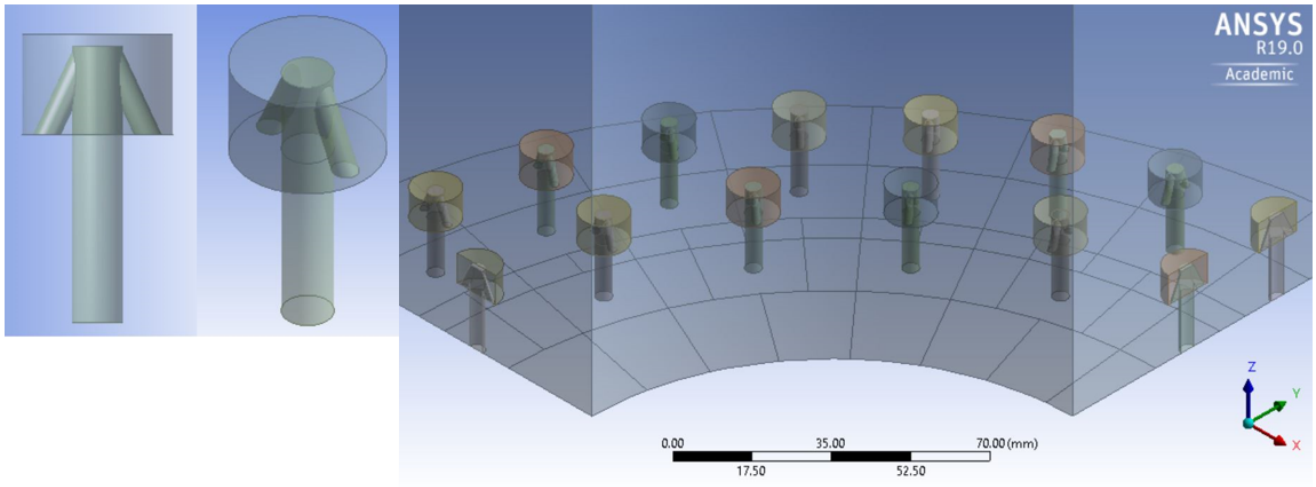

Figure 4.4: Tuyere nozzle distributor with the arrangement inside the reactor's body

4.2 Meshing

The meshing work was performed using ANSYS ICEM CFD software. It offers advanced geometry acquisition, mesh creation, and mesh diagnostic and repair tools to provide optimized mesh creation for today's sophisticated analyses. It is designed to maintain a close relationship with the geometry during mesh generation in engineering applications such as computational fluid dynamics and structural analysis. The mesh generation tools from ANSYS ICEM CFD offer the capability to compute geometry meshes in various formats [51] parametrically:

- Multi-block structured
- Unstructured hexahedral
- Unstructured tetrahedral

- Cartesian with H-grid refinement
- Hybrid meshes comprising hexahedral, tetrahedral, pyramidal and/or prismatic elements
- Quadrilateral and triangular surface meshes.

ANSYS ICEM CFD provides a direct connection between geometry and analysis. It covers the input geometry in almost any format, whether a commercial CAD design package, a third-party universal database, a scan, or point data. Starting with a robust geometry module that supports the development and modification of surfaces, curves, and points, the open geometry database of ANSYS ICEM CFD offers the flexibility to combine geometric information in different formats for mesh generation. The products of meshes, topology, inter-domain connectivity, and boundary conditions are then stored in a database. They can be easily converted into input files formatted for a specific solver.

There are several basic steps required for mesh creation on ANSYS ICEM CFD; the workflow of the overall process is summarized in Fig. 4.5. The explanation of each step is completely detailed on ANSYS ICEM CFD users manual [51].

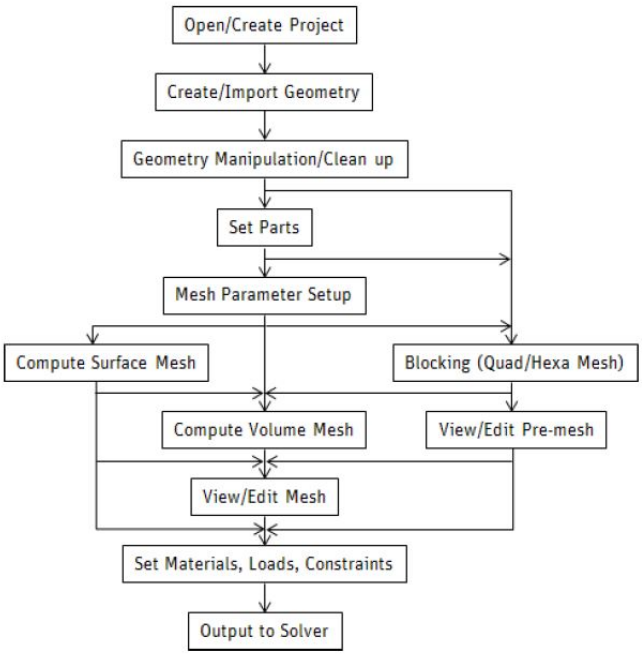

Figure 4.5: ICEM CFD overall process [51]

Mesh quality is of paramount importance in doing CFD modeling. As discussed in ANSYS FLUENT Guides [45], the recommended mesh type for doing multiphase simulation is a hexahedral or quadrilateral cell instead of tetrahedral or triangular. In dealing with the localized grid refinement and coarsening for capturing certain variables of interest, anisotropic division of hexahedral cells will not generate any mesh quality problem. Furthermore, hexahedral meshes give a more accurate solution than their tetrahedral counterparts for the same number of edges [81].

There are two general blocking techniques for mesh creation of the 3D model in Hexa Meshing ICEM CFD, commonly called Top Down or Bottom Up. The top-down blocking method starts from one block created from the 3D bounding box. The blocking topology is formed utilizing break, delete, merge, and move tools to the simulation model. While the bottom-up method, also called a 3D MultiZone, starts from the 3D CAD surface structure. It constructs a 2D blocking face for each surface, and then attempts to fill those 2D faces with 3D blocks.

The top-down approach basically has several advantages as follows [51]:

- Using this method, it is always simpler to get an all-hex mesh, since the global topology is a hex mesh. The blocking remains like all 3D mapped blocks when splits are done, and there is an index control that retains the connectivity for quick mesh calculations.
- Global topology helps avoid being stuck in a corner but needs some initial thinking on how to construct the global topology to suit the CAD topology.
- When the blocking is initialized, there are no direct connections to the CAD. The user manages those connections. The mesh can be produced, and the lock projected onto the surfaces at any time. As the blocking progresses, the user can check and add shape.

In the present work, the top-down blocking strategy was implemented. The whole complex blocks arrangement, as shown in Fig. 4.6 was first started from one single 3D bounding block. After some splitting, merging, delete and transform processes, the single block can be adjusted to fit the geometry and further meshing requirement. Unlike the 3D, the 2D blocking arrangement is straightforward, as shown in Figure. 4.8.

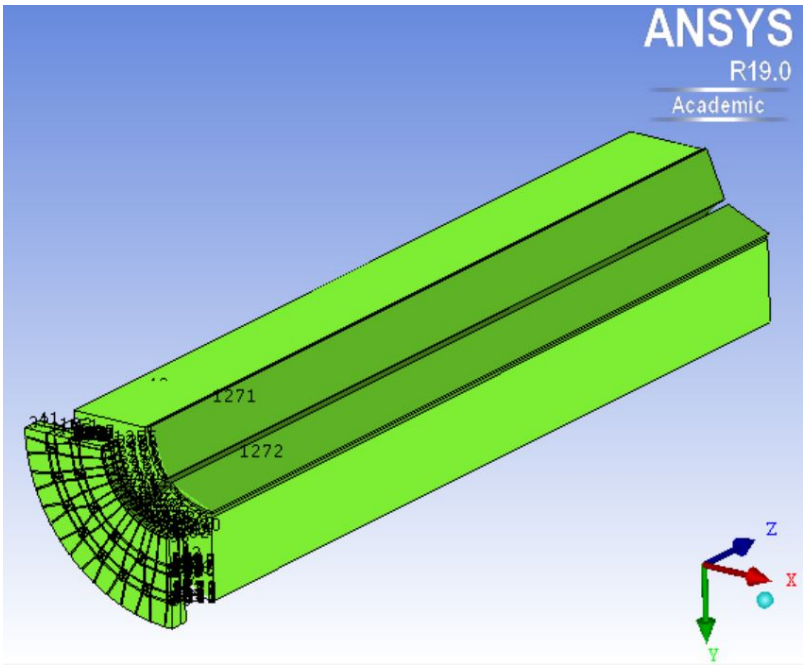

Figure 4.6: Overall 3D blocking arrangement in ANSYS ICEM CFD

The critical part of the meshing work was actually on the bottom side of the reactor, where the tuyere nozzle distributors were located. The strategy applied was to split up the block and adjust each of them to follow nozzle location by preparing the geometry splitting first on Design Modeller (Figure 4.8). This can be done quite easily following the angular distance among nozzles in the inner (18^o), and the outer (12^o) ring. However, there was still a great challenge for the split adjustment where the nozzle in the inner ring is not aligned with the outer one. By referring to the continuous splitting principle from inner to outer radial, to overcome the previous problem, some parts around the inner ring were divided more than those on the outer one while still keeping all points align. This method will then ensure the number of the elements could be kept the same once the mesh parameter is assigned.

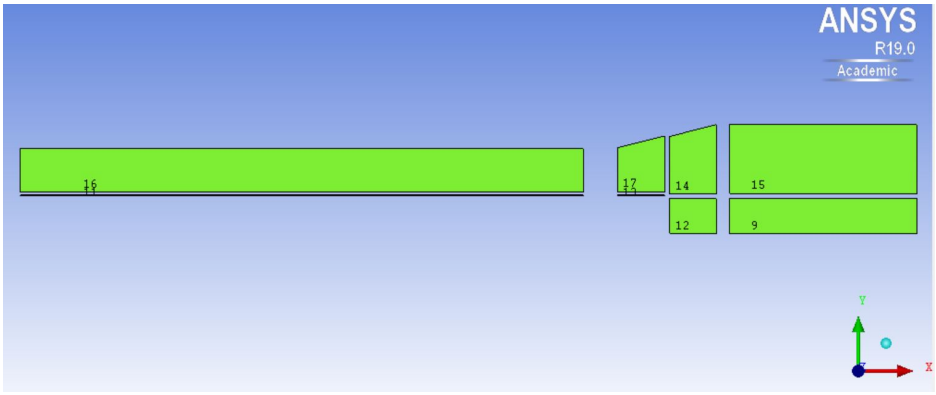

Figure 4.7: Overall 2D blocking arrangement in ANSYS ICEM CFD

Having the geometry split in the first place will tremendously ease the block splitting work on later stages on ICEM CFD. After finalizing the block split to provide the dedicated block for each nozzle, the work continued to arrange more block splitting around the boundary condition of the nozzle. Especially for the velocity inlet boundary, the block was broken down into many smaller ogrid blocks. The final block split on the bottom part of the reactor is shown in Fig. 4.8

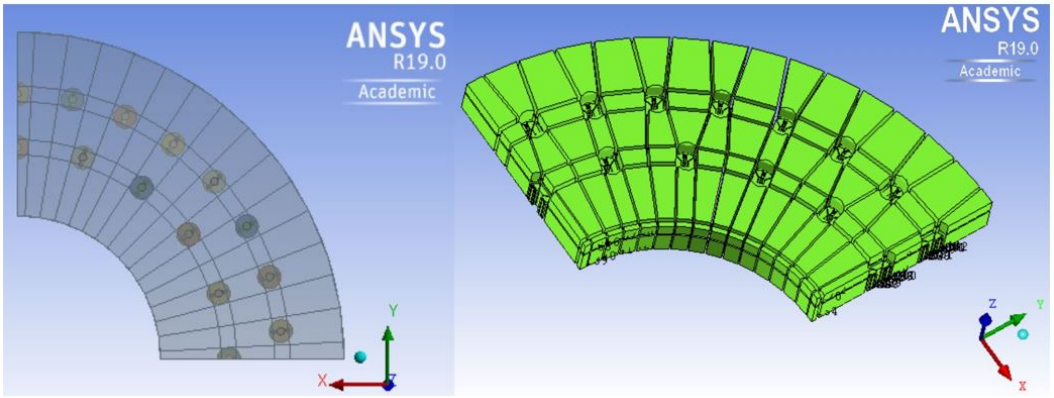

Figure 4.8: Geometry split (left) and block arrangement around nozzle distributor(right)

The final step on the meshing work is defining the mesh parameters for each edge of the block to fit the specific grid size requirement. In order to perform the grid independency test, three grid sizes of 5dp, 10dp, and 20dp (dp: diameter of the particle), which are correlated with 2.48 mm, 4.96 mm, and 9.92 mm were studied. The total elements employed on the simulation then were 8.906.701, 4.602.011, and 2.408.342, respectively. The typical mesh produced is shown in Figure 4.9.

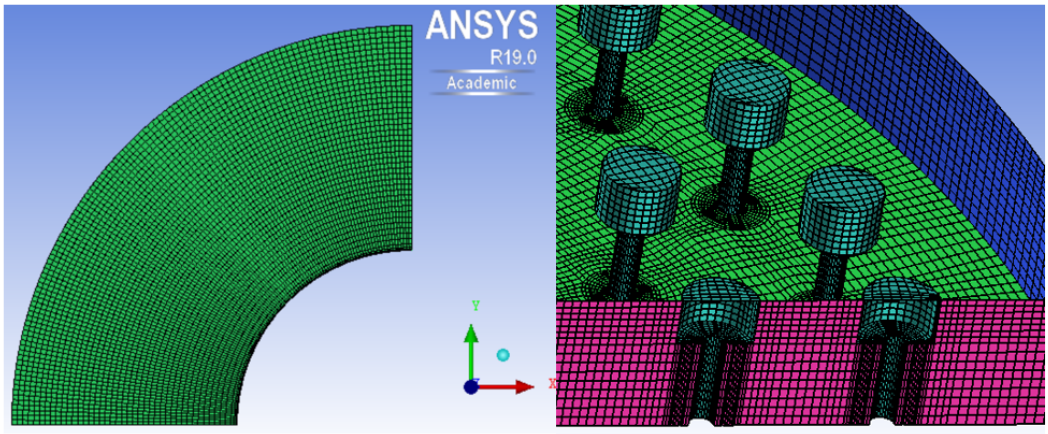

Figure 4.9: Final mesh arrangement for 5dp grid size: top part (left) and bottom part (right)

Finally, besides having a good mesh arrangement visually, it is very critical to assess the quality of the mesh comprehensively via the quality check tools on ICEM CFD. There were five quality metrics used to examine the mesh quality in the present work: quality, determinant, orthogonal, skewness and aspect ratio.

Quality is a weighted diagnostic between determinant, max. Orthogonal and max. Warp. This measure is normally used for the general overall check of the mesh. It is possible to get a negative measure of this metric if there is a negative volume detected. The quality check result on the present work is shown in Fig. 4.10 below. It can be shown that there are very few elements with the quality below 0.5 (around 0.001%), but no negative quality element at all. It means all the vertices and edges are properly connected, and there is no overlapping element. Since most of the element's quality is above 0.5, it is adequate to run the simulation smoothly with the current mesh quality.

The second measure is determinant, which can also be found in Fig. 4.10 for the checking result. This metric is properly called a relative determinant, which is the smallest determinant's ratio divided by the largest determinant of the Jacobian matrix, where each determinant is calculated at each node of the element. The quality check for the determinant was very similar to the quality metric explained before, where only a small number of elements are below 0.5. This can indicate that the bad elements referred to on this metric are the same as those mentioned on the quality metric. However, since most of the cells have a determinant of more than 0.5, it is valid to say that the mesh quality is sufficient for running the simulation.

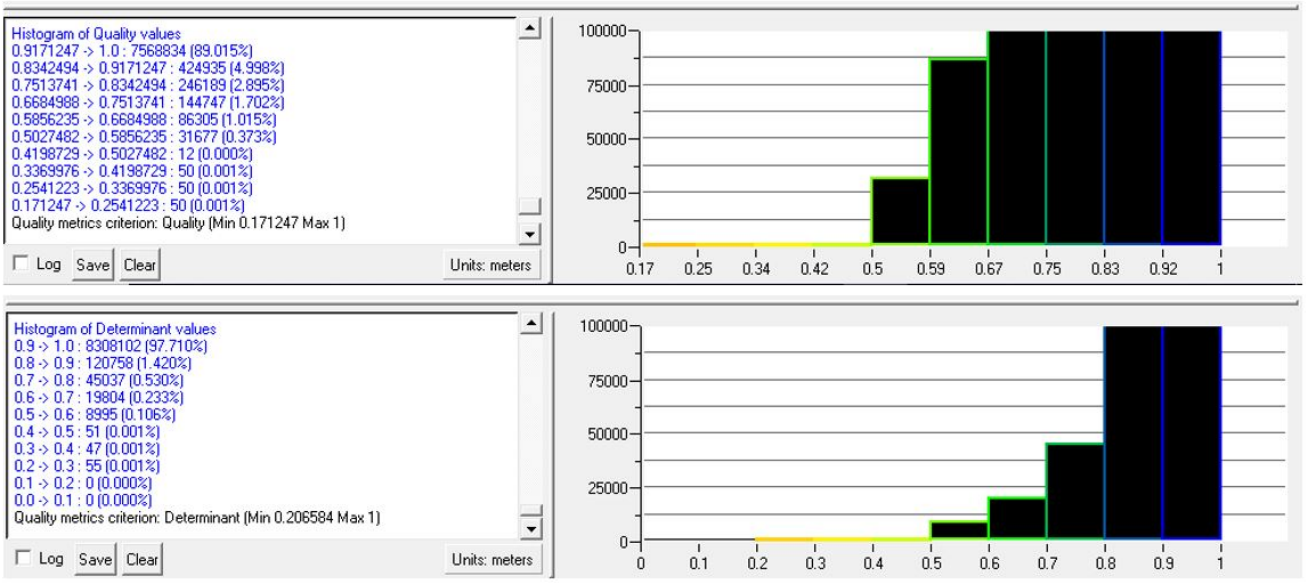

Figure 4.10: Quality and determinant check histogram

The third criterion is orthogonal quality. It is basically determined from three sets of the vector. In each face, the normal face vector (A_i), the vector from the cell centroid to the centroid of the adjacent cell (c_i), and the vector from the cell centroid to the centroid of the face (f_i) as depicted in Fig. 4.11 were used. The cosine of the angle between A_i and c_i, and between A_i and f_i were computed where the orthogonality of the cell is the smallest calculated cosine value. For a hexahedral cell, in particular, the orthogonal quality is the same as this orthogonality. They are then based on this value, the worst cell defined as the cell with an orthogonal quality close to 0 while the best one will close to 1.

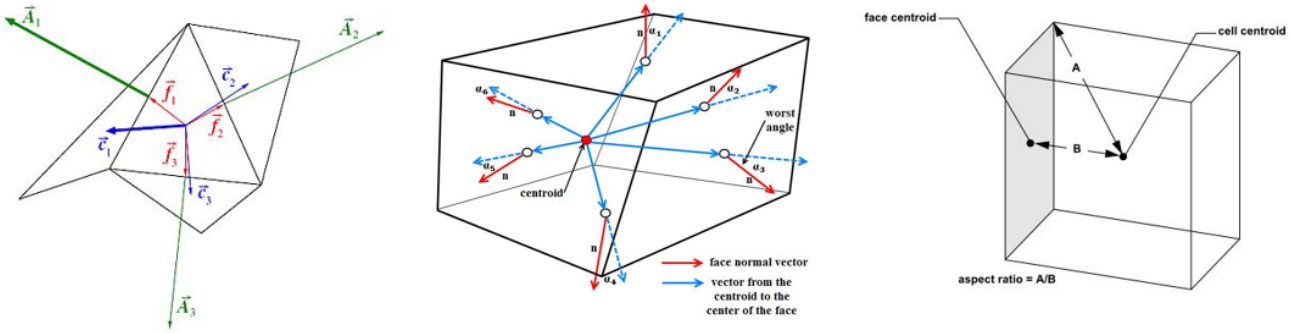

Figure 4.11: Vectors used to compute orthogonal quality, skewness and aspect ratio of a cell respectively from left to the right[51]

Based on the checking result from ICEM CFD, as shown in Fig. 4.12, the minimum orthogonal quality is 0.25, which is slightly better than those of the quality and determinant metrics. Yet the overall orthogonal quality measure has a similar distribution of good quality cells which mostly above 0.5 for 99.998 % of the total cells.

The next measure is skew. It calculates the maximum skewness of an element. Since it is normalized, one is defined as an ideal element, while 0 is the worst. For a hexahedral element, the skewness is calculated from the angle between the six face normals and the vector defined by the center of the face and the centroid of the hexahedron, as clearly drawn in Fig. 4.11.

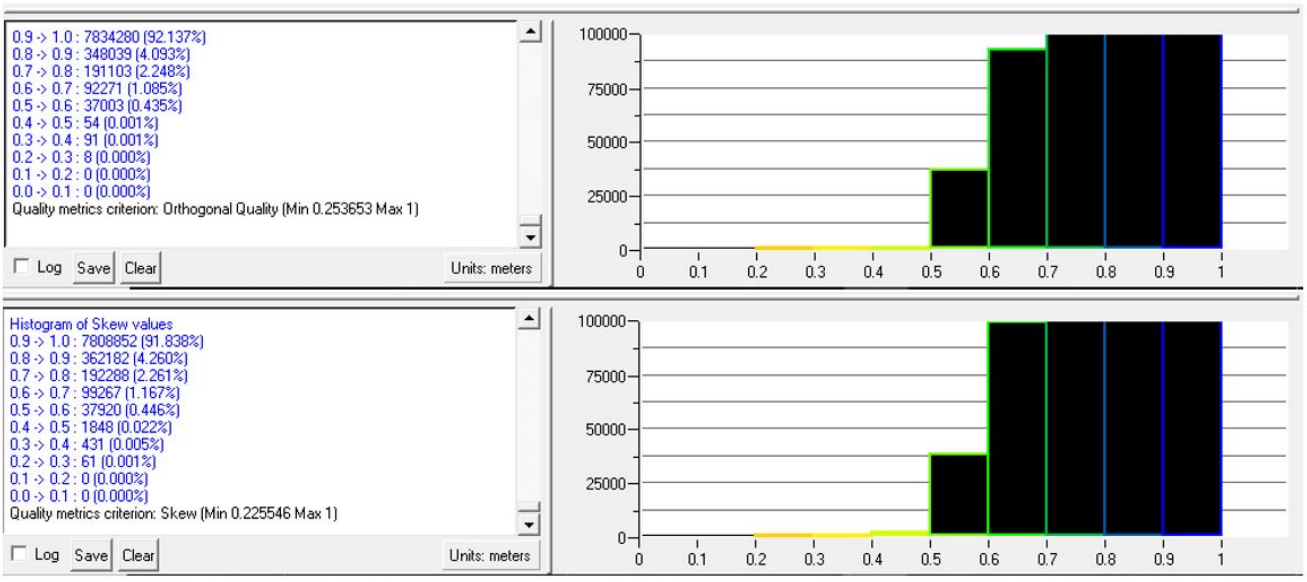

Figure 4.12: Orthogonal quality and skewness check histogram

Based on Fig. 4.12, skewness quality is slightly worse than those of other parameters where the elements on the range of 0.2-0.5 are bigger. The reason for this is possibly because of the quarter geometry that was used. On the quarter geometry, the block shape on the main body cannot be a standard cube, which has 90^o for each node. Instead, some adjustment is required for fitting the block up with four vertices in a quarter geometry which only built by three sides.

The last quality metric used on the present work was aspect ratio (used in Fluent). It is calculated as the maximum value ratio to the minimum value of the normal distances between the cell centroid and face centroid (calculated as a dot product of the distance vector and face normal and the distances between the cell centroid and nodes). The illustration is shown in Fig. 4.11. For instance, for a unit of a cube, the maximum distance is 0.866, and the minimum is 0.5. Thus the standard aspect ratio is 1.732.

Fig. 4.13 shows the aspect ratio of the mesh created. The maximum aspect ratio is on the range of 19.75-21.94 though it only comprises a small number of elements (0.008 %). Overall, it can be concluded that the majority of the element lies in the range of 0-11 (97 %). In common practice, the maximum value of aspect ratio on the scale of 18-20 is generally acceptable.

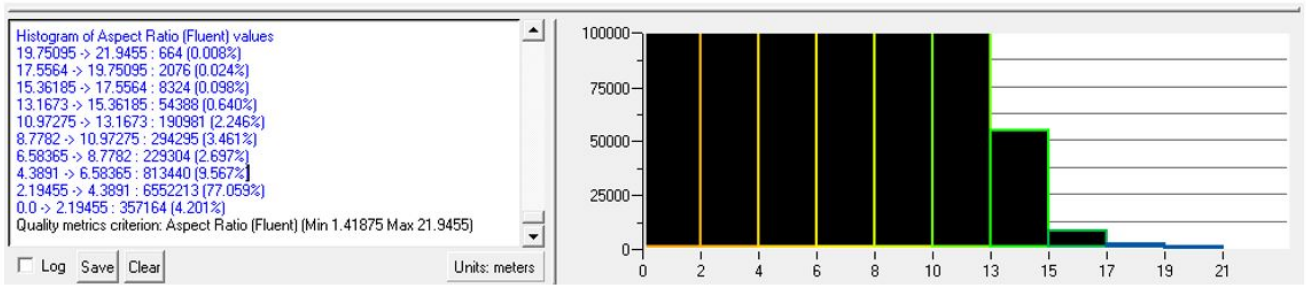

Figure 4.13: Aspect ratio check histogram

2D mesh quality check is not shown here for the brevity since, as expected, due to the much simpler geometry, the mesh quality for all of the criteria will always be far better than 3D.

4.3 Solver Setup

In principle, all the solver setup was clearly detailed on ANSYS Fluent User's Guide [82] and ANSYS Fluent Tutorial Guide [83], but some critical review and notes will be provided on this part of the subchapter.

4.3.1 Pressure based vs density based

There are two primary solver type used in Fluent, pressure-based, and density-based. Initially, the pressure-based solution is used to handle low-speed incompressible flows, whereas the density-based solution primarily used for high-speed compressible flows. Recently, however, both approaches have been modified to address a significant number of flow and process conditions beyond their conventional or original purpose.

The velocity field from the momentum equations is obtained in both systems. In the density-based solver, the density field is obtained from the continuity equation, while the pressure field is calculated from the equation of state. On the pressure-based solver, the pressure field is derived by resolving a pressure or pressure correction equation obtained by modifying continuity and momentum equations. ANSYS Fluent solves the governing integral equations for the conservation of mass and momentum, as well as energy and other scalar forms, such as turbulence and chemical species in both approaches. Both methods also used the control-volume technique.

Referring to ANSYS theoretical guidance [45], multiphase simulation, in general, can be handled by both pressure-based and density-based. In solid-gas fluidized bed simulation, particularly, the fluid mainly consists of incompressible bed material (corundum, 60 %v), and some of the compressible fluid (air, 40 %v) makes the decision of solver selection a bit complicated. However, referring to the fluid flow under the low-speed condition and there are many specific cases in the multiphase flow, which can only be managed by the pressure-based solver mentioned in the manual, in the present study, a pressure-based solution is employed.

4.3.2 Model selection

Multiphase model
There are three different multiphase Euler-Euler models available for ANSYS Fluent: the volume of void (VOF) model, the mixture model, and the Eulerian model. Out of three different models, the Eulerian model is the most complex multiphase model where it solves a set of n momentum and continuity equation for each phase. It is also explicitly mentioned that for the fluidized bed simulation involve granular flow, the Eulerian model is the best option in general.

There is some more recommendation on choosing the model based on the distribution of particle, interphase drag law, and computational issue. In the case with a wide distribution of particle / dispersed phase, the mixture model is preferable. While for the concentrated dispersed phase in the domain, the Eulerian model should be used. In terms of the drag law, if the drag model applicable for the Fluent system is available, the Eulerian model could give a more accurate result.

Furthermore, the mixing model can be a safer alternative to solve a more simple problem, which requires less computational energy. It tackles a smaller number of equations than the Eulerian model. The Eulerian model is a better choice if accuracy is more critical than computational resources. Nevertheless, note that the Eulerian model's complexity can make it less computer-stable than the mixture model.

Based on the recommendations as mentioned above, the Eulerian model was selected for the present work. There are three main reasons for this choice: the bubbling fluidized bed will have a concentrated particle region in the domain, the default gidaspow and syamlal drag model available on the system, and more emphasis is given on the accuracy of the simulation result.

Drag model
As mentioned earlier, the drag model is critical in determining the gas-solid interaction in terms of hydrodynamic behavior of the fluidized bed. There are three drag models used in the present work: Gidaspow [52], adjusted Syamlal O'Brien [53], and EMMS [28]. First of all, Gidaspow, a combination of Wen and Yu and Ergun drag model, is used because it is the simplest drag model available and the one of the recommended drag model for dense fluidized bed simulation on the Fluent [45].

Since there is no drag model on its original form that can precisely depict the actual phenomena [71], a modification of the drag model is required. In the more advanced level, the adjusted Syamlal O'Brien model enhanced their model by replacing the constant coefficient of 0.8 and 2.65 with the parameters that can be modified based on the fluid flow properties and expected minimum fluidization velocity. By doing so, they overcome the tendency to under/over predict bed expansion, for instance. In Fluent, this drag model also available at the default. Only

velocity and voidage at minimum fluidization condition need to be inserted.

The last one, the EMMS model, is the only heterogeneous model out of three drag models employed. As discussed earlier, this drag model takes into account bubbles existences that caused heterogeneity and turbulence in the fluidized bed model. This drag model is expected to have the closest result with the experimental data in term of bubbles and voidage behavior. Since it is not directly available on Fluent, a user-defined function (UDF) is needed to implement this drag model.

Turbulence model
According to Zhong et al.[23], there are two primary turbulent models used in DPRS like bubbling fluidized bed: a k-ϵ model which is based on Reynolds-averages Navier-Stokes equation (RANS) and large eddy simulation (LES) model. Though LES has higher accuracy than RANS, k-ϵ is more frequently used because it is less computationally demanding and generally implemented for practical engineering simulation.

There are also three different k-ϵ turbulence models: standard, RNG, and realizable. The latest one, a realizable model, is consistent with the physics of the turbulent flows, which implies that the model satisfies certain mathematical constraints on the Reynolds stresses. In contrast, none of the standard and RNG model is realizable. This is because the realizable model comprises a better formulation for the turbulent viscosity, and a modified dissipation rate of transport equation has been derived from the exact transport equation of the mean-square vorticity fluctuation. Hence, at present work, the realizable k-ϵ model is employed.

Radiation model
There are five different radiative transfer models in ANSYS Fluent: Rosseland, P1, Discrete Transfer radiation model (DTRM), Surface to Surface (S2S), and Discrete ordinate (DO). However, only two models are suggested from the manual for handling particulate flow, such as granular existence in the present bubbling fluidized bed: P1 and DO.

P1, the first-order equation with spherical harmonics, assumes that the radiative transfer equation (RTE) is a diffusion equation, thus less computationally demanding. It works well with the large optical thickness (>3) and isotropic radiation but has a limitation for the thin optical mediums. It also tends to overpredict the localized radiative heat source and might lose its accuracy for depending on the geometry's complexity.

The DO is the most precise differential method, but in addition to the spatial discretization of CFD, it requires an angular discretization as well as [84]. It also covers a wide variety of optical thicknesses and solving the problem from the surface to surface radiation to participating in radiation in combustion. However, for a fine angular discretization problem, the computational resources requirement could be costly.

Thus, in the present work, both P1 and DO models will be used. The computational cost versus accurateness will become the primary concern in determining the best solution.

4.3.3 Material selection

The material part in Fluent has two different types of material, and those are fluid and solid. According to ANSYS Guides [83], in TFM simulation, both solid and gas should be put on fluid type material. On the other hand, the solid type is typically used on the heat transfer simulation where the solid thickness of particular material is not zero.

The summary of material properties employed in the simulation is listed in Table 4.2. Some of them are constant values, while others are variables as a function of temperature or voidage inside the bed and introduced via the user-defined function (UDF). The variable defined as UDF will be explained in detail in the Appendix and will be finally incorporated in the simulation through a "compiled" mode.

4.3.4 Zone and boundary condition

Cell zone and boundary conditions are a very critical component of the computational fluid dynamic (CFD) simulation. Through this, the flow and thermal variables on the boundary of the physical model will be determined. The cell zone only consists of solid and fluid type. A fluid zone is a cell category that solves all active equations. While the solid zone is a category of cells for which only the problem of heat conduction will be solved, and no flow equations are solved. Since heat conduction through the wall material is not the primary interest in the present work, only one fluid zone that contains flow dynamics was used.

The selection of boundary conditions is pretty much straightforward for both 2D and 3D cases. The most critical consideration would be about the determination of flow inlet and outlet. In the present work, the available primary

Table 4.2: Material properties of corundum particle and air used in hydrodynamic and heat transfer simulation

	Hydrodynamic		Heat Transfer	
	Air	**Corundum**	**Air**	**Corundum**
Density (ρ)	0.4043 kg/m^3 (600^{o}C)	3950 kg/m^3	UDF [69]	3950 kg/m^3
Specific Heat (Cp)	-	-	1115 J/kgK	1088 J/kgK
Particle diameter (d_p)	-	496 μm	-	496 μm
Specific Heat (Cp)	-	-	1115 J/kgK	1088 J/kgK
Thermal Cond. (k_s)	-	-	UDF (Eq.27)	UDF (Eq.28)
Viscosity (μ)	3.825 e-05 kg/ms (600^{o}C)	KTGF (Eq.92)	UDF [69]	KTGF (Eq.92)
Absorption Coeff. (α_s)	-	-	0	UDF (Eq.53)
Scattering Coeff. (σ_s)	-	-	0	UDF (Eq.52)
Refractive Index (n)	-	-	1	1.76

data is the air's mass flow rate as a fluidization agent. Hence both velocity inlet and mass flow inlet boundaries could remain the two options. However, due to the fixed inlet temperature for both hydrodynamic and heat transfer simulation, lack of energy change, and constant density on the boundary, the velocity inlet boundary condition is used for the whole simulation.

Another critical boundary condition selection is the flow outlet, which is between the pressure outlet or outflow. Since the simulated pilot plant operates under atmospheric pressure conditions, the pressure on the reactor outlet can be defined, hence the pressure outlet boundary condition. Additionally, according to ANSYS Guides [82], using pressure outlet instead of outflow boundary condition will improve convergency, especially when the backflow occurs during iteration.

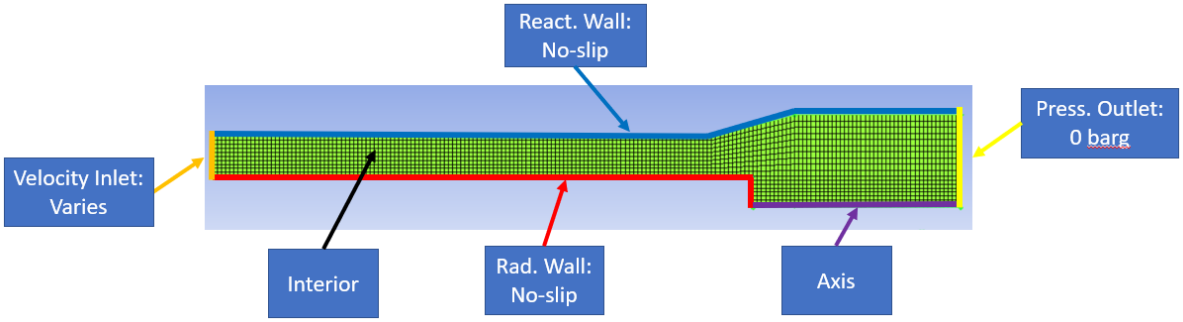

Figure 4.14: Hydrodynamic 2D boundary conditions

Besides flow inlet and outlet boundary conditions, there are some other boundary limits such as the wall, repeating, pole boundaries, and internal face boundaries. In the present work, both 2D and 3D simulations were performed, and they have slight differences in the boundary conditions used. The illustration of these boundary conditions for both system are shown in Figure 4.14 and 4.16.

The boundary condition on the 2D modeling domain consists of the velocity inlet, pressure outlet, radiant tube wall, reactor wall, axis, and interior wall, as shown in Figure 4.14. There is a unique axis boundary because the 2D axisymmetric simulation was performed. It can represent the whole volume of the reactor but minus the change in the circumferential direction. By implementing this concept, the axial center of the reactor should align with the x-axis. That's the reason why the 2D domain is lying horizontally instead of vertically.

The input value on the 2D hydrodynamic simulation before running is only air velocity. Air superficial velocity can be varied following the experimental plan to examine the hydrodynamics for each air velocity introduced to the system while the corundum velocity is kept zero at initial condition. Another input value is only about the wall friction condition, which is assumed to have a no-slip boundary condition in the present work. The detailed boundary condition is shown in Figure 4.14

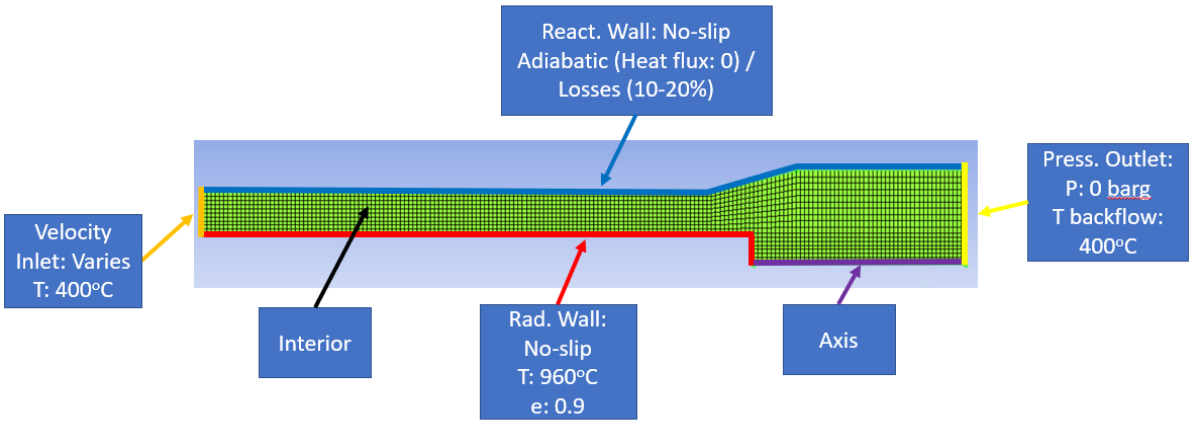

Figure 4.15: Heat transfer 2D boundary conditions

In the case of heat transfer simulation, besides inputting the superficial air velocity, the air temperature should also be involved. Another critical parameter is the reactor wall boundary that should be set either adiabatic or with certain losses by adjusting the heat flux input. Finally, the radiant burner wall boundary that supplies heat through a constant temperature value. The detailed boundary condition is shown in Figure 4.15.

In the 3D modeling domain, there is a more detailed nozzle distributor design to represent the more realistic simulation result. The boundary condition consists of velocity inlet, nozzle wall, pressure outlet, radiant burner wall, reactor wall, and symmetry. Within this model, the velocity inlet is introduced in the tuyere nozzle distributor outlet. The volume occupied by the nozzle wall was also taken into account by involving the nozzle wall boundary. Furthermore, to perform the efficient simulation, only a quarter of reactor volume is built, and symmetry boundary conditions were added to manage the missing adjacent domain. The detailed boundary condition is shown in Figure 4.16.

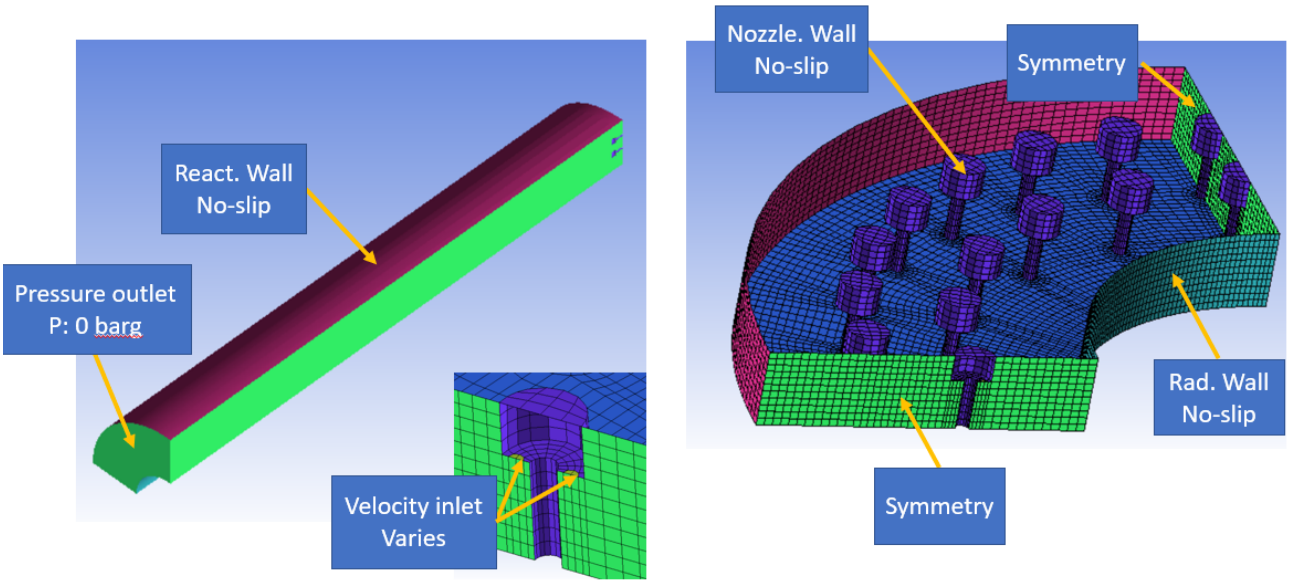

Figure 4.16: 3D boundary conditions

4.3.5 Method and controls

The numerical methods and controls are very critical to determine the accuracy and convergence of simulation. The solution methods consist of pressure-velocity coupling, spatial discretization, and transient formulation. The PC Simple or segregated pressure velocity coupling method is selected so that the memory requirement can be reduced, and simulation can be running on low computational specification. The first order discretization method for all equations was employed on the present work to ensure the complex multiphase simulation problem's stability. A

higher-order can be incorporated on a later stage, in order to improve the solution's accuracy. The summary of the methods is shown in Table 4.3.

The stability and convergence rate of the iterative process is regulated by over and under relaxation factors. Under-relaxation value improves stability, while over-relaxation value enhances the convergence. Based on ANSYS theoretical guide [51], it is prevalent to use a low under relaxation factor in the multiphase simulation since the stability is the biggest challenge. With a small under-relaxation factor, more iterations will be required to achieve the converged result. After performing hundreds of simulations and testing with various combinations of the under relaxation factors to enhance the stability and solution convergence, the determined values are summarized in Table 4.3.

Table 4.3: Solution methods and controls on the present IHBFB-SR hydrodynamic and heat transfer simulation

Solution Methods		**Solution Controls**	
Pressure-Velocity Coupling	PC SIMPLE	**Pressure**	0.1
Spatial discretization:		**Density**	1
Gradient	Least Squares Cell Based	**Body Forces**	1
Momentum	First Order Upwind	**Momentum**	0.1
Volume Fraction	First Order Upwind	**Volume Fraction**	0.2
Turbulent Kinetic Energy	First Order Upwind	**Granular Temperature**	0.1
Turbulent Dissipation Rate	First Order Upwind	**Turbulent Kinetic Energy**	0.8
Energy	First Order Upwind	**Turbulent Dissipation Rate**	0.8
Discrete Ordinates	First Order Upwind	**Turbulent Viscosity**	1
Transient Formulation	First Order Implicit	**Energy**	1
		Discrete Ordinates	1

4.3.6 Report definition and monitor

In ANSYS Fluent, it is possible to visualize the flow field at some parts of the domain. The domain portions are called surfaces, and they could be generated in several ways. These surfaces can be used to display vectors, contours, and so on or be based on producing the XY plot. For each boundary zone in the domain, a surface will be created automatically by ANSYS Fluent. All of these setups can be done via the report definition tab section on the solution configuration.

Since the simulation is conducted in transient mode, the behavior of the time-dependent variables is very crucial. There are four variables observed during the simulation of the hydrodynamic: bed height, pressure drop, axial voidage, and radial voidage, as listed in Table 4.4. All the variables are obtained based on the area-weighted average method for each surface. The simulated bed height can be determined by measuring the solid fraction nearby the expected height. There are 23 surfaces made in the present work every 5 mm of height, 12 surface above expected height, and 11 surfaces below.

For the pressure drop, two surfaces represent the actual pressure differential sensor location, and then the differences are noted as the pressure drop of the bed. The final variable measures on the hydrodynamic simulation are radial and axial voidage. The surfaces are arranged, as shown in Table 4.4. In the axial voidage measurement, the surface started from the very bottom of the bed until some points above the fluidization height. The radial voidage is measured at a certain height above the nozzle distributor, which is deemed already at a well-developed flow condition.

Table 4.4: Hydrodynamic's report definition setup on the Fluent by adding lines and points surfaces

Variables	**Variable in Fluent**	**Surface Type**	**Remark**
Bed Height	Solid volume fraction	Line	23 surfaces every 5 mm height
Pressure Drop	Static pressure	Line	2 surfaces at 0.265 and 0.975 m height
Axial voidage	Solid volume fraction	Line	24 surfaces every 21 mm height
Radial voidage	Solid volume fraction	Point	11 surfaces every 9.65 mm at 0.265 m height

In the heat transfer case, there are eight variables monitored: temperature on the sensors, axial temperature, radial temperature, absorption and scattering coefficient, thermal conductivity, radiative, and total heat flux, as shown in Table 4.5. The very first variable is the temperature of the five existing sensors on the actual reactor design. It was arranged by making surfaces at five different heights, and the measurement can somehow be compared with the experimental result. Axial and radial temperature measurements used the same surfaces as for the voidage to relate the temperature and voidage profile.

Two radiative parameters of the bed: absorption and scattering coefficient are also recorded. These two variables were measured at the same height with the first pressure differential location, at 0.265 m above nozzle distributor. Then, the effective thermal conductivity, which is a function of the voidage, is also observed at the same height of 0.265 m. Finally, the most critical variable of the heat transfer simulation is that radiative, and total heat flux is also examined, which will correlate with the average heat transfer coefficient. These variables were obtained directly from the boundary of the radiant tub wall without any surface creation.

Table 4.5: Heat transfer's report definition setup on the Fluent by adding lines and points surfaces

Variables	**Variable in Fluent**	**Surface Type**	**Remark**
Temperature Sensors	Corundum Temperature	Line	5 surfaces in 5 different heights
Axial Temp.	Corundum Temperature	Line	24 surfaces every 21 mm height
Radial Temp.	Corundum Temperature	Points	11 surfaces every 9.65 mm at 0.265 m height
Absorption Coeff.	Absorption Coeff. Mixture	Line	1 surface at 0.265 m height
Scattering Coeff.	Scattering Coeff. Mixture	Line	1 surface at 0.265 m height
Thermal Cond.	Thermal Cond. Corundum	Line	1 surface at 0.265 m height
Radiative Heat Flux	Radiative Heat Transfer	Boundary	Radiant wall boundary surface
Total Heat Flux	Total Heat Transfer	Boundary	Radiant wall boundary surface

Lastly, the criteria of the residual convergence are defined, as shown in Table 4.6. This is one of the most critical aspects that govern the simulation operation. If it is set too low, the solution will hardly converge, while if set too high the solution will converge but with less accuracy. By default, 10^{-3} is deemed sufficient for most of the equations. Continuity equation residual basically is set according to the same criteria, but a further decrease to 10^{-5} is recommended to achieve more precise results. For the energy and radiative transfer equation, 10^{-6} is the standard practice criteria.

Table 4.6: Convergence absolute criteria for all equations used

Residuals	**Convergence Criteria**
continuity	1.00E-05
u-a	1.00E-03
u-corr	1.00E-03
v-air	1.00E-03
v-corr	1.00E-03
energy-p1	1.00E-06
energy-p2	1.00E-06
k-air	1.00E-03
k-corr	1.00E-03
eps-air	1.00E-03
eps-corr	1.00E-03
do-intensity	1.00E-06
vf-corr	1.00E-03

5 Results and Discussions

5.1 Grid independency test

As fas as the computation resources are concerned, the coarser grid size is always the preferable choice for the researcher to perform the numerical simulation. However, this always is a trade-off with the accuracy and precision of the result. Grid independency test is commonly performed in the context of the numerical simulation method to ensure that the accuracy of the result is not significantly far once the grid gets coarser. According to Cloete et al. [85], the solution can be considered grid-independent for a cell size smaller than 1 mm. This cannot be done in the present work due to the diameter of the particle size used being 0.496 mm. As emphasized by Enwald et al. [86], the cell size has to be significantly larger than the particle diameter on the hydrodynamic simulation.

To check grid independency data, the pressure drop and bed height will be examined to check the sensitivity along with the coarser grid size used. Based on this also, the expected simulation time to achieve a steady result will be determined. The grid size used was 1.5, 2.5, 5, 7.5, and 10 mm (3, 5, 10, 15, and 20 times particle's diameter respectively). After doing the first trial simulation, the expected rough bed height will be around 0.42 m. Then ten measurement points from 0.41 m to 0.45 m with 0.005 (0.5cm) increment was set up to have a higher accuracy on detecting time mean average bed height.

The simulation was conducted for 5 s simulation for all of the different grid size simulations. The time-dependent profile for the pressure drop across the bed is shown in Figure 5.1. As can be seen that, with the 5s long simulation, the fluidization seems to reach it's steady-state indicated by the regular fluctuation of pressure drop with relatively stable value. Even 2.5s simulation deemed to be sufficient, which will then be used for the next following simulation.

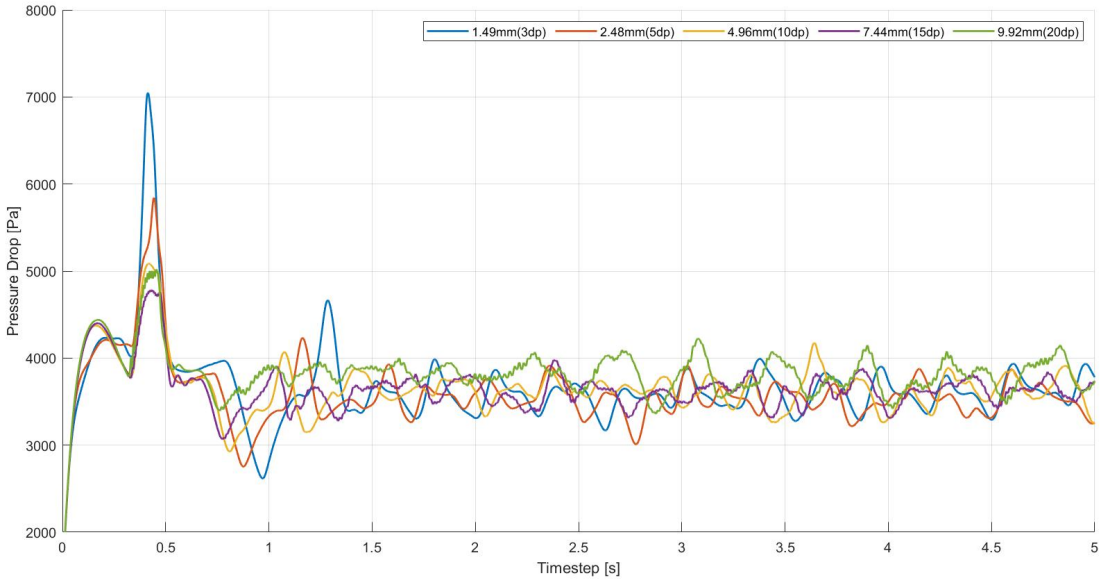

Figure 5.1: Time-dependant pressure drop data across the bed for five different grid size using Gidaspow drag model and 0.19 m/s superficial gas velocity

The following Figure 5.2 shows the example of bed fluidization height determination for 3dp grid size referring to the solid volume fraction data on ten measurement points. The time-averaged data was obtained for each measurement point based on the area-weighted average calculation ranging from 2-5 s time-dependent data on the steady fluctuation range. The 10 % threshold, as proposed by Cloete et al. [87] was applied to determine the approximate bed height determination. The solid fraction below the threshold limit is indicated by the dashed line to show a visual representation of the insignificant value above a certain height of the bed. Based on this figure, it can be clearly demonstrated that the fluidization height is 0.43 m with 5 mm margin of error.

Finally, the pressure drop and fluidization height of the bed based on the simulation for five different grid size was plotted, as displayed in Figure 5.3. The 5 mm margin of bed expansion is also included to represent the margin of error. As can be seen in that figure, there was a fluctuation of the variables measured along with the change of grid size used. The value obtained was similar for most of the cell size except for a 10 mm grid size, going far beyond the average value. Based on this observation, the cell size from 2.5 mm or 5dp is defined as the default size to perform the following overall simulation.

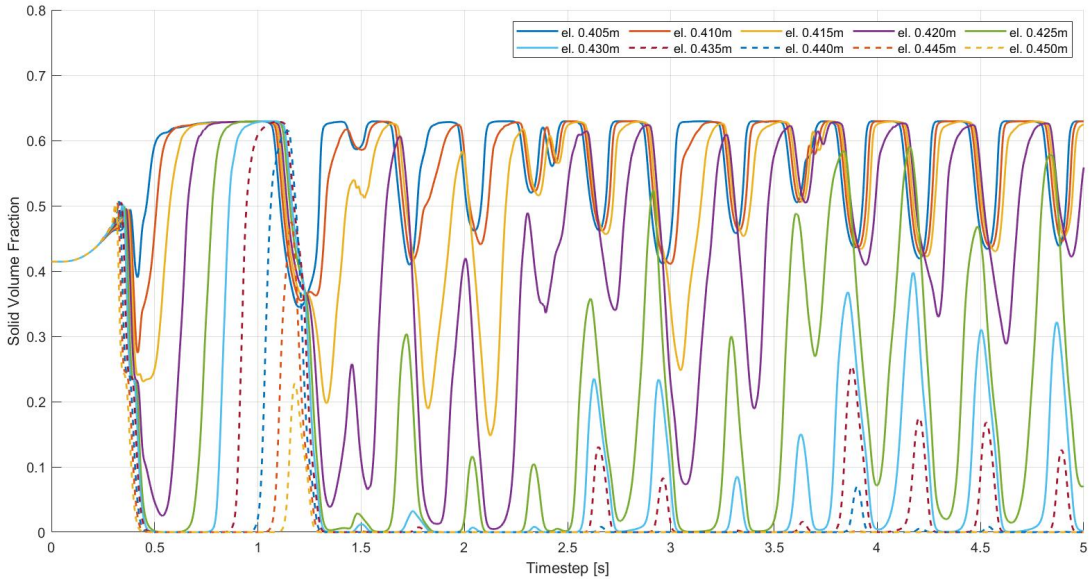

Figure 5.2: Bed height fluctuation display at 10 measurement points for 1.5 mm grid size using Gidaspow drag model and 0.19 m/s superficial gas velocity

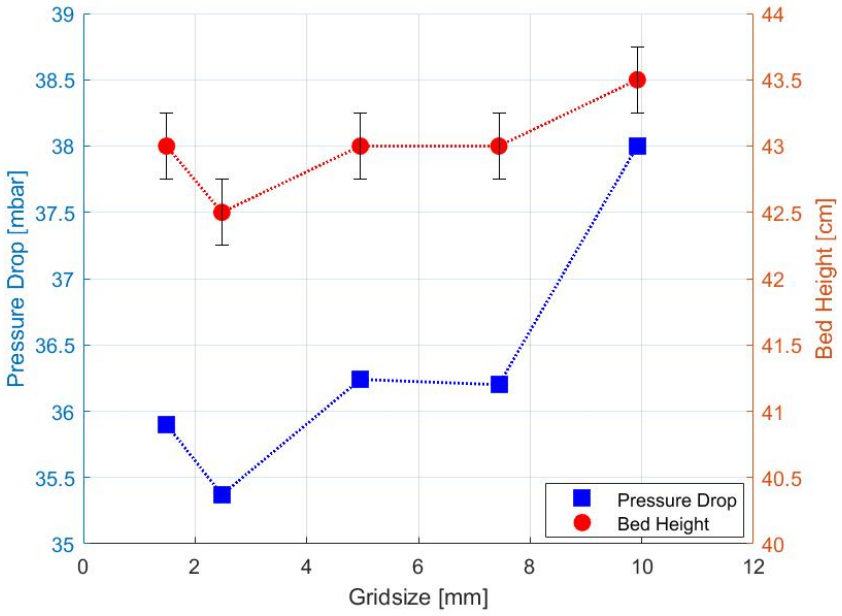

Figure 5.3: Time-averaged pressure drop and fluidization height at five different grid size based on the simulation

5.2 Minimum Fluidization Velocity

Experimental results

A key parameter for effective design, operation, and control of fluidized bed systems is the minimum fluidization velocity. The minimum velocity of fluidization depends on various factors, such as packing density, solid size, shape factor, fluidizing media viscosity, and velocity [68]. At present, minimum fluidization gas velocity for 75 kg corundum bed material loading, fluidized by air and nitrogen was examined. The experimental work was carried out on the real setup.

There are three different gas streams utilized during the fluidization of corundum inside the reactor: air (43FTC02), primary nitrogen (52FTC02), and secondary nitrogen (51FT01). Their flow rate profile over the full day of the experiment is shown in Figure 5.4. The air and primary nitrogen were entering from the windbox and flow through the tuyere nozzle distributors. This gas flow will act as a fluidizing agent. The secondary N2 flow from the side of the reactor (not through nozzle distributors) is used to keep the pressure sensors, especially the feeding system

and bunker pressurized. By doing this way, the clogging of the pressure sensors by the corundum particles can be avoided. In the case of actual gasification, this secondary nitrogen flow will prevent the produced gases from escaping through the pressure sensor connections.

In the beginning, the maximum gas flow possible, with around 22 kg/h of air and 25.8 kg/h of primary nitrogen, was employed to ensure intense fluidization and thus improve heat transfer. This method will accelerate the reactor's heating process and reach the steady-state faster. The primary nitrogen is also decreased slowly over time until it is completely absent in the reactor. Air, as the primary fluidizing agent, now takes control of bed fluidization. The decrease and the increase in the air mass flowrate determine the bed behavior and will be utilized for the minimum fluidization velocity experiment on the following part.

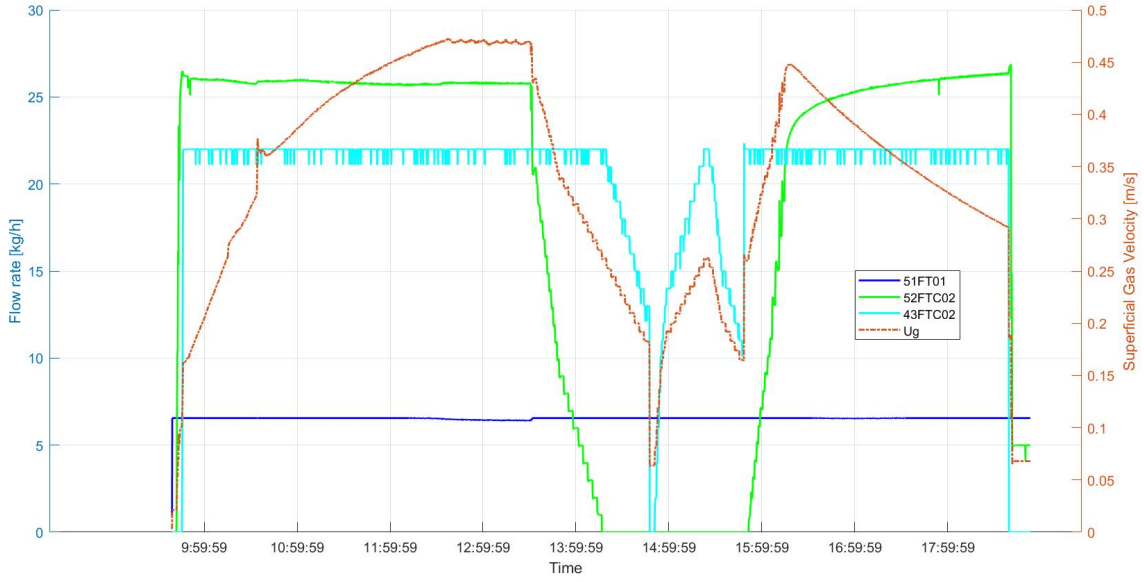

Figure 5.4: Gas mas flow rate and superficial velocity profile versus time during the experiment of 75 kg corundum loading

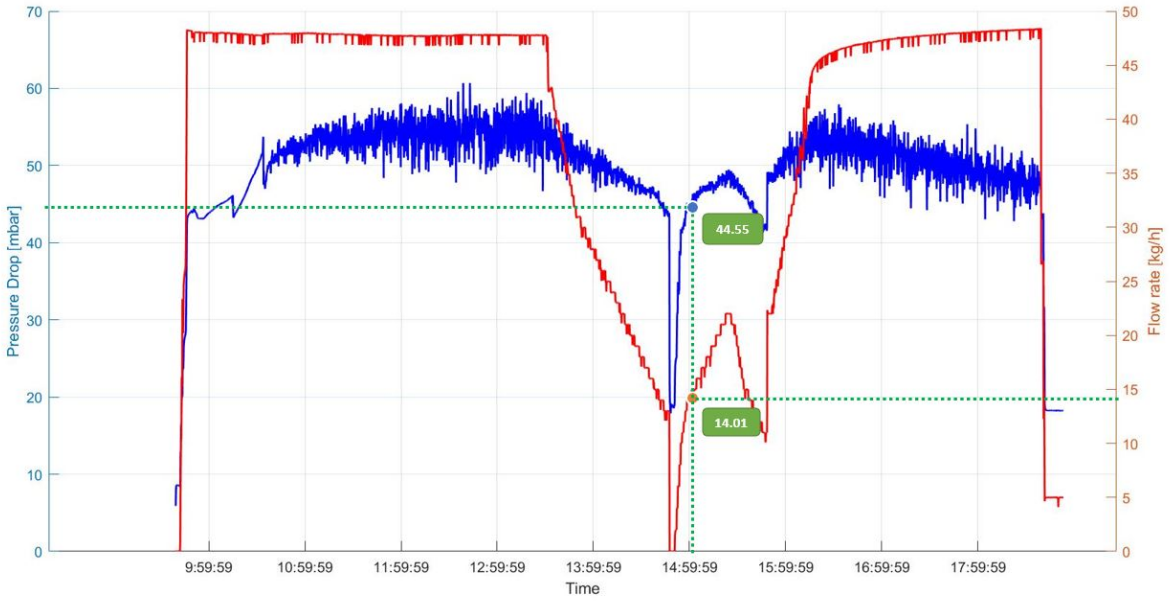

Figure 5.5: Instantaneous pressure drop and air flowrate profile against time during the 75 kg corundum loading experiment with indicative estimated minimum fluidization point

In Figure 5.5, the instantaneous pressure drop variation versus gas flow rate is showed. At the gas flow rate of 48 kg/h, the bed material was completely fluidized, referring to the approximated constant pressure difference across the bed with insignificant fluctuation. Slowly, once the flow rate is decreased, the pressure difference became smaller. The primary nitrogen flow first decreased until it entirely dismissed from the system. Then after that, the air remains as the main fluidization agent. As the air flowrate decreasing, at a certain point where the airflow rate is below 14 kg/h, the corundum stopped being fluidized, indicating a significant drop in the pressure. Once after flow rate is increased back, the bed started to re-fluidized. The condition where the bed is just fluidized is also called incipient or minimum fluidization. It is roughly noted that this condition appeared at a 14 kg/h gas flow rate and 44.55 mbar of the pressure drop, as indicated in Figure 5.5.

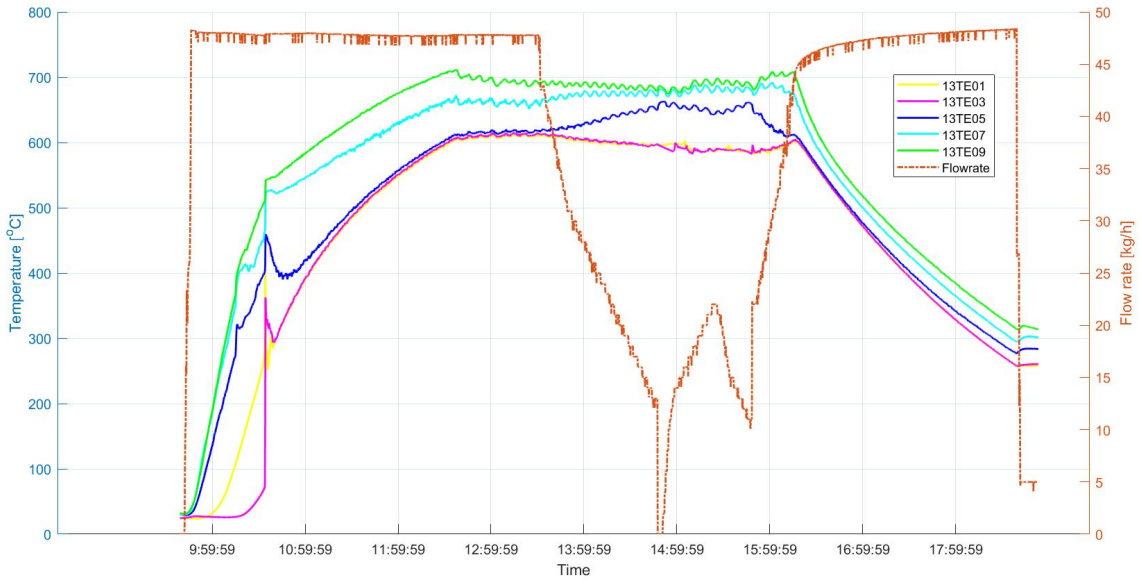

Figure 5.6: Bed temperature and gas velocity profile versus time during the experiment of 75 kg corrundum loading

The minimum fluidization condition became more apparent by referring to the bed temperature profile during the experiment (Figure 5.6). As can be seen at the beginning, as the fluidization started to occur, the temperature measurement of 13TE01 and 13TE03 was coupled together and showing a similar value. It can be evident that fluidization was happening, which means the stagnant corundum particle was transformed into a fluidlike state with the improved solid-gas interaction and an excellent heat transfer. This fluidization makes the bed has an almost uniform temperature. It can also be noted that the third thermocouple 13TE05 was joining the other two after a certain point, indicating the increase in the bed temperature and thus increase the flow rate of the fluidization agent. Based on the thermocouples involved during the experiment, the bed height can be roughly estimated from the thermocouples' elevation points. After the primary nitrogen supply was gradually decreased and completely dismissed from the reactor, the temperature measurement of 13TE05 was detached from the fluidization. This can be understood since some of the fluidization agents (nitrogen) disappeared from the system, and made the fluidization height suddenly decreased to the range of 13TE01 and 13TE03 elevation.

Along with the decrease of gas flow rate below the minimum fluidization state, the temperature measurement becomes separated between 13TE01 and 13TE03 indicating the bed drop and fluidization slowly stopped. Once the velocity was increased, the two thermocouples were started to re-couple back and showing a similar temperature again. This indicator represents the minimum fluidization condition and is shown clearly in a closer look at Figure 5.7.

In order to verify further the experimental result for the estimated value of minimum fluidization velocity and get the initial voidage at minimum fluidization condition under high-temperature operation, Subramani et al. [69] found quite simple correlation referring to 80 experimental values from various sources as mentioned on Eq. 123-126. This correlation is applicable for Geldart B particles (40 μm $< d_p <$ 500 μm), which is relevant for the corundum size used on the present work of 496 μm and temperature above ambient condition. The minimum fluidization velocity obtained based on the those equations is 0.165 m/s, which is correlated with a 17 kg/h flow rate is pretty much above the value obtained from the experiment. However, this indicates roughly the expected range of 14-17 kg/h as the minimum fluidization.

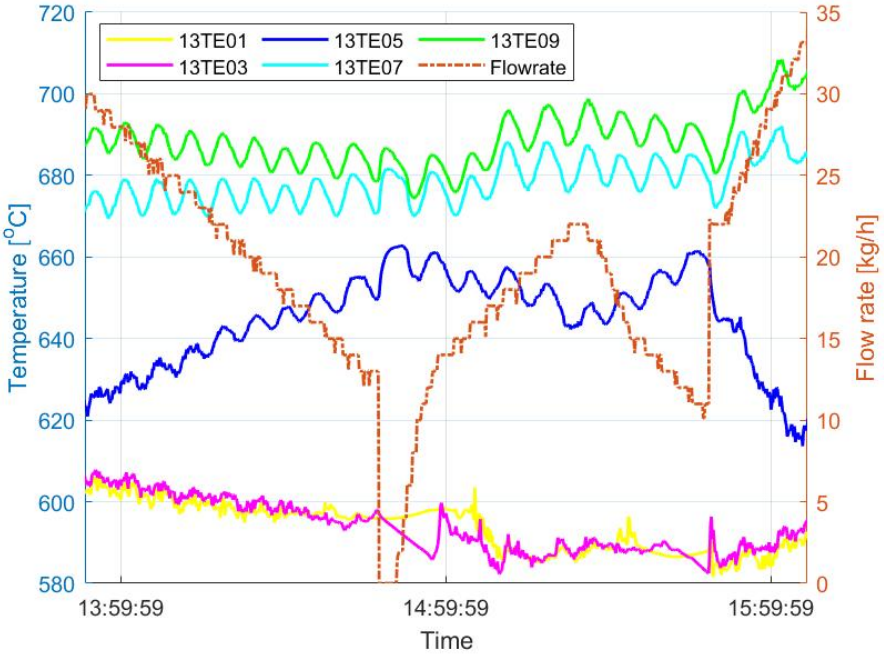

Figure 5.7: Minimum fluidization observation based on the thermocouples coupling-decoupling behavior

For the voidage under the minimum fluidization, the relevant correlation mentioned by Subramani et al. yields 0.47. Since this voidage is directly correlated to the maximum solid fraction [28], it means the maximum packing limit will be 0.53. After some investigation using the short simulation, it was found that a maximum packing limit of 0.53 does not reflect the bubbling physical behavior. It hardly produced any bubbles for higher air flowrate above the minimum fluidization condition (>30 kg/h). This can be understood since the lower the solid fraction is, the higher the bed's voidage. Thus all the air will percolate in between particles instead of forming bubbles. Referring to the expected minimum fluidization condition and its bubbles behavior, and suggested maximum packing value from Fedors et al. [60] for one uniform size of particles, a default of 0.63 maximum packing limit employed for the whole of simulation.

Pressure drop and bed expansion

Two different drag models, Gidaspow [52] and modified Syamlal [53] were used to simulate the fluidization condition for 75 kg bed material loading. The 5s simulations were performed, and the time-averaged pressure drop and bed expansion are shown in Figure 5.8. The fluidization height from the experiment has a large margin of error since there was no actual measurement. Instead, the bed's height approximation was obtained from rough estimation based on the thermocouples elevation involved in the fluidization. The experimental pressure drop referred to the average recorded data on the correlated six different gas flow rate from the experiment.

The simulated pressure drop values have a similar pattern with the one from the experiment, especially the adjusted Syamlal model, with the gradual increase with the increase of gas flowrate and become steady after the gas flowrate increase above 16 kg/hr. However, the results also demonstrated that the pressure drop and bed expansion from the simulation lies below the experimental value for both drag models. The difference is quite significant since it represents that the fluidization height only reaches the first thermocouple (13TE01) while on the experiment, it also includes the second thermocouple (13TE03).

One of the reasons for this underprediction is that the solid volume fraction resulting from the simulation is 0.6, which is closer to the maximum packing limit of 0.63 and directly affects the bed height. On the initial setup, the solid volume fraction of 0.41 was determined from the calculated bulk density. Cloete et al.[87] also discussed this under-prediction behavior of the bed expansion and pressure drop on their research as well as Ostermeier et al.[70]. Ostermeier, for instance, also has a similar condition with the present work in terms of corundum using for bed material and the particle size, which lies in Geldart B particle's category.

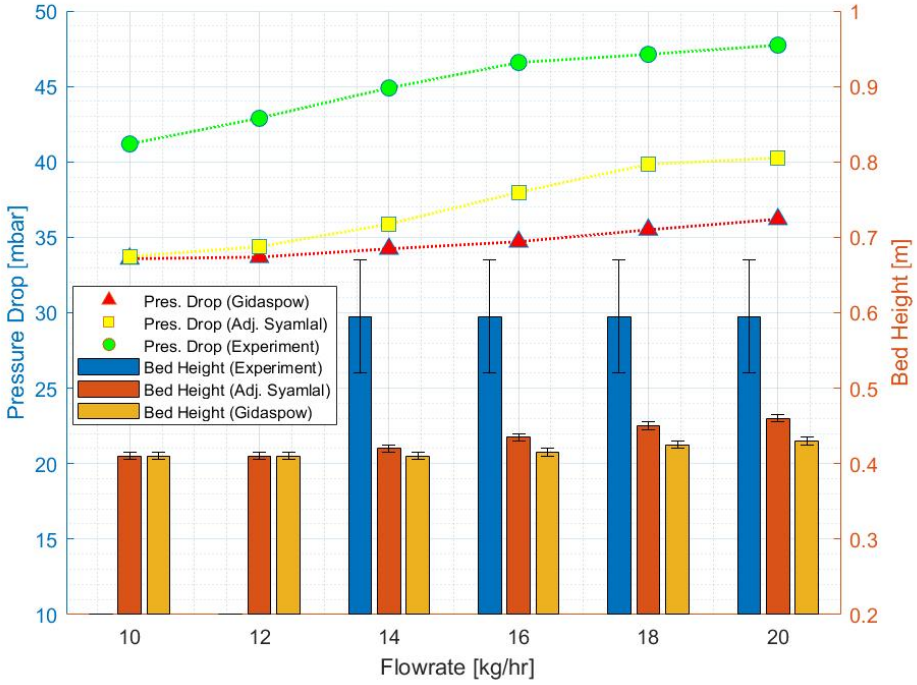

Figure 5.8: Experimental and numerical time-averaged pressure drop and bed expansion for different gas flowrate

As discussed earlier in section 3.1, Ostermeier et al.[70] demonstrated that the best pressure drop and bed expansion result could be achieved by taking into account the sphericity factor and particle size distribution (PSD) of the particle. By using Multifluid Model (MFM) which employs two different particle size, and take into account the sphericity factor on the drag model, a very close agreement with those value from the experiment can be obtained. The comparison of simulated bed averaged drag coefficient with the experiments are: 100% for MFM with $\psi = 0.82$, 72% for MFM with $\psi = 1$ and 88% for TFM with with $\psi = 0.82$. While for the strain rate obtained from KTGF: 100% for MFM with $\psi = 0.82$, 81% for MFM with $\psi = 1$ and 67% for TFM with with $\psi = 0.82$. The sphericity has a higher impact on the drag force exerted on the particles, while the number of granular phases affects the particle's strain strongly. The combination of the two effects explains the tendency of bed expansion underprediction.

The approach explained by Ostermeier et al. cannot be fastly adopted on the present work due to the complexity of the model and the limited time constraint. First, the PSD data need to be performed via the experiment. The second, involving more than one particle size in view of the numerical simulation, will add the more complex simulation which cannot be covered in the present scope of work. While the sphericity can be easily incorporated. However, at the time simulation was performed, sphericity data was not available, and put a guessed value also cannot directly justify the result. The investigation to study this sphericity effect is separately provided later in section 5.4.

At the gas flowrate below the expected minimum fluidization, there was an insignificant pressure drop difference showed by both drag models for 10 and 12 kg/h air flowrate. It is also noticeable that the bed height doesn't move appreciably between those flow rates. Compare to the pressure drop difference and bed expansion from 12 to 14 kg/h. This agrees well with Taghipour et al.[25] investigation. The discrepancy for gas flowrate below u_{mf} can be attributed to solids that are not fluidized. Thus, they are dominated by interparticle frictional forces that are not predicted by a two-fluid model for gas-solid phase simulation.

In order to verify further the minimum fluidization condition obtained from the previous simulation and calculation, another approach was proposed. It was discussed by Kunii et al.[15], for Geldart B particle, bubbles will form as soon as the gas velocity exceeds the u_{mf}. In other words, the minimum bubbling velocity approximately equal to the minimum fluidization velocity ($u_{mb} \cong u_{mf}$). Then it can be more visually observed that the u_{mf} will be roughly the velocity or flow rate where the first smooth bubbles occurred.

Resitution coeffiecient

Before presenting the bubbles simulation result, one of the critical governing parameters, such as the restitution coefficient, should be defined. It is shown that the hydrodynamics of dense gas-fluidized beds (i.e., the action of gas-bubbles) strongly depends on the amount of energy dissipated in particle-particle encounters, which is accommodated by the restitution coefficient. It is then concluded that a realistic bed dynamic on hydrodynamic model simulation could be achieved if the effect of energy dissipation due to nonideal particle-particle interaction is correctly taken into account [75].

In Figure 5.9, the simulation result of bed hydrodynamics using five different restitution coefficient is presented. The snapshot was taken at the moment of bubble eruption after 1s simulation using a 24 kg/h air flowrate. The simulation performed at the flowrate where the bubbles are expected to be rigorously developed. It can be shown that, when collisions are less ideal, where more energy dissipates due to inelastic collision, the particles are clustered tighter in the densest areas of the bed and finally resulting in the sharper contour of porosity and larger bubbles.

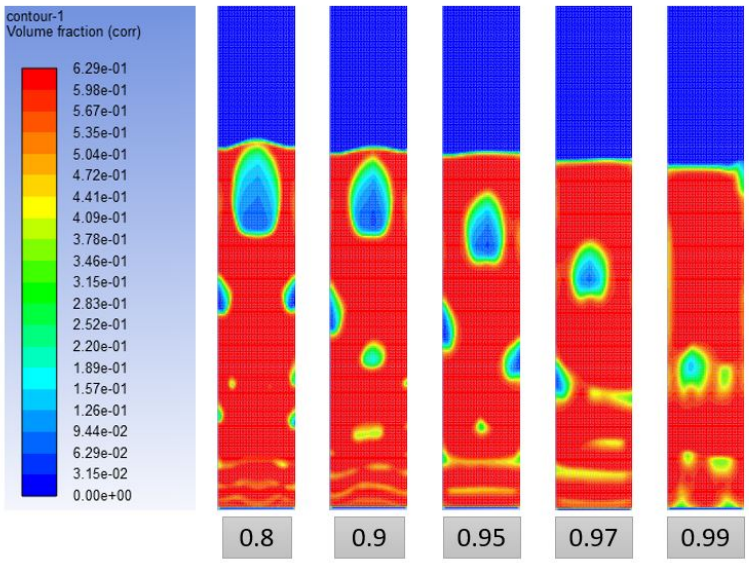

Figure 5.9: Corrundum volume fraction for various value of coefficient restitution at 24 kg/h gas flowrate using Gidaspow drag model at 1s simulation

The investigation on the time-averaged voidage for different restitution coefficient was also performed. It was found that average voidage 0.55 (not shown here for brevity) was consistently maintained during the simulation. This confirms the phenomena that, even though bubble size varies throughout the different simulation, some produce larger and fewer bubbles, some generate smaller and more bubbles, and the average voidage remains the same, which shows the change of energy dissipation behaviour.

Since no experimental data for bubbling behavior at the time of simulation was performed, the appropriate restitution coefficient was selected based on an observation of Goldschmidt et al.[75]. It was mentioned that the restitution coefficient of 0.9 shows the best of comparison between the experiment and simulation, while the too much lower coefficient would generate vigorous bubble dynamics.

2D bubble simulation

Figure 5.10 shows the solid volume fraction contour of bed simulation at various gas flowrate using Gidaspow and Modified Syamlal drag model is shown. It can be clearly displayed that the bubbles started to occur between 10-22 kg/h gas flowrate. And above this, the bubbles became bigger and bigger, rigorous, and further started to form slugging. The bubbles produced by the adjusted Syamlal model have a larger size and more distorted shape due to the bigger drag force employed, and thus bed expansion also becomes much higher.

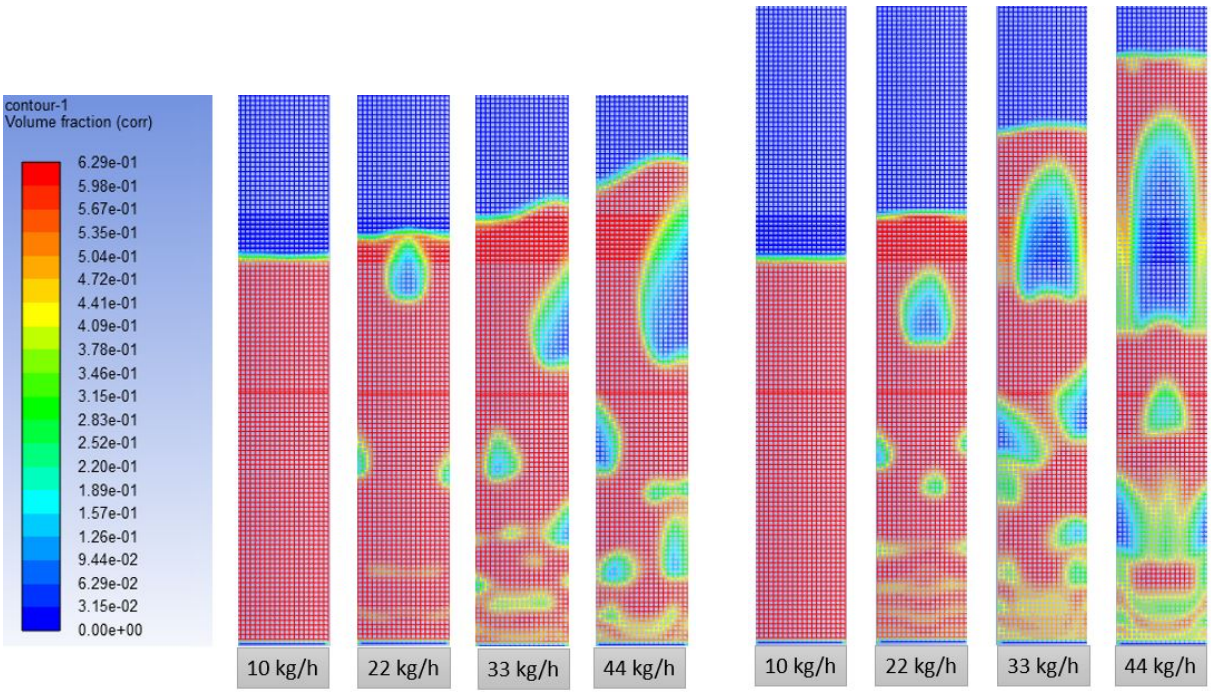

(a) Gidaspow drag model (b) Adjusted Syamlal drag model

Figure 5.10: Instantaneous solid volume fraction contour at various gas flowrate at 1s simulation time

.

In order to refine more the model solution, the bubble simulation was conducted at several gas flow rates with a smaller increment, which is between 12-18 kg/h: 12, 14, 16, and 18 kg/h. The solid volume fraction contour can be found in Figure 5.16.

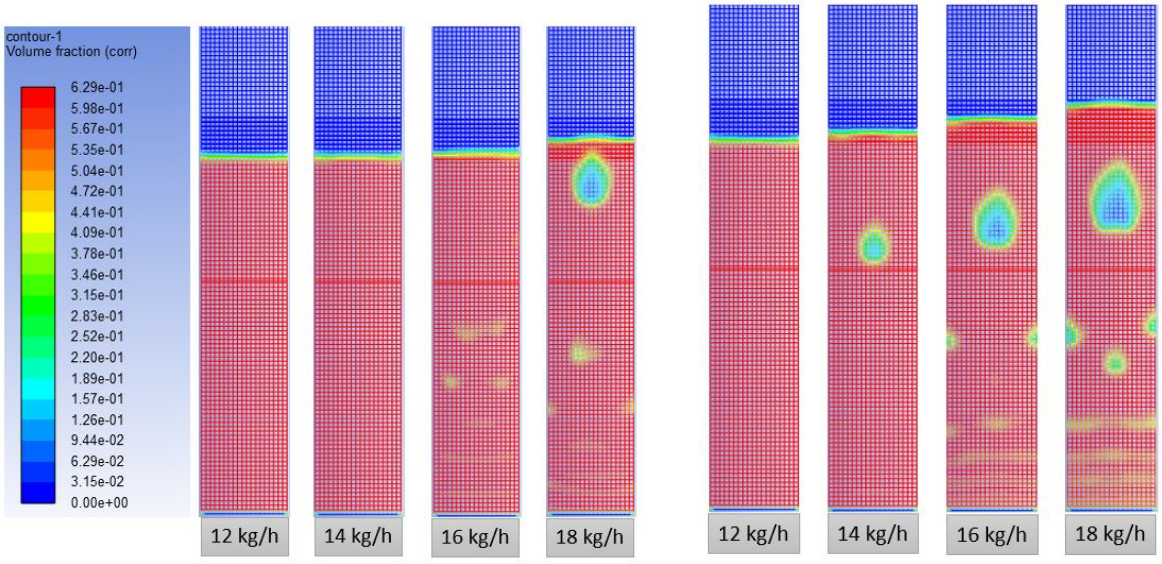

(a) Gidaspow drag model (b) Adjusted Syamlal drag model

Figure 5.11: Instantaneous 2D solid volume fraction contour at various gas flowrate at 1s simulation time

.

As can be seen, the more clearly that the gas velocity when the bed is started to generate bubbles is 18 kg/h for Gidaspow and 14 kg/hr for adjusted Syamlal. Adjusted Syamlal could produce a bubble at a much lower flow rate, thus having a lower minimum fluidization condition than Gidaspow. This is best explained by Vejahati et al.[71], as discussed in section 3.1, that presented the difference of drag coefficient from several drag models and concluded that adjusted Syamlal would predict a much higher drag coefficient results in the smaller u_{mf}. In general, these results pretty much agree with the calculation, as well as the experiment.

3D bubble simulation

The 3D results are also presented in Figure 5.12 and 5.13 to verify further the results obtained from the 2D simulation. The Gidaspow model started to produce a very fine bubble at 14 kg/h and a more solid bubble shape at 16 kg/h. In comparison, the adjusted Syamlal shows a very similar behavior with the 2D but with a more well-developed bubble at 14 kg/h. It is again lower than the one from Gidaspow for almost the same bubble size that confirms the bigger drag force exerted on the particle.

The noticeable difference between 2D and 3D in both drag models was that some bubbles produced on the wall appeared on the 2D but not in the 3D result. This was mainly because of the 2D simulation; there is no nozzle distributor included. The gas from the bottom of the reactor will go through the full reactor's cross-section surface. While in the 3D, a detailed nozzle distributor design, numbers, and placement were taken into account. This ensures that gas going out from nozzle outlet with the 20^o angle downward and will flow in the center of the bed. The nozzle distributor involvement might also be the reason, in the same voidage of the bed, the 3D model produced the bubble on the lower gas flow rate than that of the 2D because all the gas concentrated on center and induce bubble production better.

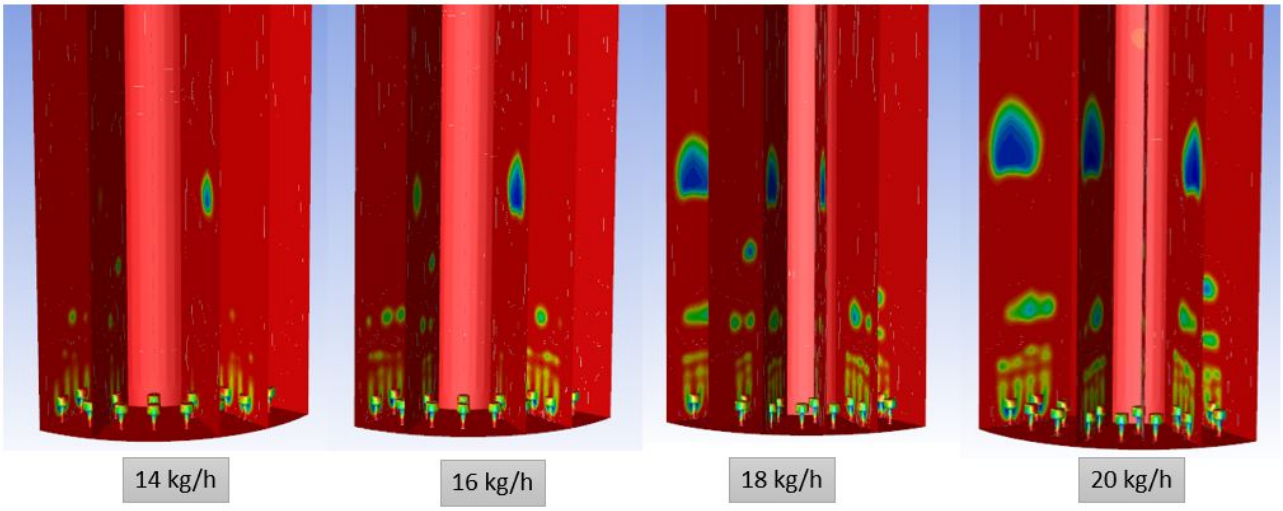

Figure 5.12: Instantaneous 3D solid volume fraction contour at various gas flowrate using Gidaspow drag model at 1s simulation time

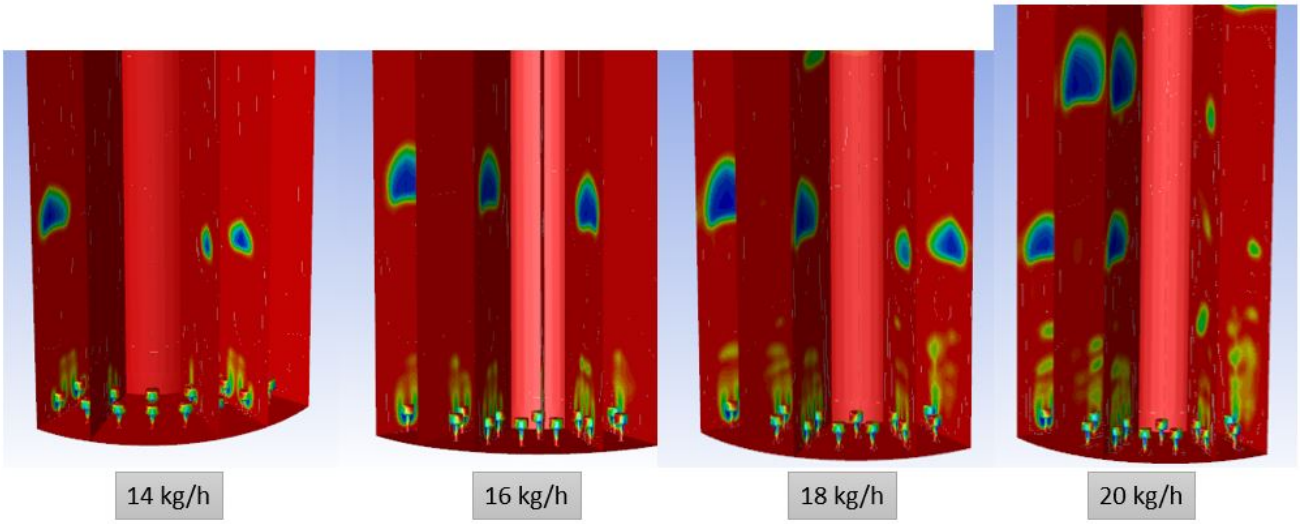

Figure 5.13: Instantaneous 3D solid volume fraction contour at various gas flowrate using adjusted Syamlal drag model at 1s simulation time

Voidage

The voidage under this minimum fluidization condition was also observed. It was calculated based on the data of time-averaged bed height with the 10% threshold following Cloete et al.[87] and the time-averaged pressure drop. And then, by following the simple correlation on Eq. 4, the voidage can be calculated. The overall bed voidage at minimum fluidization is 0.4 and 0.42 based on Gidaspow and adjusted Syamlal drag model, respectively. This difference mainly caused by the stronger drag force of the adjusted Syamlal model as mentioned earlier.

To get more insight into the bed state at minimum fluidization condition, the axial and radial solid fractions were examined. Firstly, the axial solid fraction profile over the bed height at 24 measurement sampling points was recorded. The area-weighted average value of solid fraction along all the measurement points was plotted, as shown in Figure 5.14.

This solid fraction profile shows that, in general, the corundum bed material is distributed almost uniformly and steadily at its solid density at minimum fluidization condition. This also aligns with the standard practice where the bubbling bed is working under the dense regime with a solid volume fraction above 0.5 at a relatively lower bed height. This evident agrees well with the theoretical axial solid distribution in the bubbling fluidized bed vessel discussed by Kunii et al. [15].

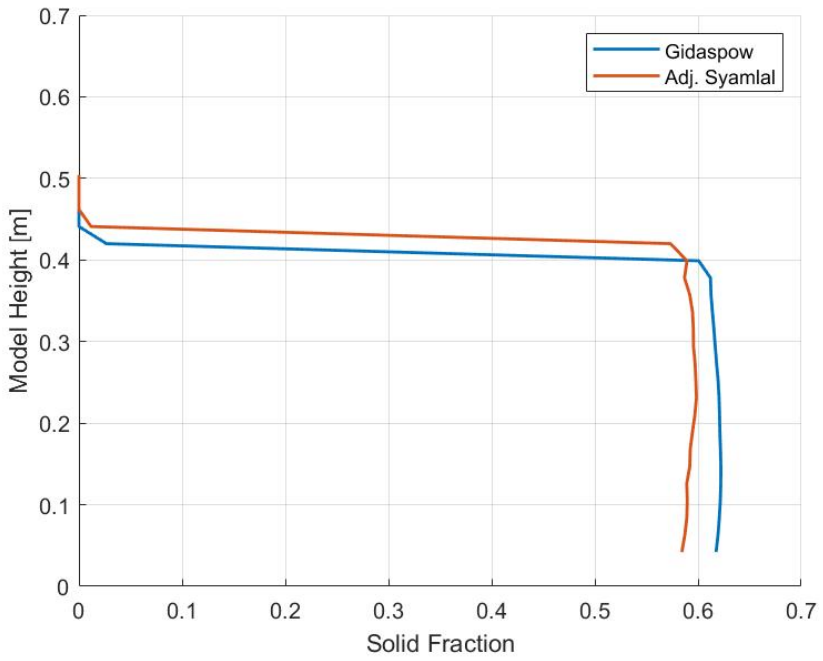

Figure 5.14: Time-averaged axial solid fraction profile using Gidaspow and Syamlal drag model at minimum fluidization

Then radial gas volume fraction profile at three different elevations was also observed. The simulation result for two different drag models is shown in Figure 5.15. The radial profile showed that the gas volume fraction profile should be relatively well distributed at minimum fluidization conditions and will grow bigger along with the increase of the elevation. However, there are some noticeable differences between both drag models.

First, adjusted Syamlal could generate a larger overall voidage than that of Gidaspow. Second, there is a tendency that voidage on the wall is higher than the one on center for adjusted Syamlal model. Conversely, the Gidaspow model predicts a dominant voidage in the center. Consequently, this affects the bubbling behavior, where more bubbles will be produced at the center of the bed for Gidaspow. In contrast, bubbles on the wall will be dominant using the adjusted Syamlal model.

Interestingly, in the 3D model, it is clearly shown based on the visual observation that there are no bubbles produced on the wall for both drag models. All of the bubbles started from nozzle distributors outlet on the center and remain on the center in the process of its development toward the reactor's height. Unfortunately, the time-averaged 3D radial voidage data requires at least three days of simulation to have reliable data; thus, no radial voidage simulations were performed for 3D at minimum fluidization condition. A similar issue will be discussed more in the following bubble properties section of the report.

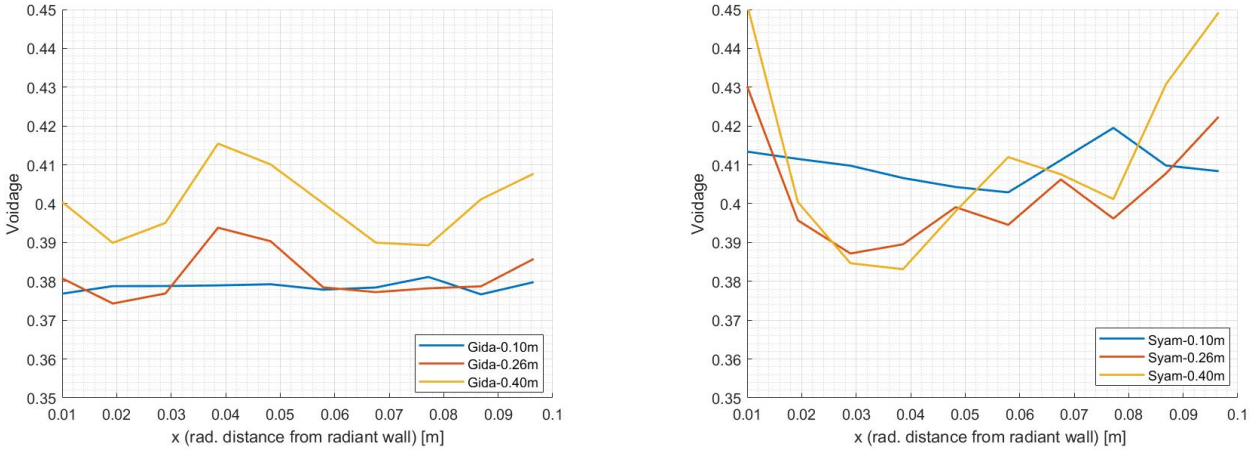

(a) Gidaspow drag model

(b) Adjusted Syamlal drag model

Figure 5.15: Time-average radial voidage at three different elevation points using Gidaspow and adjusted Syamlal drag model at minimum fluidization condition

.

5.3 Bubble properties

Bubble regime

Effective design and operational control of a fluidized bed reactor depend on accurate prediction of bubble properties. In the present work, bubble characteristics and behavior were examined. As a first step, the bubbling regime of the current setup was observed.

It is shown in Figure 5.12 and 5.13, that the bubbles started to occur at 14 kg/h gas flow rate. While on the slightly higher gas flow rate of 20 kg/h ($<$ 2Umf), the bed has started to generate slugging, which is defined as the size of the bubble approximately bigger than 0.6 of vessel diameter. This narrow bubbling regime and exploding bubble behavior for the geldart B particles and larger was discussed by Kunii et al.[15]. They mentioned that visual observations indicate that large particle beds behave differently from small particle beds. First, when approaching u_c (gas velocity where pressure fluctuation is maximum), huge exploding bubbles can be produced very quickly, particularly with the Geldart D solids. On this present work, the corundum bed material has a size almost at the end limit of Geldart B. On this condition, the transition to the turbulent regime occurs at relatively lower velocity and even far below terminal velocity.

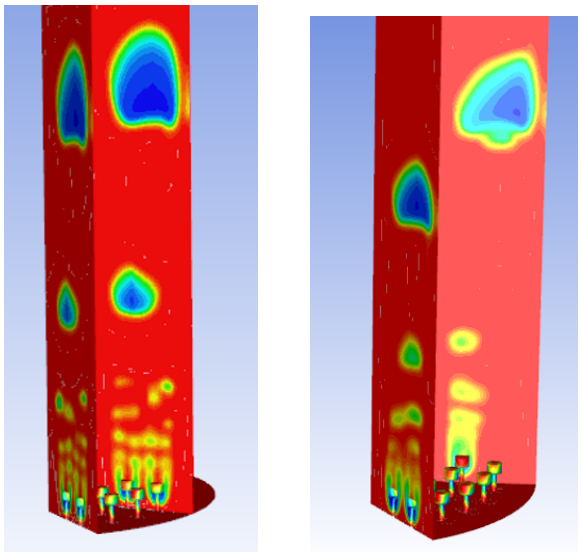

(a) Gidaspow

(b) Adjusted Syamlal

Figure 5.16: Instantaneous solid volume fraction contour using 20 kg/h as estimated slugging gas velocity at 1s simulation time

.

In order to quantify this phenomenon, the terminal velocity was calculated following the Syamlal drag formulation, specifically mentioned on Eq. 90-92. This equation takes into account Archimedes number (Ar) and Reynolds number under terminal settling condition for a single particle (Re_{ts}), also some of the empirical coefficients A, B, C1, and C2. The calculation yields 0.26 m/s for the terminal velocity on the present work, correlating with a 28 kg/h gas flow rate at a constant 600 ^{o}C.

Additionally, the minimum slugging velocity and height were computed using Eq.15 and 16. These yield 0.2 m/s for minimum slugging velocity (22 kg/h gas flow rate) and 0.39 m above distributor. At 20 kg/h, as shown in Figure 5.16, the large bubbles/slugging were generated at the height of about 0.35 m approximately, indicating the agreement with the theoretical value. This evidences showed the quantitative measure for justifying the bubbling and slugging regime on the current setup. Hence, for studying the bubbling behavior precisely, the gas flow rate of 18 kg/h was selected to make sure the simulated hydrodynamic lies in a bubbling fluidization regime.

Beds of large, uniformly distributed solids are often poorly fluidized, bumping, spouting, and slugging, causing severe structural damage in large beds. Additionally, these large particles fluidized in a much narrower range of gas flow rates: thus, shallower beds must be used [15]. While in the current setup, the ratio of height to bed diameter (h/D) is around four, where the approximate bed height is 0.4 m and the diameter of 0.0965 m. This makes the potential axial slugging generated is much bigger. The narrow bed diameter together with the big particle size used would make the bed cannot be adequately fluidized.

Bubble development

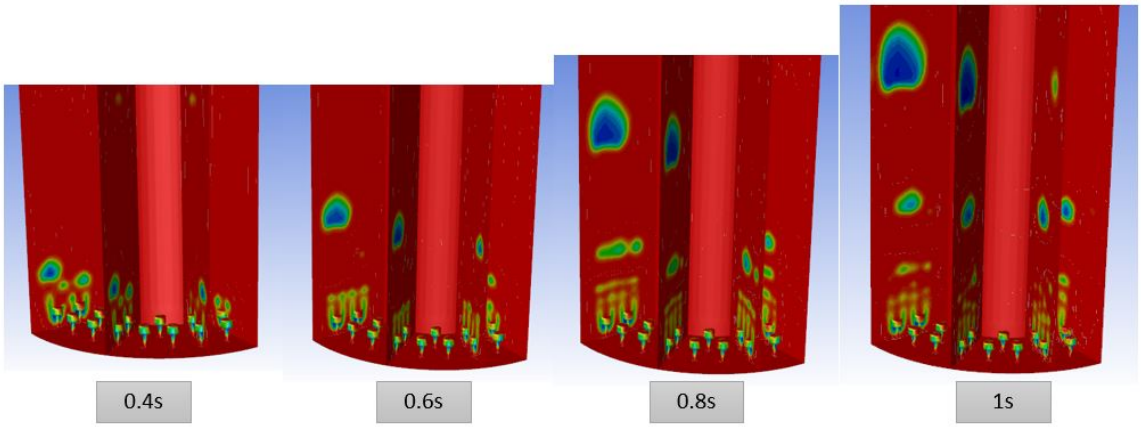

Figure 5.17: Corrundum solid distribution at instantaneous 1s time at 18 kg/h gas flowrate using Gidaspow drag model

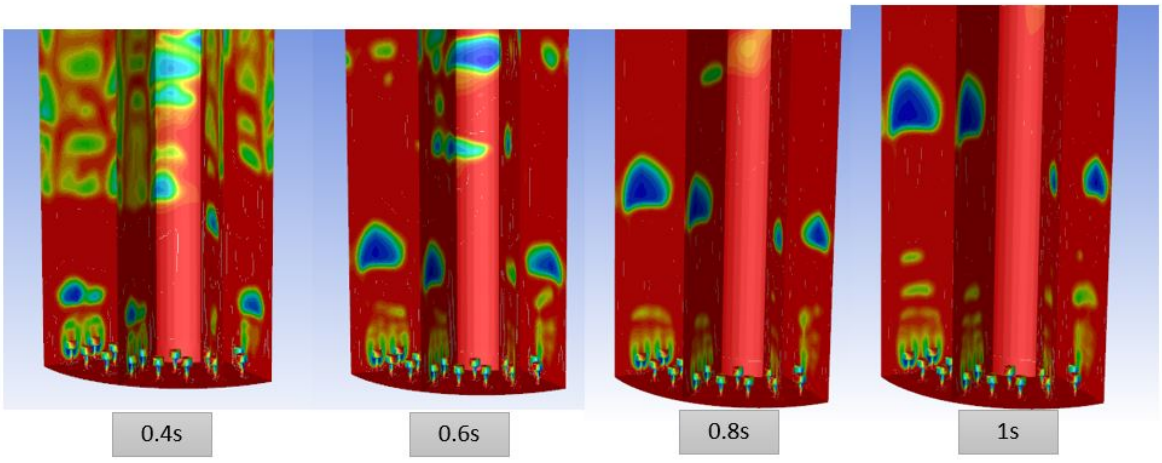

Figure 5.18: Corrundum solid distribution at instantaneous 1s time at 18 kg/h gas flowrate using adjusted Syamlal drag model

In this part of the discussion, some bubble properties were examined. Figure 5.17 and 5.18 show instantaneous corundum distribution after 1 s simulation with Gidaspow and adjusted Syamlal drag models. A similar bubbling pattern was found. It's noteworthy that smaller bubbles are generated near the nozzle distributor's outlet, then grow larger as they move upward in the bed. However, there is a difference in the bubbles' size, where the Syamlal model generated bigger bubbles than those of Gidaspow. This is because of the bigger drag force of the Syamlal model, as discussed by Esmaili et al.[72] and Vejahati et al.[71]. Even somehow that bigger drag force of Syamlal model is actually over-predicted the actual drag coefficient value for the entire range of solid volume fraction [71].

Another drag model was introduced in this bubbling study, namely the EMMS bubbling model. It is known as a heterogeneous drag model. Throughout the suspending and energy dissipation sub-systems, a bubbling fluidized bed has been resolved over three sub-phases, e.g., emulsion, bubble, and inter-phase intermediate phase [54]. Lu et al.[28] studied this drag model and compared it to other well-established models (e.g., Gidaspow and BVK). He found out that EMMS has a lower drag force and has smaller bubbles and denser emulsion phases. It also has the closest agreement with the experimental results for this particular case.

In Figure 5.19, the 3D flow simulation of EMMS bubbling within 1s is displayed. It shows a very similar behavior even closer to Gidaspow. The small bubbles generated at the bottom and growing larger along with the reactor height where most of the bubbles are in the center. The bubbles size is not that much different compare to Gidaspow and adjusted Syamlal. However, visually, it seems the EMMS drag model produces more smaller bubbles. This can be proved with more extended simulation ($>$ 2s), which is not feasible in the present work due to limited computation resources.

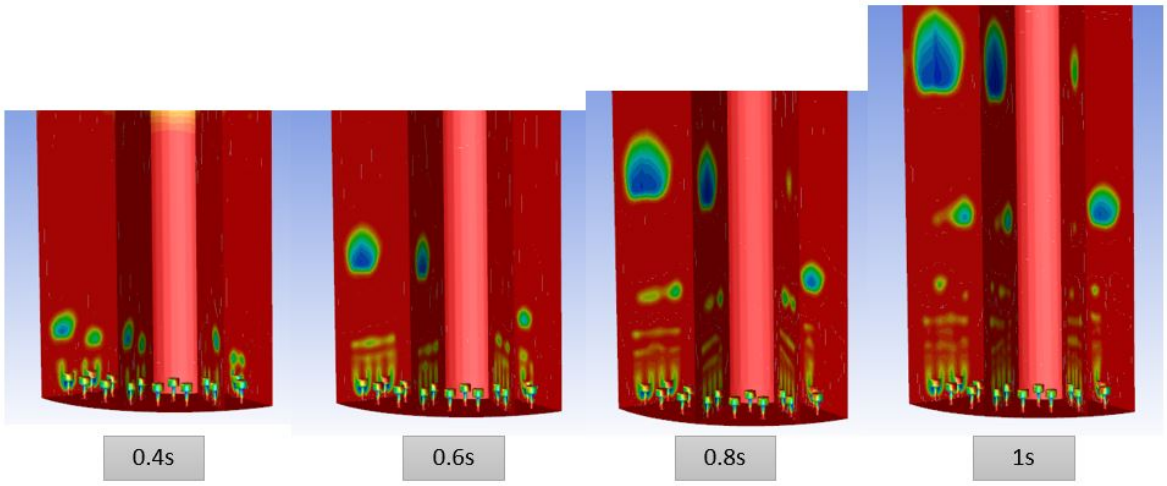

Figure 5.19: Corrundum solid distribution at instantaneous 1s time at 18 kg/h gas flowrate using EMMS drag model

Radial voidage

To have a clearer picture of the bubble behavior for three different drag models, the time-averaged radial voidage profile is shown in Figure 5.20. In the 2D simulation, the noticeable phenomena of bubbles produced in the wall was observed. This can be seen from the solid volume fraction contour and also the high time-average radial voidage on the wall. This peculiar behavior mainly because of the narrow width of the bed, and bigger bubble where the solids move together with the bubble upward and make the newly generated bubbles much more comfortable to be formed on the wall.

However, this was not the case for 3D simulation. Referring to bubble development in the previous discussion and the radial voidage profile, there are almost no bubbles formed on the wall. That is clearly shown that the biggest voidage is in the center, and on the wall was the lowest. Ostermeier et al.[70] discussed the difference between solid and bubble behavior on 3D and 2D simulations. They reveal that 2D simulation generates the bubble and vertical velocities with the too much steeper gradient in the radial direction. This results in the negative bubble velocities for the region close to the wall. This condition can be attributed to the missing wall influence or interaction, resulting in the third direction, which affects the overprediction of solid and gas velocity. Since the gas and solid phase have no chance to dissipate momentum in the horizontal direction, the higher vertical velocity magnitude is expected.

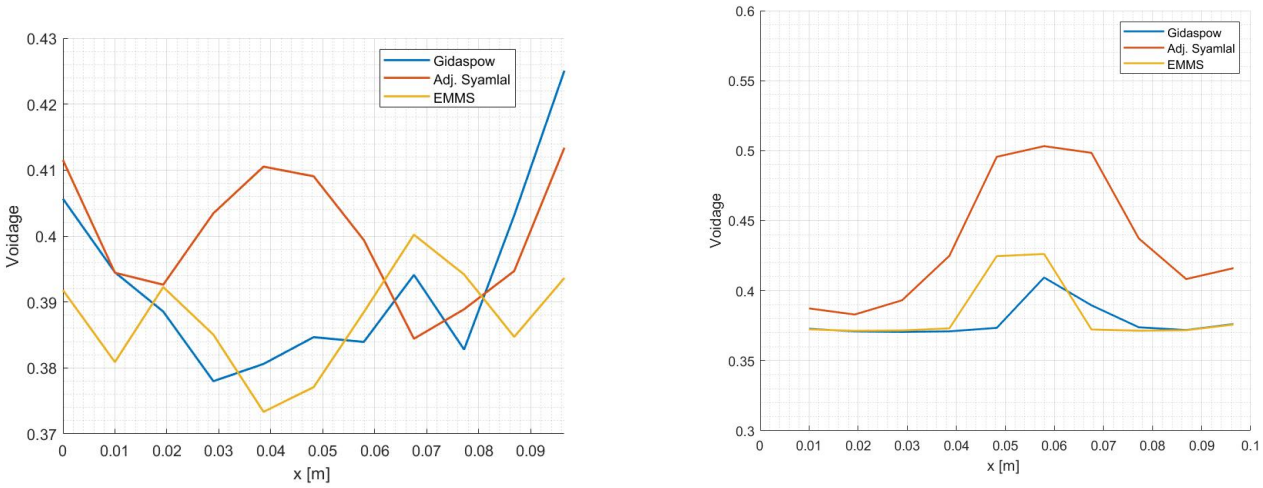

(a) Axial solid fraction profile

(b) Radial voidage profile

Figure 5.20: Time-average axial and radial (0.26 m) solid distribution profile of three different drag models

.

On Figure 5.20, the magnitude and different profiles for each drag model is presented. As mentioned earlier, the adjusted Syamlal model has a bigger drag force of all three drag models used; thus, the bubble produced represented by the bigger voidage magnitude occurred in most of all radial positions. The magnitude of Gidaspow voidage doesn't seem to be significantly different from those of EMMS. This is contrary to the Lu et al.[28] findings. This might also be due to the numerical simulation method Lu et al. used which was Eulerian-Langrangian and the much smaller particle size (half of the present study) employed on the simulation. The more relevant study done by Shi et al.[54] which is performed with the TFM numerical model, shows a better agreement. Unlike the one they found in Geldart A particle, in Geldart B particle, there is no significant difference between both standard drag model and EMMS.

Based on the above-mentioned discussion, several remarks can be drawn from the comparison of three drag models used in the simulation. The adjusted Syamlal model predicts the pressure drop and bed height much closer to the experiment than the Gidaspow, despite the underprediction. However, it tends to overpredict u_{mf} by showing much larger bubbles on 14 kg/hr. Another drag model introduced, EMMS-Bubbling, doesn't give the expected result since no significant differences are shown on the bubbles' behavior compared to Gidaspow. Further validation cannot be made due to a lack of experimental data, e.g., such as radial and axial voidage profiles at certain air flow rates. Though the solid conclusion is hardly made concerning the best drag model, Gidaspow is undoubtedly not a preferable option. Many authors have reported the adjusted Syamlal regarding its improper adjustment method. Thus, EMMS-Bubbling might be the most potential drag model as the best option.

5.4 Sphericity and specularity

In the earlier discussions on this chapter, the sphericity factor's importance was raised on determining the pressure drop and bed expansion result. In the later analysis, upon the comparison between 2D and 3D in the context of a radial voidage profile, the solid velocity differences were discussed. This velocity of particles cannot be separated from the influence of its interaction with the wall, represented by the specularity coefficient. Hence, in the final part of the hydrodynamic discussion, the significance of both parameters will be provided.

First of all, the importance of the sphericity factor was discussed. The sphericity factor (SF) defines how close the particle shape or volume is with the sphere. The perfect well-rounded particle will have SF approaching one while the smallest value will close to zero. Within this study, the two different sphericity factors were simulated using the Gidaspow drag model. And then, the time-averaged pressure drop and bed expansion were plotted together with the default of SF 1 in Figure 5.21. The SF is incorporated into the CFD simulation via UDF by adding SF term in the equation and change it to the desired value.

Based on Figure 5.21, the use of SF directly affects the pressure drop and bed expansion. The Gidaspow model with SF 0.8 increased more prominently than the model with SF 1 as a default value for both pressure drop and be expansion. This clearly confirms that the influence of the sphericity factor is significant for the simulation. Hence, the data for the accurate shape or SF of the particle is crucial to simulating the fluidized bed's hydrodynamic.

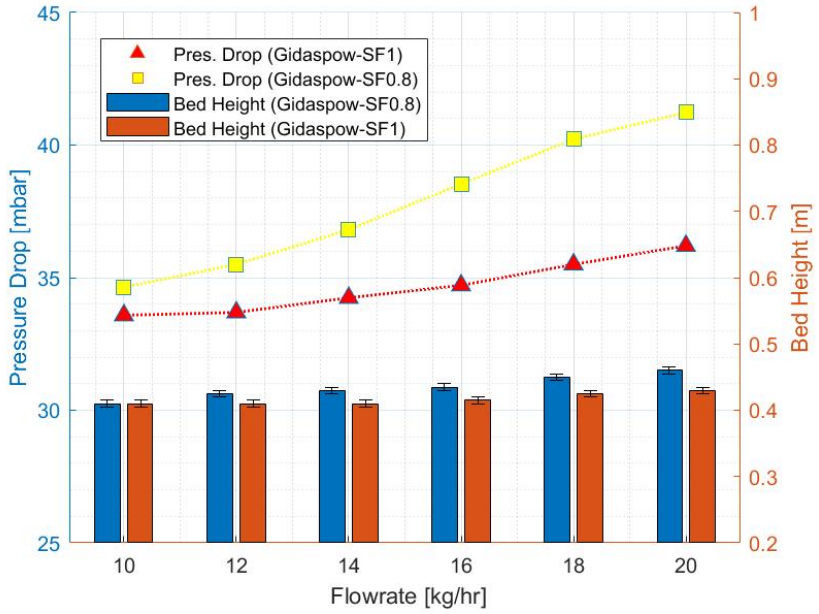

Figure 5.21: Time-averaged of pressure drop and bed expansion from simulation for different gas flowrate using two different sphericity factors

Decreasing the SF further, re-doing all the simulations, and comparing it with the experimental data might be the preferable action after referring to this result. However, at least three main constraints hinder this action. First, the actual sphericity factor data is not available. Thus decreasing or increasing the SF cannot directly justify the correct result. Second, implementing the SF on the drag model requires a modified drag function through UDF, which also demands some high workload. Finally, changing the drag model and re-doing the simulation for both 2D and 3D is not feasible in referring to the current project timeline.

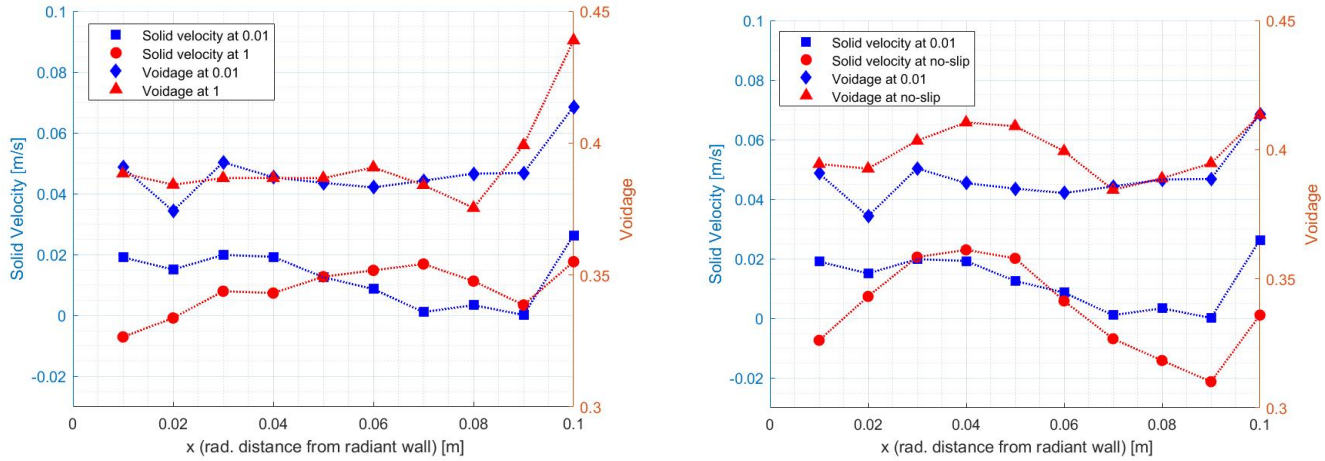

(a) Specularity 0.01 vs 1

(b) Specularity 0.01 vs no-slip

Figure 5.22: Time-averaged solid velocity and voidage from the simulation in the radial direction using two different specularity coefficients and no-slip condition

.

Secondly, another critical parameter is the specularity coefficient (SC). It can be defined as the friction of the solid movement with the wall. The 0.01 SC indicates almost no friction between the particles and the wall, while SC of 1 tells the strong effect of wall particle friction behavior. In this part of the report, the influence of two different specularity coefficients and the default no-slip condition to the solid velocity and voidage profile were elaborated. These results are shown in Figure 5.22.

The specularity of 0.01 and 1 was first examined. It is apparent that SC affects the voidage profile in the bed. That is because the SC represents the interaction of solid particles with the wall and directly affects the axial velocity primarily towards the axial direction of the bed. The solid velocity, as well as its circulation, will determine the voidage profile. It can also be noted that with the increase of SC to 1, the solid velocity will be decreased and vice versa.

Finally, it is interesting to find that the no-slip boundary condition in the wall is not directly correlated with SC 0 or around. It can be shown on the right side of Figure 5.22 that though it looked similar, there are still some differences in the solid velocity profile and its magnitude. Referring to the voidage profile on the top part of the figure, different radial profile with no-slip condition seems to have a bigger voidage. It is now verified that both sphericity factor and specularity coefficient play a crucial role in simulating the correct hydrodynamic of a solid-gas fluidized bed.

5.5 Grid refinement for heat transfer

With similar concerns with the hydrodynamic solution while implementing the numerical simulation method, the appropriate grid size is a critical aspect to be considered. As the closest area with the radiant burner will have the most significant temperature gradient and would be the most crucial part during simulation, grid refinement is required. Referring to Kuiper et al.[76] as discussed in Figure 3.14, the grid subdivision with the decreasing cell size, along with the decreasing distance from the wall, is applied.

There are four different cell subdivisions used in this simulation: 5, 4, 3, and 2 subcells. The simulation result is shown in Figure 5.23. The instantaneous heat flux profile is presented on the left part, and the time-averaged values are shown on the right. It can be clearly observed, out of four different subdivisions, only two subcells show an odd heat flux profile apart from the other three, which much lower. By doing time-averaging after the 5s measurement, the differences become clearer: dividing the cell into at least three subcells shows stable and similar heat flux. Based on this, the four sub-cells arrangement was selected and deemed sufficient to capture the large temperature gradient in the radiant wall's vicinity.

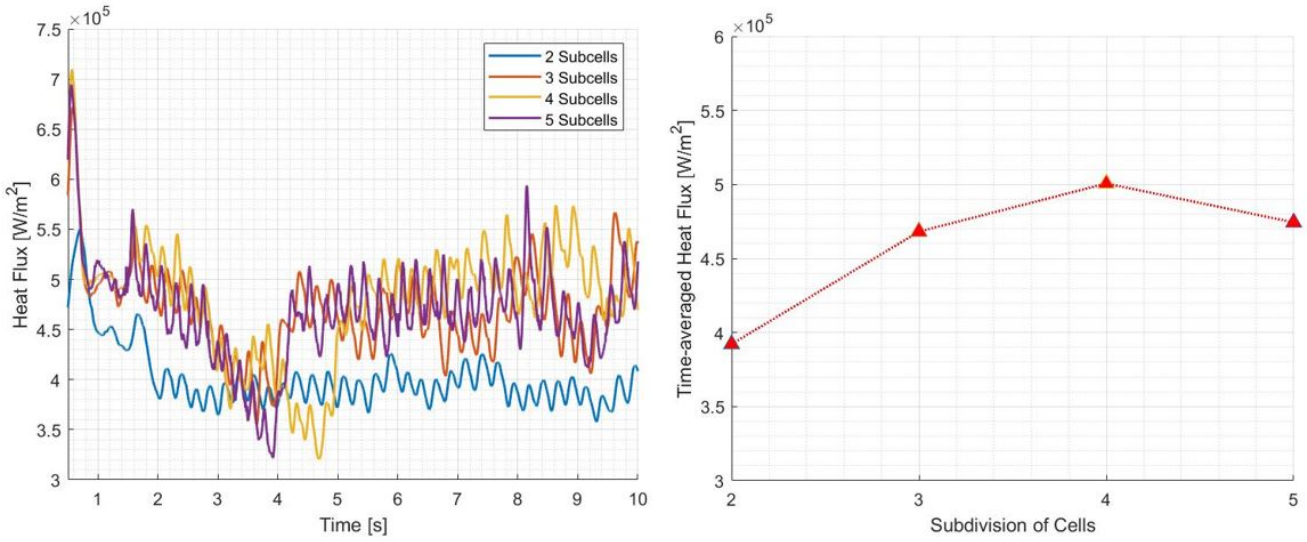

Figure 5.23: Heat flux measurement profile (left) and time-averaged heat flux (right) on four different cells division

5.6 Effective thermal conductivity

Before going further to the heat flux and heat transfer coefficient simulation, some of the heat properties e.g., effective thermal conductivity, absorption, and scattering coefficient, were examined. Firstly, the effective bed thermal conductivity is simulated, and the result shown in Figure 5.24.

As discussed thoroughly by Zehner et al. [46], the effective thermal conductivity of the bed is constructed from the effective thermal conductivity of the gas and solid material (corundum in the present work). They observed that the thermal conductivity of the component is profoundly affected by the voidage profile. Specifically, the effective bed conductivity in the operating region of fluidized bed (α_g>0.4), is significantly smaller than the corresponding microscopic transport coefficient of the material. According to the authors' result, the effective bed thermal conductivity was only 20 % of the original value.

By default, the corundum's thermal conductivity is between 5-15 W/m.K under the range of operating conditions discussed in the present work (400-1000 ^{o}C, 1 atm). Based on the simulation, the solid's effective thermal conductivity is approximately 1.6 W/m.k at maximum, which is significantly lower than the default value. The total bed conductivity then also get lower since the air conductivity is much smaller. This result agrees well with the trend discussed by Zehner et al. Furthermore, the conductivity profile is strongly affected by the voidage (or solid fraction) pattern along with the simulation. The value will be maximum on the highest solid volume fraction and minimum at the lowest solid volume fraction.

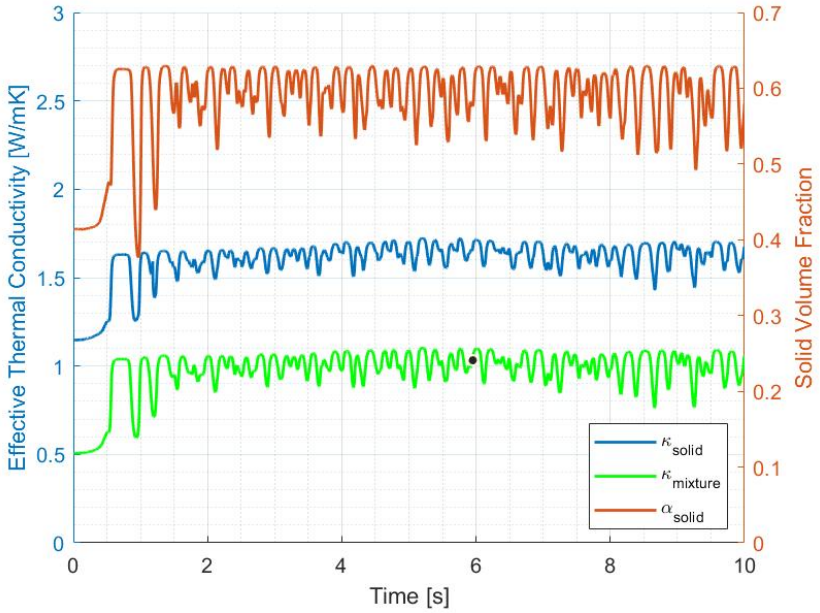

Figure 5.24: Instantaneous effective thermal conductivity of corundum material and mixture with a solid fraction profile against the simulation time (10s) at approximately 0.265 m above nozzle distributor

5.7 Radiative properties

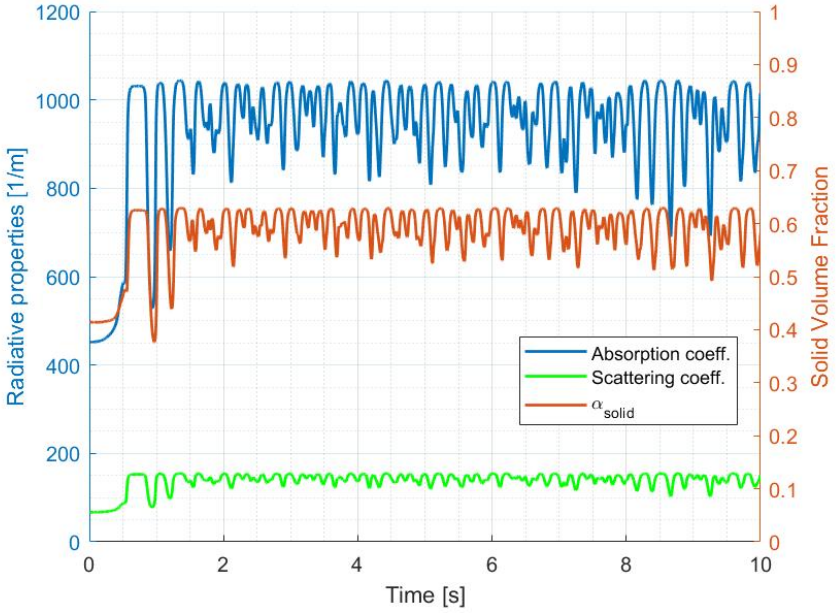

Figure 5.25: Instantaneous absorption and scattering coefficient profile together with solid volume fraction against the simulation time (5s) at approixmately 0.265 m above nozzle ditributor

A similar pattern holds for the radiative properties, absorption, and scattering coefficient, during the simulation. Figure 5.25 shows the instantaneous area-weighted averaged profile of absorption and scattering coefficient during

the simulation. Those radiative parameters have a very similar pattern with that of a solid fraction pattern along with the simulation. This phenomenon can be easily understood since the absorption and scattering coefficient directly correlates with the number of particles per unit volume of the bed, as shown in Eq. 52 and 53.

The corundum was expected to have a nearly opaque surface during the development of the model, and the simulation result shows this behavior. A high number of absorption coefficients over the simulation indicate an optically thick medium characteristic. This also implies that the radiation wavelength will have a significant absorption once passing through it, and only a small amount of photons can be further transmitted. Another interesting finding is that the scattering coefficient is much lower than the absorption coefficient. This makes the heat transfer through the radiative effect will be much similar to the heat diffusion process.

5.8 Radiative heat transfer effect

Figure 5.26 displays the instantaneous area-weighted average heat flux from the radiant burner wall along with the fluidization height range for both cases with and without radiation. At first 3s of simulation, the heat flux had a sharp decrease due to the initial high-temperature difference and reached more or less steady condition afterward. The regular fluctuation profile is also observed, which consistently indicates the bubble occurrences throughout the simulation. When the stable heat flux condition was achieved after 5s of simulation, the time-averaging process was performed.

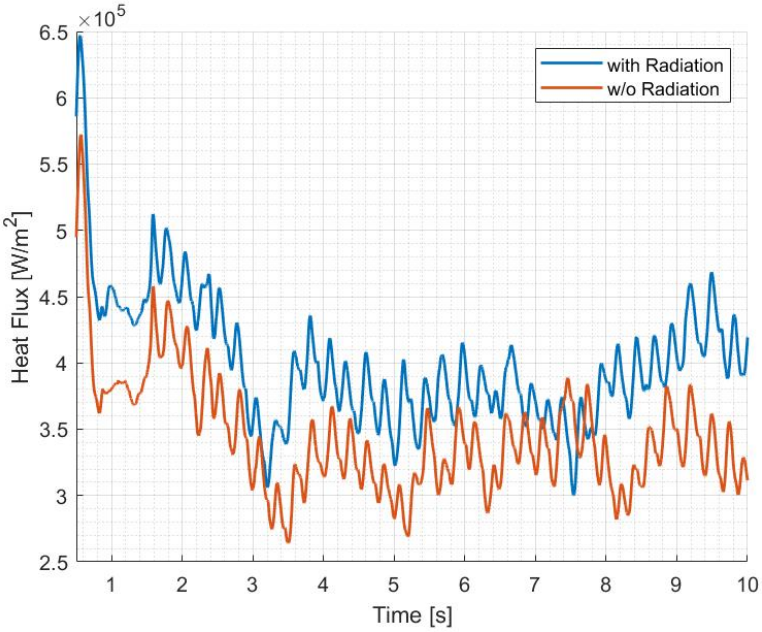

Figure 5.26: Instantaneous area-weighted averaged total heat flux profile with and without radiative transfer against the simulation time (10s) at the surface of the radiant burner.

The comparison of the total heat flux with radiation and without radiation shows a distinct difference, where the total heat flux involving radiative transfer has a larger value. Referring to the time-averaged value, the heat flux without radiation yields 330964 W/m^2 and with radiation was 384297 W/m^2, which is about 16.11 % higher. This value lies in the range of radiative contribution in the typical fluidized bed as discussed by Saxena et al.[77] in the earlier chapter.

This radiative transfer contribution to the present work confirms the theory that radiative heat transfer will play a significant role and generate a considerable contribution to the high-temperature conditions. Contrary to the case of low temperature or ambient condition, as discussed by Kuiper et al.[24], radiative heat transfer is negligible, especially for the instance when the particle volume fraction is very high ($> 30\%$). In this type of dense phase simulation, radiative heat transfer is hindered by high concentration particles[23].

5.9 Bubbles effect on heat transfer

According to Kuiper et al.[24] and Mickley and Fairbanks [43], the bubbles occurrence in bubbling fluidized bed could improve the heat transfer process. This mainly due to the fresh particles with a temperature equal to that of

the bed is maintained on the vicinity of the radiant wall by the flow of the bubbles. Hence, it keeps the temperature differences larger throughout the simulation. This issue will then be discussed by comparing the heat flux result of incipient and bubbling bed conditions and the bed with three different bubbling / voidage profiles.

Firstly, the incipient and bubbling condition was studied. As shown in Figure 5.27, the heat flux produced from the bubbling bed was always higher than that of the incipient one. The time-average of the heat flux for bubbling bed yields 384297 W/m^2, which is 17.10 % higher than that of the incipient bed, 328024 W/m^2. This evidence confirms that the bubbles' occurrences enhance the heat transfer process in the bed.

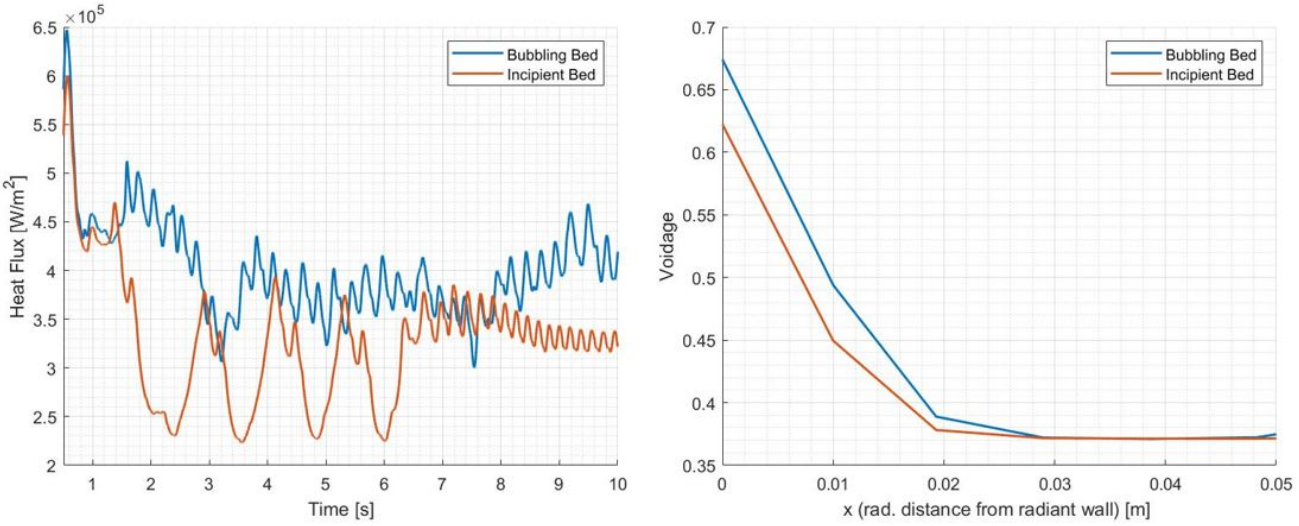

Figure 5.27: Instantaneous area-weighted averaged heat flux at incipient and bubbling bed condition against the simulation time (10s) at the surface of the radiant burner (left) and time-averaged radial voidage profile(right)

Bubbling bed has a steady heat flux fluctuation with a similar magnitude almost at the entire range, indicating the continuous bubbling frequency and size. On the other hand, the incipient bed is supposed not to have bubbles. However, some bubbles were still produced due to a heat transfer surface, which has a significantly high temperature and increases the air velocity due to the decrease of density.

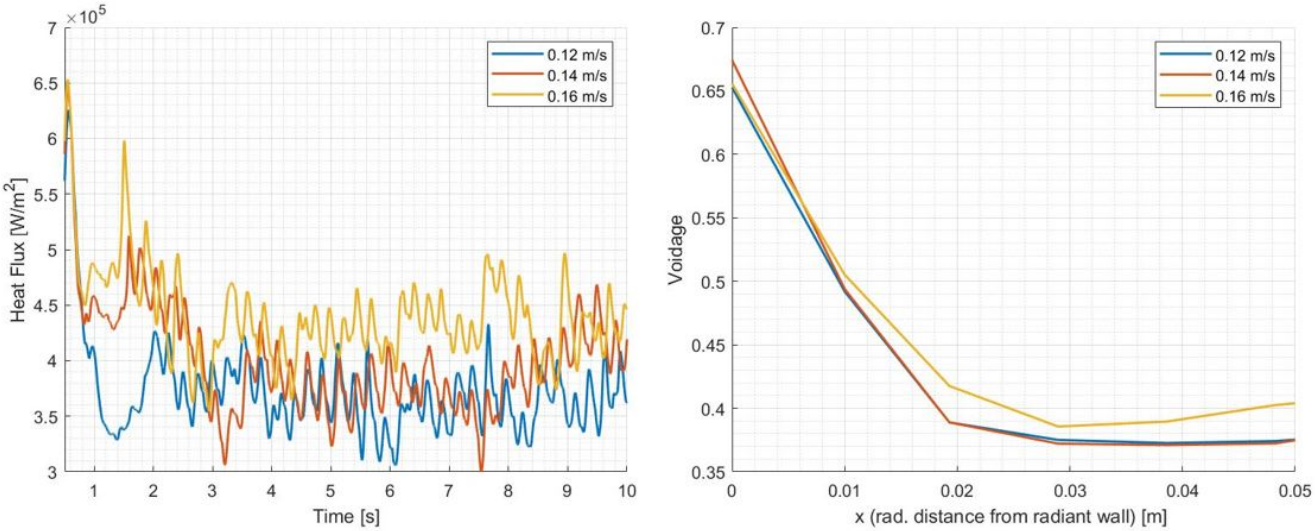

Figure 5.28: Instantaneous area-weighted averaged heat flux at bubbling bed condition with various superficial gas velocity against the simulation time (10s) at the surface of the radiant burner (left) and time-averaged radial voidage profile(right)

The right picture in Figure 5.27 shows the time-averaged bed voidage in the simulation. It verifies that although some bubbles are produced at incipient conditions, the voidage of the bubbling condition is much higher. This then strengthened the conclusion of heat transfer improvement due to bubbles' existence.

The bubble's influence on the heat transfer process was further investigated by varying the superficial gas velocity in an attempt to change the voidage behavior. As discussed in the hydrodynamic section, the increase of gas velocity or gas flow rate will increase the bubble size and the bed's voidage. The gas velocity used was 0.12, 0.14, and 0.16 m/s, and the simulation results were displayed in Figure 5.28.

As shown in the Figure 5.28, the heat flux profile increased with the increase of superficial gas velocity. The time-averaged value for each gas velocity was 360635, 384297, and 433112 W/m^2, respectively, from lowest to the highest. However, if the more critical investigation was performed, the heat flux increase from the 0.12 to 0.14 m/s gas velocity was not in the same magnitude with the increase from 0.14 to 0.16 m/s. This phenomenon can be clearly explained once the radial voidage profile was also taken into consideration.

In the right part of Figure 5.28, it shows that the voidage profile of 0.12 and 0.14 m/s gas velocity was very similar. In contrast, the 0.16 m/s gas velocity generates a much higher voidage across the bed's radial direction. The appropriate conclusion that can be drawn is that the increase of heat flux is aligned with the rise of bubbles occurrence, represented with the voidage profile.

5.10 Overall heat transfer coefficient

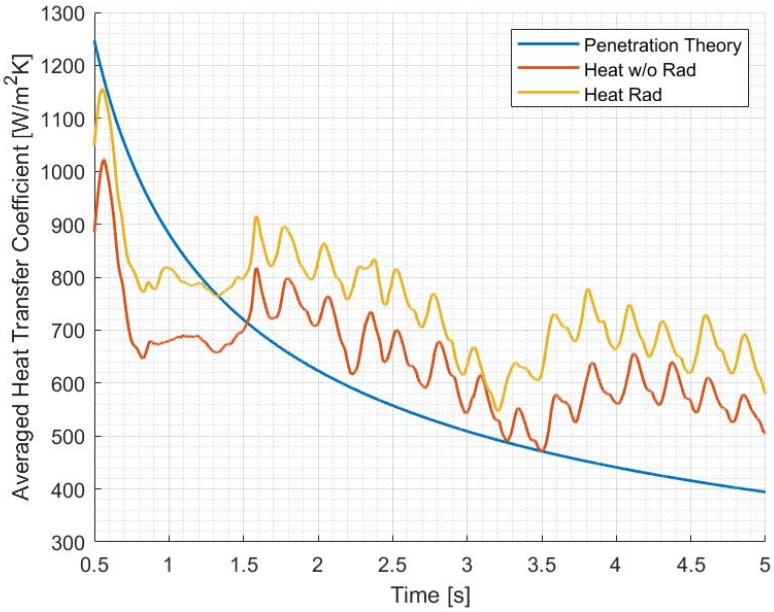

Figure 5.29: Instantaneous averaged heat transfer coefficient profile and approximated penetration theory against the simulation time (10s) over the fluidization height.

In Figure 5.29, the averaged heat transfer coefficient at approximately 0.265 m above the nozzle distributor plate against penetration theory from Mickley et al.[43] is presented. It can be found that the average heat transfer coefficient from the simulation pretty much agrees well with the one calculated from the penetration theory, especially for the one without the radiative transfer. This is understandable since the penetration theory considers the governing mechanism of heat transfer is the heat diffusion process and neglect the radiative heat transfer. In the case of radiative transfer was involved, the heat transfer coefficient was also improved.

The fluctuation of the value demonstrates the influence of the bubbles on the heat transfer coefficient. Packets of the particle (or parcels of the emulsion phase) at the bulk bed temperature are swept to the heat transfer surface on the wall due to the bubbles' existence. The packet will stay in contact for a short time and be swept back to the bed. This process has been discussed earlier, which has a positive impact on heat transfer. This is also why the heat transfer coefficient from the simulation is a bit higher than that provided by the penetration theory, which is based on the incipient condition.

5.11 Temperature profile

After 10s of heat transfer simulation, the temperature profile was examined for the model with and without radiative transfer. The differences contour between P1 and DO radiative models were also observed. As shown in Figure 5.30 and 5.31, there is a significant difference between the model that took into account the radiative model and the one that only considered conductive and convective heat transfer that confirm the significance of the radiative heat transfer model on the present work. The main differences are shown in the gas part, especially above the bed. This was because the absorption coefficient is very low compared to the corundum particle, and thus the radiative heat could penetrate better and faster on the gas phase. While in the corundum, which is considered as an optically thick medium, the heat transfer is slower as it depends on the diffusion process.

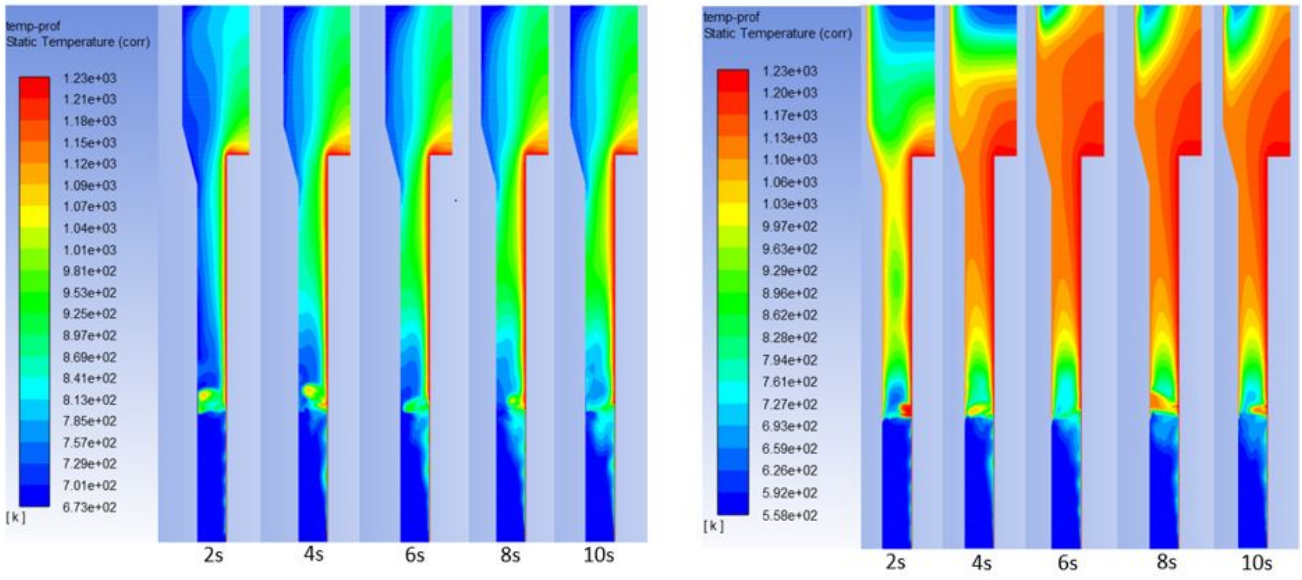

Figure 5.30: Instantaneous temperature contour after 10s of the simulation without radiation (left) and with radiation using P1 radiative transfer model (right)

There was one apparent difference in the temperature contour between the P1 and DO model. On the DO model, the lowest and highest temperature still lies within the setup temperature, which is 1233 K for rad wall and 673 K for Air inlet. This shows the expected temperature range since the heat source is only coming from the rad wall, and no heat loss is possible (adiabatic outer wall condition). In the simulation with P1, there was a considerable temperature decrease in the lower part of the bed than the predicted lowest temperature of 673 K. There was almost 100-degree temperature decrease, which must be wrong. The possible reason is the complexity of the simulation that cannot be handled by the P1 model, especially the optically thick medium above ten that is out of the recommended range by ANSYS technical guide [45].

In order to check further the temperature of the bed, the temperature at five different measurements following the five thermocouple positions on the real setup was compared between the experiment and simulation. The average bed temperature in the experiments was 600 ^{o}C, based on two thermocouples involve in the fluidization (13 TE 01 and 13 TE 03). In comparison, the temperature from the simulation used was the time-averaged temperature on the steady range between 8-10s of simulation. As has been discussed earlier for some bed height underprediction, only one thermocouple is within the bed fluidization (13 TE 01) on the simulation. The result is shown in Figure 5.32.

As depicted in Figure 5.32, the temperature profile without radiation has the closest proximity to the experiment's data. The temperature rises very quickly for radiative model inclusion, especially for the air above the bed (13 TE 03 - 13 TE 09). As the bed does not reach the second thermocouple in the simulation (13 TE 03), the temperature measurement is much higher than that of 13 TE 01 since it measures the air temperature. In contrast with the apparent air temperature measurement between non-radiative and radiative cases, the corundum phase has a slight temperature difference, indicating the radiation's insignificant contribution.

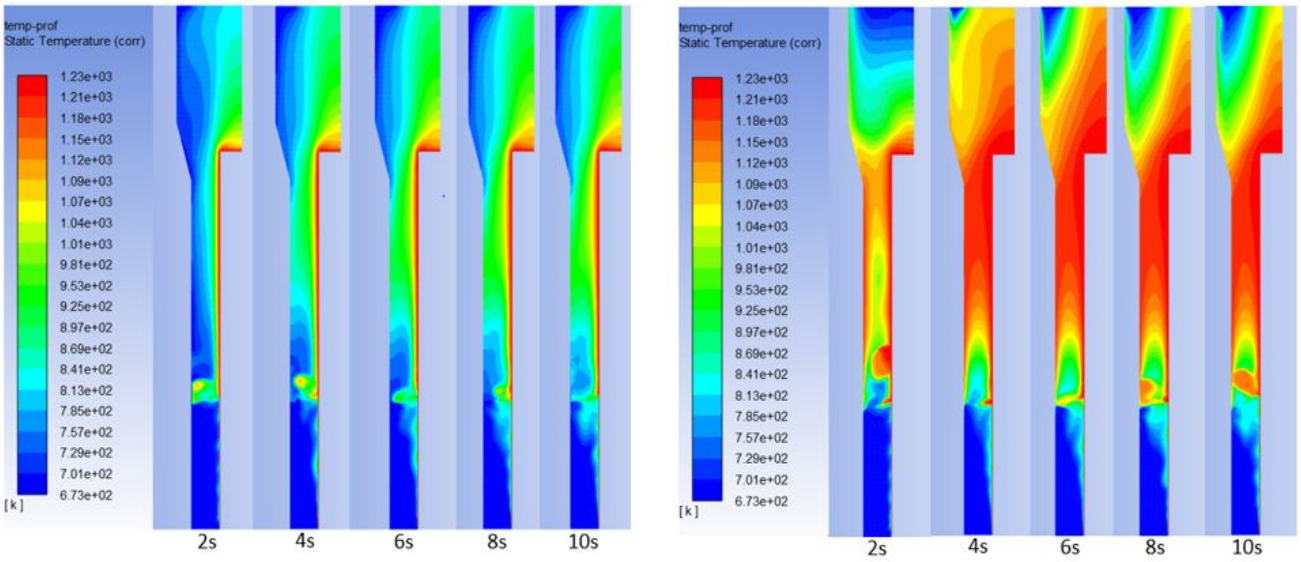

Figure 5.31: Instantaneous temperature contour after 10s of the simulation without radiation (left) and with radiation using DO radiative transfer model (right)

The first reason behind these differences might be the heat losses, which are not included in this simulation. By introducing the heat loss, the temperature will be lower, and the heat flux will be much higher due to higher temperature differences between the bed and radiant wall. The second reason could be the different environments used in the simulation compared to the experiment. In the experiment, before reaching the steady-state, the gas flowrate with 400 ^{o}C was almost three times the gas flowrate on the current simulation (48 kg/h). This situation will surely increase the heat transfer process on the bed by introducing more bubbles and bigger voidage. After the bed temperature reached a steady 600 ^{o}C bed temperature, the gas flow then is lowered and maintained on the constant flowrate. In contrast, in the simulation, one constant low flow rate was used with 400 ^{o}C and the bed temperature of 400 ^{o}C. It was expected to also reach the same bed temperature at the end (600 ^{o}C); however, it did not succeed.

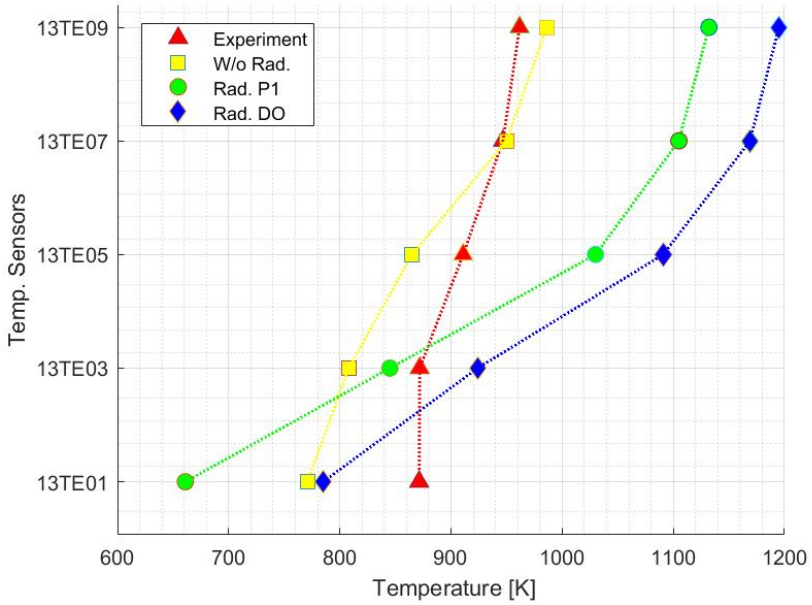

Figure 5.32: The comparison of experimental steady-state temperature with the time-averaged temperature measurement without radiation and with radiation using P1 and DO radiative transfer model at five different height measurements

Another essential reason that might affect the simulation results would be the less accurate bed hydrodynamic representation on 2D simulation. Ostermeier et al.[70] even firmly concluded the less precise results might happen for the 2D simulation. As discussed earlier, the voidage and bubbles' behavior is significantly different between 2D and 3D. Additionally, the solid particle and bubble velocity profile overpredicted on 2D has a steeper gradient than 3D. This will undoubtedly affect the particle contact and, thus, mass transfer between the rad wall and the bed.

The differences between P1 and DO were also clearly shown. They provided almost a similar pattern while different in magnitude. As discussed earlier, P1 shows a strange bed temperature, which is below 673 K while DO and another case without radiation resulted in a much higher temperature. This then concludes that DO radiative model is capable of handling the present simulation.

5.12 Heat loss

As the significant differences in temperature between experimental and simulation results appear in the previous discussion, consideration of heat loss was raised for a possible reason. Due to the restriction of numerical stability, only 5% of heat loss was simulated, just to investigate the influence on the heat flux and the temperature profile.

The heat flux profile for comparison of the adiabatic and the 5% losses is shown in Figure 5.33. It is observed that basically, both adiabatic and with 5% losses show a similar pattern of heat flux. The time-averaged heat flux value of the adiabatic condition was 384297 W/m^2, while the one with heat loss was 389060 W/m^2, which is slightly higher. This is understandable since, by the introduction for heat loss through some heat flux towards outside, the temperature differences will be slightly higher, which then will increase the heat transfer from the radiant wall.

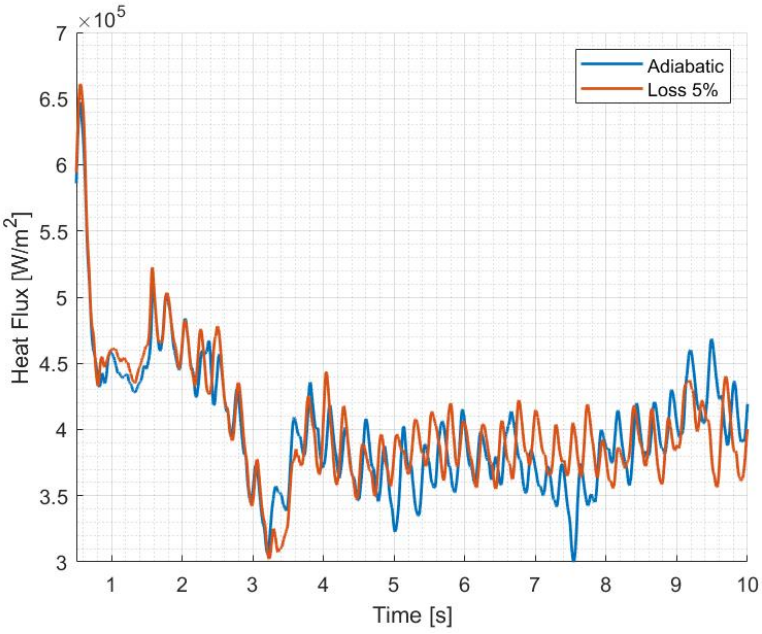

Figure 5.33: Instantaneous area-weighted averaged total heat flux profile at adiabatic and with 5% heat losses against the simulation time (10s) at the surface of the radiant burner

The comparison of the temperature contour for both adiabatic and with losses was also studied. In Figure 5.34, the instantaneous temperature contour shows that the main difference was mainly found on the top of the radiant wall while the rest remains similar. The bottom limit of the temperature range is started to decrease slightly due to some losses outside the reactor.

To clearly observe the change in temperature profile, five different height measurements for the case with and without losses and experimental data were compared. Figure 5.35 shows that by the account of the heat loss, there was a slight decrease in temperature on the topsides, while the rest are similar. The bed temperature was also not significantly different. This might be because the small losses assumed. The bigger and more realistic losses above 5 % could be examined further to confirm whether the heat loss does not considerably influence the reactor's temperature profile, especially the bed part.

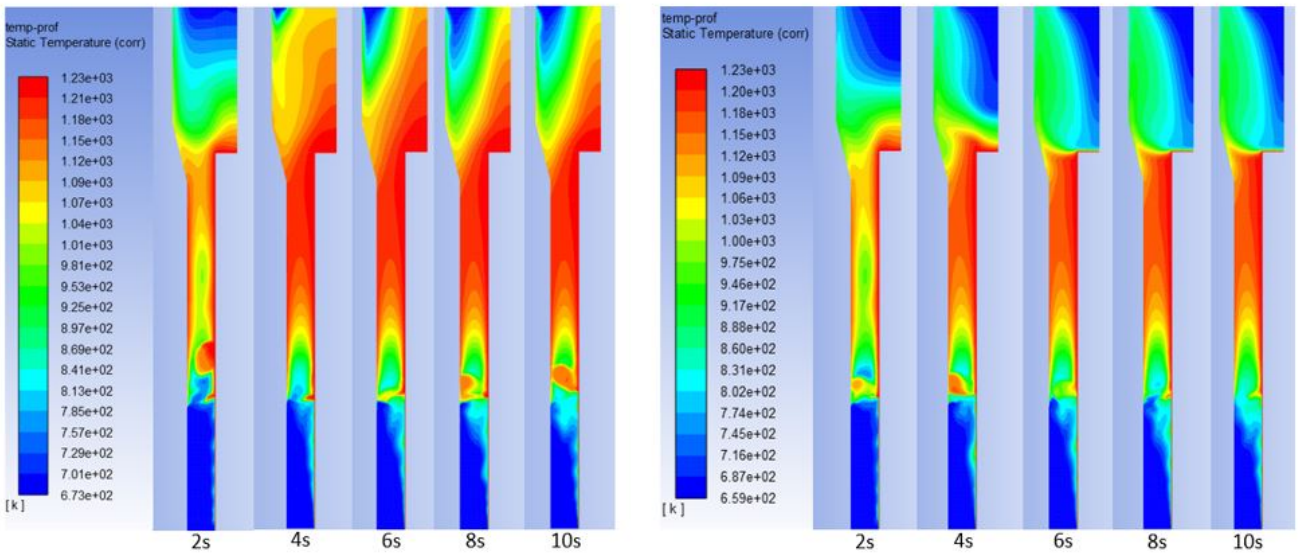

Figure 5.34: Instantaneous temperature contour after 10s of the simulation at adiabatic (left) and with 5% heat losses using DO radiative transfer model (right)

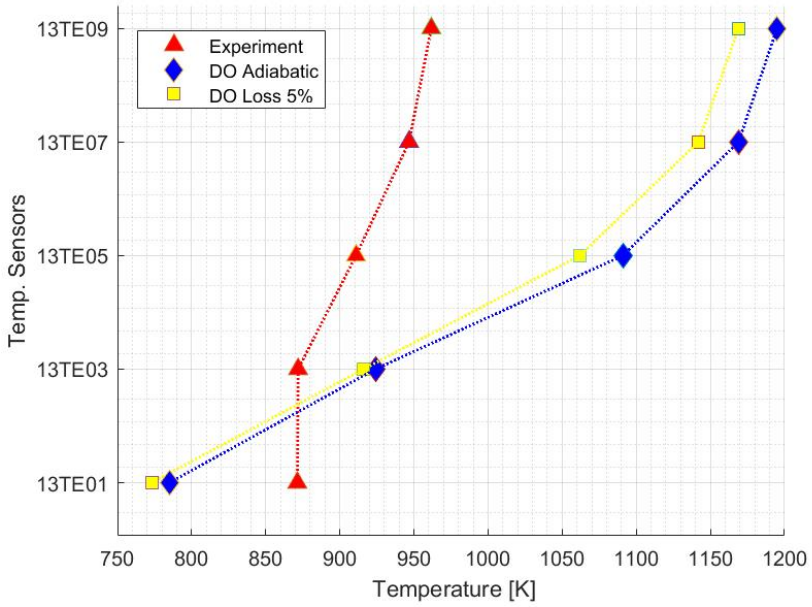

Figure 5.35: The comparison of experimental steady-state temperature with the time-averaged temperature measurement at adiabatic and with 5% heat losses using DO radiative transfer model at five different height measurements.

6 Conclusions and Recommendations

A series of research questions were proposed at the beginning of this study. To answer the questions, a 2D and 3D CFD model of the IHBFB-SR reactor was developed and simulated. After a comprehensive phase of model development, detailed simulation for both the hydrodynamic and heat transfer processes, with the use of experimental results for validation, the research questions can be answered. This chapter provides the final conclusions and also recommendations for future work.

6.1 Conclusions

1) What is the optimal grid size of the CFD mesh model?
Five different grid sizes were examined in the simulation. It is concluded that the acceptable grid size for simulating the IHBFB-SR with a bed material particle size of 0.496 mm should at least 7.5 mm or 15 times the corundum particle size. The present work used 2.5 mm or five times dp to refine more the simulation results and considered the feasibility of the current computational resources.

2) What is the minimum fluidization condition on the current setup?
There are slight differences between the experimental and simulation results of both 2D and 3D. However, the value remains in the range of 14-16 kg/h. Since the 3D simulation is considered to have the highest accuracy based on the common practice and the comprehensive design taking into account the tuyere nozzle design and arrangement, the minimum fluidization condition should lie around 14 kg/h.

3) Which drag model (gidaspow or adjusted syamlal) could give the closest result to the experimental data?
Both Gidaspow and adjusted Syamlal drag models were extensively used in the present work. It was found that the adjusted Syamlal gives the closest result compared to the experimental data. However, as discussed earlier, the drag modification, based only on minimum fluidization conditions like Syamlal, tends to overpredict the drag coefficient on the entire range of solid volume fraction.

Another noteworthy finding is, it is clear that both drag models underpredicted the pressure drop and bed expansion in the reactor. The two main reasons for that was the absence of proper representation of particle shape through a sphericity factor and the lack of precise simulation of particle size distribution. The present work only considers a perfect rounded sphere of corundum with a sphericity factor of 1 and considers one uniform size of the particle.

4) What is the bubbling and slugging flow regime?
The corundum particle used in this simulation has a diameter almost at the limit of the Geldart B range. The implication of this result is typically a narrow range of bubbling regimes, where at 14 kg/h of airflow, the bed just fluidized, and at 20 kg/h, which is less than two times Umf, the bed has started to slugging. It also has a lower terminal velocity, which is around 28 kg/h.

5) How can the bubbling and voidage behavior of the bed be described? How much is the significance of using Energy Minimization Multi-Scale (EMMS) bubbling drag model?
The bubble and voidage behavior was studied with three different drag models in 2D and 3D simulation domains. It can be concluded that the bubbles and voidage profile can be represented correctly with the 3D simulation domain, which considers the tuyere nozzle distributor. The bubbles will start small at the outlet of the nozzle in the center of the bed, and growing bigger while they travel across the bed. The radial voidage profile at a certain height has also confirmed these findings, where the highest voidage will be in the center, and the lowest one is towards the wall.

Comparing three different drag models, there are no significant differences in the bubbles or voidage profiles. Adjusted Syamlal has a slightly larger bubble while Gidaspow and EMMS bubbling has a bit smaller one. The expected better result of using EMMS bubbling drag model does not appear to have a considerable impact on the case of Geldart B or larger particles.

6) How is the effect of bubbling and voidage behavior on the heat transfer process?
It is found from the simulation that the increase of the bubbles frequency and size as represented on the voidage profile would improve the heat transfer process, as shown by the increase of the heat flux. The bubbles' occurrence on the bed plays a critical role in the improvement of the mass transfer from and to the vicinity of the radiant burner wall, thus increasing heat transfer. In contrast with the voidage, the increase of superficial gas velocity does not directly influence the heat flux.

7) How significant is the radiative heat transfer affecting the overall heat transfer process?
The radiative heat transfer has improved the overall heat flux in this bubbling fluidized bed reactor by about 16.11 %. Though it appears small, this contribution fits within the range of the findings of other proven works, which have a similar operating environment and particle size used on the simulation/experiment.

8) What is the proper radiative heat transfer model for this simulation?
There are two different radiative models performed in the simulation: first-order spherical harmonics method (P1) and discrete ordinate method (DO). They both presented a similar trend, and the magnitude of radiation, with P1, has a slightly higher value. However, there is a distinct difference that P1 shows the peculiar result of having the temperature lower than the lowest temperature set up on the system in adiabatic condition. In contrast, that is not the case for the DO, which is well known for its accuracy but a higher demand on computational cost. It is then concluded that for the current particular setup, the DO model is better to simulate the radiative transfer.

9) How close the CFD simulation result could depict the heat transfer process of the reactor?
There are no specific experimental data available for validating the heat transfer properties, thus only the final steady temperature values of five different thermocouples were used. Based on the comparison with the simulation result, the present work has not reached satisfied result due to overprediction of temperature above the bed and underprediction of bed temperature. Some improvements are required, as presented in the recommendations section.

6.2 Recommendations

1) Multi-fluid model (MFM)
The uniform one size of the corundum particle assumption used in the present work seems not realistic. As discussed earlier, at least two different groups of particle sizes, small and large groups of particles should be used. This then will upgrade the numerical method to the Multi-fluid model (MFM), which considers two particle sizes/phases. This has been proved by Ostermeier et al. [70] to have the closest agreement with the experiment.

2) Specific corundum properties
There are many assumptions used for the corundum properties in this simulation, while they have a significant influence on the hydrodynamic and heat transfer simulation. Some of them are, namely, maximum packing limit, restitution coefficient, sphericity factor, and specularity coefficient. Since the limited available data, the values were assumed based on the standard and generally accepted theory.

The maximum packing limit should not only refer to the typical value of 0.63 since it directly determines the estimated voidage of the bed, which also affects the pressure drop and fluidization height. As has been discussed, one the reason for the underprediction on the present study was due to the higher maximum packing limit, which seems not accurately represent the real value. One of the good methods to calculate it was proposed by Fedors et al.[60]. Same with the restitution coefficient, the default value of 0.9 cannot be trusted fully. As discussed by Goldschmidt et al.[75], it is critical to take the effect of the non-ideal particle-particle collision into account.

The sphericity factor and specularity coefficient influence have been discussed thoroughly before, especially for the solid and bubble velocity profile across the bed. Simply assuming the full spherical particle and no-slip wall condition might not represent the actual condition in the real setup.

3) Full 3D simulation
The full 3D simulation is recommended for the next following work based on the current findings. As the stepping stone of the 3D modeling work, the successful development of the present work should ease the model development on a higher level. It is because by only using the 3D model, the real hydrodynamic behavior can be predicted, and so does also the heat transfer process. This might also be the solution for the improvement of the heat transfer simulation, which currently still not reached the proper result due to the missing solid-gas interaction in the third direction. The primary constraint remains only the computational resources on the cluster account that needs to be granted more special access, e.g., four nodes with more than one-day simulation, and at least four tasks limit at one time.

4) Improved drag model
The discussion on the advantages and disadvantages of three different drag models used in this simulation was presented. The EMMS bubbling drag, which is expected to have better formulation on handling the bubbling fluidized bed simulation, seems to have their limitations when it comes to the Geldart B particle size. It might also be a good idea to introduce the new type of drag modification proposed by Vejahati et al.[71] and Esmaili et al.[72]: adjusted Di Felice model that gives the best result based on their researches.

5) Voidage measurement
At the time of simulation was performed, there is no bubbles profiles and voidage data obtained from the experiment. This situation leads to uncertainty on the validation of the model before performing the more extensive simulation. Hence, it would offer a great benefit if this data can be recorded through an installation of the voidmeter on the pilot plant. If it is not feasible, then the smaller prototype with the transparent glass setup would be much helpful to understand bubbles and the voidage behavior by using specific corundum particle size.

6) Heat transfer coefficient
In the present heat transfer simulation work, only the steady temperature profile of five different thermocouples were compared. While typically, on the basic heat transfer simulation, at least the averaged heat transfer coefficient from the experiment is known. At some more advanced research, the investigator observes the angular or wall to bed heat transfer coefficient, like the one performed by Ostermeier et al. [88]. Hence, some more data on validating the simulation are required to get a robust and reliable model development.

7) Heat transfer simulation method
As discussed earlier, one of the main reasons for the differences encountered in the simulation was due to the simulation method that was not precisely following the experimental condition. At which the steady-state of the experiment, the bed temperature was around 600 ^{o}C, with the air inlet of 400 ^{o}C. In the current study, the same temperature of the gas inlet and bed inside the reactor were assumed at 400 ^{o}C at the initial stage, with the purpose to simulate the heat transfer process that at the end will reach the bed temperature around 600 ^{o}C with the specific air flow rate. However, this was failed due to some higher flowrate was introduced first on the experiment before using the lower steady flowrate. Thus it is recommended on the future simulation; the bed temperature can be directly set on the 600 ^{o}C at the beginning of the simulation. This way, the heat flux will be much lower due to the smaller temperature differences, and the overprediction of air temperature on the steady-state can be reduced. By doing this, the temperature profile can be more comparable with the one from the experiment.

Appendices

A User Defined Functions (UDF)

A.1 EMMS drag model for 2D

```
#include "udf.h"
#define pi 4.*atan(1.)
#define diam2 4.96e-4

/* Define custom drag model */
DEFINE_EXCHANGE_PROPERTY(custom_drag,cell,mix_thread,s_col,f_col)
{
Thread *thread_g, *thread_s;
real x_vel_g, x_vel_s, y_vel_g, y_vel_s, abs_v, slip_x, slip_y, rho_g, rho_s, mu_g, reyp, void_g, cd, k_g_s;

/* find the threads for the gas (primary phase) and solids (secondary phase) */
thread_g = THREAD_SUB_THREAD(mix_thread, s_col);/* gas phase */
thread_s = THREAD_SUB_THREAD(mix_thread, f_col);/* solid phase*/

/* find phase velocities and properties*/
x_vel_g = C_U(cell, thread_g);
y_vel_g = C_V(cell, thread_g);
x_vel_s = C_U(cell, thread_s);
y_vel_s = C_V(cell, thread_s);

/* find slip velocities */
slip_x = x_vel_g - x_vel_s;
slip_y = y_vel_g - y_vel_s;

/* get the density and viscosity */
rho_g = C_R(cell, thread_g);
rho_s = C_R(cell, thread_s);
mu_g = C_MU_L(cell, thread_g);

/*compute slip*/
abs_v = sqrt(slip_x*slip_x + slip_y*slip_y);

/* gas vol frac*/
void_g = C_VOF(cell, thread_g);

/*compute Reynold's number*/
reyp = rho_g*abs_v*diam2/mu_g;

/*compute cd*/
if(reyp<1000)
        cd = 24*(1+0.15*pow(reyp,0.687))/reyp;
else
        cd = 0.44;

/*compute drag and return drag coeff, k_g_s*/
if(void_g<0.41)
        k_g_s = (150*(1-void_g)+1.75*reyp)*(1-void_g)*mu_g/void_g/diam2/diam2;
else if(0.41<=void_g  &  &  void_g<0.515)
        k_g_s = 0.75*cd*(1-void_g)*mu_g*reyp*pow(void_g,-2.65)/diam2/diam2*(0.017*exp(void_g/0.1256)-0.0328);
else
        k_g_s = 0.75*cd*(1-void_g)*mu_g*reyp*pow(void_g,-2.65)/diam2/diam2;

return k_g_s;

}
```

A.2 EMMS drag model for 3D

```
#include "udf.h"
#define pi 4.*atan(1.)
#define diam2 4.96e-4

/* Define custom drag model */
DEFINE_EXCHANGE_PROPERTY(custom_drag,cell,mix_thread,s_col,f_col)
{
Thread *thread_g, *thread_s;
real x_vel_g, x_vel_s, y_vel_g, y_vel_s, z_vel_g, z_vel_s, abs_v, slip_x, slip_y, slip_z, rho_g, rho_s, mu_g,
reyp, void_g, cd, k_g_s;

/* find the threads for the gas (primary phase) and solids (secondary phase) */
thread_g = THREAD_SUB_THREAD(mix_thread, s_col);/* gas phase */
thread_s = THREAD_SUB_THREAD(mix_thread, f_col);/* solid phase*/

/* find phase velocities and properties*/
x_vel_g = C_U(cell, thread_g);
y_vel_g = C_V(cell, thread_g);
z_vel_g = C_W(cell, thread_g);
x_vel_s = C_U(cell, thread_s);
y_vel_s = C_V(cell, thread_s);
z_vel_s = C_W(cell, thread_s);

/* find slip velocities */
slip_x = x_vel_g - x_vel_s;
slip_y = y_vel_g - y_vel_s;
slip_z = z_vel_g - z_vel_s;

/* get the density and viscosity */
rho_g = C_R(cell, thread_g);
rho_s = C_R(cell, thread_s);
mu_g = C_MU_L(cell, thread_g);

/*compute slip*/
abs_v = sqrt(slip_x*slip_x + slip_y*slip_y + slip_z*slip_z);

/* gas vol frac*/
void_g = C_VOF(cell, thread_g);

/*compute Reynold's number*/
reyp = rho_g*abs_v*diam2/mu_g;

/*compute cd*/
if(reyp<1000)
        cd = 24*(1+0.15*pow(reyp,0.687))/reyp;
else
        cd = 0.44;

/*compute drag and return drag coeff, k_g_s*/
if(void_g<0.41)
        k_g_s = (150*(1-void_g)+1.75*reyp)*(1-void_g)*mu_g/void_g/diam2/diam2;
else if(0.41<=void_g  &  &  void_g<0.515)
        k_g_s = 0.75*cd*(1-void_g)*mu_g*reyp*pow(void_g,-2.65)/diam2/diam2*(0.017*exp(void_g/0.1256)-0.0328);
else
        k_g_s = 0.75*cd*(1-void_g)*mu_g*reyp*pow(void_g,-2.65)/diam2/diam2;

return k_g_s;

}
```

A.3 Adjusted Gidaspow for sphericity factor 0.6

This drag model adjustment implements the sphericity factor on the standard Gidaspow model (sphericity factor of 1). The example used a sphericity factor of 0.6. Other values of the sphericity factor can be incorporated by changing 0.6 to the determined value.

```
#include "udf.h"
#define pi 4.*atan(1.)
#define diam2 4.96e-4

/* Define custom drag model */
DEFINE_EXCHANGE_PROPERTY(custom_drag,cell,mix_thread,s_col,f_col)
{
Thread *thread_g, *thread_s;
real x_vel_g, x_vel_s, y_vel_g, y_vel_s, abs_v, slip_x, slip_y, rho_g, rho_s, mu_g, reyp, void_g, cd, k_g_s;

/* find the threads for the gas (primary phase) and solids (secondary phase) */
thread_g = THREAD_SUB_THREAD(mix_thread, s_col);/* gas phase */
thread_s = THREAD_SUB_THREAD(mix_thread, f_col);/* solid phase*/

/* find phase velocities and properties*/
x_vel_g = C_U(cell, thread_g);
y_vel_g = C_V(cell, thread_g);
x_vel_s = C_U(cell, thread_s);
y_vel_s = C_V(cell, thread_s);

/* find slip velocities */
slip_x = x_vel_g - x_vel_s;
slip_y = y_vel_g - y_vel_s;

/* get the density and viscosity */
rho_g = C_R(cell, thread_g);
rho_s = C_R(cell, thread_s);
mu_g = C_MU_L(cell, thread_g);

/*compute slip*/
abs_v = sqrt(slip_x*slip_x + slip_y*slip_y);

/* gas vol frac*/
void_g = C_VOF(cell, thread_g);

/*compute Reynold's number*/
reyp = rho_g*abs_v*diam2/mu_g;

/*compute cd*/
cd = 24*(1+0.15*pow(reyp,0.687))/reyp;

/*compute drag and return drag coeff, k_g_s*/
if(void_g<=0.8)
        k_g_s = (150*(1-void_g)+1.75*reyp)*(1-void_g)*mu_g/void_g/(diam2*0.6)/(diam2*0.6);
else
        k_g_s = 0.75*cd*(1-void_g)*mu_g*reyp*pow(void_g,-2.65)/(diam2*0.6)/(diam2*0.6);

return k_g_s;

}
```

A.4 Effective thermal conductivity

```
#include "udf.h"
#include "math.h"
#define OMEGA 7.26E-3

/*Define effective thermal conductivity of solid*/
DEFINE_PROPERTY(conduct_solid,cell,thread)
{
Thread *mix, *sol, *gas;
mix = THREAD_SUPER_THREAD(thread);
sol = THREAD_SUB_THREAD(mix,1);
gas = THREAD_SUB_THREAD(mix,0);

real T_s = C_T(cell,sol);
real T_f = C_T(cell,gas);
real C1 = -2.86458333333338E-11;
real C2 = 1.21906250000002E-7;
real C3 = -0.000177135713541671;
real C4 = 0.0909158071562532;
real C5 = 0.760492182678705;
real D1 = 1.5797E-17;
real D2 = 9.46E-14;
real D3 = 2.2012E-10;
real D4 = -2.3758E-7;
real D5 = 1.7082E-4;
real D6 = -7.488E-3;

/*Temperature dependence microscopic conductivity*/
real K_S0 = C1*pow(T_s,4)+C2*pow(T_s,3)+C3*pow(T_s,2)+C4*T_s+C5;
real K_F0 = D1*pow(T_f,5)+D2*pow(T_f,4)+D3*pow(T_f,3)+D4*pow(T_f,2)+D5*T_f+D6;

real k_sol;
real void_max = 1.-10*SD_EPS;
real void_g = MIN( void_max, (1.-C_VOF(cell,thread)));

real a = K_S0/K_F0;
real b = 1.25*pow((1.-void_g)/void_g, 10./9.);
real t1 = (a-1.)/pow((1.-b/a),2.0)*(b/a)*log(a/b);
real t2 = -((b-1.)/(1.-b/a))-0.5*(b+1.);
real gm = (2./(1.-b/a))*(t1+t2);
real k_bs = K_F0*(OMEGA*a + (1.-OMEGA)*gm);
k_sol = k_bs/sqrt(1.-void_g);
return (k_sol);

}

/*Define effective thermal conductivity of gas*/
DEFINE_PROPERTY(conduct_gas,cell,thread)
{
Thread *mix, *sol, *gas;
mix = THREAD_SUPER_THREAD(thread);
sol = THREAD_SUB_THREAD(mix,1);
gas = THREAD_SUB_THREAD(mix,0);

real k_bf, k_gas;
real D1 = 1.5797E-17;
real D2 = 9.46E-14;
real D3 = 2.2012E-10;
real D4 = -2.3758E-7;
real D5 = 1.7082E-4;
real D6 = -7.488E-3;
```

```
real T_f = C_T(cell,gas);
real K_F0 = D1*pow(T_f,5)+D2*pow(T_f,4)+D3*pow(T_f,3)+D4*pow(T_f,2)+D5*T_f+D6;
real void_g = C_VOF(cell,thread);

/*Temperature dependence microscopic conductivity*/
k_bf = K_F0*(1.-sqrt(1.-void_g));
k_gas = k_bf/void_g;
return (k_gas);

}
```

A.5 Absorption and scattering coefficient

```
/*Define absorption coefficient of solids*/
DEFINE_PROPERTY(abs_solid,cell,thread)
{
real abs_sol;
real E = 0.871;
real d = 496E-6;
real v_f = C_VOF(cell,thread);
abs_sol = 3*v_f*E/(2*d);
return (abs_sol);

}

/*Define scattering coefficient of solids*/
DEFINE_PROPERTY(scat_sol,cell,thread)
{
real scat_sol;
real E = 0.871;
real d = 496E-6;
real v_f = C_VOF(cell,thread);
scat_sol = 3*v_f*(1-E)/(2*d);
return (scat_sol);

}
```

A.6 Temperature dependence air density and viscosity

```
/*Define temperature dependence density of air*/
DEFINE_PROPERTY(air_density, cell, thread)
{
real T_f = C_T(cell,thread);
real rho = 1.2*293./T_f;
return (rho);

}

/*Define temperature dependence viscosity of air*/
DEFINE_PROPERTY(air_viscosity, cell, thread)
{
real T_f = C_T(cell,thread);
real mu = 1.46E-06*pow(T_f,1.504)/(T_f + 120.);
return (mu);

}
```

Bibliography

[1] "Energy consumption decreased in 2018." [Online]. Available: https://www.cbs.nl/nl-nl/nieuws/2019/16/energieverbruik-gedaald-in-2018

[2] "Database - Eurostat." [Online]. Available: https://ec.europa.eu/eurostat/data/database

[3] "How the Netherlands Feeds the World." [Online]. Available: https://www.nationalgeographic.com/magazine/2017/09/holland-agriculture-sustainable-farming/

[4] "StatLine - Energy balance; supply, conversion and consumption." [Online]. Available: https://opendata.cbs.nl/statline/{#}/CBS/nl/dataset/83140NED/table?fromstatweb

[5] W. van't Hof, "Energy transition in the Netherlands – Outline of Dutch Energy Policy," no. October, pp. 1–11, 2018.

[6] R. Rauch, J. Hrbek, and H. Hofbauer, "Biomass gasification for synthesis gas production and applications of the syngas," *Wiley Interdisciplinary Reviews: Energy and Environment*, vol. 3, no. 4, pp. 343–362, 2014.

[7] O. Roelofsen, A. de Pee, and E. Speelman, "Accelerating the energy transition: cost or opportunity?" *McKinseyCompany*, p. 48, 2016. [Online]. Available: papers3://publication/uuid/044AC47F-0CB1-4352-8E06-68FCD5441F1B

[8] A. Demirbaş, "Biomass resource facilities and biomass conversion processing for fuels and chemicals," *Energy Conversion and Management*, vol. 42, no. 11, pp. 1357–1378, 2001.

[9] I. Dincer, "Green methods for hydrogen production," *International Journal of Hydrogen Energy*, vol. 37, no. 2, pp. 1954–1971, 2012. [Online]. Available: http://dx.doi.org/10.1016/j.ijhydene.2011.03.173

[10] Y. Kalinci, A. Hepbasli, and I. Dincer, "Biomass-based hydrogen production: A review and analysis," *International Journal of Hydrogen Energy*, vol. 34, no. 21, pp. 8799–8817, 2009. [Online]. Available: http://dx.doi.org/10.1016/j.ijhydene.2009.08.078

[11] D. Das and T. N. Veziroğlu, "Hydrogen production by biological processes: A survey of literature," *International Journal of Hydrogen Energy*, vol. 26, no. 1, pp. 13–28, 2001.

[12] S. Sharma and P. N. Sheth, "Air-steam biomass gasification: Experiments, modeling and simulation," *Energy Conversion and Management*, vol. 110, pp. 307–318, 2016. [Online]. Available: http://dx.doi.org/10.1016/j.enconman.2015.12.030

[13] S. Czernik, R. Evans, and R. French, "Hydrogen from biomass-production by steam reforming of biomass pyrolysis oil," *Catalysis Today*, vol. 129, no. 3-4, pp. 265–268, 2007.

[14] P. Tanger, J. L. Field, C. E. Jahn, M. W. DeFoort, and J. E. Leach, "Biomass for thermochemical conversion: Targets and challenges," *Frontiers in Plant Science*, vol. 4, no. JUL, pp. 1–20, 2013.

[15] H. Brenner, A. Acrivos, J. E. Bailey, and L.-s. Fan, *Butterworth-Heinemann Series in Chemical Engineering*, 1994.

[16] C. Srinivasakannan and N. Balasubramanian, "The significance of indirectly heated gasifiers for the generation of medium calorific value syngas through biomass gasification," *Energy Sources, Part A: Recovery, Utilization and Environmental Effects*, vol. 32, no. 17, pp. 1579–1586, 2010.

[17] H. Hofbauer and M. Materazzi, *Waste gasification processes for SNG production*. Elsevier Inc., 2019. [Online]. Available: http://dx.doi.org/10.1016/B978-0-12-815554-7.00007-6

[18] C. M. V. D. Meijden, H. J. Veringa, A. V. D. Drift, and B. J. Vreugdenhil, "The 800 kWth allothermal biomass gasifier MILENA," *16th European Biomass Conference*, no. June, pp. 2–6, 2008.

[19] J. Karl, "Biomass heat pipe reformer-design and performance of an indirectly heated steam gasifier," *Biomass Conversion and Biorefinery*, vol. 4, no. 1, pp. 1–14, 2014.

[20] C. M. van der Meijden, A. van der Drift, and B. Vreugdenhil, "Experimental results from the allothermal biomass gasifier Milena," *15th European Biomass Conference*, no. May, pp. 7–11, 2007.

[21] A. van der Drift, C. M. van der Meijden, and H. Boerrigter, "MILENA gasification technology for high efficient SNG production from biomass," *October*, no. October, pp. 17–21, 2005.

[22] L. Rabou and M. Overwijk, "The Alkmaar 4 MW bio-SNG demo project," no. March, 2016. [Online]. Available: https://www.ecn.nl/publications/PdfFetch.aspx?nr=ECN-M--16-032

[23] W. Zhong, A. Yu, G. Zhou, J. Xie, and H. Zhang, "CFD simulation of dense particulate reaction system: Approaches, recent advances and applications," *Chemical Engineering Science*, vol. 140, pp. 16–43, 2016. [Online]. Available: http://dx.doi.org/10.1016/j.ces.2015.09.035

[24] J. A. M. Kuipers, K. J. V. Duin, F. P. H. V. Beckum, and W. P. M. V. Swaaij, "A Numerical Model of Gas Fluidized Beds," *Chemical Engineering Science*, vol. 47, no. 8, pp. 1913–1924, 1992.

[25] F. Taghipour, N. Ellis, and C. Wong, "Experimental and computational study of gas-solid fluidized bed hydrodynamics," *Chemical Engineering Science*, vol. 60, no. 24, pp. 6857–6867, 2005.

[26] Y. Tsuji, "Multi-scale modeling of dense phase gas-particle flow," *Chemical Engineering Science*, vol. 62, no. 13, pp. 3410–3418, 2007.

[27] C. L. Wu, O. Ayeni, A. S. Berrouk, and K. Nandakumar, "Parallel algorithms for CFD-DEM modeling of dense particulate flows," *Chemical Engineering Science*, vol. 118, pp. 221–244, 2014.

[28] L. Lu, A. Konan, and S. Benyahia, "Influence of grid resolution, parcel size and drag models on bubbling fluidized bed simulation," *Chemical Engineering Journal*, vol. 326, pp. 627–639, 2017.

[29] "Biomass Steam Reforming | Petrogas." [Online]. Available: https://www.petrogas.nl/process-systems/biomass-steam-reforming/

[30] J. Xie, W. Zhong, B. Jin, Y. Shao, and H. Liu, "Three-dimensional eulerian-eulerian modeling of gaseous pollutant emissions from circulating fluidized-bed combustors," *Energy and Fuels*, vol. 28, no. 8, pp. 5523–5533, 2014.

[31] D. Geldart, "Types of Gas Fluidization," *Powder Technology*, vol. 7, pp. 285–292, 1973.

[32] H. Toomey, R. and Johnstone, "Gas Fluidization of Solid Particles," *Chemical Engineering Progress*, vol. 48, pp. 220–226, 1952. [Online]. Available: https://www.scirp.org/(S(351jmbntvnsjt1aadkposzje))/reference/ReferencesPapers.aspx?ReferenceID=1984946

[33] J. Werther, "Ullmann's Encyclopedia of Industrial Chemistry," *Journal of Chemical Education*, vol. 38, no. 8, pp. 382–391, 2012.

[34] A.B. Whitehead, *Academic Press*, p. 173, 1985.

[35] M. Yamazaki, K. Fukuta, and J. Tokumoto, *Proc. 3rd World Cong. of Chem. Eng*, 1986.

[36] J. Lin, M. M. Chen, and B. Chao, *AIChE Journal*, vol. 31, p. 465, 1985.

[37] T. Tsutsui, S. Furusaki, and T. Miyauchi, *Kagaku Kogaku Ronbunshu*, vol. 6, p. 501, 1980.

[38] Golfers, *Kagaku Kogaku Ronbunshu*, vol. 8, p. 464, 1982.

[39] L. Glicksman, W. Lord, and M. Sakagami, *Chem. Eng. Sci.*, vol. 42, p. 479, 1987.

[40] S. Mori and C. Wen, *AIChE Journal*, vol. 21, p. 109, 1975.

[41] P. Stewart and J. Davidson, *Powder Technology*, vol. 1, p. 60, 1965.

[42] J. Baeyens and D. Geldart, *Chem. Eng. Sci.*, vol. 29, p. 255, 1974.

[43] H. S. Mickley and D. F. Fairbanks, "Mechanism of heat transfer to fluidized beds," *AIChE Journal*, vol. 1, no. 3, pp. 374–384, 1955.

[44] V. N. Korolev; N. I. Syromyatnikov; E.M. Tolmachev, "Structure of A Fixed Bed and A Fluidized Bed of Material Near An Immersed Surface (Wall)," no. 28, pp. 1475–1478, 1969.

[45] ANSYS® Academic Research Mechanical, "ANSYS Fluent Theory Guide," *ANSYS Inc., USA*, vol. 15317, no. November, pp. 1–759, 2013. [Online]. Available: http://www.pmt.usp.br/ACADEMIC/martoran/NotasModelosGrad/ANSYSFluentTheoryGuide15.pdf

[46] P. Zehner and E. U. Schlünder, "Warmeleitfahigkeit von Schuttungen bei mässigen Temperaturen," *Chemie Ingenieur Technik*, vol. 42, pp. 933–941, 1970.

[47] D. J. Gunn, "Transfer of heat or mass to particles in fixed and fluidised beds," *International Journal of Heat and Mass Transfer*, vol. 21, no. 4, pp. 467–476, 1978.

[48] M. F. Modest, *Radiative Heat Transfer*. Elsevier Inc., 2013. [Online]. Available: http://dx.doi.org/10.1016/B978-0-12-386944-9.50027-3

[49] C.-L. Tien and B. L. Drolen, "Thermal Radiation In Particulate Media With Dependent And IndependentT Scattering," *Annual Review of Heat Transfer*, vol. 1, no. 1, pp. 1–32, 1987. [Online]. Available: https://doi.org/10.1615%2Fannualrevheattransfer.v1.30

[50] R. I. Singh, A. Brink, and M. Hupa, "CFD modeling to study fluidized bed combustion and gasification," *Applied Thermal Engineering*, vol. 52, no. 2, pp. 585–614, 2013.

[51] ANSYS Inc., "ANSYS ICEM CFD User Manual," *Knowledge Creation Diffusion Utilization*, vol. 15317, no. October, pp. 724–746, 2012.

[52] J. Ding and D. Gidaspow, "A bubbling fluidization model using kinetic theory of granular flow," *AIChE Journal*, vol. 36, no. 4, pp. 523–538, 1990.

[53] M. Syamlal, W. Rogers, and T. O'Brien, "MFIX documentation theory guide," *Technology*, vol. 1004, no. December, 1993. [Online]. Available: http://www.osti.gov/servlets/purl/10145548-7h5O7m/native/

[54] Z. Shi, W. Wang, and J. Li, "A bubble-based emms model for gas–solid bubbling fluidization," *Chemical Engineering Science*, vol. 66, no. 22, pp. 5541 – 5555, 2011. [Online]. Available: http://www.sciencedirect.com/science/article/pii/S0009250911004817

[55] M. Syamial and T. J. O'Brien, "Computer simulation of bubbles in a fluidized bed," *Fluidization and Fluid Particle Systems: Fundamentals and Applications. Papers Presented At Aiche Annual Meeting, Washington,*, no. 270) }edited by L. S. Fan], New York, U.S.A., American Institute Chemical Engineers, 1989, p.22-31. (IS, 1989.

[56] J. F. Richardson and W. N. Zaki, "Sedimentation and fluidization: Part I," *Process Safety and Environmental Protection: Transactions of the Institution of Chemical Engineers, Part B*, vol. 75, no. Suppl, pp. S82–S100, 1997. [Online]. Available: http://dx.doi.org/10.1016/S0263-8762(97)80006-8

[57] J. Garslde and M. R. Al-Dibouni, "Velocity-Voidage Relationships for Fluidization and Sedimentation in Solid-Liquid Systems," *Industrial and Engineering Chemistry Process Design and Development*, vol. 16, no. 2, pp. 206–214, 1977.

[58] S. Sundaresan, "Modeling the hydrodynamics of multiphase flow reactors: Current status and challenges," *AIChE Journal*, vol. 46, no. 6, pp. 1102–1105, 2000.

[59] J. Li and M. Kwauk, *The Energy-Minimization-Multi-Scale Method*, 1994.

[60] R. F. Fedors and R. F. Landel, "An Empirical method of estimating the void fraction in mixtures of uniform particles of different size," *Powder Technology*, vol. 23, no. 2, pp. 225–231, 1979.

[61] D. Gidaspow, R. Bezburuah, and J. Ding, "Hydrodynamics of circulating fluidized beds: Kinetic theory approach."

[62] D. G. Schaeffer, "Instability in the evolution equations describing incompressible granular flow," *Journal of Differential Equations*, vol. 66, no. 1, pp. 19–50, 1987.

[63] C. K. K. Lun, S. B. Savage, D. J. Jeffrey, and N. Chepurniy, "Kinetic theories for granular flow: inelastic particles in couette flow and slightly inelastic particles in a general flowfield," *Journal of Fluid Mechanics*, vol. 140, p. 223–256, 1984.

[64] Chapman and Cowling, "The Mathematical Theory of Non-Uniform Gases," 1970.

[65] P. C. Johnson and R. Jackson, "Frictional–collisional constitutive relations for granular materials, with application to plane shearing," *Journal of Fluid Mechanics*, vol. 176, p. 67–93, 1987.

[66] J. O. Hinze, *Turbulence*, 2nd ed. New York, N.Y. : McGraw-Hill, 1975, includes bibliographical references and indexes. [Online]. Available: http://www.ulb.tu-darmstadt.de/tocs/84073039.pdf

[67] C. Simonin, P. Viollet *et al.*, "Predictions of an oxygen droplet pulverization in a compressible subsonic coflowing hydrogen flow," *Numerical Methods for Multiphase Flows*, vol. 91, no. 2, pp. 65–82, 1990.

[68] S. Gosavi, N. Kulkarni, C. S. Mathpati, and D. Mandal, "CFD modeling to determine the minimum fluidization velocity of particles in gas-solid fluidized bed at different temperatures," *Powder Technology*, vol. 327, pp. 109–119, 2018. [Online]. Available: https://doi.org/10.1016/j.powtec.2017.12.026

[69] H. J. Subramani, M. B. Mothivel Balaiyya, and L. R. Miranda, "Minimum fluidization velocity at elevated temperatures for Geldart's group-B powders," *Experimental Thermal and Fluid Science*, vol. 32, no. 1, pp. 166–173, 2007.

[70] P. Ostermeier, A. Vandersickel, S. Gleis, and H. Spliethoff, "Three dimensional multi fluid modeling of Geldart B bubbling fluidized bed with complex inlet geometries," *Powder Technology*, vol. 312, pp. 89–102, 2017. [Online]. Available: http://dx.doi.org/10.1016/j.powtec.2017.02.015

[71] F. Vejahati, N. Mahinpey, N. Ellis, and M. B. Nikoo, "CFD simulation of gas-solid bubbling fluidized bed: A new method for adjusting drag law," *Canadian Journal of Chemical Engineering*, vol. 87, no. 1, pp. 19–30, 2009.

[72] E. Esmaili and N. Mahinpey, "Adjustment of drag coefficient correlations in three dimensional CFD simulation of gas-solid bubbling fluidized bed," *Advances in Engineering Software*, vol. 42, no. 6, pp. 375–386, 2011. [Online]. Available: http://dx.doi.org/10.1016/j.advengsoft.2011.03.005

[73] H. Zhu, J. Zhu, G. Li, and F. Li, "Detailed measurements of flow structure inside a dense gas-solids fluidized bed," *Powder Technology*, vol. 180, no. 3, pp. 339–349, 2008.

[74] N. Xie, F. Battaglia, and S. Pannala, "Effects of using two- versus three-dimensional computational modeling of fluidized beds. Part I, hydrodynamics," *Powder Technology*, vol. 182, no. 1, pp. 1–13, 2008.

[75] M. J. Goldschmidt, J. A. Kuipers, and W. P. Van Swaaij, "Hydrodynamic modelling of dense gas-fluidised beds using the kinetic theory of granular flow: Effect of coefficient of restitution on bed dynamics," *Chemical Engineering Science*, vol. 56, no. 2, pp. 571–578, 2001.

[76] J. A. Kuipers, W. Prins, and W. P. Van Swaaij, "Numerical calculation of wall[U+2010]to[U+2010]bed heat[U+2010]transfer coefficients in gas[U+2010]fluidized beds," *AIChE Journal*, vol. 38, no. 7, pp. 1079–1091, 1992.

[77] S. C. Saxena, K. K. Srivastava, and R. Vadivel, "Experimental techniques for the measurement of radiative and total heat transfer in gas fluidized beds: A review," *Experimental Thermal and Fluid Science*, vol. 2, no. 3, pp. 350–364, 1989.

[78] A. I. Il'chenko, V. S. Pikashov, and K.E. Makhorin, "Study of Radiative Heat Transfer in a Fluidized Bed," *J. Eng. Phys.*, vol. 14, pp. 321–324, 1968.

[79] P. Basu, "Bed-to-Wall Heat Transfer in a Fluidized Bed Coal Combustor, in Fluidization: Application to Coal Conversion Processes," *AIChE Symp.*, vol. 74, pp. 187–193, 1978.

[80] A. Mathur and S. C. Saxena, "Total and Radiative Heat Transfer to an Immersed Surface in a Gas-Fluidized Bed," *AIChE Journal*, vol. 33, pp. 1124–1135, 1987.

[81] R. Biwas and R. C. Strawn, "Tetrahedral and hexahedral mesh adaptation for CFD problems," 1395.

[82] *ANSYS Fluent User Guide 15.0*, 2013, vol. 15317, no. November.

[83] *ANSYS Fluent Tutorial Guide 18.0*, 2018, no. April.

[84] S. Silvestri and D. Roekaerts, "Mixed Convection and Radiation Heat Transfer in Porous Media for Solar Thermal Applications," *Convective Heat Transfer in Porous Media*, pp. 227–262, 2019.

[85] S. Cloete, S. T. Johansen, and S. Amini, "Grid independence behaviour of fluidized bed reactor simulations using the Two Fluid Model: Detailed parametric study," *Powder Technology*, vol. 289, pp. 65–70, 2016. [Online]. Available: http://dx.doi.org/10.1016/j.powtec.2015.11.011

[86] H. Enwald, E. Peirano, and A. E. Almstedt, "Eulerian two-phase flow theory applied to fluidization," *International Journal of Multiphase Flow*, vol. 22, no. SUPPL. 1, pp. 21–66, 1996.

[87] S. Cloete, A. Zaabout, S. T. Johansen, M. van Sint Annaland, F. Gallucci, and S. Amini, "The generality of the standard 2D TFM approach in predicting bubbling fluidized bed hydrodynamics," *Powder Technology*, vol. 235, pp. 735–746, 2013. [Online]. Available: http://dx.doi.org/10.1016/j.powtec.2012.11.041

[88] P. Ostermeier, F. Dawo, A. Vandersickel, S. Gleis, and H. Spliethoff, "Numerical calculation of wall-to-bed heat transfer coefficients in Geldart B bubbling fluidized beds with immersed horizontal tubes," *Powder Technology*, vol. 333, pp. 193–208, 2018. [Online]. Available: https://doi.org/10.1016/j.powtec.2018.04.028

AUGUST, 2020

FIDLLAN NURKHOIR

Student number : 4796500

Project duration : January 2020 - August 2020

Daily supervisor : Christos Tsekos M.Sc.

Thesis Committee :

Prof. Dr. Ir. J. T. Padding	Supervisor-Chair
Prof. Dr. D. J. E. M. Roekaerts	Supervisor
Dr. E. M. Moghaddam	Supervisor
Dr. Ir. J. W. R. Peeters	

TU Delft Delft University of Technology

lpdp lembaga pengelola dana pendidikan

PETROGAS GAS SYSTEMS